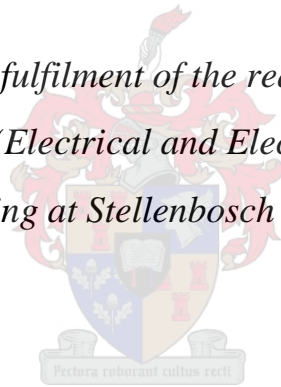# Pasteurisation of Rooibos Tea Leaves Using Microwave Radiation and the Development of Associated Hardware

by

Bernardus Johannes van der Merwe

Thesis presented in partial fulfilment of the requirements for the degree of Master of Engineering (Electrical and Electronic) in the Faculty of Engineering at Stellenbosch University

Supervisor: Professor JB de Swardt

March 2020

DECLARATION

By submitting this thesis electronically, I declare that the entirety of the work contained therein is my own, original work, that I am the sole author thereof (save to the extent explicitly otherwise stated), that reproduction and publication thereof by Stellenbosch University will not infringe any third party rights and that I have not previously in its entirety or in part submitted it for obtaining any qualification.

Date: March 2020

Abstract

Rooibos tea is a herbal tea that is gaining popularity worldwide. In order for it to be safe for consumption by consumers, the tea leaves are pasteurised with steam in commercial processing plants. The viability of using microwave radiation to pasteurise Rooibos tea leaves was investigated in this research project. Hardware associated with these microwave systems, in the form of microwave applicators, a directional coupler and a prototype power detector, was also developed. This project showed that microwave radiation may be an alternative way to process Rooibos tea leaves and may produce a higher quality product.

Control circuitry that controlled the output power of the microwave generator (magnetron) was developed. It used a TRIAC to control the phase angle of the supply voltage to the transformer that supplied power to the magnetron.

Two special applicators were developed in order to conduct pasteurisation experiments on the Rooibos tea leaves. An air-cooling applicator cooled down a sample of Rooibos tea leaves while it was being irradiated. This was to test whether the so-called non-thermal, or microwave specific, effects of microwave radiation was able to pasteurise tea leaves at ambient temperatures. The other applicator was a travelling wave applicator that heated samples evenly. The temperature of the sample was measured and a control system was developed that could heat a sample to a desired temperature.

Tests were conducted in order to determine the viability of microwave pasteurisation of Rooibos tea leaves. Sterilised Rooibos tea leaves, which were inoculated with bacteria, were used. The tests showed that Gram-negative *Escherichia coli* was eliminated from the samples after being irradiated for 2.5 minutes at $90\,°C$. Gram-positive bacteria (*Lactococcus lactis*) was also tested. After a 5 minute period of being irradiated at $100\,°C$, a four-fold reduction in bacteria was observed.

Microwave pasteurisation at ambient temperatures was tested. The tests showed no significant reduction in bacteria and it was concluded that any microwave specific effects were insignificant at low temperatures.

In order to measure the power output of the microwave system, a directional coupler and power detector was developed. The directional coupler used an innovative design to achieve a constant coupling of $35\,dB$ and a directivity greater than $20\,dB$ over the microwave oven frequencies of $2.4 - 2.5\,GHz$. The power detector was a prototype that showed that a thermistor-based design can produce an output that was linearly proportional to the input power to the power detector.

It was concluded that microwave radiation appears to be a viable method of pasteurising Rooibos tea leaves, but that more testing is required using unsterilised Rooibos tea leaves. The hardware that was developed worked well. The prototype power detector can be developed further by using high frequency thermistors.

Opsomming

Rooibos tee is 'n kruietee wat tans wêreld-wyd meer bekend raak. Om te verseker dat die tee veilig is vir verbruikers word die tee blare gepasteuriseer met stoom in kommersiële fabrieke. Die moontlikheid van die gebruik van mikrogolfstraling vir pasteurisering van Rooibos tee blare is in hierdie navorsingsprojek ondersoek. Hardeware wat verband hou met hierdie mikrogolf stelsels, in die vorm van mikrogolf toedieners, 'n direksionele-koppelaar en 'n prototipe drywingsdetektor, is ook ontwikkel. Hierdie projek het getoon dat mikrogolfstraling 'n alternatiewe manier kan wees om Rooibos tee blare te verwerk en kan moontlik 'n hoër kwaliteit produk lewer.

'n Beheerstroombaan is ontwikkel wat die uittree drywing van die mikrogolf-bron (magnetron) beheer. Dit het 'n TRIAC gebruik om die fase hoek van die toevoerspanning aan die magnetron se transformator te beheer.

Twee spesiale toedieners is ontwikkel om pasteurisasie eksperimente op die Rooibos tee blare uit te oefen. 'n Lugverkoeling toediener het 'n monster van Rooibos tee blare afgekoel terwyl dit bestraal is. Dit was om te toets of die sogenaamde nie-termiese, of mikrogolf-spesifieke, effekte van mikrogolfstraling in staat was om tee blare te pasteurisasie teen kamertemperatuur. Die ander toediener was 'n golfleier toediener wat die monsters eweredig verhit het. Die temperatuur van die monster is gemeet en 'n beheerstelsel is ontwikkel wat 'n monster tot 'n gestelde temperatuur kon verhit.

Toetse is gedoen om die moontlikheid van mikrogolf-pasteurisasie van Rooibos tee blare te bepaal. Gesteriliseerde Rooibos tee blare, wat met bakterieë ingeënt is, is gebruik. Die toetse het getoon dat alle Gram-negatiewe *Escherichia coli* selle dood was nadat dit bestraal is vir 2.5 minute teen $90\,°C$. Gram-positiewe bakterieë (*Lactococcus lactis*) is ook getoets. Na 5 minute se bestraling teen $100\,°C$ is 'n viervoudige afname in bakterieë waargeneem.

Mikrogolf-pasteurisasie teen kamertemperatuur is getoets. Die toetse het geen beduidende afname in bakterieë getoon nie en die aanname is dus gemaak dat enige mikrogolf-spesifieke effekte geen impak gehad het teen lae temperature nie.

Om die uittree drywing van die mikrogolf stelsel te meet is 'n direksionele-koppelaar en 'n drywingsdetektor ontwikkel. Die direksionele-koppelaar het 'n innoverende ontwerp gebruik om 'n konstante koppeling van $35\,dB$ en 'n direktiwiteit groter as $20\,dB$ oor die mikrogolf-oondfrekwensies van $2.4 - 2.5\,GHz$. Die drywingsdetektor was 'n prototipe wat getoon het dat 'n termistor gebaseerde ontwerp 'n uittree kan produseer wat lineêr eweredig is aan die intree drywing.

Daar is tot die gevolgtrekking gekom dat mikrogolfstraling 'n moontlike metode van pasteurisasie van Rooibos tee blare blyk te wees, maar dat meer toetse vereis word met die gebruik van rou Rooibos tee blare. Die hardeware wat ontwikkel is, het goed gewerk. Die prototipe drywingsdetektor kan verder ontwikkel word deur die gebruik van hoë frekwensie termistors.

Acknowledgements

A thesis is not a one-man project. Thank you to all who were involved in making this project a reality. I would like to thank the following people:

Prof de Swardt for his continued guidance and mentoring throughout this project. Thank you for giving me the freedom to explore.

Dr van Staden for many hours invested into help with all the microbiological tests done in this project. Thank you for showing me how it's done and answering many questions.

Wessel Croukamp for his clever, practical advice and attention to detail in the construction of components.

Anneke Bester for her friendly assistance in the high frequency lab.

Murray in the electronics lab for his assistance in finding tucked-away components.

Wynand van Eeden for his assistance with PCB manufacturing.

Prisca, Jordan, Devon and Gunther for all assisting in one way or another. Sometimes verbal processing or encouragement was all that was needed. Thank you, Gunther and Jacques, for your editing skills.

My parents for loving, supporting and backing me throughout my studies (and my life). Thank you Mieneke, Joy and Hubert for loving your "little brother".

Jesus for the unmerited favour that he keeps on giving.

Table of contents

List of figures

List of tables

Abbreviations

AC	Alternating Current
ADC	Analog to digital converter
AWR	National Instruments AWR Design Environment 14, also known as Microwave Office
CFU	Colony-forming unit
CST	CST Studio Suite 2019
CW	Continuous wave
DC	Direct Current
E. coli	*Escherichia coli*
IC	Integrated Circuit
ISM	Industrial, Scientific and Medical
L. lactis	*Lactococcus lactis*
NTC	Negative thermal coefficient
OCR	Output Compare Register
PCB	Printed Circuit Board
Pot	Potentiometer
PTC	Positive thermal coefficient
RF	Radio Frequency
SMD	Surface Mount Device
S-parameters	Scattering parameters
T-parameters	Transmission parameters
VNA	Vector Network Analyser
VSWR	Voltage Standing Wave Ratio
W	Watt

1 Introduction

1.1 Background

The use of microwave radiation as a method for pasteurisation has been investigated at Stellenbosch University since 2014 as part of the Electro Heating Group. Both dry and liquid media has been investigated in the form of Rooibos tea leaves and liquid growth media. The research has made use of modified conventional microwave ovens. The modifications allowed the output power of the microwave oven to be controlled so that a sample could be heated to a desired temperature or with a desired power level (as opposed to the conventional duty cycle control method). Therefore, much more control was possible which allowed for scientific investigation to take place [1], [2].

This research project continued the investigation into the pasteurisation of Rooibos tea leaves. Rooibos tea is a herbal tea that is grown only in South Africa and is gaining popularity worldwide due to its health benefits [3], [4]. Rooibos tea leaves naturally have a high microbial load, particularly due to the fermentation process that the tea goes through. Therefore, the tea needs to be processed in order to be safe for consumption, according to local and international standards [5].

Steam is currently used in industry to pasteurise Rooibos tea leaves. Rooibos tea leaves are exposed to steam over a period of two and a half minutes and heats up to about $90\ °C$. The two disadvantages of steam are that it adds moisture to the tea leaves, which causes some of the beneficial compounds in the tea to dissolve, and that it uses high temperatures, which causes some of the volatile compounds in the tea to be broken down. Therefore, an alternative method of pasteurisation may be able to deliver a higher quality product [5].

This research project investigated microwave radiation as an alternative method of pasteurising Rooibos tea leaves. Microwave radiation does not add moisture to the product that is irradiated. Furthermore, it is well known that microwave radiation induces seemingly non-thermal effects on bacteria, termed microwave specific effects – an effect that, if pronounced enough, held the potential to pasteurise the tea leaves at ambient temperatures.

Previous tests on Rooibos tea leaves conducted by van der Merwe [2] investigated the effect of low power ($150\ W$) microwave radiation on Rooibos tea leaves. However, the results were inconclusive. Batching issues were observed, where control samples taken from the same source varied greatly in the number of bacteria present. Also, for the observed temperature profiles, a decrease in bacteria was expected, whereas an increase was sometimes observed, as shown in Figure 1.1.
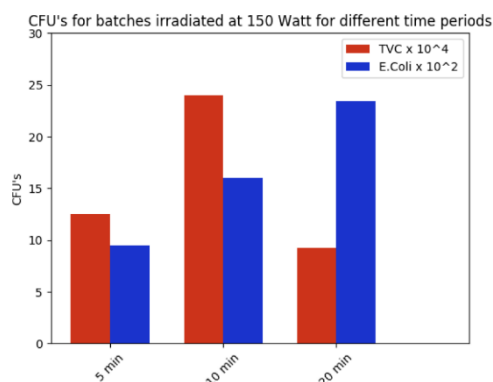
Figure 1.1: Tests conducted by van der Merwe [2] displayed an increase in bacteria, even after long exposure times with high temperatures.

The hardware that van der Merwe [2] used was able to measure how much microwave power was absorbed by a sample. A waveguide directional coupler and diode-based power detectors were used. These were expensive off-the-shelf components that significantly increased the cost of the system. In

addition, the diode-based power detectors had a non-linear output. Therefore, computationally expensive processing was required to determine the average power delivered to the sample.

1.2 Problem statement

Rooibos tea has many health benefits, but the quality of the tea is lowered by the steam processing used to pasteurise the tea leaves. The aim of this research project was to investigate an alternative pasteurisation process that uses microwave radiation. A secondary aim was to develop hardware that was needed to control and measure the microwave system.

1.3 Objectives

The objectives of this project were as follows:

1. To develop a system that could investigate the pasteurisation of Rooibos tea leaves. This included the following:
   1.1. The output power from the microwave generator (magnetron) needed to be controllable.
   1.2. An applicator was required that could irradiate Rooibos tea leaves while they were also being cooled down. The applicator needed to have an even distribution of microwave power inside it.
   1.3. Another applicator was required that could measure the temperature of a sample so that the temperature could be controlled. A well-defined distribution of microwave power was required to guarantee that the sample was evenly heated.
2. To test whether microwave radiation was able to pasteurise Rooibos tea leaves. The presence of a significant microwave specific effect also needed to be tested in order to establish whether ambient temperature pasteurisation was possible.
3. To develop hardware that would assist future developments of the Electro Heating Group in developing similar systems. These included:
   3.1. A low-cost waveguide directional coupler.
   3.2. A low cost, linear power detector.

1.4 Chapter format
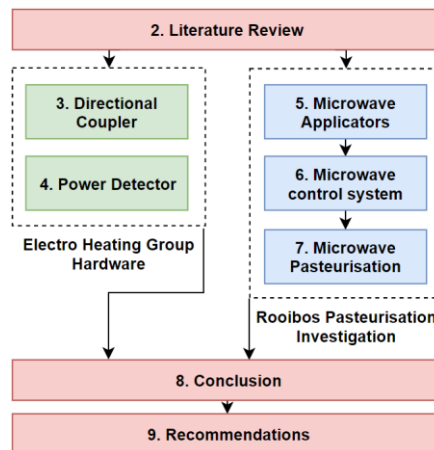
Figure 1.2: Layout of the chapters in this thesis.

2   Literature review

The literature review firstly investigates microwaves as a broader topic. It discusses how microwave heating works, how the hardware of a microwave oven works and so on. It then discusses some microbiology terms that may be unfamiliar to readers who do not have a background in microbiology. Lastly, it discusses Rooibos tea and how it is processed commercially.

3   Directional coupler

The directional coupler is one of the two components that were developed for future use by the Electro Heating Group. An innovative waveguide directional coupler design is presented that operates over the microwave oven frequencies. The design was simple and therefore inexpensive to manufacture.

4   Power detector

The power detector is the other component that was developed for future use by the Electro Heating Group. This chapter presents a prototype thermistor-based power detector. The main advantage of the power detector was that the output was linearly proportional to the input power.

5   Microwave applicators

This chapter starts off the discussion into pasteurising Rooibos tea leaves using microwave radiation. The two applicators that were developed for testing the pasteurisation of Rooibos tea leaves are discussed in this chapter. The two applicators that were developed was the air-cooling applicator and the travelling wave applicator.

6   Microwave control system

The discussion on pasteurising Rooibos tea leaves are continued in this chapter. This chapter discusses the hardware that was used to control the output power of the magnetron. It also discusses the control system that was developed to heat samples to a set temperature, and it explains the algorithm that controlled the timing of the TRIAC.

7   Microwave pasteurisation

The pasteurisation of Rooibos tea leaves using microwave radiation is investigated in this chapter. In collaboration with the Department of Microbiology, five tests were carried out to investigate the viability of using microwave radiation to pasteurise Rooibos tea leaves.

8   Conclusion

Concluding remarks on all the work that was done is given in this chapter.

9   Recommendations

Final recommendations and next steps to be taken are given in this chapter.

Appendix A Calculations

Additional calculations are discussed.

Appendix B Transitions

Several bends and transitions that were relevant to Ch. 3 are discussed in this appendix.

2 Literature review

2.1 Chapter introduction and summary

This literature review investigates microwaves, some microbiology and Rooibos tea.

Various factors pertaining to microwaves are investigated. The theory behind microwave heating and the operation of the magnetron are discussed. The circuitry of a conventional microwave oven and power control methods are investigated. Overcoming the issues with uneven heating is discussed, after which microwave specific effects and sterilisation are discussed.

The section on microbiology briefly discusses some definitions that may be helpful for those with little prior knowledge of concepts used in the field of microbiology.

Lastly, Rooibos tea is discussed. The current processing method and the food safety standards are investigated.

2.2 Microwave ovens

2.2.1 Microwaves and microwave ovens

Microwaves refer to a frequency range in the electromagnetic spectrum of between 1 and 300 GHz [6] (although this definition is not exactly clear – Pozar [7, p. 1], for example, defines it from 3 to 300 GHz).

A **microwave oven** is a device that irradiates food with microwave radiation in order to heat it up. Most microwave ovens make use of the 2.4 GHz Industrial, Scientific and Medical (ISM) frequency band, which stretches from 2.4 to 2.5 GHz. Some microwave ovens operate in the 0.9 or 5.8 GHz ISM bands [8].

Microwave radiation is often confused with ionizing radiation such as gamma rays. The word 'radiation' simply refers to the emission of energy as waves or as particles [9]. Microwaves are inherently non-ionizing and are therefore not radioactive.

2.2.2 Microwave heating

Microwave radiation can heat up insulating materials. The mechanisms that cause heating will be briefly discussed.

But first, some definitions:

A polar molecule, or **dipole**, is a molecule that has an unequal charge distribution. This means that the one side of the molecule has a positive pole and the other side a negative pole [10].

In this context, **polarisation** is the action of causing a material to have a separation of charges, thereby having poles [11].

Polarisation is what causes the dissipation of power within the insulating material. There are four polarisation effects that take place when an electric field is applied to an insulator: electronic, atomic, dipolar and interfacial polarisation [12, pp. 5–6].

At a sub-atomic level, an applied electric field can cause the negatively charged electrons within an atom to be displaced. This is electronic polarisation [12, pp. 5–6].

Atomic polarisation occurs when an applied electric field causes a displacement of atomic nuclei. This essentially forces atoms to become dipolar [12, pp. 5–6].

As mentioned earlier, polar molecules (or dipoles) have a positive and a negative pole. Water, for example, is a polar molecule (see Figure 2.1). The more positive hydrogen molecules are repelled by

electrons in the oxygen and are therefore pushed to the one side of the molecule. This causes a positive charge to be seen on the hydrogen side of the molecule, and a negative charge on the oxygen side [10].
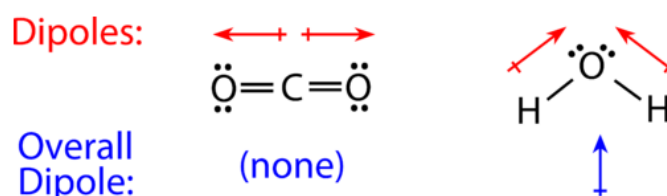
Figure 2.1: A comparison of a non-polar molecule (CO2) with a polar molecule (H2O). The dipoles of the individual bonds are shown in red and the overall dipoles is shown in blue [10].

A material can be heated up by means of dipolar polarisation. When an electric field is applied to a material that consists of polar molecules, the molecules align themselves with the electric field. If the polarity of the electric field is alternated, the molecules continuously align themselves with the field. However, if the field is varied fast enough (high frequency), the molecules can no longer keep up. This causes a phase difference between the orientation of these polar molecules and the orientation of the electric field. This phase difference is caused by friction and friction causes heat [12, pp. 5–6].

The phase difference is dependent on the properties of the material being heated. A larger phase difference is indicative of larger losses i.e. the material heats up more. The frequency cannot be increased indefinitely, however, since at some point the electric field will vary so fast that the molecules stop moving altogether, and are no longer heated up [12, pp. 9–11].
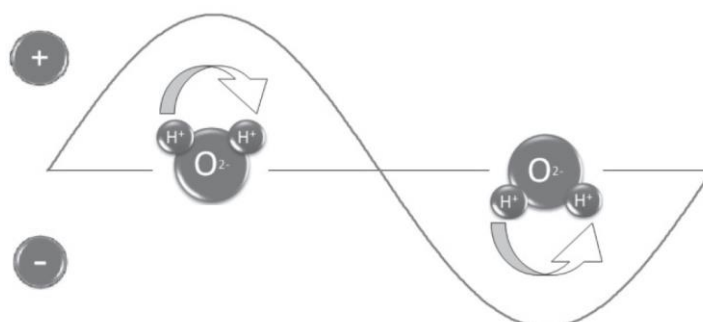
Figure 2.2: An alternating electric field causes polar molecules to align themselves with the electric field [29].

Interfacial polarisation occurs in materials with a heterogeneous mixture of conducting and insulating materials. At interfaces between these materials, an applied field can cause a build-up of free charged particles to occur. Alternating the applied field causes a movement of particles that heats up the material [12, pp. 5–6], [13].

In terms of microwave heating, only one of these effects contribute significantly to the heating of a material. Electronic and atomic polarisation are only effective at very high frequencies such as infrared and visible light. Interfacial polarisation has a significant heating effect at the frequencies below microwave frequencies, but its effect becomes negligible above 1 GHz. Therefore, at 2.4 GHz, the only effect of significance is dipolar polarisation [12, pp. 9–11].

The permittivity of a material defines how it interacts with electromagnetic waves. It is written as a complex number in the form of

$$\epsilon = \epsilon' - j\epsilon''. \tag{1}$$

In this equation, ϵ' is defined as $\epsilon' = \epsilon_r \epsilon_0$, where ϵ_r is defined as the dielectric constant of a material and ϵ_0 as the permittivity of free space. The amount of energy stored in the material is defined by ϵ' [7], [12, pp. 9–11].

5

The loss factor is denoted by ϵ'' and it defines how much energy is lost through heating. In other words, ϵ'' defines how much a material will be heated up by microwave radiation. It is dependent on the frequency being applied and the temperature of the material [7, pp. 10–11], [12, pp. 9–11].

The permittivity of a material is not constant. It depends on the frequency being applied, the temperature of the material and anything that changes the makeup of the material itself, such as a change in moisture content [12, pp. 38–41]. The data from Table 2.1 will be used to further investigate these properties.

Frequency (GHz)	Temperature (°C)	ϵ'	ϵ''
	25	55.21	21.74
	30	61.30	25.40
0.433	35	50.79	21.83
	40	61.25	21.07
	45	61.83	20.84
	25	54.64	12.10
	30	60.12	13.85
0.915	35	49.49	11.70
	40	60.25	11.60
	45	61.15	11.34
	25	53.18	10.13
	30	58.36	11.01
2.45	35	47.90	8.93
	40	58.82	9.45
	45	59.81	9.16

Table 2.1: Dielectric properties for a mixture of water (95 %) and Java tea leaves (5 %) at different frequencies and temperatures [14].

The data in Table 2.1 shows the dielectric properties of a mixture of water and Java tea leaves (Orthosiphon Stamineus). The mixture consisted of 95 % water and 5 % leaves [14].

It can be observed that as the frequency increases, the values for ϵ'' decreases. This is because at lower frequencies interfacial polarisation effects also come into play [12, pp. 38–41].

The value for ϵ'' typically decreases with temperature for materials with a high water content, as in Table 2.1. The loss factor does, however, tend to increase if there is a significant amount of salt dissolved into the water. For materials with a low water content (less than 25 % water), the loss factor tends to increase with temperature [12, pp. 38–41].

Intuitively, changing the properties of the material will change its loss factor. The moisture content of a material is particularly likely to change when heated in a microwave due to evaporation. Water in materials can be categorised as bound water and free water. Bound water is bonded to other molecules or absorbed into a dry material. Free water is not chemically bonded to and can exist in small spaces in a material.

The loss factor increases with an increase in moisture content, but it increases much more for free water than for bound water. This is because free water is more free to rotate, and thus greater losses due to friction can occur [12, pp. 38–41].

2.2.3 Magnetron

The magnetron is a device that is typically used in commercial microwave ovens to generate microwave radiation. Magnetrons can produce high power outputs in excess of 3 kW average power [15].

The magnetron will now be explained (as described in [12, pp. 241–243], [16]). A magnetron is a high-power vacuum tube. It consists of a cathode, an anode and a magnet (see Figure 2.3).

The cathode is a conductor that runs through the centre of the anode. A low voltage and a high current is applied to it in order to heat it up, which releases electrons.

The anode is a circular structure that has several cavities centred around the cathode. The cavities are open towards the cathode. The cavities are designed to resonate at the desired frequency.

A magnetic field is set up to run in parallel with the length of the cathode.

A high voltage is applied to the anode with respect to the cathode. This causes the electrons released by the cathode to be drawn to the anode. However, since there is a magnetic field present, this causes the electrons to move in a circular motion around the cathode. Whilst moving in a circular motion, some of these electrons enter the cavities and resonate at the design frequency.

Power is coupled out of the magnetron using a coupling loop or a probe that is placed within one of the resonant cavities. This functions as the radiating antenna of the magnetron [12, pp. 241–243], [16].
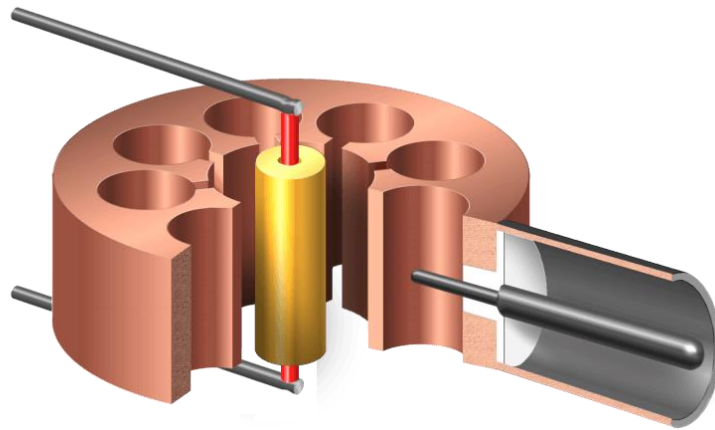
Figure 2.3: A cutaway of a magnetron. The yellow cathode is in the centre of the copper anode, with resonant cavities, around it. On the right-hand side, the grey probe is used to couple power out of the magnetron [16].

If the anode voltage is too low, the electrons move around the cathode but never reach the resonant cavities. In this state the magnetron does not emit microwave power and draws little current. At a certain voltage, the electrons reach the resonant cavities and the magnetron emits microwave energy, drawing much more current [12, p. 243]. A typical magnetron's anode voltage-current properties are shown in Figure 2.4, where the curve has been simplified to a piecewise linear function [17].
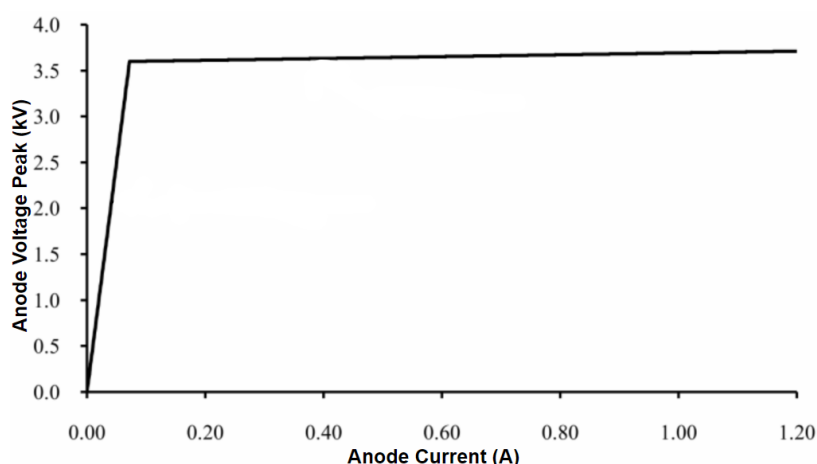
Figure 2.4: A typical magnetron anode voltage-current curve that has been simplified to a piecewise linear function. Adapted from [17].

The output power and -frequency of the magnetron is affected by the load that is being irradiated. A reactive load in effect adds capacitance or inductance to the magnetron's resonator cavities, thus affecting its frequency. A resistive load alters the output power [12, p. 244].

7

The relationship between the load and the output power and -frequency of a magnetron is typically plotted on a Rieke diagram, as shown in Figure 2.5. It is plotted on a polar VSWR chart and indicates the output power and –frequency for a specific load impedance [12, p. 245].
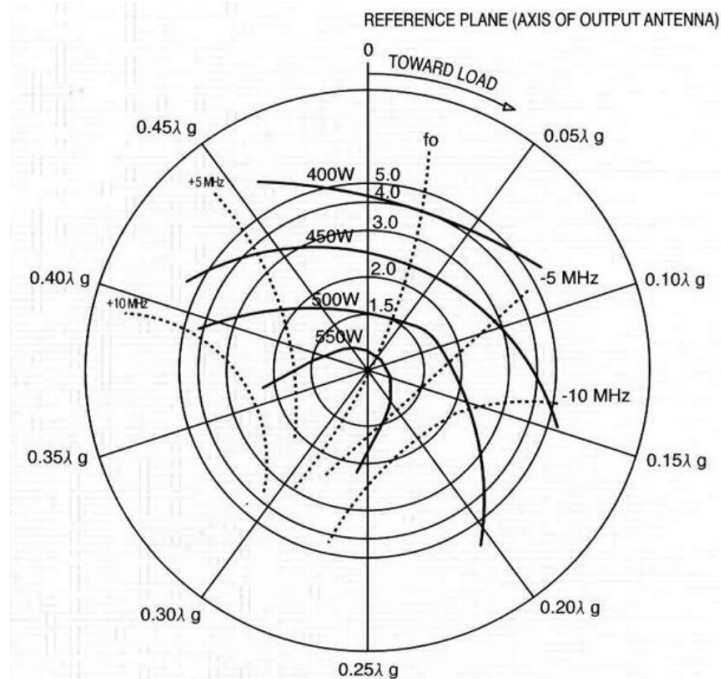
Figure 2.5: A Rieke diagram for a 600 W magnetron. The data is plotted on a polar VSWR chart. The solid lines indicate power output and the dotted lines indicate output frequency [87].

In order to ensure that the magnetron is always well matched, a circulator is often placed between the magnetron and the load. The circulator directs the reflected energy away from the magnetron, thereby forming a matched load [12, pp. 244–245].

2.2.4 Standard hardware (operating circuit)

2.2.4.1 Introduction

The standard hardware that is found in a typical conventional microwave oven will be discussed. This is important because the same components and the same basic operating principal is used in this research project.

The circuit schematic for the microwave oven used in this research project, a Defy DMO 368, is shown in Figure 2.6.
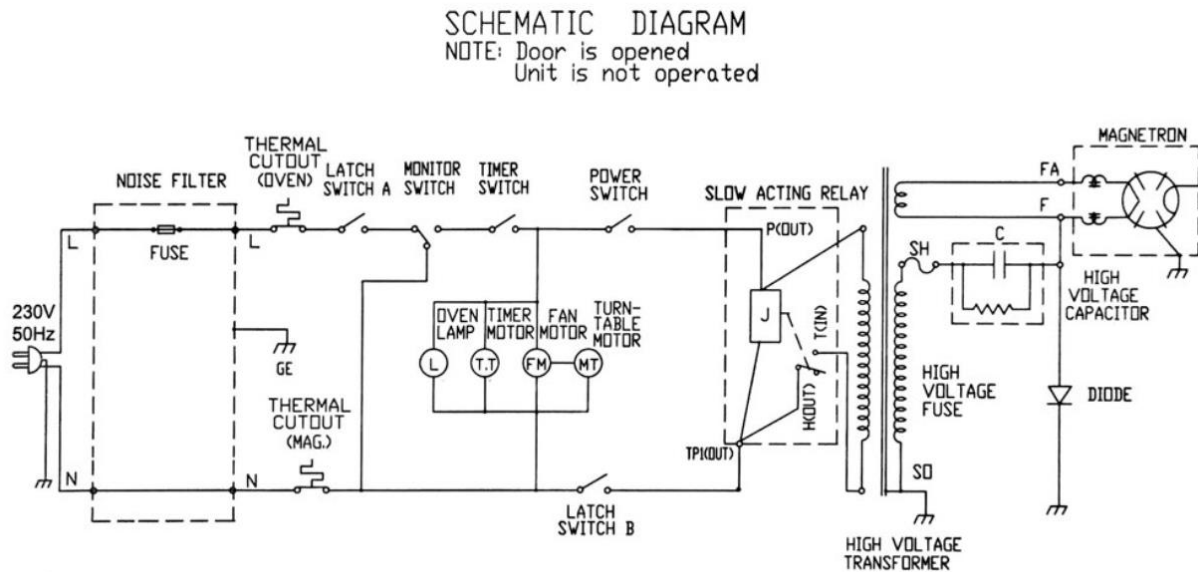
Figure 2.6: Circuit Schematic Diagram for a Defy DMO368 microwave oven as found on the inside of the metal casing

2.2.4.2 Auxiliary circuit

Mains power is applied on the very left-hand side of the schematic. The power is passed through a noise filter and then passes through various operational and safety switches for the door, timer and thermal cut-out sensors. In the centre of the diagram, power is supplied to several of the oven's accessories while the microwave oven is operational. These include the lamp, timer, fan and turn-table. The power switch and latch switch B governs the power to the magnetron and is controlled by the power setting knob. If the switches are closed, the power passes through the slow acting relay to the high voltage transformer.

2.2.4.3 Magnetron circuit

The circuit on the right-hand side of the transformer drives the magnetron. The secondary coil at the top part of the transformer supplies a low voltage to heat the cathode. The main coil is attached to a voltage doubler. In the one half cycle of incoming power, the capacitor is charged. On the following half cycle, the charged voltage of the capacitor is added to the voltage at the coil, effectively doubling the voltage to the magnetron. This voltage is high enough to turn on the magnetron. Using this configuration means that the magnetron is only switched on during every other half cycle of the mains power [18, p. 132]. The high voltage transformer and the capacitor also regulate the current to the anode, as described in Sec. 2.2.5 [12, pp. 247–248].

2.2.5 Magnetron power control

2.2.5.1 Introduction

There are multiple ways of controlling the output power of a magnetron. Low power magnetrons, such as the one used in this research project, are most often controlled by altering the anode current [12, p. 244]. Duty cycle, saturable reactor and TRIAC control will be discussed as these were the most relevant to this research project. A simplified schematic is shown in Figure 2.7. The red blocks indicated where power control could be implemented with these methods.
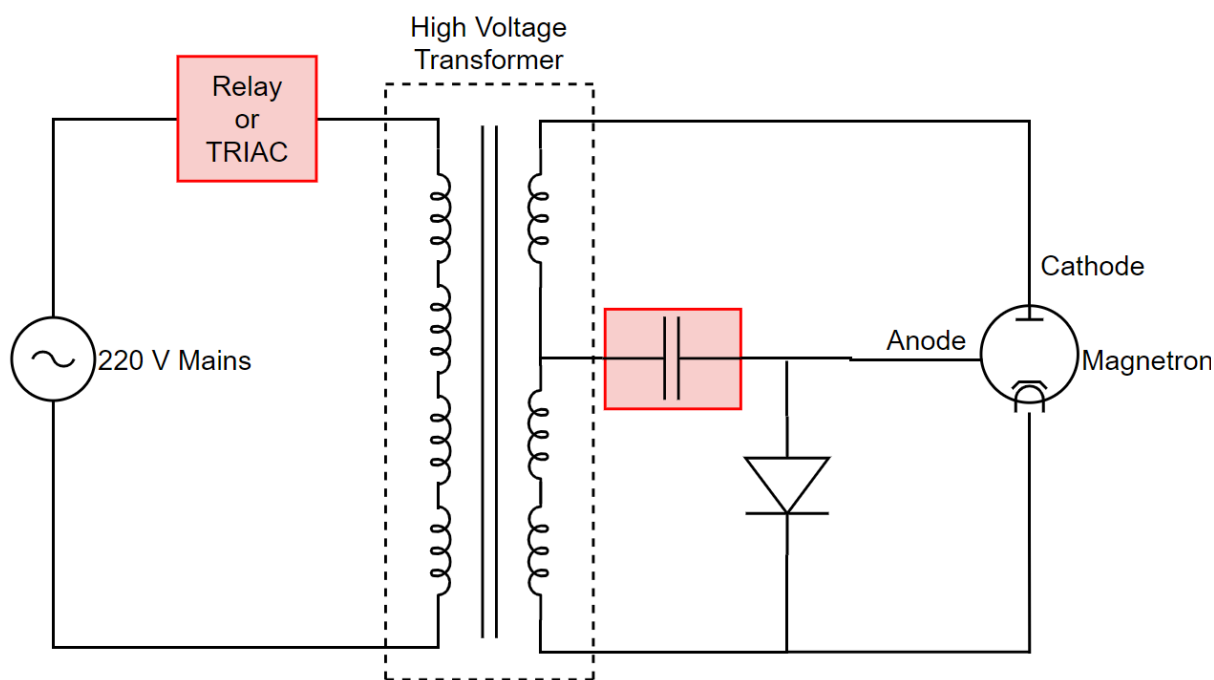
Figure 2.7: Simplified circuit schematic for a household microwave oven [88]. *Blocks marked in red indicate where control can be implemented* [12, pp. 246–250].

2.2.5.2 Duty cycle control

Duty cycle control was used in the Defy DMO386 that was described in Sec. 2.2.4. This method uses a relay to switch the magnetron on and off over a period of seconds. The magnetron switches between being fully on and completely off. For example, at 50 % power, the magnetron may be switched on for 15 seconds and then switched off for 15 seconds. Therefore, over a 30 second time period, the average power will be 50 % [19].

2.2.5.3 Saturable reactor control

Saturable reactor control is a passive control method. Most household microwave ovens, including the Defy DMO386, make use of this control method (in addition to duty cycle control). By saturating a non-linear reactor (inductor) of an LC resonant circuit, it lowers the inductance of the resonator and thereby shifts the resonant frequency upwards. This increases the impedance of the circuit, which reduces the flow of current [12, pp. 247–248].

In a microwave oven, an inductor is placed in series with a high voltage capacitor to form a resonant circuit. Typically, the reactance from the high voltage winding of the transformer is sufficient to function as the inductor, and as such a separate inductor is not needed. The resonator frequency is designed to be about 15 % higher than the mains frequency (50 Hz in the case of the Defy DMO386). As power is applied to the circuit, more current flows, which causes the transformer to saturate and to lower the value of its reactance. As mentioned, this increases the impedance of the circuit which limits the current to the anode of the magnetron [12, pp. 247–248].

In addition, the resonant frequency can be increased by fixed amounts by decreasing the capacitance. This will further increase the impedance and lower the anode current [20].

2.2.5.4 TRIAC control

TRIAC control uses a TRIAC to control the phase angle at which the supply to the high voltage transformer is turned on, limiting the anode current [20]. A TRIAC is a high speed electronic switch that can switch an AC waveform (triode for alternating current) [21].

A TRIAC is a three terminal device. It has two main terminals, through which the load current flows. The third terminal, the gate, is used to turn the TRIAC on so that it starts conducting. If the TRIAC is

10

on but the signal to the gate terminal is low, the TRIAC only switches off once no more current is flowing through the main terminals. This means that when the TRIAC is on, it can only stop conducting an AC signal once the conduction current changes direction (voltage changes polarity) [21].
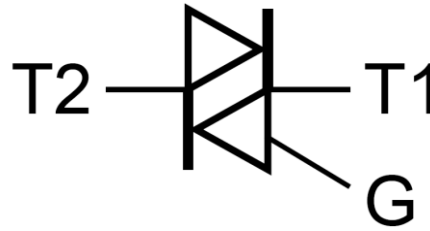
Figure 2.8: TRIAC circuit symbol [81].

In order to use a TRIAC for conventional mains AC power, the zero crossings of the signal need to be detected. After a zero crossing is detected, the TRIAC is turned on after a specified delay time. This delay time can be related to the phase angle by the following formula:

$$t_{delay} = \frac{T \times \phi}{360°} \tag{2}$$

where t_{delay} is the delay time, T is the period of the signal ($T = \frac{1}{frequency}$) and ϕ is the desired phase angle [17].

Figure 2.9 shows a waveform voltage over a resistive load that is switched with a TRIAC with a 90° phase angle.
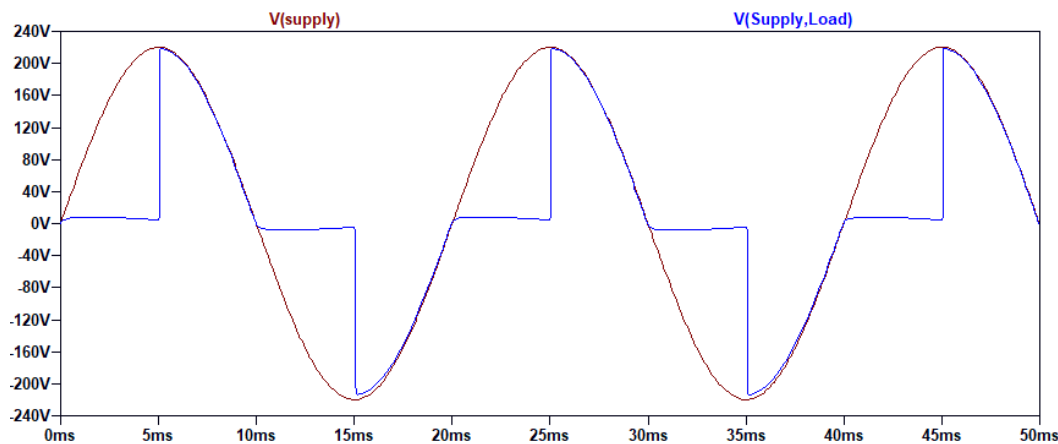
Figure 2.9: An LTspice simulation showing the voltage across a resistive load, V(Supply,Load), *when switched with a TRIAC with a 90° phase angle. The supply voltage,* V(supply), *is a 50 Hz 220 V signal.*

TRIACs are typically used to control resistive loads. Power to a resistive load scales linearly i.e. at a phase angle of 0° the load will receive maximum power and at a phase angle of 180°, the load will receive no power. The power absorbed between phase angles of 0 ° and 180 ° will scale linearly [17].

For magnetron power control, the TRIAC does not see a linear, resistive load. The TRIAC is connected to the low voltage side of the transformer, which acts as an inductor. In addition, the magnetron on the other side of the transformer is not a linear load. It draws little current until its turn-on voltage is reached, after which it draws significantly more current (see Figure 2.4). Nonetheless, there is a set of phase angles that can produce a somewhat linear output [17]. Figure 2.10 shows the phase angle versus the output power of a typical magnetron, plotted for different high voltage capacitor values [20].
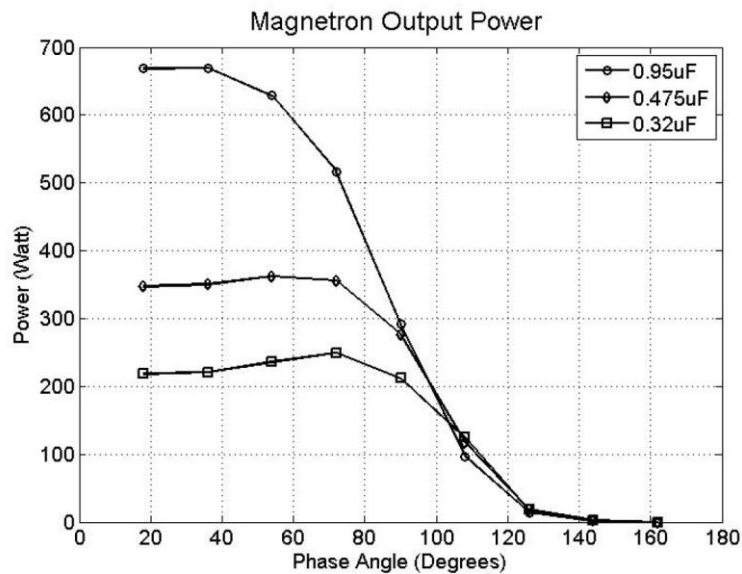
Figure 2.10: The TRIAC phase angle versus the output power of a typical magnetron, plotted for different high voltage capacitor values [20].

2.2.6 Uneven heating: Multimode cavities and a travelling wave applicator

It is well know that one of the main drawbacks of microwave ovens is that they heat unevenly [12, p. 130]. This will now be investigated.

2.2.6.1 Multimode cavities

Conventional microwave ovens make use of a multimode cavity. A multimode cavity is a closed metal box that can support multiple different resonant modes, or electromagnetic field patterns, at and around the operating frequency. Over 50 different modes could exist over the operating frequency range of a conventional microwave oven. These field patterns superimpose onto each other, forming a resultant field pattern that is non-uniform. This non-uniform field pattern will therefore heat a load unevenly [12, pp. 130–138].

The effect of uneven heating in a multimode cavity can be reduced by moving the load, using a mode stirrer or by using a different way of feeding the cavity [12, pp. 137–138].

A turn table is typically used to **move the load** inside the cavity. The load is moved through the antinodes of the field pattern, thus heating it more evenly [12, pp. 137–138].

A **mode stirrer** can be placed inside the cavity to 'stir' the field pattern. It is typically a rotating metal fan, or some other moving object. The mode stirrer perturbs the field and causes different modes to be excited. Since it is moving, different modes are continuously generated. Thus the field pattern is continuously varied and is more uniform over a period of time [12, pp. 137–138].

Different ways of feeding the cavity can also be used. These either move the feeding point or uses an alternative way to couple into the cavity (such as using slots) and is used in conjunction with a mode stirrer [12, pp. 137–138].

2.2.6.2 Travelling wave applicator

Another way of dealing with uneven heating is to use a different applicator altogether. For example, a travelling wave inside a single-mode waveguide has a very well defined field pattern, unlike the multimode cavity [12, p. 104]. The electric and magnetic field patterns for a rectangular waveguide operating in the TE_{10} mode is shown in Figure 2.11 [7, p. 118].

12
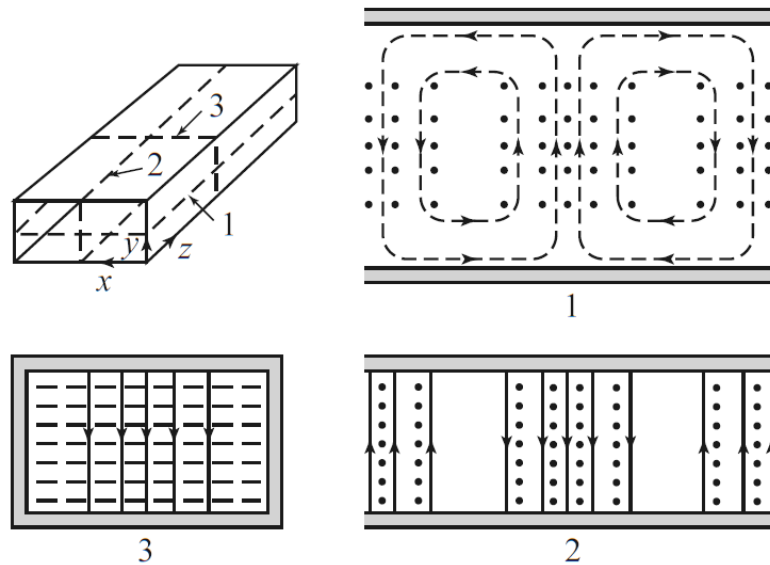
Figure 2.11: The electric and magnetic field patterns for a rectangular waveguide operating in the TE_{10} mode. The electric field is represented by solid lines and the magnetic field by dashed lines [7, p. 118].

The electric field in a travelling wave applicator is very predictable and therefore a load can be placed in the area of greatest electric field intensity. In Figure 2.11, the load should be placed along the centre of the waveguide, parallel to the electric field, for maximum exposure [12, pp. 114–116].

A travelling wave applicator has a generator on the one side and a matched load at the other end. In this way the wave is always travelling through the applicator, but does not reflect and cause a standing wave pattern [12, pp. 114–116].

2.2.7 Microwave specific effects

There is ongoing controversy and debate about the possible non-thermal effect of microwave radiation. As discussed in [22], various studies have attempted to prove or disprove this effect. Shamis et al. [23] suggests that many of the non-thermal observations may be due to poor experimental control protocols and due to a microwave specific effect that is still thermal in nature.

This microwave specific effect may be due to a high instantaneous temperature (T_i) that occurs at a molecular level. This is a much higher temperature than the bulk temperature (T_B) of a sample and occurs over a very short time, after which the heat is conducted to the rest of the sample. The appearance of T_i may be attributed to the direct interaction of microwaves with the molecules of the material. Therefore, seemingly non-thermal effects may be thermal in nature, but still specific to microwaves [23].

For example, a study has been conducted by Celandroni et al. [24] to investigate the effect of microwave radiation on Bacillus subtilis spores. Their study showed that both microwave radiation and conventional heating has a similar killing effect on the spores. However, they did indicate a significant difference in the structure of the spores after being treated by the two methods. After treating the spores, both methods showed a similarly damaged nucleoid of the spore. However, the cortex (a thick layer between the inner and outer membrane of a spore [25]) of the heat treated samples were far more relaxed compared to the irradiated samples, as shown in Figure 2.12 [24].
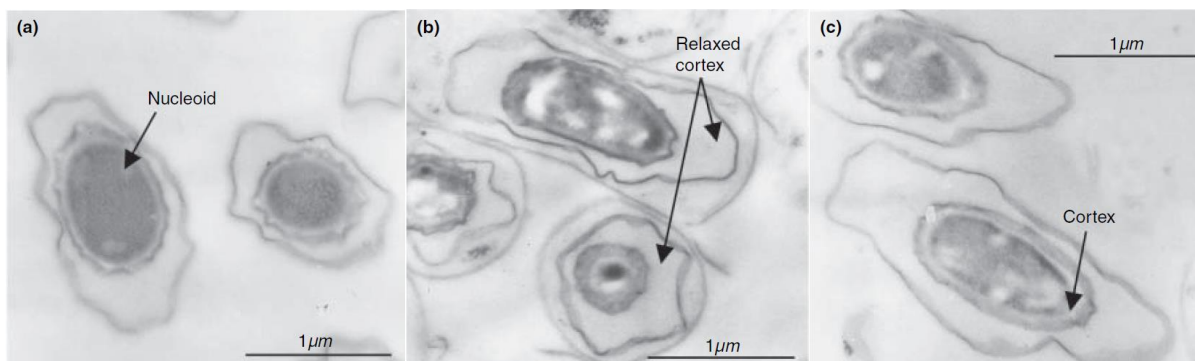
Figure 2.12: Electron micrographs of Bacillus subtilis spores: (a) not-treated, (b) conventionally heated, and (c) microwave irradiated. Arrows indicate the cortex layer. Taken directly from [24].

In conclusion, there is plenty of evidence of the existence of a microwave specific effect, which may or may not be thermal in nature. The investigation in [24] indicates such an effect, however, it is unclear whether it is a non-thermal effect.

2.2.8   Sterilisation and microwave radiation

Achieving pasteurisation or sterilisation of foods using microwaves hold great potential. This is primarily due to the short heating times of the microwaves [26].

Sterilisation is a process in which all microorganisms and their spores are destroyed. Pasteurisation eliminates only the vegetative forms of bacteria but does not eliminate all the spores. Therefore sterilised food have a longer shelf life than pasteurised foods [27].

When using microwave radiation, microbial inactivation occurs primarily through thermal effects. High temperatures denature (alter the molecular structure in a destructive manner [28]) enzymes, proteins, and nucleic acids. These compounds are vital to the survival of microorganisms and therefore their destruction means that the microorganisms die [29].

In general, food reduces in quality when it is kept at a high temperature for a long period of time. Bacteria, however, can be eliminated by being exposed to high temperatures for a short period of time. Using microwave radiation, food can be treated at a high temperature for a shorter amount of time, thereby increasing the quality of the food compared to conventional heating techniques [26].

Using microwaves for sterilisation has not been widely adopted due to the non-uniform heating pattern in large cavities, as discussed in 2.2.6. This is problematic since it cannot be guaranteed that the entire sample has been sterilised. Measuring the temperature of a sample is also not straightforward since metal probes alter the field inside the cavity [26].

2.3   Microbiology definitions

This section will provide several definitions to terms that are commonly used within the field of microbiology and that are relevant to this research project.

Gram-negative bacteria have a thin outer layer (as opposed to **Gram-positive** bacteria that have a thick outer layer) [30]. This makes them more vulnerable to heat treatments [31].

Escherichia coli (*E. coli*) bacteria is Gram-negative and is commonly found in the digestive systems of humans and animals. Some strains, however, can cause illnesses such as diarrhoea. Extreme cases can become life threatening [32].

Lactococcus lactis is a Gram positive bacterium that is often associated with milk fermentation and the conversion of lactose (milk sugar) to lactate [33].

Viability in biology refers to the ability to live [34]. For example, a viable cell is a living cell.

Agar is a jelly-like substance extracted from red seaweed. An **agar plate** is a petri dish containing agar. Microorganisms are said to be *plated* onto an agar plate, after which it is incubated at a set temperature for a set amount of time. Colonies form during incubation, and these are counted after incubation to determine the amount of microorganisms that was present in the original sample [35].
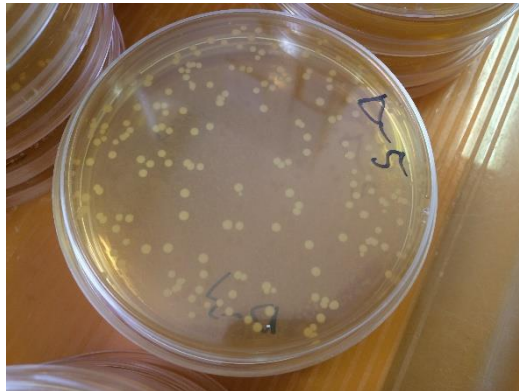
Figure 2.13: An agar plate that was used in this research project. The white dots are colonies.

A **colony-forming unit (CFU)** is a measure of how many bacteria there are in a sample. Each colony that grew on an agar plate is assumed to have grown from a CFU. A measure of the amount of bacteria is usually indicated in CFU/ml of CFU/g [36].

2.4   Rooibos tea

2.4.1   Introduction

Rooibos tea is a herbal tea grown only in the Cederberg region of South Africa. It is a very popular domestic beverage and it is gaining popularity worldwide [4]. Some tea drinkers prefer Rooibos since it has little tannin and it naturally contains no caffeine. It is also known for its health benefits. Studies have shown that consuming Rooibos tea may help in preventing cancer and heart disease, and may help in reducing stress and insomnia, among other benefits [3].

Rooibos is typically sold in its unflavoured form but may also be found in tea blends. Green Rooibos, which is unfermented Rooibos, is also growing in popularity [3].

Figure 2.14: Short cut Rooibos tea leaves [89].

2.4.2   Processing

Rooibos undergoes several processing steps before it is sold to consumers, as shown in Figure 2.15 [5].
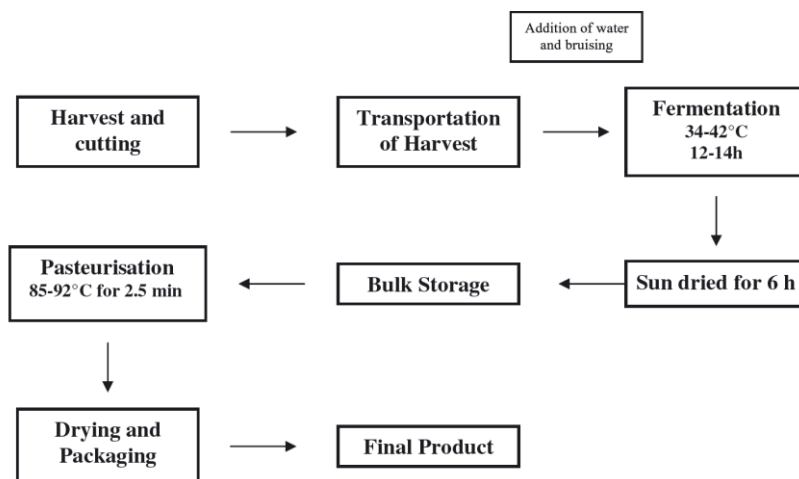
Figure 2.15: Rooibos tea processing steps [5].

After harvesting, the tea is cut into fine pieces of around 4 mm. Water is then added to the tea and the tea is bruised. The added water and bruising accelerates the next step of fermentation [5].

During fermentation, the tea is placed in heaps. The tea is left to ferment for 12 to 14 hours, and, due to the fermentation process, the tea typically reaches temperatures of between 38 and 42 °C. The fermentation process turns the tea from green to red and enhances the flavour. Green Rooibos skips the fermentation step [5].

Next the tea is sprayed onto broad cement floors and left to dry in the sun for about 6 hours. The tea is then collected and stored until it is pasteurised[5].

The tea leaves are then passed through steam, which is at approximately 180 °C, for 2.5 minutes. This heats up the leaves to between 85 and 92 °C. Pasteurisation kills almost all of the bacteria but may leave spores behind. Using steam adversely affects the taste and health benefits of the tea [5].

Thereafter the tea is air dried. Drying the tea reduces its water activity. This prevents the remaining spores from developing into moulds, therefore extending the shelf life of the tea [5].

Hereafter the tea is placed in bulk storage. It is now ready to be packaged into various form that can be sold to consumers [5].

2.4.3   Microbial standards

Rooibos tea naturally contains a large variety and quantity of microorganisms. It may contain pathogenic bacteria such as *Escherichia coli (E. coli)* and *Salmonella*, amongst others. Therefore, eliminating pathogens is vital to make the tea safe to consume [5].

The tea is made safe and kept safe for consumers by three main actions.

During processing, the tea leaves are pasteurised. Pasteurisation kills most of the bacteria present, but may leave behind spores and temperature resistant bacteria [37].

To prevent the spores and remaining bacteria from growing, the product is dried. Drying lowers the water activity of the leaves. A sufficiently low water activity prevents the growth of any mould or bacteria [5].

Finally, the tea is prepared with boiling water. The boiling water, as with the heat of pasteurisation, eliminates most of the bacteria and ensures that the beverage is safe to consume [5].

Microbiological standards must be adhered to so as to ensure that the tea is safe for consumers. Table 2.2, taken from [5], shows the domestic and European guidelines.

16

Microbial contaminant	Europe*	South Africa†
Aerobic plate count	$1.0 \times 10^8 \; CFU \; g^{-1}$	$7.5 \times 10^4 \; CFU \; g^{-1} \; (bulk)$; $1.5 \times 10^5 \; CFU \; g^{-1} \; (retail)$
Yeasts	$1.0 \times 10^6 \; CFU \; g^{-1}$	
Moulds	$1.0 \times 10^6 \; CFU \; g^{-1}$	
Escherichia coli	$1.0 \times 10^4 \; CFU \; g^{-1}$	$2.0 \times 10^1 \; CFU \; g^{-1}$
Salmonella	$Absent \; in \; 5 \times 25$	0
*Guidelines extracted from European Herbal Infusion Association Microbiological Guidelines.		
†Regulations governing microbiological standards for foodstuffs and related matters, Foodstuffs, Cosmetics and Disinfectants Act of South Africa, 1972.		

Table 2.2: Microbiological guidelines for Rooibos tea in Europe and South Africa [5]*.*

2.4.4 Conclusion

Rooibos tea is gaining popularity worldwide. Therefore, ensuring that the product is of a high quality and is safe for export is important for the local industry. The South African microbiological guidelines require less than $2.0 \times 10^1 \; CFU \; g^{-1}$ of *E. coli* to be present and has a zero tolerance for *Salmonella*. Steam is currently used to pasteurise the leaves, but it adversely affects the quality of the tea. Therefore, an alternative method of pasteurisation is desired.

2.5 Chapter conclusion

This chapter discussed various subjects concerning microwaves, such as their operating principal and that they can be used to achieve sterilisation. Some microbiology concepts were also discussed, and Rooibos tea was investigated.

3 Directional Coupler

3.1 Chapter summary

This chapter investigates the design of an innovative, inexpensive waveguide directional coupler that worked over the 2.4 GHz ISM frequency band.

A literature review is presented first. It discusses directional couplers in general and then considers their operating principals. It then investigates several waveguide directional couplers.

Next the specifications for the directional coupler that was required for this research project is discussed.

Hereafter the design section investigates each component that was relevant to the directional coupler: the waveguide to coaxial transition, the waveguide with pins and the branch-line hybrid. Various important transitions that were used is discussed in App. B. The design section concludes with measurements of the directional coupler.

Finally, a conclusion and recommendations are given.

3.2 Literature Review

3.2.1 Description

A directional coupler is a passive microwave component that is used for power division or power combining. The power may be divided equally between the output ports, or in other ratios. Directional couplers are four-port devices, although some appear to be three port devices since one of the ports are internally terminated by a matched load [7, p. 317].

A reflectometer uses either a single or two directional couplers to measure forward and reverse power simultaneously. This is commonly used in vector network analysers to measure scattering parameters [7, p. 374].

3.2.2 Brief History

The development of modern microwave components began in the early 1930's. G. C. Southworth began experimenting with waveguides in 1932 while working at Bell Telephone Laboratories. By the late 1930's, most of the theory behind waveguides had been developed and published by G. C. Southworth and S. A. Shelkunhoff, as well as W. L. Barrow and L. J. Chu [38].

In 1940, the high-power pulsed magnetron was developed in England [39]. This led to the development of high-resolution radar, which gave the Allies a major technological advantage in World War II. The research and development of microwave technologies was therefore highly accelerated during the war. It is in the publications from these advances that various modern waveguide directional couplers are found [40].

Since then the field of directional couplers has developed significantly, with theoretical, experimental and numerical innovation driving the way forward [40].

3.2.3 Working Principal

A directional coupler is a four-port device. The ports are named as follows, with reference to Figure 3.1:

1. Input port
2. Through port
3. Coupled port
4. Isolated port
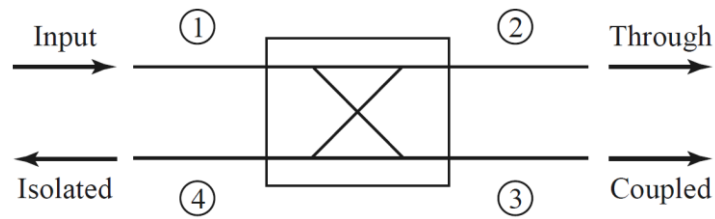
Figure 3.1: Directional coupler schematic [7, p. 322].

Power enters the coupler through port 1, the input port. Some of the power is coupled to port 3, the coupled port. In an ideal coupler, no power goes to port 4, the isolated port (provided that all the ports are connected to matched loads). However, in practice, some power will always go to port 4. All of the remaining power goes to port 2, the through port [7, p. 322].

A directional coupler is often defined by the following characteristics (where P_x denotes the power measured at port x) [7, p. 322]:

Coupling (C) is the amount of power from the input port (port 1) that is delivered to the coupled port (port 3):

$$C = 10 \log \frac{P_1}{P_3} \, dB = -|S_{31}| \, dB \tag{3}$$

Isolation (I) is the amount of power from the input port (port 1) that is delivered to the isolated port (port 4):

$$I = 10 \log \frac{P_1}{P_4} \, dB = -|S_{41}| \, dB \tag{4}$$

Insertion Loss (L) is the amount of power from the input (port 1) that is delivered to the through port (port 2).

$$L = 10 \log \frac{P_1}{P_2} \, dB = -|S_{21}| \, dB \tag{5}$$

Directivity (D) is the ability of the coupler to separate forward and backward power.

$$D = 10 \log \frac{P_3}{P_4} \, dB = \frac{|S_{31}|}{|S_{41}|} \, dB \tag{6}$$

3.2.4 Design Options

There are two main categories of waveguide couplers: waveguide-to-waveguide couplers and loop couplers. Waveguide-to-waveguide couplers have an opening in one of the walls of the primary waveguide that couples some energy into the secondary waveguide. Loop couplers have a wire or stripline loop into the primary waveguide that couples some of the energy directly to a coaxial line. A comparison of the couplers is shown in Table 3.1.

The following couplers were investigated:

A **Bethe-Hole Coupler** is a waveguide-to-waveguide coupler that uses a single hole at (or near) the centre of the common broad wall (or common narrow wall) of the waveguides. These couplers have flat coupling i.e. the coupling is constant over a wide bandwidth. They do, however, have a narrow directivity (the directivity is high over a narrow bandwidth). The amount of coupling is controlled by the radius of the hole. The directivity is controlled by either setting the secondary waveguide at an angle relative to the first, or by choosing the hole to be off-centre [41, pp. 416–419].

Two-Hole Couplers are waveguide-to-waveguide couplers that use two holes, spaced a quarter wavelength apart, to couple into the secondary waveguide [41, pp. 419–420]. Coupling can be from

19

broad wall to broad wall or from side wall to side wall for higher power handling capabilities [42]. They have fairly flat coupling and narrow directivity. The amount of coupling is controlled by the radius of the hole. The directivity is high at the design frequency i.e. where the holes are exactly a quarter wavelength apart [41, pp. 419–420].

Multi-Hole Couplers work on the same principal as Two-Hole Couplers, but have multiple holes in order to increase the bandwidth of the directivity [41, p. 422].

A **Schwinger Reversed-Phase Coupler** couples to the secondary waveguide using two slots. The secondary waveguide is coupled to through its side wall. This causes the coupling to be quite narrow, but the directivity to be much wider [41, pp. 420–421].

The **Moreno Cross Guide Coupler** is a waveguide-to-waveguide coupler in which the secondary coupler is at a 90° angle relative to the primary. The holes are cross-shaped slots to provide tighter coupling [7, p. 372]. This coupler has fairly flat coupling and fairly wide directivity, but the directivity is not that high [42].

A **Riblet-Saad Coupler** is a waveguide-to-waveguide coupler that couples through the broad wall with two slots arranged in a T-shape. The coupler has tight coupling, fairly flat coupling and very high and very wide directivity [42].

Loop Couplers use a single waveguide and a secondary loop, typically of wire or stripline, to couple directly to a coaxial connection. Since only one waveguide is used, loop couplers are typically much smaller than waveguide-to-waveguide couplers. They typically have flat coupling with high, but sharp, directivity [43].

Type of Coupler	Coupling (dB)	Range for Constant Coupling*	Maximum Directivity (dB)	Range for Directivity 20 dB*
Bethe-Hole [41, p. 419]	30	$11\% \pm 1\,dB$	>32	9%
Two Hole	20	$12\% \pm 0.7\,dB$	37	8%
Schwinger Reversed-Phase	20	$25\% \pm 1.5\,dB$	30	25%
Moreno Crossed Guide	20	$15\% \pm 0.1\,dB$	23	12% ($for\ 15\,dB$)
Riblet-Saad	20	$15\% \pm 0.25\,dB$	54	25%
Loop [43, p. 239]	24	$15\% \pm 1\,dB$	>40	$>15\%$
*Percentages calculated by dividing the operating frequency range of the parameter by the operating frequency range of the waveguide that was used.				

Table 3.1: Comparison of directional coupler properties. Data from [42] *unless otherwise indicated.*

Although a **branch-line hybrid** is not a waveguide coupler, it is important for the discussion that follows. A branch-line hybrid is a microstrip coupler that divides power equally between its two output ports (3 dB directional coupler), but with a 90° phase difference between the output ports (ports 2 and 3). Port 4, the isolated port, receives no power if the other ports are connected to matched loads. Figure 3.2 shows the basic dimensions, impedances and ports of a single section branch-line hybrid [7, p. 343].
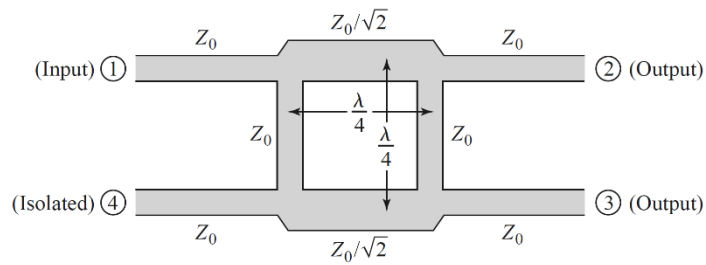
Figure 3.2: Single section branch-line hybrid layout [7, p. 343].

Since the branch-line hybrid is symmetrical, any one of the ports can be used as the input signal. It can be operated in reverse: that is, ports 2 and 3 can each be fed with a signal of magnitude A, but with a 90° phase difference between them. Port 1 then becomes the output port and receives a signal with a magnitude of $\sqrt{2}A$ (twice the power). Port 4 still receives no power. The mathematics behind this can easily be derived by repeating the Even-Odd Mode Analysis done in [7, pp. 344–355], but with an added $A_4 = j$ incident on port 4.

The bandwidth of a branch-line hybrid is quite narrow (15 % fractional bandwidth). The bandwidth can be increased by adding more shunt lines, known as multi-section hybrids (similar to the Multi-Hole Coupler) [44].

3.3   Specifications

A directional coupler was to be built for use in a modified microwave system. A directional coupler was able to add the functionality of knowing how much power was absorbed by a certain load in a microwave system, and how much was reflected. Therefore, standardised tests could have been developed where different applicators were used for treating samples (such as Rooibos tea leaves), but with the same amount of power being applied regardless of the applicator.

The following specifications were required:

1. A directional coupler, which could separate forward and reverse power, was required. With this, the power absorbed by a load could have been calculated by subtracting the reverse power from the forward power.
2. A coupling factor of around $35\ dB$ was required so that the power level at the outputs were small enough to be measured by a power detector.
3. The required frequency range was from $2.4 – 2.5\ GHz$, the operating frequency range of a conventional microwave oven.
4. A *waveguide* directional coupler was required. Waveguides are capable of handling high power throughputs and have low losses [7, p. 158]. The magnetron used in this project had a maximum power output of $700\ W$. In addition, the microwave oven cavity and the waveguide applicators used in this research project used waveguides as their interface, which was where the coupler was required.
5. The dimensions of the WR340 waveguide standard had to be designed for. WR340 indicates 'Waveguide Rectangular' with an inner width of $3.4\ inches$, or $86.36\ mm$, and an inner height of $1.7\ inches$, or $43.18\ mm$ [45]. It supported a recommended frequency range of 2.2 to $3.3\ GHz$ [46].
6. A modular design was preferred so that each component of the coupler could be optimised on its own before assembling the coupler.
7. A low-cost factor was favourable. As such, a design that used inexpensive components and that was simple to construct was preferred.

3.4   Design

3.4.1   Introduction
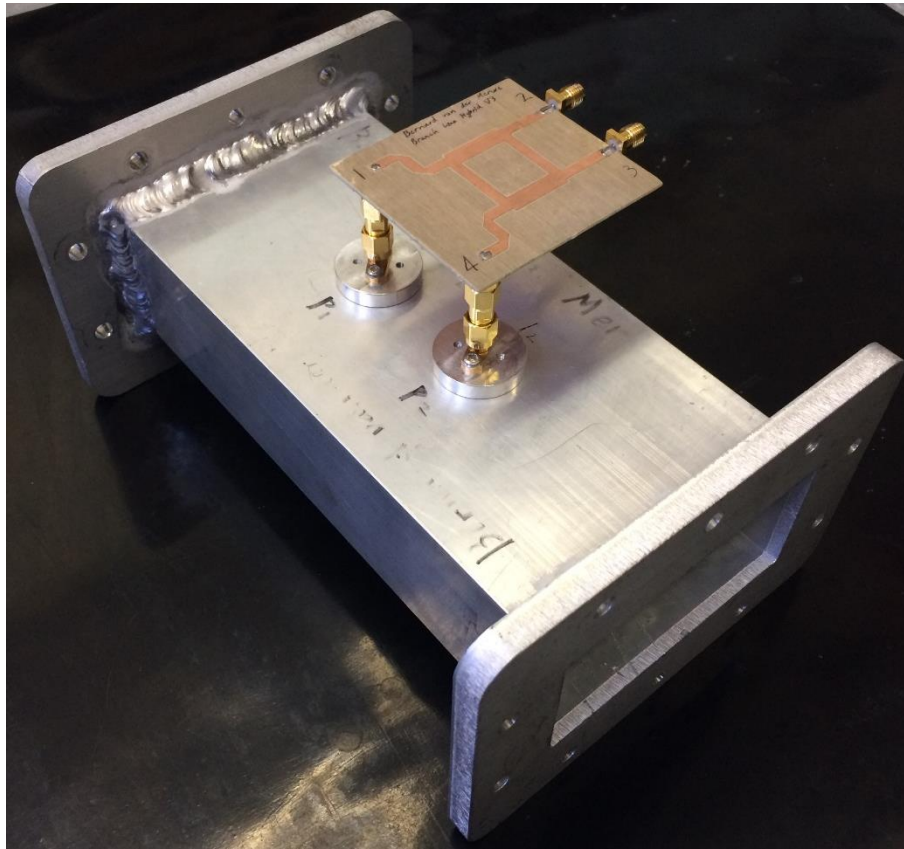
Figure 3.3: The directional coupler that was developed.

An innovative directional coupler design is presented. This was a waveguide directional coupler, with coaxial outputs, that operated over the 2.45 *GHz* ISM band.

Two equal probes, spaced a quarter wavelength apart, were inserted into the centre of the broad wall of a waveguide, orientated along the length of the guide, as shown in Figure 3.4. The output of these probes was fed into a branch line hybrid (Figure 3.5). Here the signals added and subtracted to form the coupled- and isolated port of the directional coupler.
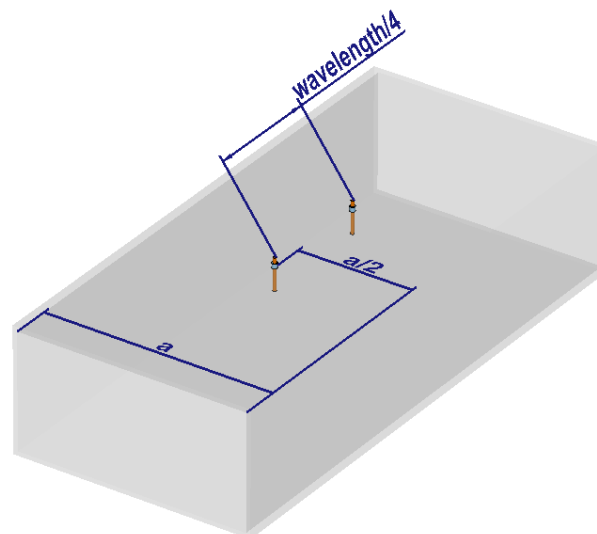
Figure 3.4: The location of the pins relative to the waveguide.
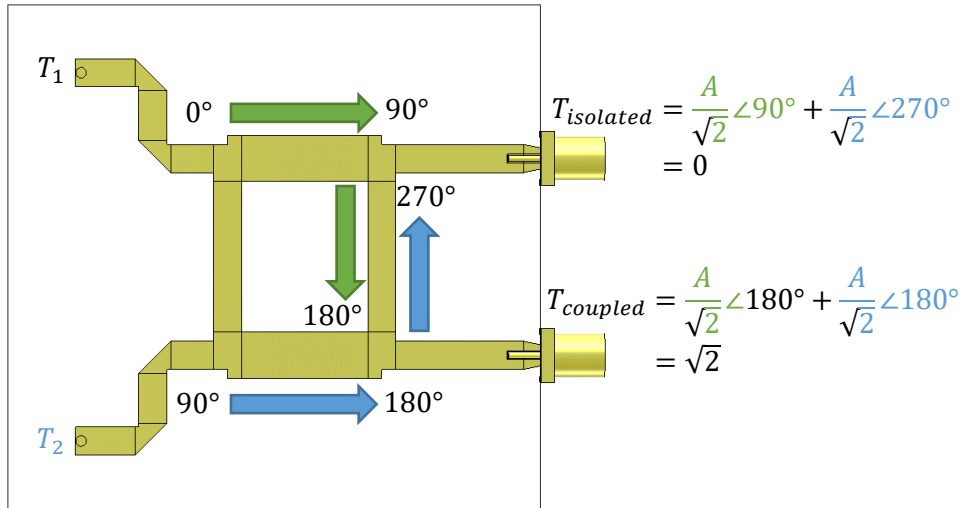
Figure 3.5: Signal flow in the branch-line hybrid, with the output equations displayed at each output port.

Theoretically, the device worked as follows: as an electromagnetic wave travelled through the waveguide, it induced a signal of magnitude A into each of the probes. Since the probes were a quarter wavelength ($\lambda_g/4$) apart, the signals were 90° out of phase i.e.

$$T_1 = A\angle 0° \tag{7}$$

$$T_2 = A\angle 90° \tag{8}$$

Each signal was then fed into a port on the same side of a branch-line hybrid, as shown in Figure 3.5. The output port (coupled port) of the branch-line hybrid then saw a signal of magnitude A (at an angle of $\theta = 180°$) i.e.

$$T_{coupled} =, \tag{9}$$

which was twice the power of one of the input signals (the $\sqrt{2}$ is introduced by the $Z_0/\sqrt{2}$ impedance sections). The angle (θ) was actually an arbitrary angle here since it was dependent on the length of the lines feeding into and out of the branch-line hybrid. The isolated port had a zero output.
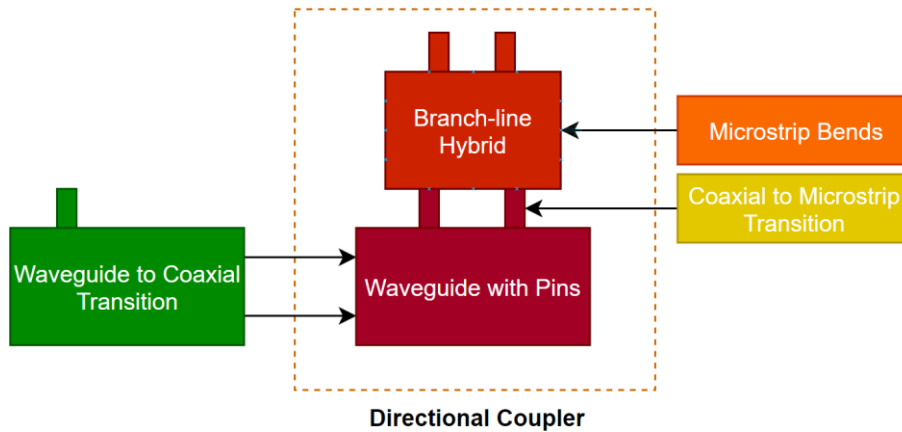
Figure 3.6: Overview of the components discussed in the design section of this chapter.

Figure 3.6 shows an overview of the components discussed in the following sections. The directional coupler consisted of two main components: the waveguide with pins and the branch-line hybrid. As a first step towards the waveguide with pins, a waveguide to coaxial transition was investigated. Thereafter the waveguide with pins and the branch-line hybrid was discussed. App. B investigated some of the details pertaining to the branch-line hybrid by investigating optimal microstrip bends and optimal coaxial to waveguide transitions. Lastly, the coupler was assembled and measured.

3.4.2 Waveguide to coaxial transition

3.4.2.1 Introduction
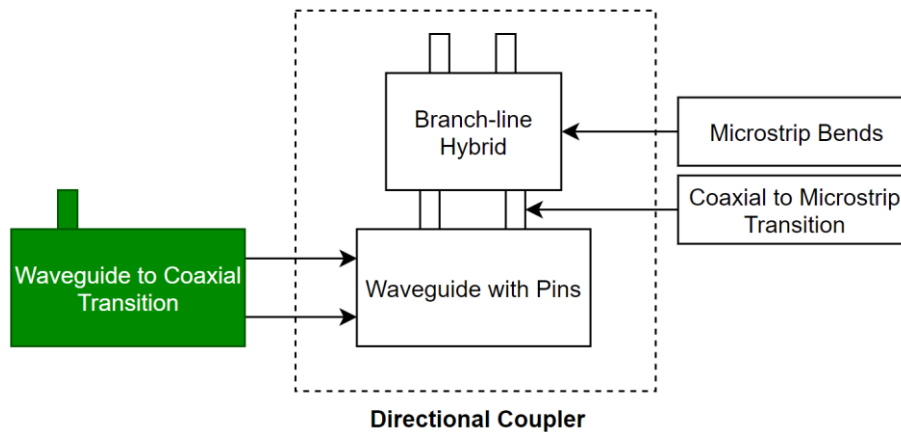
Figure 3.7: The waveguide to coaxial transition is discussed in this subsection.

As a first step to designing the directional coupler, a waveguide to coaxial transition was developed. The transition was a passive device that acted as an interface between WR340 waveguide components and equipment that worked with a coaxial interface, such as a network analyser. Figure 3.7 shows how the transition was used to interface with the directional coupler. A network analyser was typically connected to the coaxial port of the transition.

This was a key component used to measure up the directional coupler. Moreover, it also laid some of the theoretical foundations for the design of the directional coupler.

3.4.2.2 Specifications

The waveguide to coaxial transition needed to be compatible with a WR340 sized waveguide and to an N-type coaxial connector. Maximum power transfer was critical, and as such the input reflection coefficients, S_{11} and S_{22}, had to be minimal. The transition had to work between $2.4 - 2.5\ GHz$. However, for the transition to be usable as general lab equipment, it was preferred if the transition could have worked over the entire recommended frequency range of a WR340 waveguide ($2.2 - 3.3\ GHz$).

3.4.2.3 Design

Electric field coupling was used to couple from a coaxial transmission line to a waveguide. To do this, a probe was inserted at the centre of the broad wall of the guide, as shown in Figure 3.8. Theoretically, it was placed approximately a quarter of a wavelength, or $\lambda_g/4$, from the back of the guide, where λ_g indicates the wavelength in the waveguide. This coupled the TE_{10} mode into the waveguide.
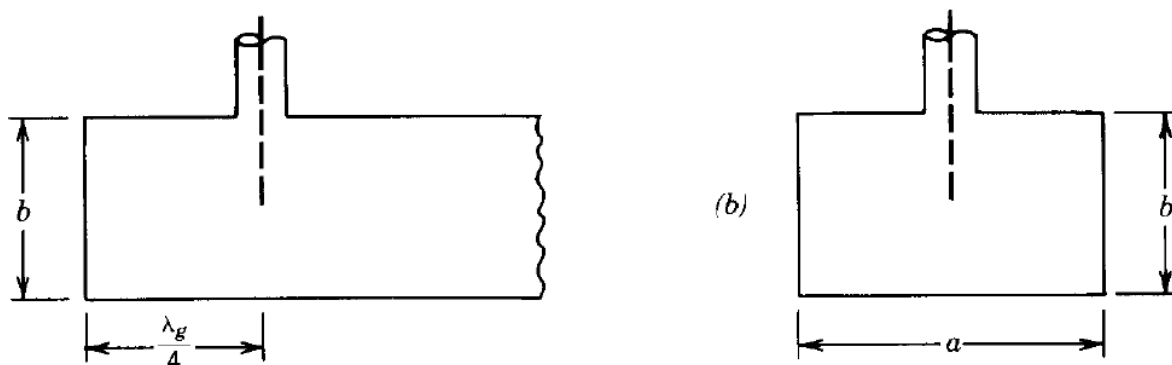
Figure 3.8: Probe location for coupling into a waveguide [13, p. 385].

The wavelength in a WR340 waveguide was calculated as follows [41, p. 191]:

$$\lambda_g = \frac{c_0}{f} \times \frac{1}{\sqrt{1 - \left(\frac{c_0}{2 \cdot a \cdot f}\right)^2}} = 173.38 \; mm, \tag{10}$$

where c_0 is the speed of light in a vacuum, f is the desired frequency and a is the width of the waveguide. The values of $f = 2.45 \; GHz$ and $a = 86.36 \; mm$ were used.

Thus,

$$\lambda_g/4 = 43.35 \; mm. \tag{11}$$

Balanis [47, p. 384] notes that the probe's distance from the back of the guide can be adjusted for better impedance matching. The thickness and the length of the probe and the effect of dielectric material around the probe, however, is not commonly discussed in mainstream textbooks [7, p. 214], [47, p. 385]. These parameters were investigated using a simulation.

3.4.2.4   Simulation

A full 3D simulation was set up using CST Studio Suite 2019 (referred to as CST). The simulation was used to optimise the parameters of the coaxial to waveguide transition. The following parameters were investigated, as shown in Figure 3.9: d_p, the distance of the probe from the back of the waveguide; l_p, the length of the probe into the waveguide; r_p, the radius of the probe and l_g, the length of the waveguide. The effect of dielectric material around the probe was also investigated. Figure 3.10 shows a perspective view of the CST model.
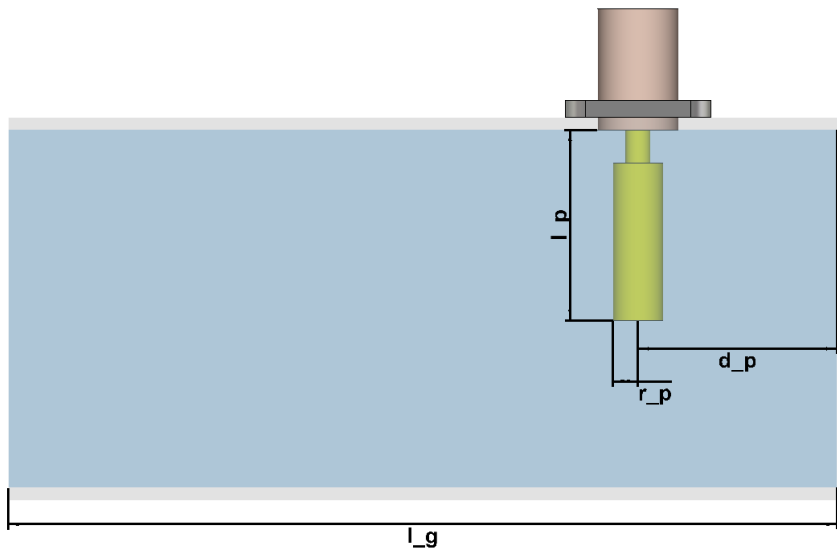
Figure 3.9: Indicated on the CST model are the waveguide to coaxial transition parameters that were optimised.

26
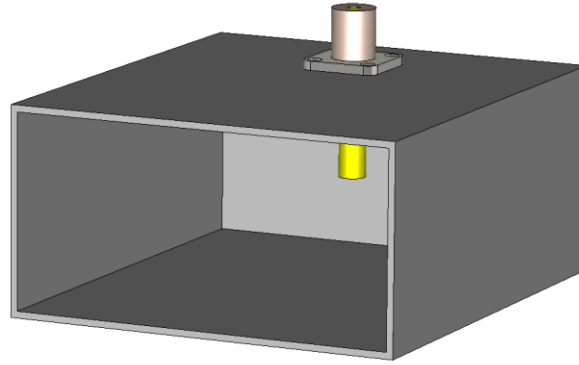
Figure 3.10: Perspective view of the CST model of the waveguide to coaxial transition.

The simulation revealed that an optimal length of l_p was dependant on the length of d_p, and vice versa. In the optimal design they were almost equal. Interestingly, the distance from the back of the waveguide, d_p, was almost half of the theoretically calculated value, coming close to $\lambda_g/8$. Using dielectric material such as Teflon worsened the results and was thus avoided. Using a thicker probe improved the bandwidth of the transition. l_g was made long enough such that it had a negligible effect on the results.

Figure 3.11 shows the simulated scattering parameters (S-parameters) of the optimal design. The cut-off frequency of the waveguide can clearly be seen at about $f_c = 1.8\ GHz$, where at $f < f_c$ waves no longer propagated in the waveguide.

Since this was a passive device, $S_{11} = S_{22}$. A result of $S_{11} \leq -20\ dB$ was achieved between $2.32 - 2.80\ GHz$. An $S_{11} \leq -15\ dB$ was found from $f = 2.22\ GHz$ to $f \geq 3.3\ GHz$, which essentially covered the entire optimal operating range of a WR340 waveguide.
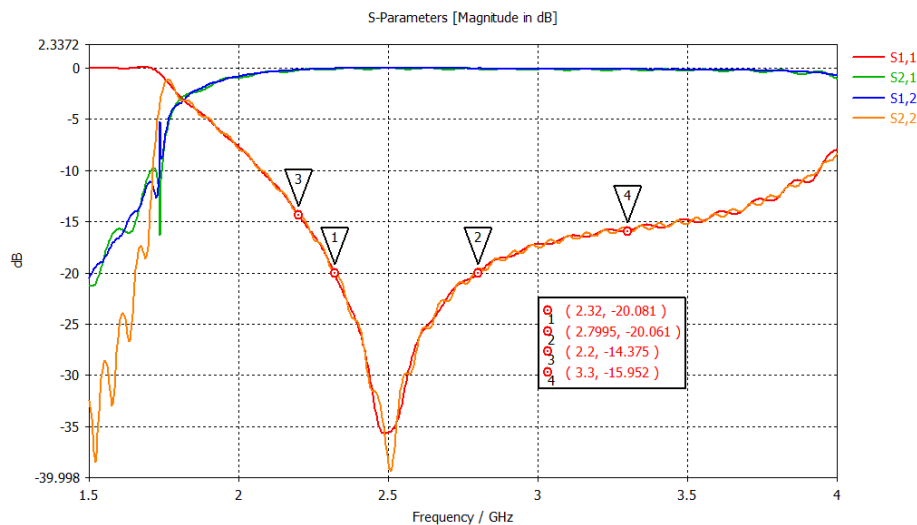
Figure 3.11: Simulated scattering parameters for the optimal waveguide to coaxial transition.

The optimal dimensions were:

Property	Symbol	Value
Waveguide type	$-$	WR340
Distance of the probe from the back of the waveguide	d_p	$24\ mm$
Length of the probe into the waveguide	l_p	$23\ mm$
Radius of the probe	r_p	$6\ mm$
Length of the waveguide	l_g	$100\ mm$

Table 3.2: Optimal dimension for the waveguide to coaxial transition.

27

3.4.2.5   Results
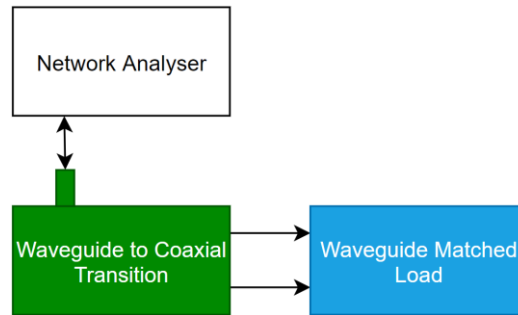
Figure 3.12: Block diagram of the measurement setup used to measure the waveguide to coaxial transition.

A block diagram of the measurement setup is shown in Figure 3.12. The waveguide to coaxial transition (Figure 3.13) was measured up using a network analyser (N5242A PNA-X Microwave Network Analyzer). The waveguide port was connected to a matched waveguide load, as shown in Figure 3.14. The inside of the matched waveguide load can be seen in Figure 3.15.

Figure 3.13: Front view of the built transition.
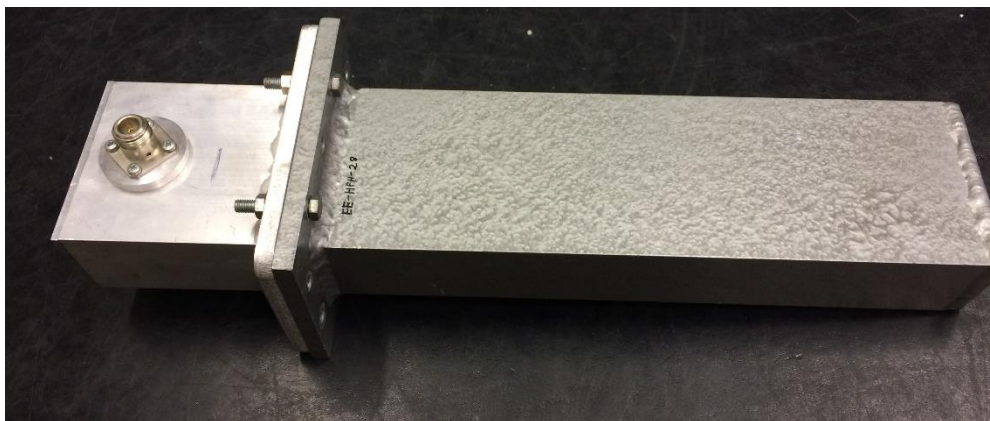
Figure 3.14: Built transition attached to the matched load.

28
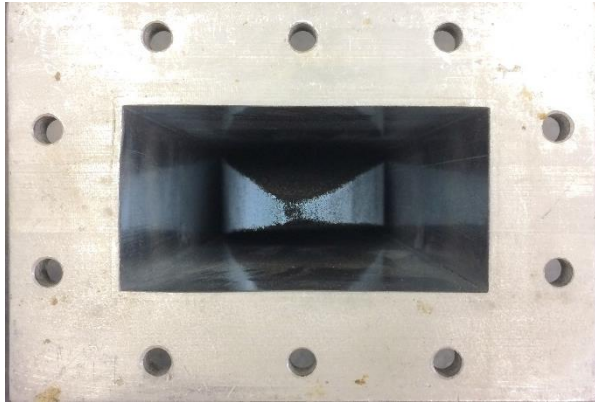
Figure 3.15: Front view of the matched load containing a pyramid of absorbing foam.
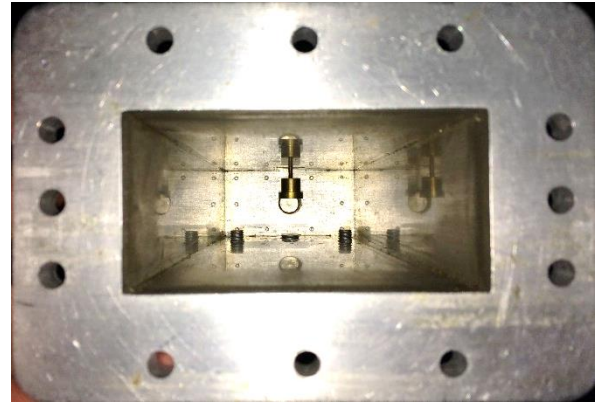
Figure 3.16: Front view of the transition from the calibration kit.

The built transition was also compared to a transition from a calibration kit, as shown in Figure 3.16. This transition had tuning screws and an even wider tip at the end of the pin. Due to these factors it was expected to outperform the built transition.

This measurement setup was only able to measure S_{11}. This was, however, sufficient at this stage since the input reflection coefficients were the critical parameters ($S_{11} = S_{22}$ since the device was passive). The results are shown in Figure 3.17, Table 3.3 and Table 3.4.
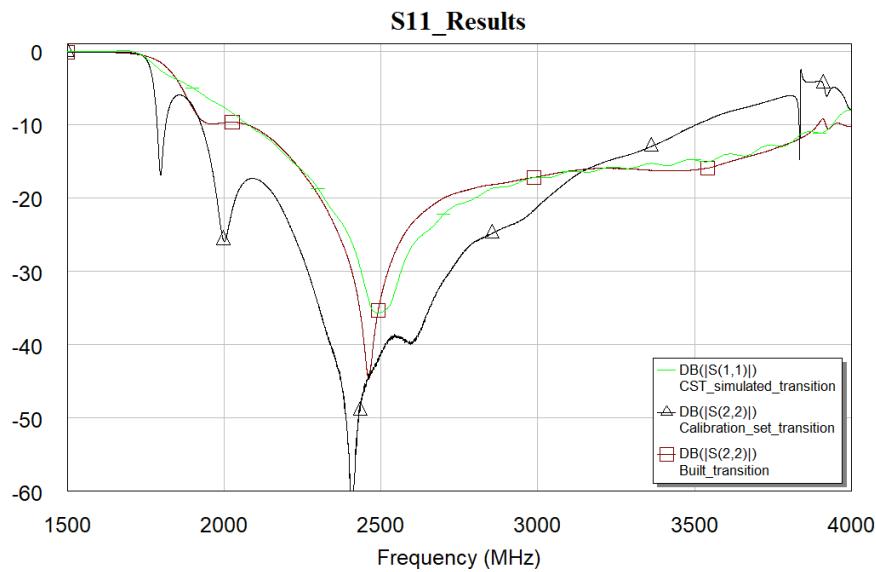
Figure 3.17: Comparison of the measured S_{11} of the built transition, the calibration kit transition and the simulated transition.

Parameter	Frequency (GHz)	CST (dB)	Built transition (dB)	Calibration set transition (dB)
$|S_{11}|$	2.2	-14.36	-13.97	-22.92
$|S_{11}|$	2.4	-25.33	-28.98	-58.22
$|S_{11}|$	2.45	-32.35	-41.59	-45.52
$|S_{11}|$	2.5	-35.59	-33.36	-41.62
$|S_{11}|$	3.3	-15.95	-16.05	-14.01

Table 3.3: Magnitude of S_{11} for the simulated-, built- and calibration set transition at key frequencies.

Parameter	CST (GHz)	Built transition (GHz)	Calibration set transition (GHz)
$\lvert S_{11} \rvert \leq -20\, dB$	$2.32 - 2.80$	$2.31 - 2.70$	$2.17 - 3.03$
$\lvert S_{11} \rvert \leq -15\, dB$	$2.22 - 3.46$	$2.22 - 3.62$	$1.96 - 3.22$

Table 3.4: Operational frequencies for the transitions for different magnitudes of S_{11}.

The built transition worked as designed and matched the CST simulation very closely. It had an even smaller S_{11} than the simulation between 2.4 and 2.5 GHz, which was very desirable. The built transition also had a wide operating frequency, if $S_{11} \leq -15\, dB$ was considered acceptable.

The transition from the calibration kit improved on the built transition by having a smaller S_{11} for the same operating frequencies (except for the highest frequencies).

3.4.2.6   Conclusion

The waveguide to coaxial transition worked well. It had a reflection coefficient of less than $-20\, dB$ over the desired frequency range of 2.4 to 2.5 GHz. It very almost also covered the recommended frequency range of the WR340 waveguide with a reflection coefficient of less than $-15\, dB$.

A duplicate of the built transition was constructed. This was so that 2-port measurements could be made. Using two transitions, a Thru, Reflect, Load/Line (TRL) calibration could have been used with a network analyser in order to remove the effect of the transitions from waveguide measurements.

As seen with the transition from the calibration kit, tuning screws could still have been added to improve the response further. The shape of the pin inside the waveguide could also have been investigated further for a wider bandwidth.

3.4.3   Waveguide with pins

3.4.3.1   Introduction
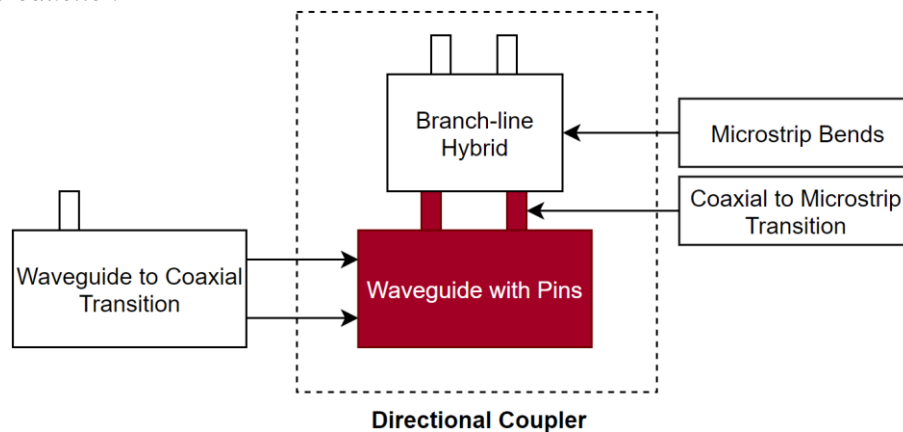
Figure 3.18: The waveguide with pins is discussed in this subsection.

The waveguide with pins was used to couple a small amount of energy from the waveguide onto two coaxial transmission lines. Theoretically, the signal coupled to each transmission line was equal in magnitude, but 90° out of phase. The transmission lines fed the branch-line hybrid, where the signals were added and subtracted (see Figure 3.18 above).

3.4.3.2   Design

The waveguide with pins consisted of a WR340 waveguide with two pins inserted into it. The pins were placed in the centre of the broad wall where the electric field was at a maximum. The pins were placed a quarter wavelength ($\lambda_g/4$) apart so that the signals from the pins would be 90° out of phase with each other (λ_g denotes the wavelength inside the waveguide). The pins transitioned to coaxial transmission lines that terminated in female SMA connectors. Figure 3.19 shows the location of the pins relative to the waveguide.
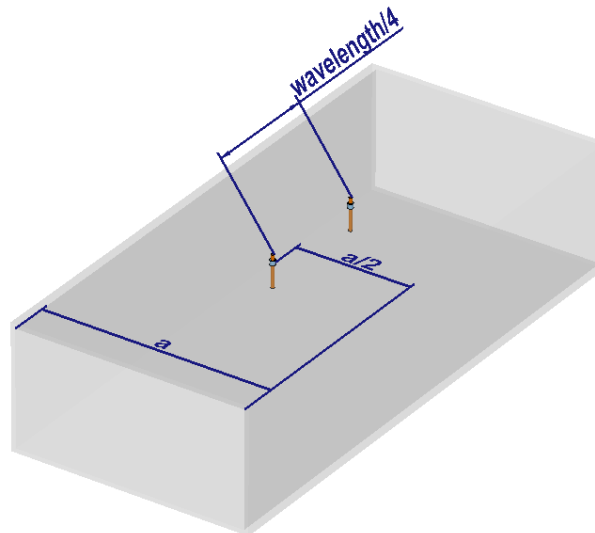
Figure 3.19: The location of the pins relative to the waveguide for the waveguide with pins.

The design of the waveguide with pins borrowed elements from the waveguide to coaxial transition (Sec. 3.4.2). It also used a pin inserted into the broad wall of the waveguide in order to couple power from the waveguide onto a coaxial transmission line. However, whereas the transition coupled *maximum* power onto the transmission line, the waveguide with pins only coupled a *small amount* of power.

There were several parameters that could have been adjusted to control the amount of energy coupled to the pins: the radius of the pins, the location of the pins relative to the centre of the broad wall and the length of the pins.

The radius of the pins was that of the centre pin of an SMA connector. Therefore, a stock SMA panel mount connector was used, as shown in Figure 3.20.
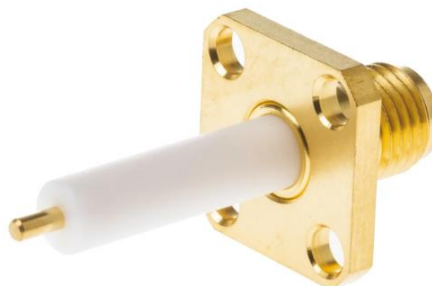
Figure 3.20: A typical panel mount female SMA connector [90].

The pins were placed in the centre of the broad wall. In this way the only parameter that needed to be modified in order to change the coupling was the length of the pin. This simplified the design practically, since the pin of the panel mount connector could simply have been cut shorter to reduce the coupling.

3.4.3.3 Simulation
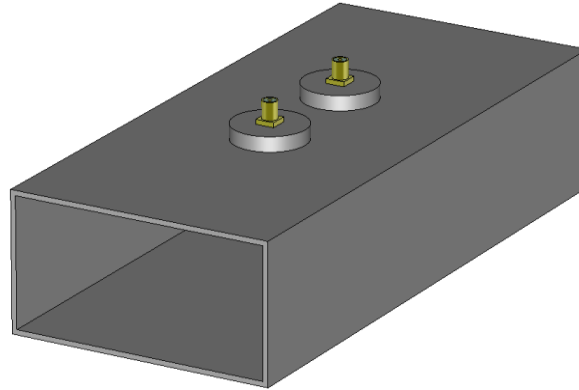
Figure 3.21: CST model of the waveguide with pins.

Property	Symbol	Value
Waveguide type	$-$	WR340
Distance of the pins from each other	d_{pp}	$43.3\ mm$
Length of each pin into the waveguide	l_p	$3.1\ mm$
Radius of the pins	r_p	$0.65\ mm$
Length of the waveguide	l_g	$200\ mm$

Table 3.5: Optimal dimension for the waveguide with pins.

The waveguide with pins was simulated in CST, as shown in Figure 3.21, with the dimensions given in Table 3.5. The distance between the pins was fine-tuned so that a 90° phase difference was found between the pins at 2.45 GHz. This can be seen in the electric field plot of the travelling wave shown in Figure 3.22. Table 3.6 marks the phase difference between the pins at three different frequencies.
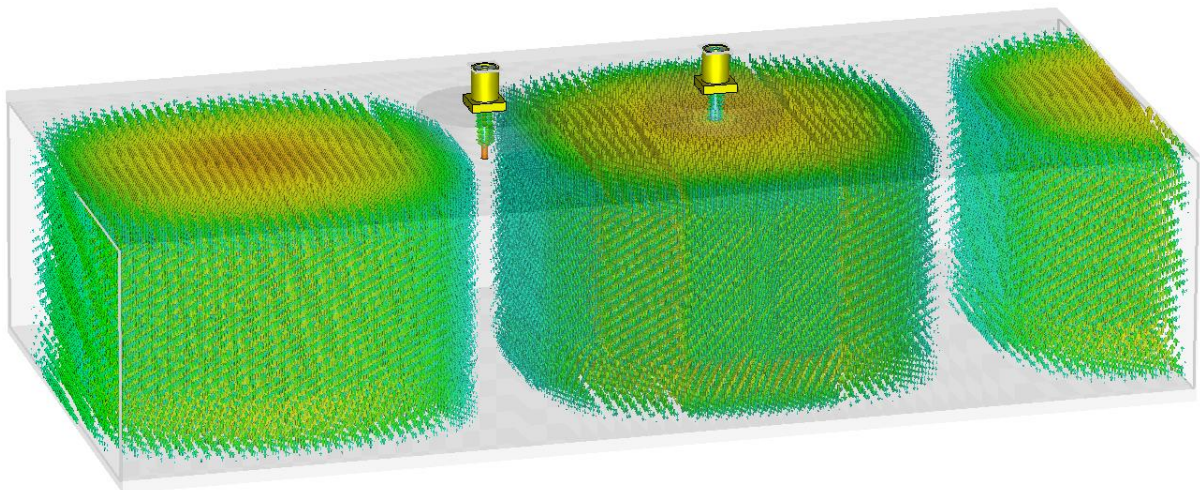
Figure 3.22: At this instance in time, the 3D electric field plot of the waveguide with pins clearly shows how the amplitude of the electric field is at a null at one pin while it is at a maximum at the other pin.

32

Frequency	Phase difference between pins
2.4 GHz	86.4°
2.45 GHz	90.13°
2.5 GHz	93.77°

Table 3.6: Phase difference between the pins over the operating frequency range.

The length of the pins was modified to determine the amount of coupling. They were designed for a coupling of around 37 dB. In this way the pins could still have been cut afterwards to reduce the coupling further, or attenuators could simply have been added to the output of the directional coupler in order to reduce the effective coupling.
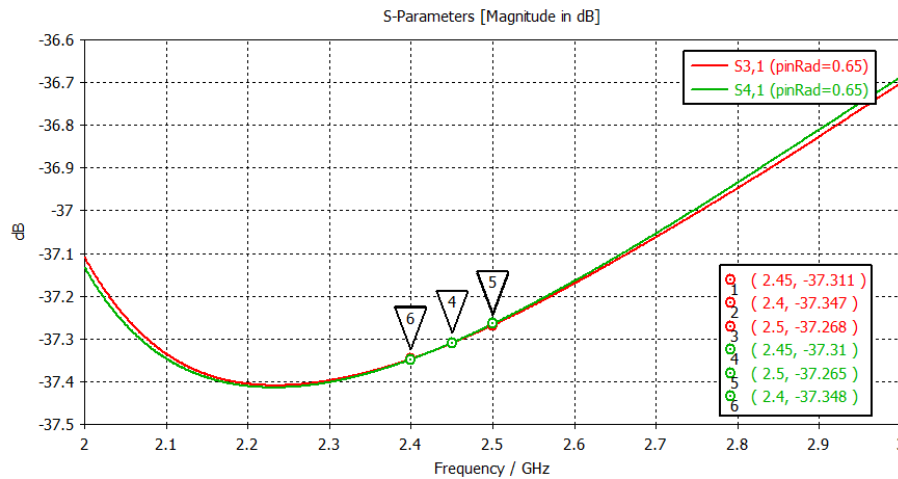
Figure 3.23: S_{31} and S_{41} for the waveguide with pins shows the amount of coupling between the power in the waveguide and the power seen at the SMA connectors.

3.4.3.4   Results

Figure 3.24: The waveguide with pins.

The waveguide with pins was constructed using square aluminium tubing with the dimensions of a WR340 waveguide. The flanges were welded on. The SMA panel mount connectors were mounted onto

33

aluminium disks that were inserted into the waveguide at $\lambda_g/4$ from each other. The pins of the SMA connectors were trimmed to the correct length and the Teflon was removed for the section of the pin that protruded into the waveguide. The waveguide with pins is shown in Figure 3.24.
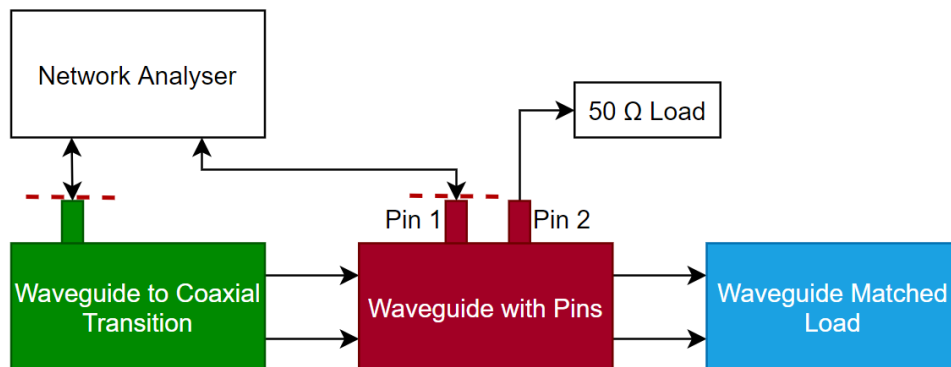
Figure 3.25: Block diagram of the measurement setup for the waveguide with pins. The reference plane for the calibration of the network analyser is indicated with the red dashed lines.

A block diagram of the measurement setup is shown in Figure 3.25. The one port of the network analyser (N5242A PNA-X Microwave Network Analyzer) was connected to the waveguide with pins through the waveguide to coaxial transition of the calibration set. The other network analyser port was connected to one of the pins of the waveguide with pins. The other pin of the waveguide with pins was connected to a 50 Ω load. The other waveguide port of the waveguide with pins was terminated with the matched waveguide load. The physical measurement setup is shown in Figure 3.26.
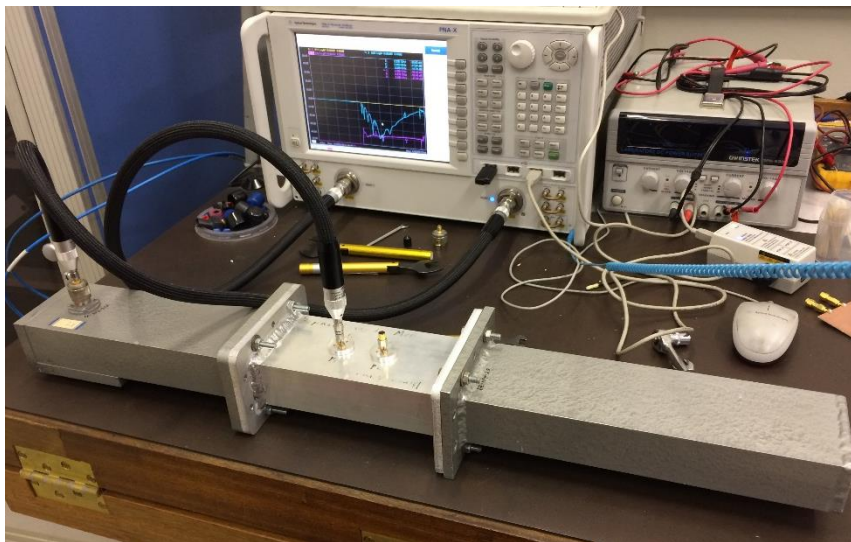
Figure 3.26: The measurement setup for the waveguide with pins.

The coaxial cables of the network analyser were calibrated out. However, the waveguide to coaxial transition could not be calibrated out since both ports of the network analyser had to be calibrated to either a coaxial termination or a waveguide termination. Nonetheless, the transition was a good transition, as shown in Sec. 3.4.2.5. It will now be shown that the impact of the transition was negligible.

Assuming that, in the worst case, that the transition had a reflection coefficient of $S_{11} = -15 \, dB$, and that the network analyser supplied $P_{NA} = -5 \, dBm = 3.16 \, mW$ of input power, then:

$$P_{loss} = P_{NA} - S_{11} = -20 \, dBm = 0.01 \, mW \tag{12}$$

This translates to a loss of less than 0.7 % between $1.96 - 3.22 \, GHz$ (see Table 3.4). Furthermore, between $2.17 - 3.03 \, GHz$, the reflection coefficient of the transition was less than $S_{11} \leq -20 \, dB$, resulting in a loss of less than 0.2 % over most of the desired frequency range. This was considered negligible.

34

The measured data is compared to the simulated data in Figure 3.27 and Figure 3.28. Important data points are displayed in Table 3.7 and Table 3.8.
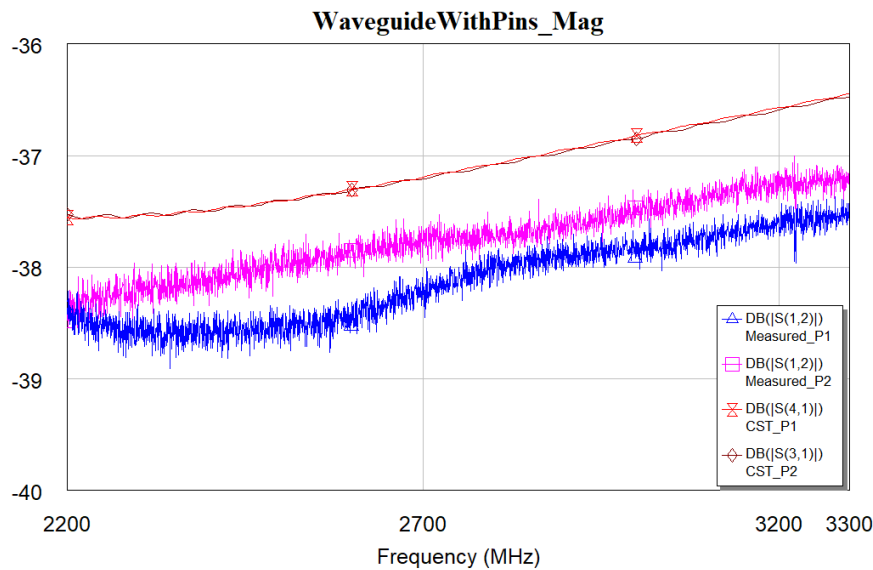
Figure 3.27: Comparison of the measured $|S_{21}|$ of the waveguide with pins to that of the CST simulation.

Frequency (GHz)	Measured $|S_{21}|$ of pin 1 (dB)	Simulated $|S_{21}|$ of pin 1 (dB)	Measured $|S_{21}|$ of pin 2 (dB)	Simulated $|S_{21}|$ of pin 2 (dB)
2.2	-38.35	-37.56	-38.35	-37.56
2.4	-38.53	-37.50	-38.05	-37.50
2.45	-38.56	-37.45	-38.01	-37.45
2.5	-38.52	-37.41	-37.97	-37.41
3.3	-37.53	-36.44	-37.19	-36.44

Table 3.7: Magnitude of S_{21} at key frequencies for the waveguide with pins.

The simulated magnitude of S_{21} for the waveguide with pins was within $1.2 \, dB$ of the measured data, which was quite accurate. A difference of no more than $0.6 \, dB$ was seen between the magnitudes of S_{21} for the pins. This difference was attributed to construction tolerances, such as the length of the pins not being exactly equal.
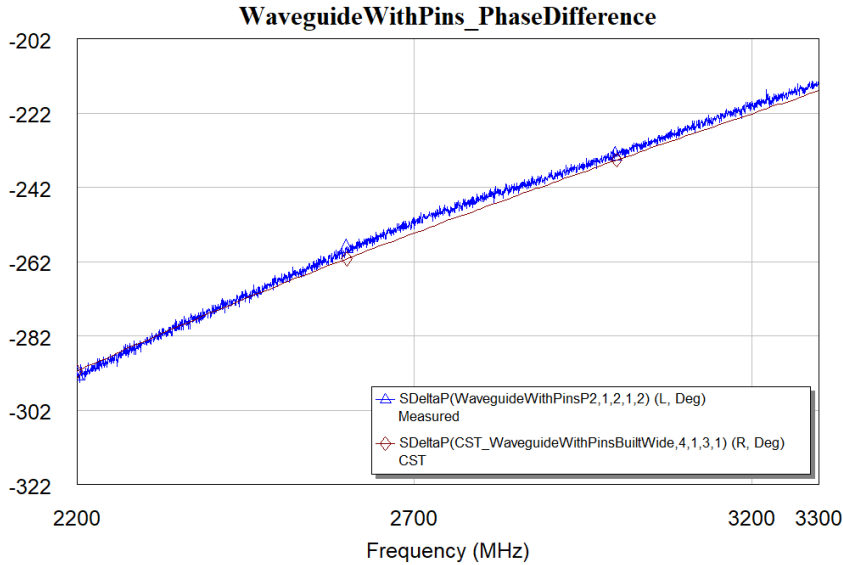
Figure 3.28: The difference in phase of S_{21} between the two pins of the waveguide with pins are shown. The left axis indicates the phase angle in degrees.

Frequency (*GHz*)	Measured phase difference (°)	Simulated phase difference (°)
2.2	67.4	70.1
2.4	84.9	86.5
2.45	88.0	90.2
2.5	93.6	93.8
3.3	146.2	146.0

Table 3.8: Phase difference between the pins of the waveguide with pins at key frequencies. Note that the values displayed in Figure 3.28 has been converted so that they are between 0° and 360°.

The axes of Figure 3.28 are plotted in degrees; thus both axes could have been converted to values between 0° and 360°, as was done in Table 3.8 (360° + *left axis* and *right axis* − 360°).

The gradient of the phase difference between the pins were very similar between the simulation and the measured data. The phase difference at 2.45 *GHz* was measured as 88.0°, which was very close to the designed value of 90°.

3.4.3.5 Conclusion

The waveguide with pins worked well. A phase difference of around 90° was seen between the pins at 2.45 *GHz*. About −38 *dB* of power coupled to each pin. There was, however, a difference of 0.6 *dB* between the magnitude of the power at each of the pins, which affected how well the branch-line hybrid was able to add and subtract the signals from each other.

A next iteration of the waveguide with pins can investigate using wider tips at the end of the pins, as was done with the waveguide to coaxial transition. This may improve the frequency range of the 90° phase response.

3.4.4   Branch-line hybrid

3.4.4.1   Introduction
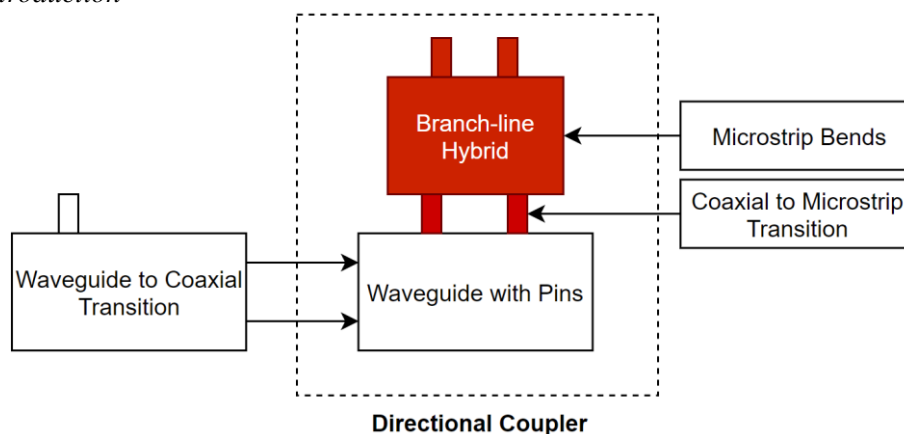
Figure 3.29: The branch-line hybrid is discussed in this subsection.

The purpose of the branch-line hybrid in this system was to differentiate between the forward and reverse signals in the waveguide. It did this by adding or subtracting the two signals that came from the waveguide with pins, as shown in the block diagram of Figure 3.29. The two signals were equal in magnitude but were 90° out of phase. This meant that, for a signal travelling only in one direction in the waveguide, constructive superposition would occur at the one output port and deconstructive superposition at the other. For a signal travelling in the opposite direction, the ports at which constructive and deconstructive superposition takes place will be swopped around. Thus a forward travelling wave in the waveguide will only appear at one of the output ports of the branch-line hybrid, and a reverse travelling wave at the other output port.

The input side of the branch-line hybrid was connected to the outputs from the waveguide with pins, as shown in Figure 3.30. The output side could either have both ports connected to power detectors or have the deconstructive superposition port connected to a matched load and the remaining port to a power detector. The former configuration has additional uncertainty since perfect superposition is not realisable. This means that some power may 'leak' from the wave travelling in the opposite direction to that being measured. The latter configuration requires the pins with the branch-line hybrid to be duplicated on the opposite side of the waveguide so that power travelling in the opposite direction could also be measured. An attenuator may also have been inserted between the branch-line hybrid and the power detector to change the amount of power passed to the power detector.
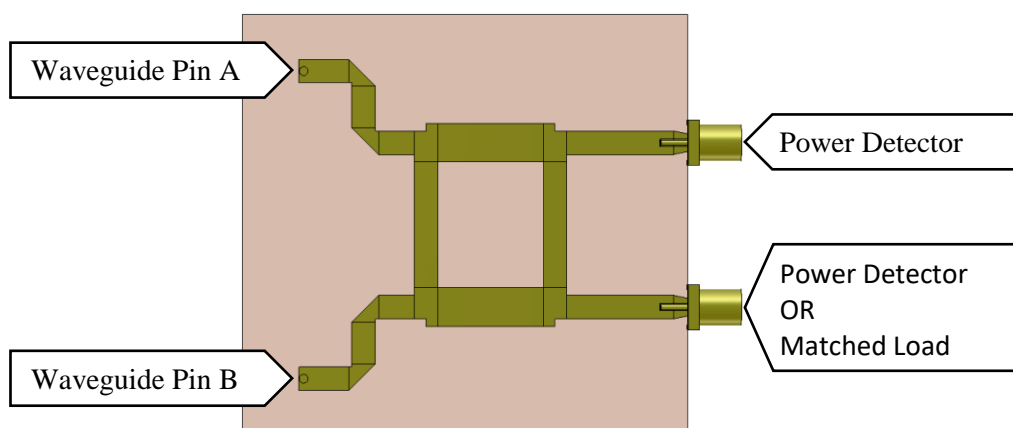
Figure 3.30: System layout for the branch-line hybrid.

3.4.4.2   Design and simulation

A branch-line hybrid divides power between its two output ports. Theoretically, the output at one port was 90° out of phase with the other output, and the magnitude of each was $-3\ dB$ less than the input power (since the power was divided equally between the ports).

37

The basic theoretical design of the branch-line hybrid is discussed in more detail at the end of section 3.2.4: Design Options. This design subsection builds on that discussion.

Using a line impedance of Z_0 and $Z_0/2$ at the relevant line sections ensured that an input impedance of 50 Ω was seen at the ports. The line impedance of microstrip line is dependent on the dielectric constant of the substrate, the thickness of the substrate and the width of the line. This impedance is frequency dependant. The line width was determined for $1.524\ mm$ Rogers 4003C substrate by using the following formulas [7, p. 148]:

$$W = \frac{2d}{\pi}\left[B - 1 - \ln(2B - 1) + \frac{\epsilon_r - 1}{2\epsilon_r}\left\{\ln(B - 1) + 0.39 - \frac{0.61}{\epsilon_r}\right\}\right] \tag{13}$$

which is valid for $W > 2d$, with

$$B = \frac{377\pi}{2Z_0\sqrt{\epsilon_r}}. \tag{14}$$

Referring to Figure 3.31, W denotes the line width and d and ϵ_r denotes the thickness and the dielectric constant of the substrate, respectively.
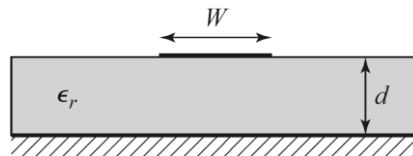
Figure 3.31: Dimensions of a microstrip line [7, p. 148].

The line impedance was then simulated and fine-tuned in AWR. A line width of $3.31\ mm$ and $5.44\ mm$ was determined for Z_0 and $Z_0/2$, respectively.

To be able to connect the branch-line hybrid to the waveguide with pins, the input pins physically had to be apart by a quarter wavelength in a waveguide ($\lambda_{WG}/4$). As such, the input pins had to be moved outwards. Two mitred bends were inserted into each input line section from that side of the board. These bends are discussed in detail in App. B.2.

In the theoretical design of a branch-line hybrid the length of the shunt and parallel lines should be exactly a quarter wavelength ($\lambda_{MS}/4$). In practice, however, these lengths needed to be fine-tuned since the effective length of these lines were affected by the input lines into the branch-line hybrid. This was done using an AWR simulation. As shown in Figure 3.32, lengths of $17.70\ mm$ and $14.84\ mm$ were determined for the shunt and parallel lines, respectively.
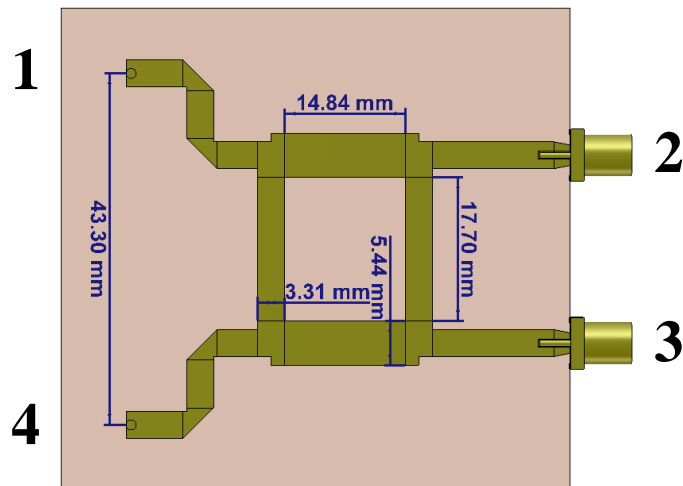
Figure 3.32: Physical dimensions of the branch-line hybrid. Port numbering is also shown.

End launch SMA connectors (with no connector legs and an optimised taper) were used at the output side of the branch-line hybrid. Bottom-fed SMA connectors were used at the input side to replicate a fully integrated system where the pins from the waveguide with pins would have run directly into the branch-line hybrid. In order to include the non-ideal effects of these transitions, a full 3D simulation was run using CST (see App. B.3 for a full discussion of the different transitions that were used). The model is shown in Figure 3.33.
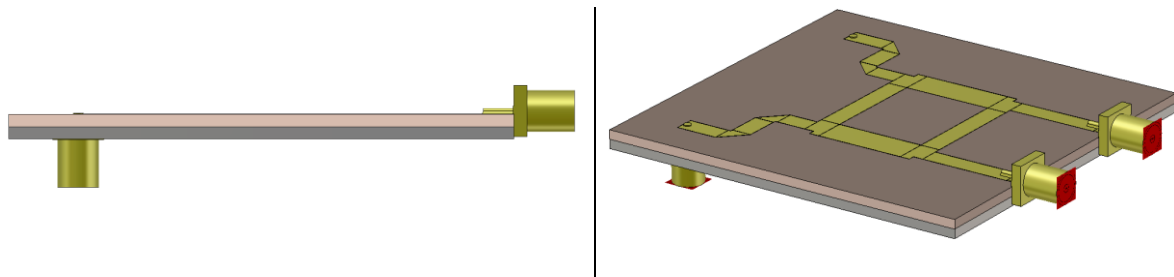
Figure 3.33: Side and perspective view of the CST Studio Suite 2019 model of the branch-line hybrid

3.4.4.3 Results

After the board was built (Figure 3.34), it was measured up with a network analyser (N5242A PNA-X Microwave Network Analyzer). A comparison between the S-parameters of the AWR and CST simulations and the measured results are shown in Figure 3.35, Figure 3.36, Figure 3.37 and Figure 3.38 and in Table 3.9 and Table 3.10. Port numbering follows that of Figure 3.32.
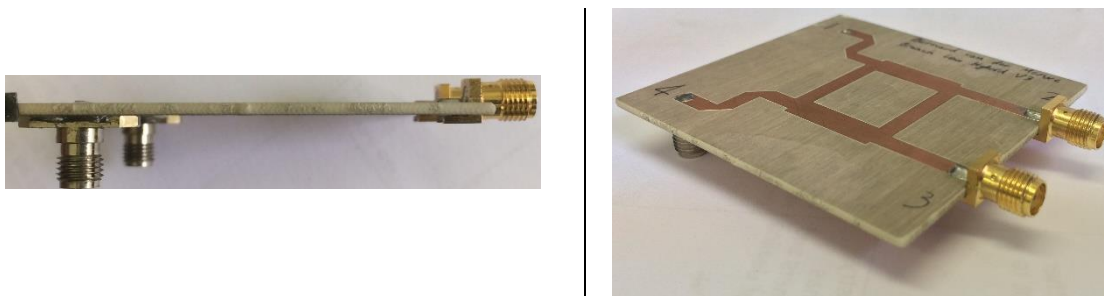
Figure 3.34: Side and perspective view of the branch-line hybrid that was built and measured up.
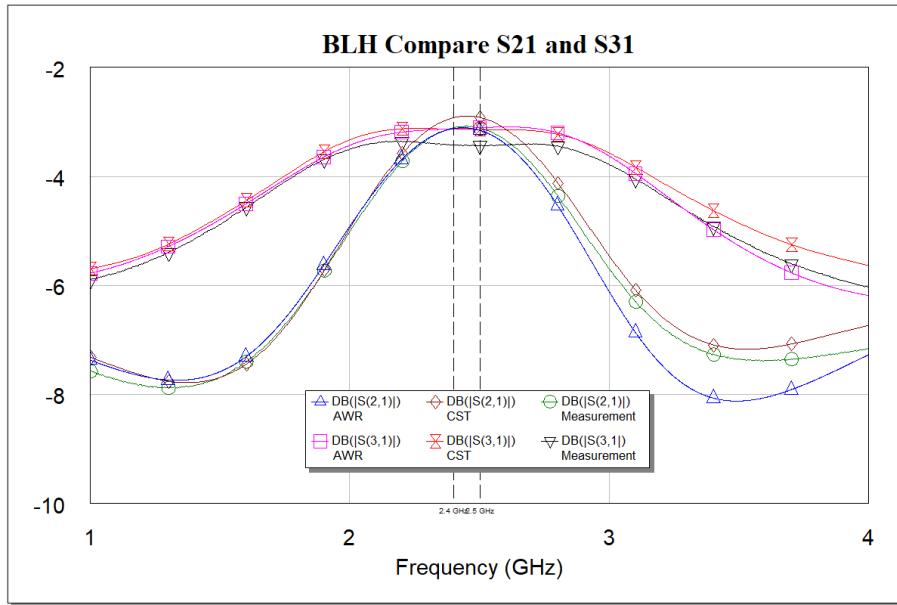
Figure 3.35: Comparison of S_{21} and S_{31} between AWR, CST and the measured up branch-line hybrid measured from 1 to 4 GHz.
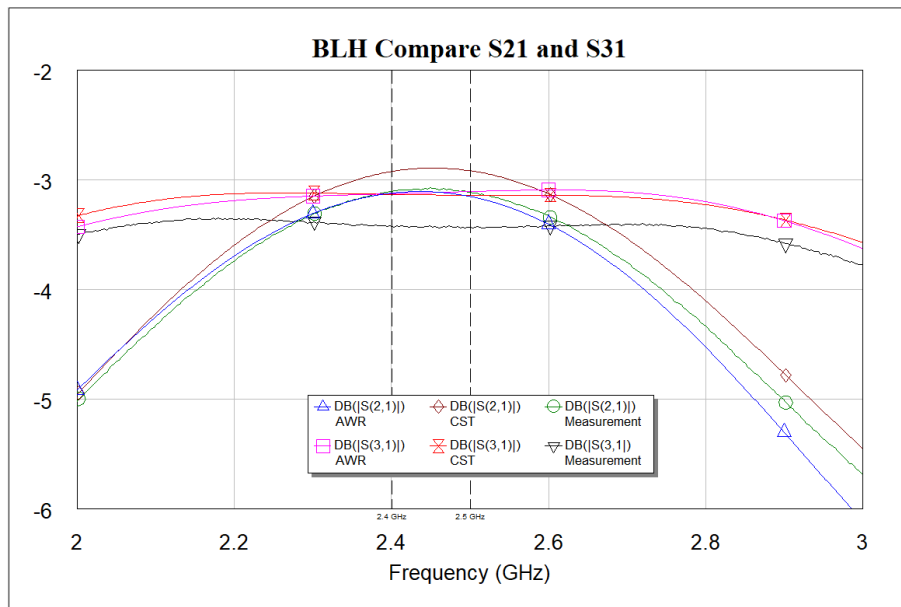
Figure 3.36: Comparison of S_{21} and S_{31} between AWR, CST and the measured up branch-line hybrid measured from 2 to 3 GHz.

40
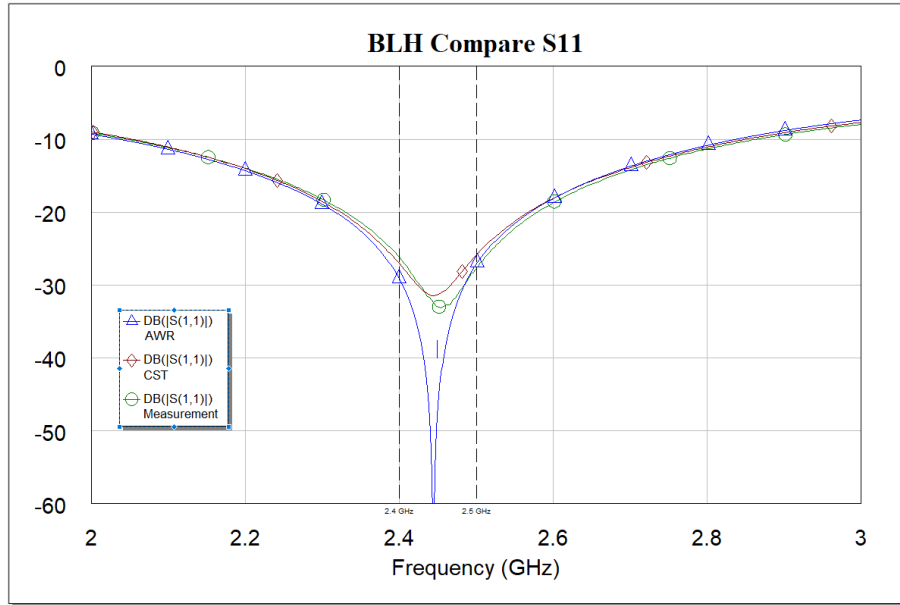
Figure 3.37: Comparison of S_{11} between AWR, CST and the measured up branch-line hybrid measured from 2 to 3 GHz.
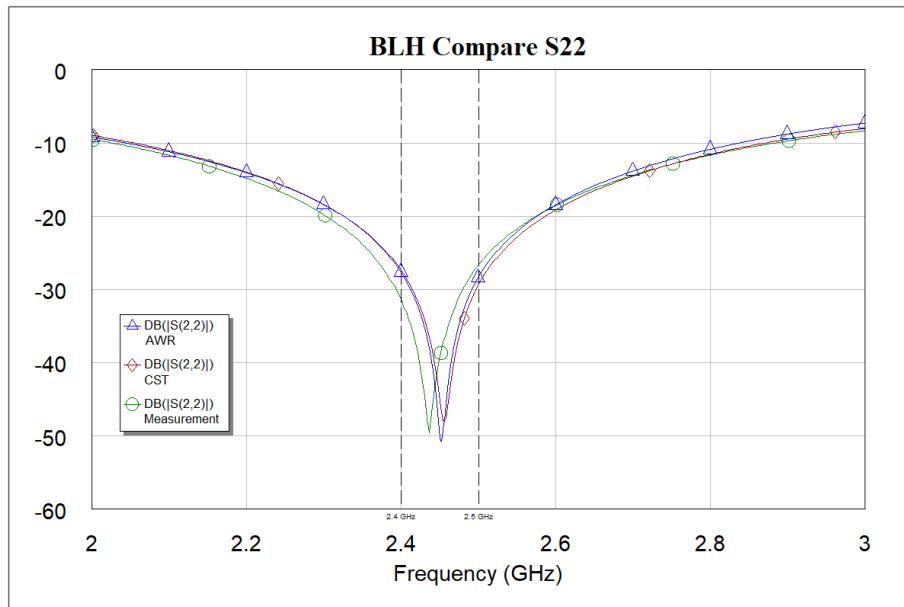
Figure 3.38: Comparison of S_{22} between AWR, CST and the measured up branch-line hybrid measured from 2 to 3 GHz.

Parameter	Frequency (GHz)	AWR (dB)	CST (dB)	Measurement (dB)
$\|S_{21}\|$	2.4	-3.12	-2.92	-3.11
$\|S_{21}\|$	2.45	-3.11	-2.89	-3.07
$\|S_{21}\|$	2.5	-3.15	-2.92	-3.11
$\|S_{31}\|$	2.4	-3.13	-3.13	-3.42
$\|S_{31}\|$	2.45	-3.12	-3.14	-3.42
$\|S_{31}\|$	2.5	-3.11	-3.14	-3.43
$\|S_{21}\| - \|S_{31}\|$	2.45	0.01	0.25	0.35

Table 3.9: Comparison of specific data points between AWR, CST and the measured up branch-line hybrid.

Parameter	AWR (%)	CST (%)	Measurement (%)
Fractional Bandwidth*	18.4 %	21.6 %	22.5 %

Table 3.10: Comparison of the fractional bandwidth between AWR, CST and the measured up branch-line hybrid.

*Fractional bandwidth is defined as [48]:

$$FBW = \frac{f_2 - f_1}{f_c},$$

(15)

where $f_c = \frac{f_2 + f_1}{2}$ and where a power difference of less than $0.5\ dB$ between $|S_{21}|$ and $|S_{31}|$ was considered acceptable.

A good fractional bandwidth was achieved. Literature suggests a fractional bandwidth of 15 % is achievable, considering a power difference of less than $0.5\ dB$ between the two output ports (difference between $|S_{21}|$ and $|S_{31}|$) [44]. This branch-line hybrid improved on this by 7.5 %.

The simulations matched the measured results very well. Assuming that the full 3D CST simulation was more accurate, it appeared that both $|S_{21}|$ and $|S_{31}|$ was smaller than what was simulated. This was likely due to minor mismatches that occured due to tolerances in manufacturing (e.g. the line impedance may not have been exactly 50 Ω). It may also have been due to losses in the microstrip.

3.4.4.4 Conclusion

The branch-line hybrid had a good fractional bandwidth. It included bends and different connectors at the inputs and outputs. The measured data matched the simulation well.

As a next step, stripline could be used instead of microstrip. This would make the branch-line hybrid less susceptible to interference. The bandwidth could also be improved by adding more sections to create a multi-section branch-line hybrid.

3.4.5 Directional coupler

3.4.5.1 Introduction
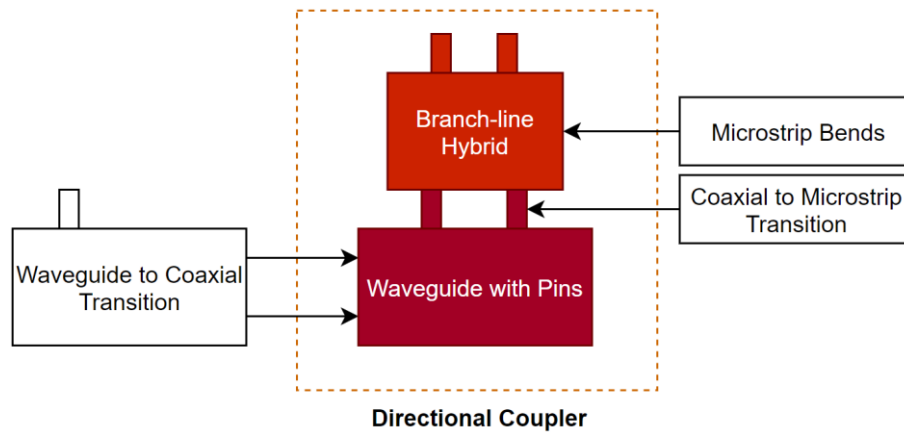
Figure 3.39: The complete directional coupler is discussed in this subsection.

Once each of the components of the directional coupler was constructed, it was all put together and measured up. The pin from the waveguide with pins that coupled less power was connected to the side of the branch-line hybrid that output slightly more power so as to compensate. Figure 3.39 indicates where this subsection fits in with the chapter. A picture of the directional coupler is shown in Figure 3.40.
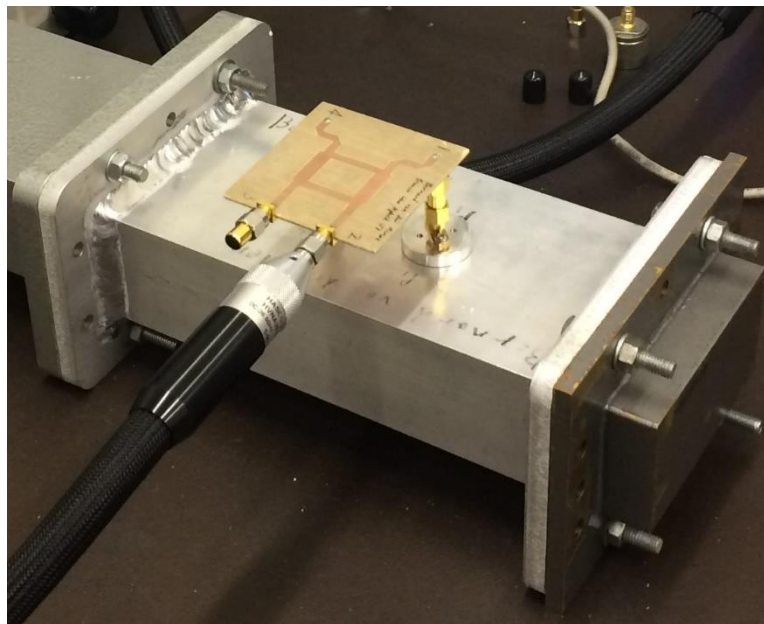
Figure 3.40: The directional coupler being measured up.

3.4.5.2   Results
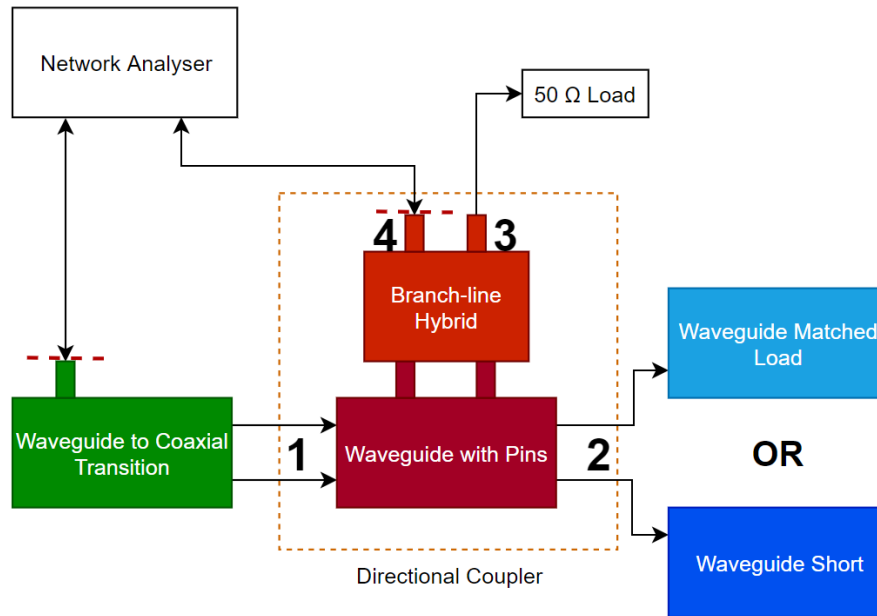
Figure 3.41: Block diagram of the measurement setup for the complete directional coupler. Both port 3 and 4 of the directional coupler were measured. Both the waveguide load and the waveguide short was attached at port 2. The directional coupler was also measured in reverse such that ports 1 and 2 were swopped (and therefore port 3 and 4 as well).

The directional coupler was measured up in a similar manner to the waveguide with pins. The block diagram of the setup is shown in Figure 3.41. The input waveguide port to the coupler was connected to the network analyser through the waveguide to coaxial transition from the WR340 calibration set. The other port of the network analyser was connected, in turn, to each of the ports of the branch-line hybrid, with a 50 Ω load connected to the other port of the branch-line hybrid (ports 3 and 4). The output waveguide port of the coupler was first connected to a load and then connected to a short. All the same measurements were also made with the coupler turned around i.e. with the output waveguide port (port 2) connected to the waveguide to coaxial transition and the input waveguide port (port 1) connected to the load and short. The directional coupler, with port numbers, are shown in Figure 3.42.

As with the waveguide with pins, the waveguide to coaxial transition was used. This incurred a small measurement inaccuracy, but, as shown in Sec. 3.4.3.4, this was negligible. The reference planes for the network analyser are shown with red dashed lines in Figure 3.41.

The measured results are shown in Figure 3.43 and Figure 3.44. The measured quantities was directly relatable to the directional coupler parameters specified with eq. 3 to 6 from Sec. 3.2.3. They are repeated here and the related parameters are explained:

Coupling (C) is the amount of power from the input port (port 1) that is delivered to the coupled port (port 3):

$$C = 10 \log \frac{P_1}{P_3} \, dB = -|S_{31}| \, dB \tag{16}$$

In terms of the forwards connected coupler, $C = -|S_{31 \, Load \, Attached}|$. For the reverse connected coupler, $C = -|S_{42 \, Load \, Attached}|$.

Isolation (I) is the amount of power from the input port (port 1) that is delivered to the isolated port (port 4):

$$I = 10 \log \frac{P_1}{P_4} \, dB = -|S_{41}| \, dB \tag{17}$$

44

In terms of the forwards connected coupler, $I = -|S_{41\ Load\ Attached}|$. For the reverse connected coupler, $D = -|S_{32\ Load\ Attached}|$.

Insertion Loss (L) is the amount of power from the input (port 1) that is delivered to the through port (port 2).

$$L = 10 \log \frac{P_1}{P_2}\ dB = -|S_{21}|\ dB \qquad (18)$$

Due to the small amount of coupling, a very small insertion loss was expected. Due to the losses in the waveguide to coaxial transition, it would have been very hard to discern between the actual insertion loss and the loss in the transitions.

Directivity (D) is the ability of the coupler to separate forward and backward power.

$$D = 10 \log \frac{P_3}{P_4}\ dB = \frac{|S_{31}|}{|S_{41}|}\ dB \qquad (19)$$

The directivity was calculated for the forward and backward connected coupler by $D = \frac{|S_{31\ Load\ Attached}|}{|S_{41\ Load\ Attached}|}$ and $D = \frac{|S_{42\ Load\ Attached}|}{|S_{32\ Load\ Attached}|}$, respectively.
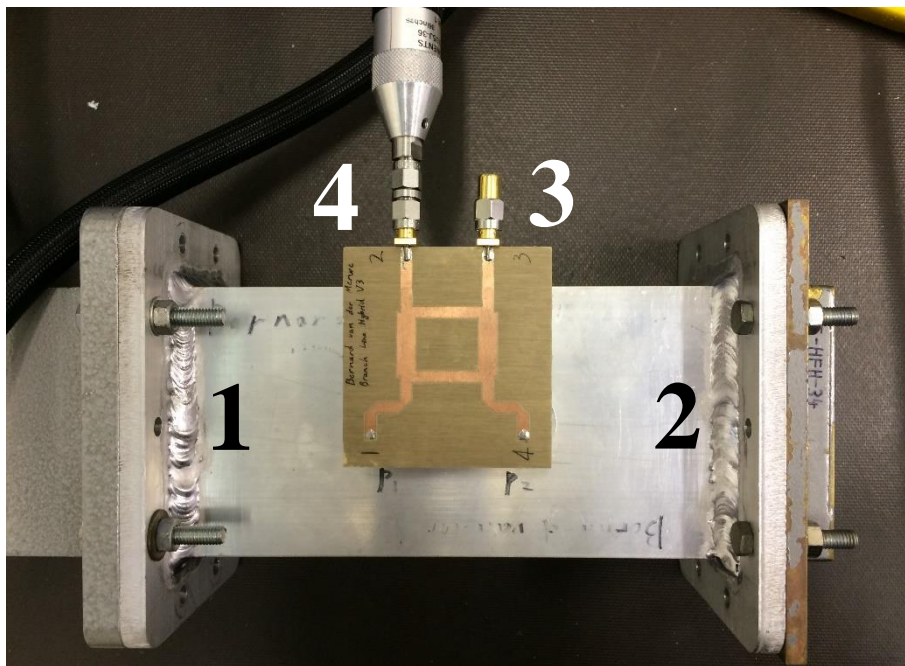
Figure 3.42: The directional coupler with port numbers indicated. Pictured here is the waveguide to coaxial transition connected to port 1, the waveguide short attached to port 2, the 50 Ω load attached to port 3 and the network analyser attached to port 4.

45
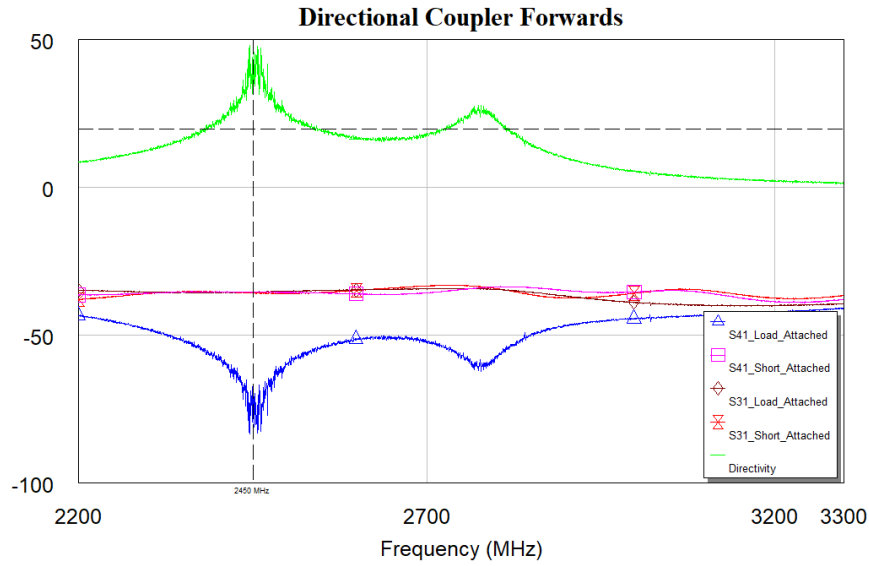
Figure 3.43: Measurements of $|S_{31}|$ and $|S_{41}|$ for the directional coupler in the forward orientation (i.e. port 1 connected to the waveguide to coaxial transition). The directivity is also shown. The horizontal line indicates $20\ dB$ and the vertical line indicates $2.45\ GHz$.

Frequency (GHz)	$\|S_{31}\|$ Load Attached (dB)	$\|S_{31}\|$ Short Attached (dB)	$\|S_{41}\|$ Load Attached (dB)	$\|S_{41}\|$ Short Attached (dB)	Directivity (dB)
2.2	-34.75	-37.89	-43.36	-36.33	8.66
2.4	-35.45	-35.21	-57.94	-35.22	22.50
2.45	-35.39	-35.63	-78.40	-35.39	43.01
2.5	-35.11	-35.82	-59.74	-35.49	24.63
3.3	-39.29	-36.49	-40.78	-37.92	1.49

Table 3.11: Magnitude of the S-parameters and the directivity of the directional coupler in the forward orientation for key frequencies.

Parameter	Frequency range (GHz)
Directivity $\geq 20\ dB$	$2.38 - 2.54$
Constant coupling range ($\|S_{31}\|^* \pm 0.5\ dB$)	$2.30 - 2.54$
*Considers $\|S_{31}\|$ with both the load and the short attached.	

Table 3.12: Operational frequencies for the directivity and for constant coupling for the directional coupler in the forward orientation.
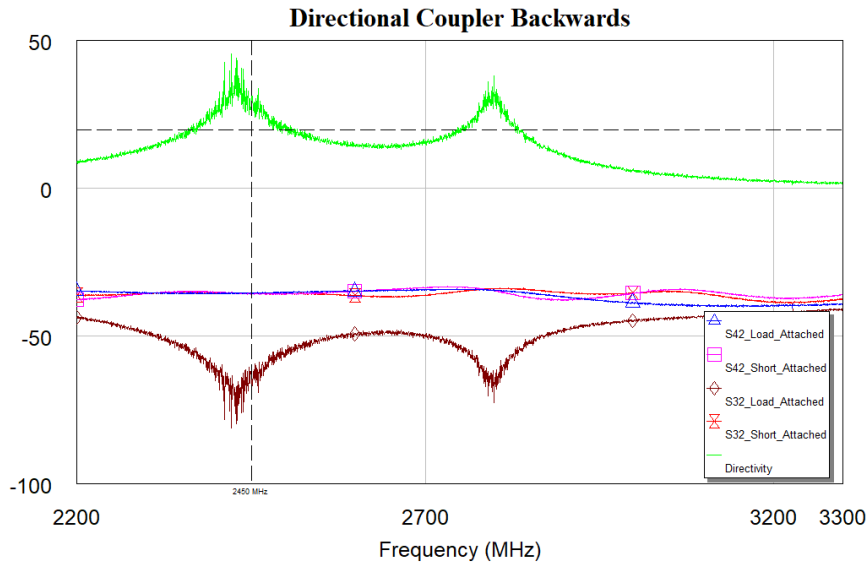
Figure 3.44: Measurements of $|S_{32}|$ and $|S_{42}|$ for the directional coupler in the backwards orientation (i.e. port 2 connected to the waveguide to coaxial transition). The directivity is also shown. The horizontal line indicates 20 dB and the vertical line indicates 2.45 GHz.

Frequency (GHz)	$|S_{32}|$ Load Attached (dB)	$|S_{32}|$ Short Attached (dB)	$|S_{42}|$ Load Attached (dB)	$|S_{42}|$ Short Attached (dB)	Directivity (dB)
2.2	−43.65	−36.09	−34.67	−36.09	8.97
2.4	−60.12	−35.24	−35.58	−35.15	24.5
2.45	−62.30	−35.46	−35.40	−35.58	27
2.5	−55.74	−35.49	−35.18	−35.77	20.6
3.3	−41.02	−37.46	−39.07	−36.07	1.95

Table 3.13: Magnitude of the S-parameters and the directivity of the directional coupler in the backwards orientation for key frequencies.

Parameter	Frequency range (GHz)
Directivity $\geq 20\ dB$	$2.36 - 2.51$
Constant coupling range ($|S_{42}|^* \pm 0.5\ dB$)	$2.27 - 2.55$
*Considers $|S_{42}|$ with both the load and the short attached.	

Table 3.14: Operational frequencies for the directivity and for constant coupling for the directional coupler in the backwards orientation.

The measured results satisfied the specification and was comparable with other directional couplers. The coupling was sufficiently constant between 2.4 and 2.5 GHz. The coupler had a directivity of over 20 dB over this desired frequency range. The coupling over these frequencies was virtually unchanged even with a short attached to port 2 of the coupler, which was indicative of the high directivity.

Another point of high directivity was observed around 2.78 GHz over a small frequency range. This was not investigated further.

The parameters of this directional coupler was compared to those shown in Table 3.1. The data from Table 3.1 are repeated here for completeness. The directional coupler developed in this research project is titled here as the "Waveguide with pins" and is shown in Table 3.15.

Type of Coupler	Coupling (dB)	Range for Constant Coupling	Maximum Directivity (dB)	Range for Directivity 20 dB
Waveguide with pins	35.4	10.5 % $\pm$ 0.5 dB	43	8.4 %
Bethe-Hole [41, p. 419]	30	11 % $\pm$ 1 dB	> 32	9 %
Two Hole	20	12 % $\pm$ 0.7 dB	37	8 %
Schwinger Reversed-Phase	20	25 % $\pm$ 1.5 dB	30	25 %
Moreno Crossed Guide	20	15 % $\pm$ 0.1 dB	23	12 % (for 15 dB)
Riblet-Saad	20	15 % $\pm$ 0.25 dB	54	25 %
Loop [43, p. 239]	24	15 % $\pm$ 1 dB	> 40	> 15 %
*Percentages calculated by dividing the operating frequency range of the parameter by the operating frequency range of the waveguide that was used.				

Table 3.15: Comparison of directional coupler properties. Data from [42] *unless otherwise indicated.*

3.5 Chapter conclusion

A waveguide directional coupler was built that could accurately measure over the 2.4 GHz ISM band so that it could measure the power absorbed by a load inside a microwave applicator. It had a coupling factor of 35.4 dB and a directivity of over 20 dB over the frequency range.

The directional coupler was designed in a modular format. This meant that each component was individually optimised before everything was put together. This also means that each component can still be optimised or upgraded further.

The design was inexpensive. The waveguide with pins used aluminium tubing rather than store-bought waveguide. The branch-line hybrid was etched using a desk-top PCB mill. The SMA connectors were the most expensive components. The construction of the coupler needed to be precise, but did not require any extraordinary machinery in order to construct it.

3.6 Chapter recommendations

The coupler worked well - yet it can still be improved further.

The SMA connectors between the waveguide with pins and the branch-line hybrid could be replaced with pins that run straight from the waveguide with pins into the branch-line hybrid. This would make the coupler more compact and it would save on cost by not needing four SMA connectors.

Improving the operational frequency range can still be investigated. For the waveguide with pins, wider pins, or ends with a special end (like Figure 3.16), can be investigated. The operating frequency range of the branch-line hybrid can be improved by adding more sections to form a multi-section branch-line hybrid.

The branch-line hybrid could also be designed using stripline, or enclosed in a metal case, to reduce possible electromagnetic interference or interference due to touch. This may be important since many modern communication devices used the 2.45 GHz ISM bandwidth.

4 Power Detector

4.1 Chapter summary

This chapter investigates a prototype for a linear power detector that was based on a thermistor sensor.

The topic is introduced, after which the design requirements are stated. Then a literature review investigates different sensors that could have been used to build a power detector with. The chosen design is then discussed, along with the simulation of the design. After this the calibration is discussed, after which a conclusion and recommendations are given.

4.2 Chapter introduction

In order to know how much power was absorbed by a certain load in a microwave system, a directional coupler was developed (Ch. 3). To measure the power coupled by the directional coupler, two power detectors were required.

This chapter discusses the development of a prototype power detector. The advantages of this power detector was that it was much less expensive than an off-the-shelf solution and that it produced a linear output.

The possibility of a linear output was a particularly attractive solution for a microwave system. The output power from a microwave system was not continuous. Notice in Figure 4.1 how the power is pulsed in $10\ ms$ intervals in a conventional microwave oven. Therefore, using a linear power detector meant that it was very simple to calculate the average power.

A non-linear detector (such as a diode detector) required an integration calculation to determine the average power. Figure 4.1 shows the output of a diode detector. The output voltage cannot be directly related to power values since a diode detector has a log-linear output function. Therefore, in order to determine the average power, the signal has to be sampled accurately, integrated and then averaged.
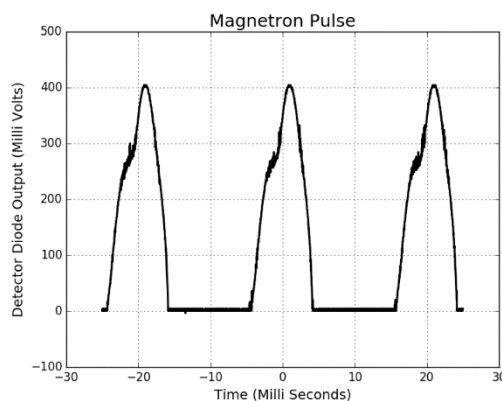
Figure 4.1: Typical non-linear output waveform of a diode detector measuring the power delivered in a conventional microwave oven [2].

A linear power detector, however, has a direct relationship between the output voltage and the measured power. Therefore, no more than a first order analog filter is required to determine the average power.

The power detector was developed as a prototype. The thermistors that were used were large and easy to develop multiple iterations of designs with. However, they performed poorly at high frequencies (see the end of Sec. 4.6.2). Focus was given to the development of an operational prototype – in particular to the fundamental concepts that made the circuit work and to the development of a well-functioning driving circuit.

4.3 Specifications

A microwave power detector was required that could measure average power between $2.4 - 2.5\ GHz$.

49

The magnetron used in this project could produce a maximum of $700\ W$ ($58.45\ dBm$) of power. A $10\ W$ ($40\ dBm$) resolution was to be sufficient for a working control system. It was also assumed that a $-40\ dB$ coupler would be used. Therefore, the power detector needed to be able to measure between $1\ mW$ and $70\ mW$ (0 and $18.45\ dBm$), with a $1\ mW$ resolution.

The output of the sensor was to be read with an Atmel Atmega 32u4; therefore the output voltage had to range between $0\ V$ and $5\ V$, and max not have exceeded $5.5\ V$ [49].

A linear output was desired. A linear output would enable an analog low pass filter to be added to the output so that the average power could be measured without the need for additional processing, such as a processor intensive integration operation.

In order for measurements to be consistent, external dependencies such as ambient temperature changes needed to be minimized.

In order to make the prototype viable for production, a low complexity and a low cost of components were desired.

4.4 Literature Review

Microwave power detection (often referred to as radio frequency (RF) power detection) refers to the measurement of microwave power within a circuit. This differs slightly from microwave power *measurement*, which typically refers to a measurement of microwave power of a wireless signal in the air [50].

There are three dominant technologies that are used to detect microwave power. Either thermistor, thermocouple or diode technologies are used. These will now be discussed. Table 4.1 shows a summary of these technologies compared to the desired specifications.

4.4.1 Thermistor

A thermistor acts as a type of bolometer. A bolometer measures power by taking the temperature difference between a device absorbing energy as heat and the ambient temperature [51]. The difference in temperature is directly related to the amount of energy, and thus power, being absorbed [50].

A thermistor is a temperature dependent resistor. Since a certain amount of self-heating takes place, the thermistor itself can be used as both the heating element and the thermometer in a bolometer configuration. Two variations of a thermistor exist: a positive thermal coefficient (PTC) and a negative thermal coefficient (NTC).

A PTC thermistor increases in resistance as the temperature increases. They are very non-linear and are often used as a fuse [52].

An NTC thermistor decreases in resistance as the temperature increases. They exhibit a log-linear resistance versus temperature curve. They are often used for high sensitivity temperature measurements. NTC thermistors with low tolerances and a small package size (PCB mount size down to 0201) are readily available commercially [53].

Although thermistors have a log-linear voltage to current relationship, they can be used in a self-biasing circuit to effectively have a linear power output [51].
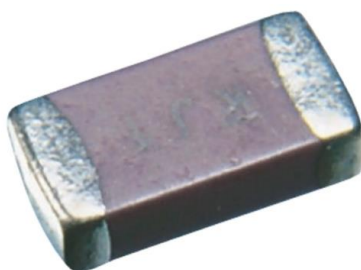
Figure 4.2: A Murata SMD thermistor [58].

4.4.2 Thermocouple

A thermocouple sensor works by measuring the voltage difference that arises between two dissimilar metals when the common end of the metals is heated. A detailed description of the working principal is discussed in [51].

Similar to the thermistor, a thermocouple can measure microwave power by absorbing the microwave energy as heat. One of the two metals are set up such that it functions as a resistor. It is constructed in such a way that the hottest part of the resistor is at the junction between the two dissimilar metals. Therefore, as microwave energy is dissipated as heat in the resistor, the thermocouple voltage changes and can be measured. It can then be related back directly to the amount of power flowing through the resistor [51].

They can handle more power than thermistors and as such can measure a wide range of powers. They can also be designed to have higher sensitivities [51].

51

Microwave power detection thermocouple sensors are, however, less than a millimetre in size, which requires special construction techniques. They are also not quite linear, requiring linearization through software [51].
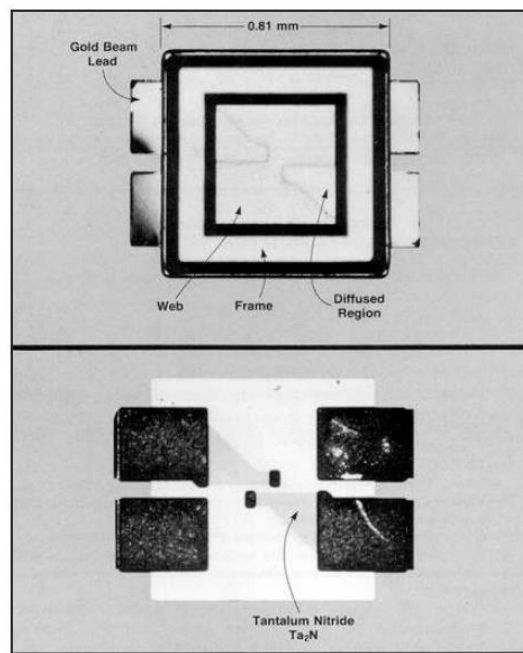
Figure 4.3: A photo-micrograph of the thermocouple chip used in the Keysight 8481A. Note the scale indicated at the top [51].

4.4.3 Diode

Diodes can detect the envelope of an incoming signal. This envelope can then be related back to power values. They are inherently non-linear, which gives them the capability of rectifying an AC signal [51].

Schottky diodes are used for microwave power detection. Unlike p-n diodes, they do not store charge. This allows them to have a much wider bandwidth than p-n diodes. They have a low turn-on voltage of $0.3\,V$. This means that the smallest signal it can detect must have a voltage of at least $0.3\,V$ to be detected. To overcome this problem, the diodes are forward biased to $0.3\,V$. This increase the range by about $10\,dB$, but no more, due to drift and noise that the biasing adds [51].

For a wider power detection range, planar-doped barrier diodes are used. These diodes have a junction capacitance that is very small and that is barely affected by the bias voltage. Therefore these diodes are much less affected by biasing and can thus achieve a wider measurement range. They also offer a wider bandwidth [51].

Diodes offer a wide measurement range and a wide bandwidth. They are, however, dependent on temperature [51]. They are also non-linear devices and they measure voltage, not power, and as such an integrator is required to convert the measured voltage value to a power value [54].

Figure 4.4: A digital render of a MACOM diode [55].

4.4.4 Comparison

Property	Specification	Thermistor [51]	Thermo-couple [51]	Low barrier Schottky Diode (MACOM MA4E2054 Series) [55]	Complete IC (Mini-Circuits ZX47-40+) [56]
Frequency range	$2.4 - 2.5\ GHz$	$10\ MHz - 18\ GHz$	$100\ kHz - 18\ GHz$	$< 12\ GHz$	$10\ MHz$ to $8\ GHz$
Measurement range	$0\ to + 18.45\ dBm$	$-30\ to + 10\ dBm$ [57]	$-30\ dBm\ to + 24\ dBm$	$-50\ to + 10\ dBm$	$-40\ to + 20\ dBm$
Linearity	Linear	Log linear (but can be operated linearly)	Somewhat linear	Non-linear	Log linear
Temperature dependence	Minimal	Low with compensation circuit	Low with compensation circuit	Up to 500 % voltage change between $-50\ °C$ and $125\ °C$	$< 10\ \%$ voltage change between $-40\ °C$ and $85\ °C$
Complexity of design	Minimal	DC and microwave sensor, bias circuit, instrumentation amplifier, low pass filter	Requires special sensor, DC and microwave sensor, instrumenta-tion amplifier	Detection, matching circuit, isothermal environ-ment, requires integrator	Plug and play, requires integrator
Cost of sensor (Oct 2019)	Minimal	R 0.60 per thermistor [58]	N/A	R 21.60 per diode [59]	R 1300 per IC [60]
Components Available	Yes	Yes	No	Yes	Yes

Table 4.1: Comparison of the different types of technologies that were available for the microwave power detector, compared to the desired specification. A complete IC was also included.

Table 4.1 shows a comparison of all the technologies described, as well as the desired specifications. A complete, off-the-shelf IC was also included (Mini-Circuits ZX47-40+).

The thermocouple was not available as a sensor, but only as a complete sensor head. This sensor head could only be used with a specific power meter, so the use of a thermocouple was ruled out.

All the options fit the required frequency range. Only the complete IC could measure the desired power range. However, the use of Surface Mount Device (SMD) thermistors could increase the thermistor power range to 20 dBm.

Only the thermistor could be operated linearly. All the other options would have required digital processing before the average power could have been calculated.

A complete IC was the simplest to integrate into a system.

The costs displayed here were only for the sensing components themselves (except for the IC). The circuitry to drive these sensors would have incurred additional costs.

4.5 Design overview

4.5.1 Chosen Design

A design based on thermistors and a DC self-biasing bridge was chosen. This design was most suited to the requirements. The design allowed for average power to be measured directly, which did not require any further digital manipulation other than a linear calibration. It was also feasible for relatively simple construction since standard off-the-shelf components could be used (as opposed to a thermocouple design which would have required a sub-millimetre sized sensor). Ambient temperature fluctuations were to be eliminated with a compensation circuit. Additional ambient temperature effects were calibrated out using temperature sensors. Based on the initial research, the design appeared to be cost effective too. Figure 4.5 shows the DC biasing circuits of the Keysight 432A power meter upon which this design was based [51].

The circuit measured power using a self-balancing bridge. This circuit kept the thermistor(s) at a constant temperature. The more microwave power was applied to the thermistor, proportionally less DC power was required to keep the thermistor at the same temperature. This proportional difference is how the microwave power was measured.

Figure 4.5: The DC biasing circuits of the Keysight 432A power meter. Note the DC biasing circuit for the microwave (RF) thermistors at the top and the DC biasing circuit for the compensation thermistors at the bottom [51].

For example, consider a thermistor circuit that was designed to keep the thermistor at a constant temperature of $25\ °C$. Let's say that $50\ mW$ of DC power needed to be applied to keep the thermistor at this temperature when no microwave power was applied. If, after applying microwave power, only $40\ mW$ of DC power was required to keep the thermistor at $25\ °C$, it meant that $10\ mW$ of microwave power was being applied to the thermistor. Figure 4.6 shows this idea diagrammatically.

Figure 4.6: Arrows show how microwave power can be measured by knowing the proportion of DC bias power that is applied to the thermistor.

The thermistor sensor had to compensate for changes in the ambient temperature. An additional thermistor, with its own DC biasing circuit, was placed next to the primary thermistor. This thermistor did not receive any microwave power. Therefore, when no microwave power was applied, both thermistor circuits should have required the same amount of DC power to maintain a constant temperature. Once microwave power was applied to the primary thermistor, the difference in power contributed by each DC biasing circuit was proportional to the microwave power applied.

However, no two thermistors were the same due to component tolerances. This meant that potentially more DC power was required from one of the DC bias circuits to keep each thermistor (microwave and compensation) at the same temperature. This required a way to 'zero-set' the circuits so that both thermistors had the same DC power applied to it. In addition, no two power detectors were the same. To solve this, adjustable gain was required at the output.

4.5.2 System Overview

The power detector consisted of three main components: the thermistor sensor head, the driver circuitry and a microprocessor, as shown in Figure 4.7. The entire system is shown in Figure 4.8.

The thermistor sensor head contained two pairs of thermistors – one pair to measure the microwave power and the other to compensate for ambient temperature fluctuations. The pair that measured microwave power included a DC block and a microwave choke. The sensor head was enclosed in an aluminium block to minimize the effect of ambient temperature spikes and to protect the sensor from interference. A temperature sensor was attached to the outside of the block.

The driver circuitry consisted of two DC biasing circuits (one for each of the thermistor pairs), an instrumentation amplifier, output ranging, a low pass filter, output protection, power supply regulators and an amplifier for the temperature sensor.

The microprocessor read the output from the thermistor sensor and the temperature sensor. It used this data to fit a calibration line to the measured data and so determined the power dissipated in the sensor.

A duplicate of the power detector was built with the idea of measuring both forward and reverse power when used in a microwave system.
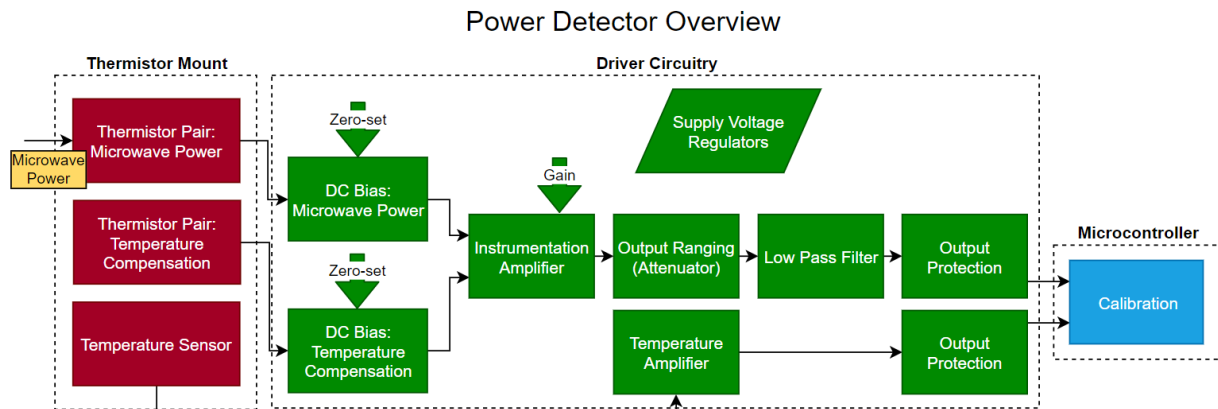
Figure 4.7: Block diagram of the power detector circuit.
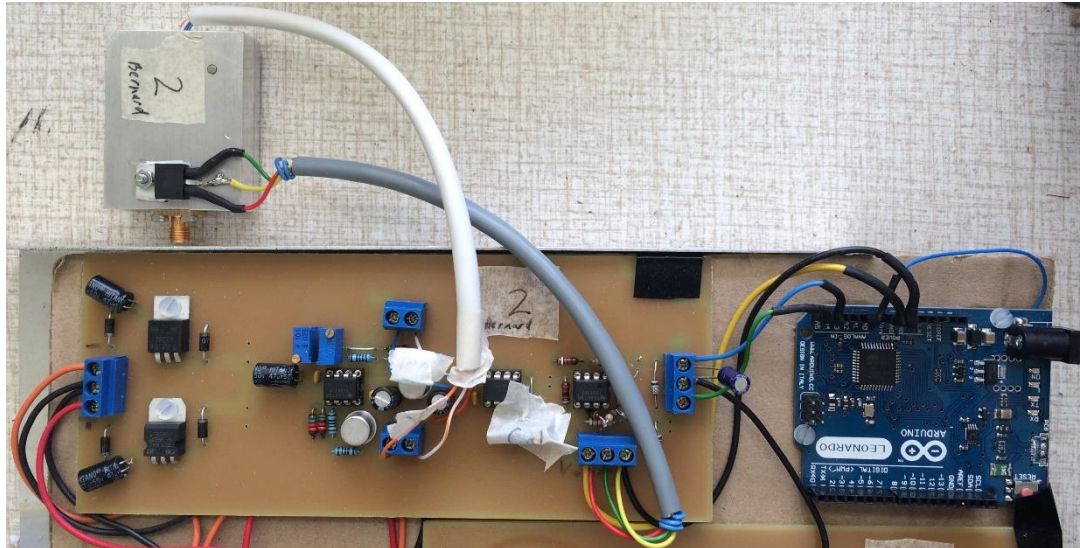
Figure 4.8: The power detector.

4.6 Design: Thermistor mount
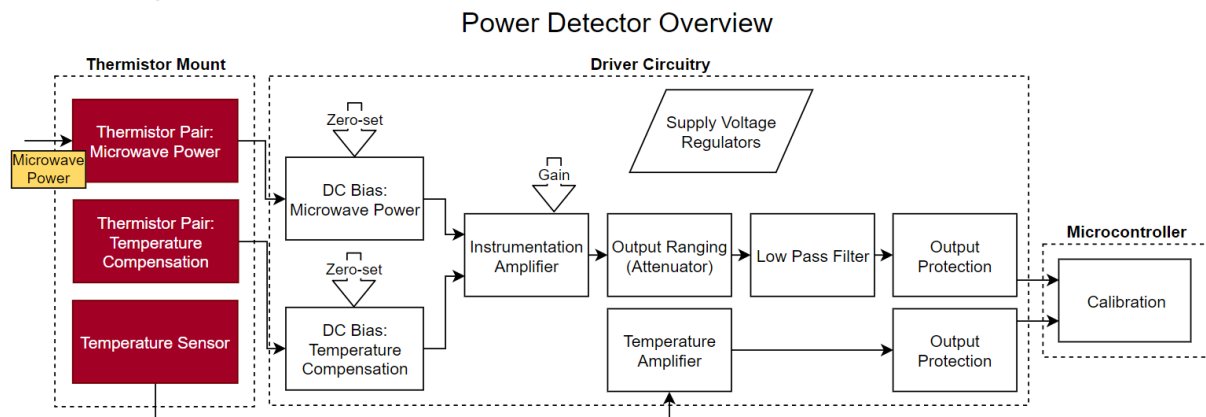
Figure 4.9: Overview of the thermistor mount section.

In this section, the design of the thermistor sensor will be discussed, as shown in Figure 4.9. This included the thermistor pairs, the enclosure and the external temperature sensor.

A thermistor is a temperature dependent resistor. A certain amount of self-heating occurred when power was dissipated in a thermistor. This factor is called the dissipation constant (δ) and is defined in units of $mW/°C$. It is the amount of power needed to raise the thermistor's temperature by $1\ °C$. This constant was greater for physically smaller components. This self-heating principal was core to the working of the thermistor power detector.

Negative Thermal Coefficient (NTC) thermistors decrease in resistance as the temperature increases. This meant that as power was applied to the thermistor, it heated up, and therefore its resistance value went down. The power detector circuit exploited this factor to force the thermistor to a fixed resistance value by applying enough power to heat it to that value. This discussion is expanded in Ch. 4.7.

Two pairs of thermistors were used. The one pair received microwave power and the other did not, in order to compensate for changes in the ambient temperature. The circuit schematic is shown in Figure 4.10.

4.6.1 Thermistor Pair: Microwave Power

The pair of thermistors that received microwave power were connected in a series/parallel configuration [51], as shown in the top part of Figure 4.10. Capacitors $C1$ and $C2$ were used to create a DC open

circuit and microwave short circuit. Two $100\,\Omega\;@\;25\,°C$ thermistors were connected such that the microwave circuit saw the two thermistors connected in parallel, creating a $50\,\Omega$ matched load. The DC biasing circuit saw these thermistors connected in series, forming a DC load of $200\,\Omega$.
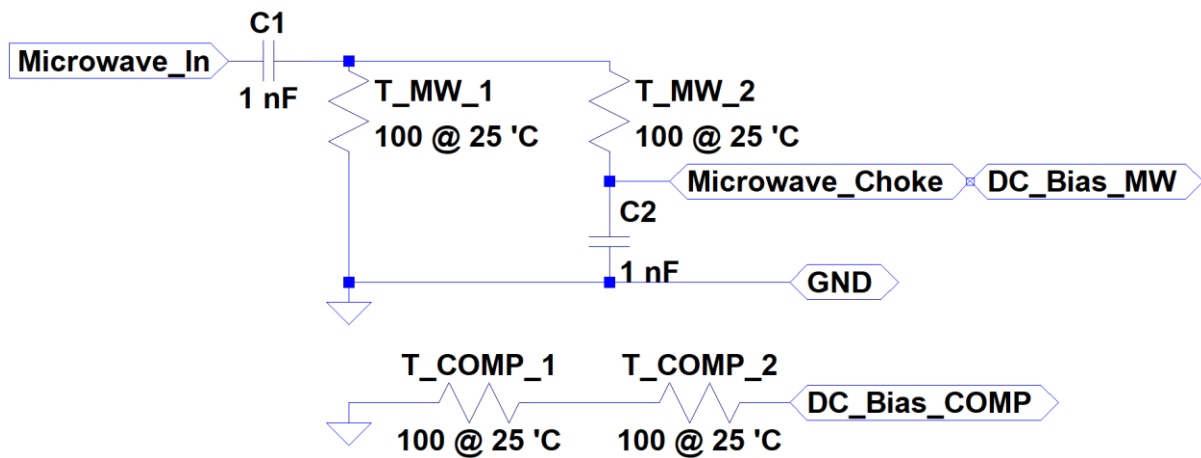
Figure 4.10: Circuit schematic for the thermistor sensor. MW denotes Microwave and COMP denotes Compensation.

Using the series configuration for the DC biasing circuit was advantageous. This configuration meant that double the voltage was used to drive the thermistors, as compared to using only a single thermistor (the derivation is shown in App. A.1). Since the output was measured in voltage, this meant that a finer measurement could be made. It also meant that only half the current was needed, which is a limiting factor for op amps (the DC biasing circuit was driven by an op amp – see Ch. 4.7.2.2). In addition, less current meant that the balancing resistor, R_b, also experienced less self-heating.

Using a parallel configuration for the microwave circuit meant that higher power levels could be detected. A thermistor has a maximum amount of power that it can dissipate. Therefore, dividing the power across the thermistors meant that each thermistor only had to dissipate half as much power.

As mentioned, using the parallel configuration theoretically created a $50\,\Omega$ input impedance at microwave frequencies. It was important to design the power detector to be matched to ensure maximum power transfer from the microwave source.

In order for the circuit to function correctly, it was critical that the capacitors still operated as capacitors at microwave frequencies. At shorter wavelengths (higher frequencies), the physical size of a component became important as it increased the inductance of the component. If the component was large enough relative to the wavelength, it could have functioned as an inductor instead. An inductor could have choked the microwave signal.

To verify the operation of the $1\,nF$ capacitor a simple circuit was constructed, as shown in Figure 4.11. An SMA connector was connected to a $50\,\Omega$ transmission line. The $1\,nF$ capacitor was placed in series with a $51\,\Omega$ resistor. A good impedance match was thus expected.

The $1\,nF$ capacitor had a tolerance of 10 % and was 0805 sized ($2 \times 1.2\,mm$). The $51\,\Omega$ resistor had a tolerance of 5 % and was sized 1206 ($3.2 \times 1.6\,mm$). A $50\,\Omega$ resistance would have been ideal for a good match, but was not available at the time. A $51\,\Omega$ resistor was sufficient since qualitative, and not quantitative, results were required.
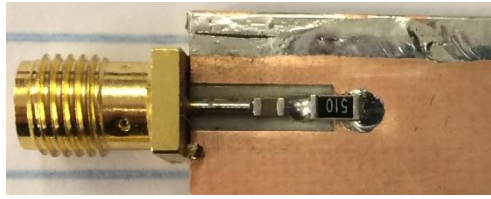
Figure 4.11: Circuit to test capacitor properties at 2.5 GHz.

The input reflection coefficient, S_{11}, was measured using a network analyser (N5242A PNA-X Microwave Network Analyzer). The result was plotted on the Smith chart, shown in Figure 4.12.
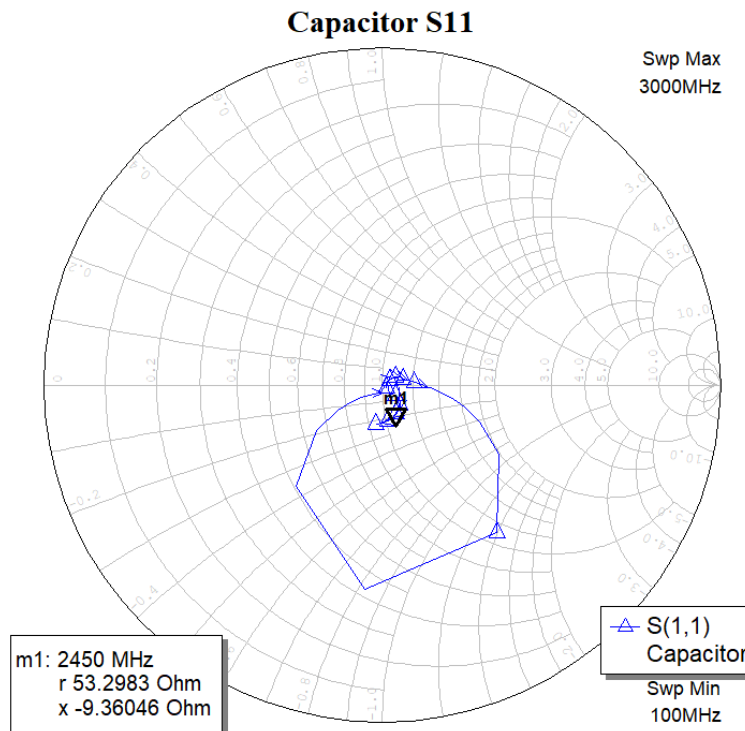
Figure 4.12: A Smith chart plot of S_{11} of the capacitor test setup, measured between $0.1 - 3\ GHz$.

Marker 1 shows the input impedance at $2.45\ GHz$ as $53.30 - j9.36\ \Omega$ (and $|S_{11}| = -20.38\ dB$). The negative reactance indicates that the component was still operating as a capacitor. The qualitatively measured impedance was sufficiently close to being a 50 Ω match.

Just as the capacitor isolated the DC voltage from the microwave power source, so a microwave choke was needed to isolate the microwave power from interfering with the DC bias circuit.

A microstrip bias tee, using quarter wavelength sections, was used. The quarter wavelength sections caused an open circuit to be seen at port 1, indicated in Figure 4.13. It consisted of a quarter wavelength transmission line with a quarter wavelength shunt stub connected to it. A radial stub was used for the shunt stub to increase the bandwidth [61].
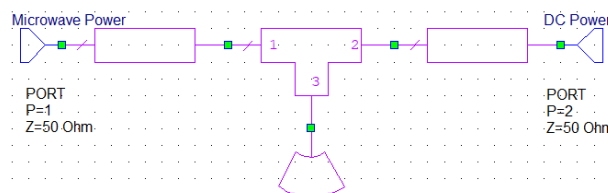
Figure 4.13: AWR schematic of the microstrip bias tee.

This circuit was modelled and fine-tuned in AWR Design Environment 14 (Microwave Office). 50 Ω transmission lines were used. The radial stub had an angle of 90° and a radius of $12.1\ mm$. S_{11}, from DC to $3\ GHz$, was plotted on a denormalised Smith chart, shown in Figure 4.14.

59
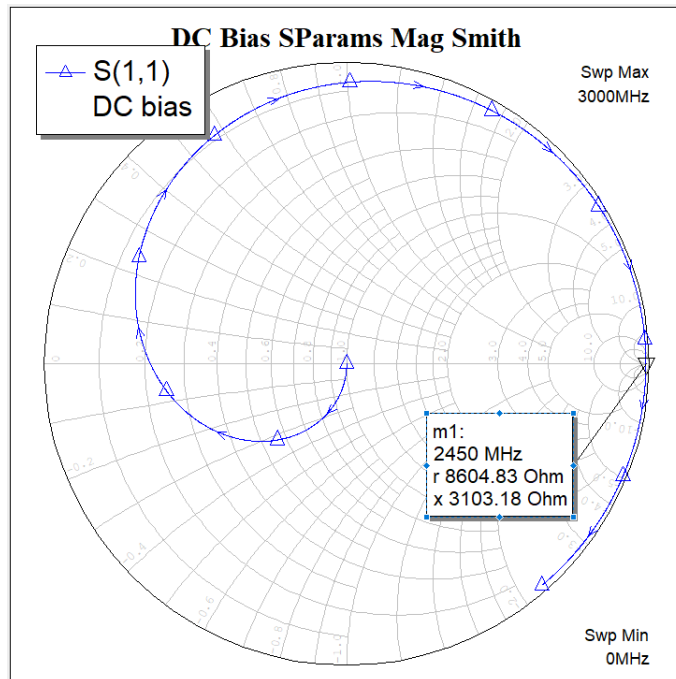
Figure 4.14: A denormalised Smith chart plot of S_{11} of the microstrip bias tee, measured from DC $-3\ GHz$.

The Smith chart showed a perfect match at DC, since the circuit functioned as a short circuit here. At 2.45 GHz (m1 on the graph), a very large impedance was seen, effectively making the circuit an open circuit at this frequency.

The large footprint that the bias tee required was thought to add some thermal stability to the board. However, this effect became negligible after the board was mounted inside an enclosure. As such, a next iteration of the design could use an inductor as a microwave choke. This would make the entire thermistor mount much smaller physically (see Figure 4.17 as a reference).

4.6.2 Thermistor choice

The thermistor needed to operate within its power handling capabilities. Smaller thermistors had the benefit of having a higher dissipation constant, but were also more limited in the maximum power they could dissipate [53, p. 3].

To meet specification, the sensor needed to be able to dissipate 70 mW (18.45 dBm). Since the thermistors were configured in parallel, each thermistor needed to be able to dissipate half of the power, or 35 mW.

Size code (EIA)	0201	0402	0603
Operating Temperature Range	$-40\ to\ 125\ °C$		
Rated Maximum Power Dissipation	33 mW	66 mW	100 mW
Dissipation Factor*	Approximately 1 $mW/°C$	Approximately 2 $mW/°C$	Approximately 3 $mW/°C$
*The constant amount power required to raise the temperature of the thermistor 1 $°C$ through self-heat generation under stable temperatures. Dissipation factor is the reference value when mounted on a glass epoxy board (1.6 mm thickness).			

Table 4.2: Thermistor properties based on component size [53].

Thermistors sized 0603 (1.6 × 0.8 mm) could typically dissipate up to 100 mW while at or below 25 °C, as shown in Table 4.2 [53]. It was good practice to not drive components close to their maximum operating limits. Driving the thermistors with microwave power of 35 % of the allowable maximum

60

was a sufficient safety factor. In addition, the uncertainty of the dissipation factor meant that more power may have been needed to bias the thermistor.

The operating temperature of the circuit depended on the properties of the thermistor. A balance was required in having the operating temperature above ambient temperature, yet low enough so that the power limit of the thermistor was not exceeded when self-heating the thermistor to the operating temperature.

To determine how much power was needed to heat a thermistor to a desired temperature, the dissipation constant (δ), defined in units of $mW/°C$, was used as follows:

$$P_{bias} = \delta \cdot T_\Delta \tag{20}$$

with

$$T_\Delta = T_{operating} - T_{ambient} \tag{21}$$

A low ambient temperature of $15\,°C$ was chosen because it was unlikely that the room temperature would be colder than this. Assuming an operating temperature of $25\,°C$ and typical dissipation constant (for a 0603 thermistor) of $3\,mW/°C$ [53], the bias power was found to be

$$P_{bias} = 3 \cdot 10 = 30\,mW. \tag{22}$$

At first glance, this result would have meant that when maximum microwave power was applied $(35\,mW)$ that the thermistor would have heated beyond the operating temperature. However, the dissipation constant was approximate and was greatly dependant on how the component was mounted. Practical testing suggested that the value was higher in the context of this design.

A resistance of $100\,\Omega$ was required so that the parallel circuit could form a $50\,\Omega$ matched load. At the time, only two values of thermistors that had a resistance close to the desired range and with the desired power handling capabilities were readily available. These were $100\,\Omega\,@\,25\,°C$ and $150\,\Omega\,@\,25\,°C$, as shown in Table 4.3.

Thermistor	muRata (NCP18XF101J03RB)	TE Connectivity (NTC0805J150R)
Resistance at 25 °C (Ω)	100	150
Size	0603	0805
B-value (K)	3250	2750
Rated Maximum Power Dissipation (mW)	100	125
Resistance tolerance	$\pm 5\,\%$	$\pm 5\,\%$
B-value tolerance	$\pm 3\,\%$	$\pm 5\,\%$

Table 4.3: Comparison of thermistor properties for thermistors that were readily available [58], [62].

The resistance, R, of a thermistor at a specific temperature is defined by the following equation:

$$R = R_0 \exp\left(B\left(\frac{1}{T} - \frac{1}{T_0}\right) \right), \tag{23}$$

where R_0 is defined as the resistance at the Standard Temperature, B is the thermistor constant, T is the actual temperature of the thermistor and T_0 is defined as the Standard Temperature of $298.15\,K$ $(25.15\,°C)$ [53].

The required operating temperatures were calculated in order for the thermistors to have a resistance of $100\,\Omega$. Eq. 23 was manipulated to give

$$T = \frac{1}{\dfrac{\log R}{B \log R_0} + \dfrac{1}{T_0}}. \tag{24}$$

The muRata thermistor was, as specified, at $100\ \Omega$ at $25\ °C$. The TE Connectivity thermistor was found to be at $100\ \Omega$ at $38.85\ °C$.

The power required to heat each thermistor was then calculated. Using eq. 20, and assuming an ambient temperature of $15\ °C$ and a dissipation constant of $3\ mW/°C$, the required power was calculated. For the TE Connectivity thermistor:

$$P_{bias} = \delta \cdot T_\Delta \tag{25}$$
$$= 3 \cdot (38.85 - 15) \tag{26}$$
$$= 71.55\ mW \tag{27}$$

Similarly, $P_{bias} = 30\ mW$ was found for the muRata thermistor.

Based on the assumption of a $3\ mW/°C$ dissipation constant, the muRata thermistor would have operated at 30 % of its rated maximum power dissipation and the TE Connectivity thermistor at 57 %.

Although the TE Connectivity thermistor seemed like a better choice since it could operate at higher ambient temperatures, the muRata thermistor was chosen. This was because the actual dissipation constant was unknown and as such it was less likely that the muRata thermistor would exceed its maximum power limit should the dissipation constant be significantly higher than $3\ mW/°C$.

Next, the high frequency performance of the thermistors were measured. This measurement was made after the thermistor mount was fully constructed (see Sec. 4.6.4). The input reflection coefficient, S_{11}, is plotted for both thermistor mounts in Figure 4.15.
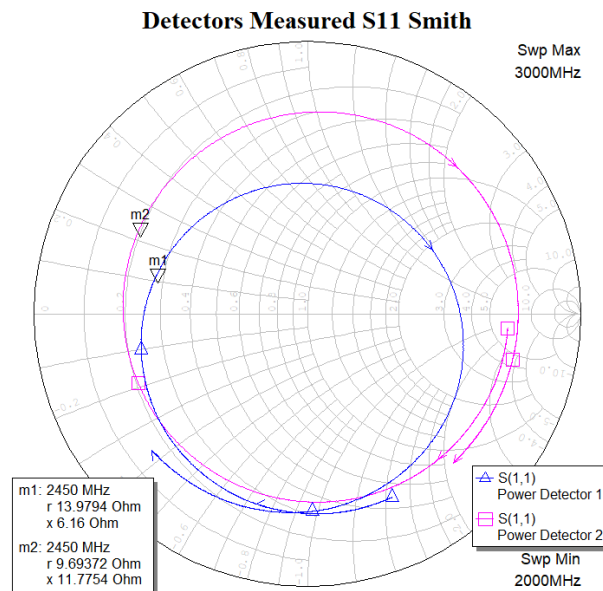
Figure 4.15: A Smith chart plot of S_{11} of the two thermistor mounts at the microwave power input, measured from $2 - 3\ GHz$.

The thermistors did not perform well at high frequencies. The thermistors were far from being matched to $50\ \Omega$, as can be seen by the values given by the markers m1 and m2. The magnitude to the input reflection coefficients at $2.45\ GHz$ was $|S_{11}| = -3.23\ dB$ and $|S_{11}| = -4.90\ dB$ for power detector 1 and 2, respectively.

At this point of the development of the prototype it was decided to continue using these thermistors. They were large enough to be easy to solder, in contrast to even smaller thermistors that would likely

perform better at high frequencies. More importantly, the focus of the prototype was develop an operational circuit that investigated all the fundamental concepts necessary to develop a thermistor-based power detector. The chosen thermistors were still adequate to achieve this goal. A matching circuit could be investigated for the next iteration of the design.

4.6.3 Thermistor Pair: Temperature Compensation

The temperature compensation thermistors used the same thermistors as for the microwave power circuit. The thermistors were connected in series to form a resistance of $200\ \Omega$ (bottom of Figure 4.10), which was the same as the DC bias resistance for the microwave power circuit.

4.6.4 Physical Layout

Since physically small thermistors were used, a thin transmission line was desired in order to form a good match between the microstrip line and the components. As such, a thin substrate was needed. Rogers 4003 substrate with a thickness of $0.508\ mm$ was used. The substrate had a permittivity of $\epsilon_r = 3.48$.

The transmission line width for a $50\ \Omega$ line was calculated using eq. 13 from Sec. 3.4.4.2. It was fine-tuned using AWR. The optimal line was $1.10\ mm$ wide. This was a sufficient compromise between the $1.2\ mm$ width of the capacitor and the $0.8\ mm$ width of the thermistor.
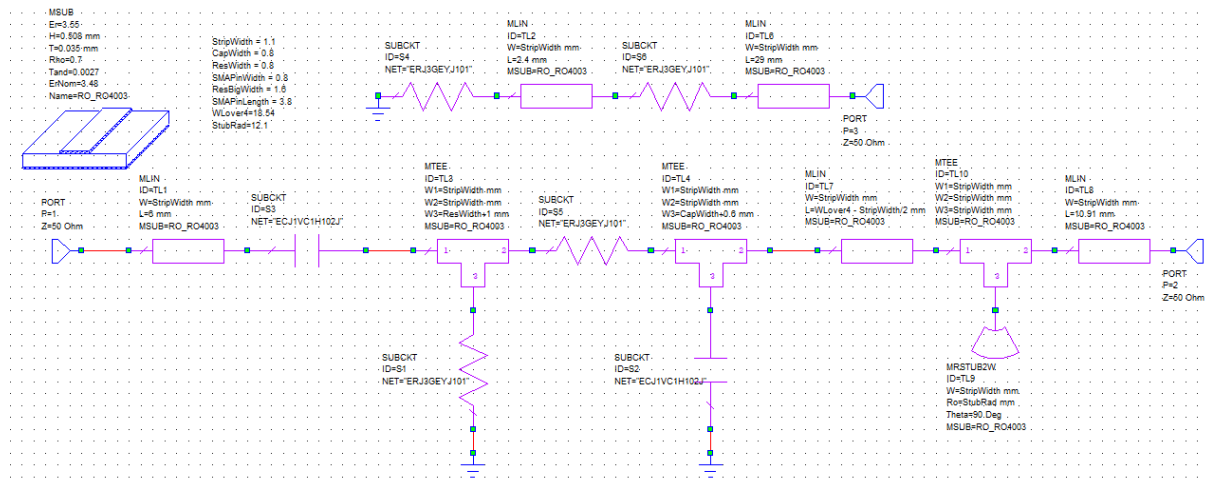
Figure 4.16: AWR schematic of the thermistor sensor.

63
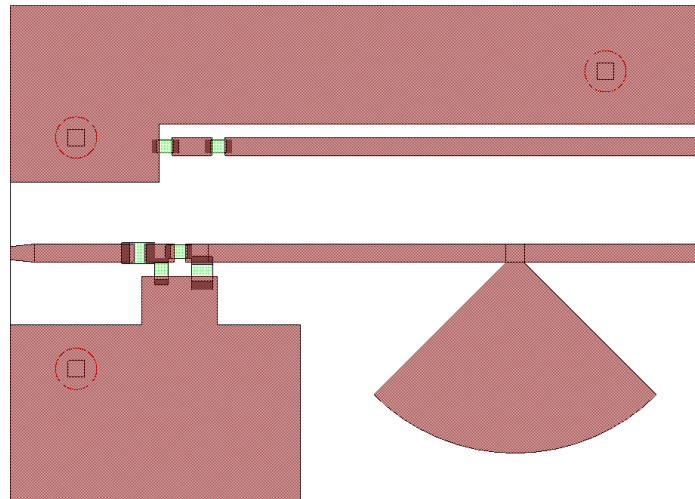
Figure 4.17: AWR physical layout of the thermistor sensor.

A schematic and physical layout of the thermistor sensor's PCB layout is shown in Figure 4.16 and Figure 4.17. An SMA connector was soldered onto the taper on the left, and wires were soldered onto the end of the lines on the right.

A good ground plane was needed to ground the microwave components. Therefore a large plane was provided for the thermistor and capacitor in the bottom left of the layout. The two top-side ground planes were connected to the bottom-side ground plane (and the metal enclosure) through mounting screws. The holes for the screws are indicated on Figure 4.17 with the squares with red circles around. The ground planes were kept far from the microstrip line so that the microstrip would not become a coplanar waveguide.

The temperature compensation thermistors were placed in the same vicinity as the microwave thermistors so that they would couple thermally. But they were placed far enough so as not to couple electrically.

Although the layout was done in AWR, a simulation was not feasible since a thermistor model was not available (a simulation model was constructed in LTspice, shown in Sec. 4.8).

A close-up of the SMD components mounted on the PCB and a picture of the entire populated PCB are shown in Figure 4.18.
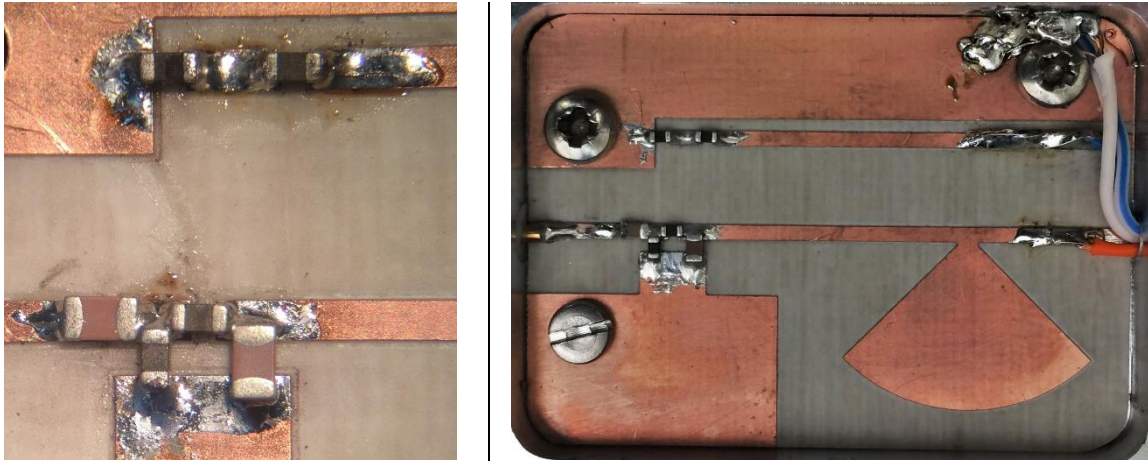
Figure 4.18: Picture of the SMD components and a picture of the entire on the thermistor sensor PCB.

4.6.5 Enclosure

The thermistor PCB was mounted in a metal case. The case reduced the impact of sudden fluctuations in ambient temperature, shielded the circuit from electrical interference and made the sensor more robust.

Aluminium with a 5 mm thickness was used to ensure thermal stability.

The space above the microstrip line needed to be large enough so as to not alter the impedance or the effective permittivity of the microstrip line. Figure 4.19, taken from [63, p. 190], shows this setup. The graphs shown in Figure 4.20 show how the characteristic impedance and the effective permittivity scales depending on the ratio of the space above the circuit to the height of the substrate, or a/h. The enclosure was designed to be 5 mm deep, therefore creating an effective a/h ratio of 4.5/0.5, or 9/1. It can be seen from the graphs that at an a/h ratio of greater than 8/1, the effect of the lid becomes negligible, both for the impedance and the effective permittivity of the line. Although the graphs are plotted for a permittivity of $\epsilon_r = 9.8$, the impedance and the effective permittivity scales linearly with a change in permittivity, so the result is still applicable [63, p. 124].
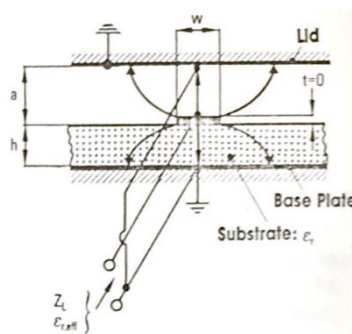
Figure 4.19: Diagram of a microstrip line with a grounded lid [63, p. 190].
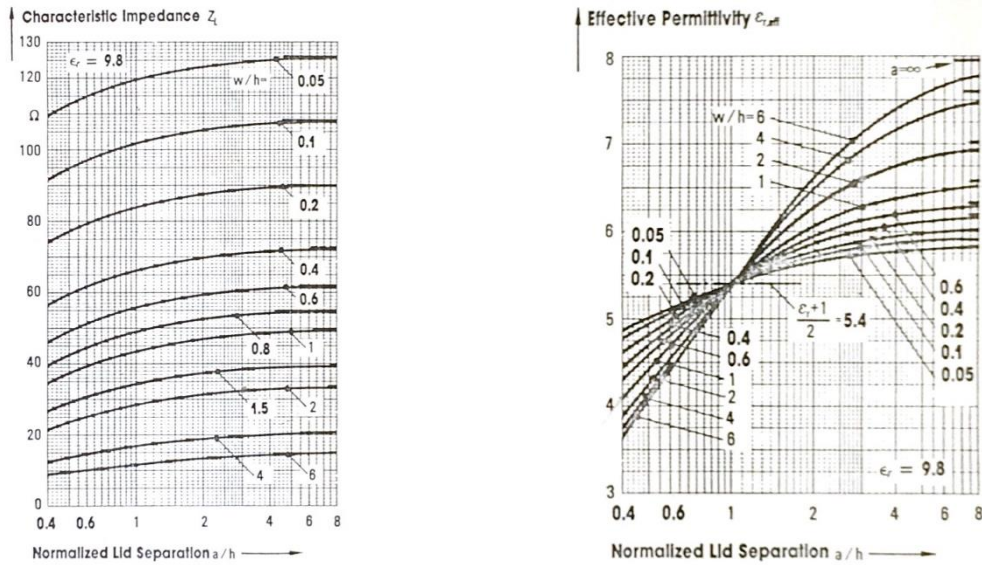
Figure 4.20: Change in characteristic impedance (a) and effective permittivity (b) depending on the ratio of the grounded lid to the thickness of the microstrip substrate, as well as the microstrip line's dimensions [63, p. 190].

The enclosure was sketched in Autodesk AutoCAD 2019 for manufacture, as shown in Figure 4.21 (note that an older PCB layout is displayed). Figure 4.22 shows the physical enclosure with the thermistor sensor mounted inside.
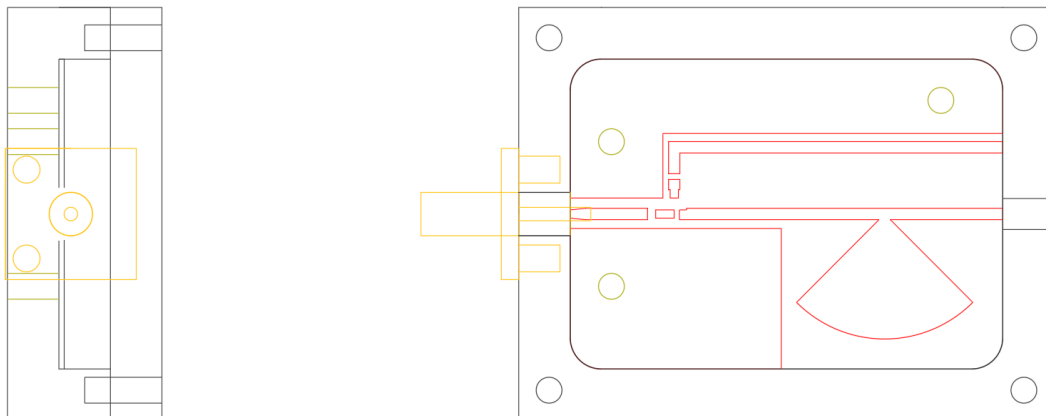
Figure 4.21: Autodesk AutoCAD 2019 sketch of the side view and top view of the thermistor enclosure.

Figure 4.22: Side view and top view of the thermistor enclosure.

4.6.6   Temperature sensor

Despite the action of the compensation thermistors to remove the effects of ambient temperature changes, the output of power detector was still dependant on the ambient temperature. To compensate for this effect, a LM35 temperature sensor was mounted onto the outside of the case. It was placed on the outside wall of the case, as close as possible to the thermistors. The temperature of the case was incorporated into the calibration of the sensor.

The LM35 was accurate to at least half a degree Celsius. It gave an output of $10 \, mV/°C$, as shown in Figure 4.23 [64]. The physical sensor is shown in Figure 4.24. The output was passed through an amplifier before being read by the microcontroller (see 4.7.7: Temperature sensor amplifier for the design of the amplifier).
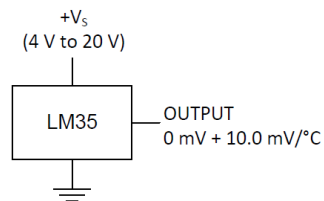
Figure 4.23: Operating parameters of the LM35 temperature sensor [64].

Figure 4.24: LM35 temperature sensor mounted on the outside of the enclosure.

4.7 Design: Driver circuitry

4.7.1 Introduction
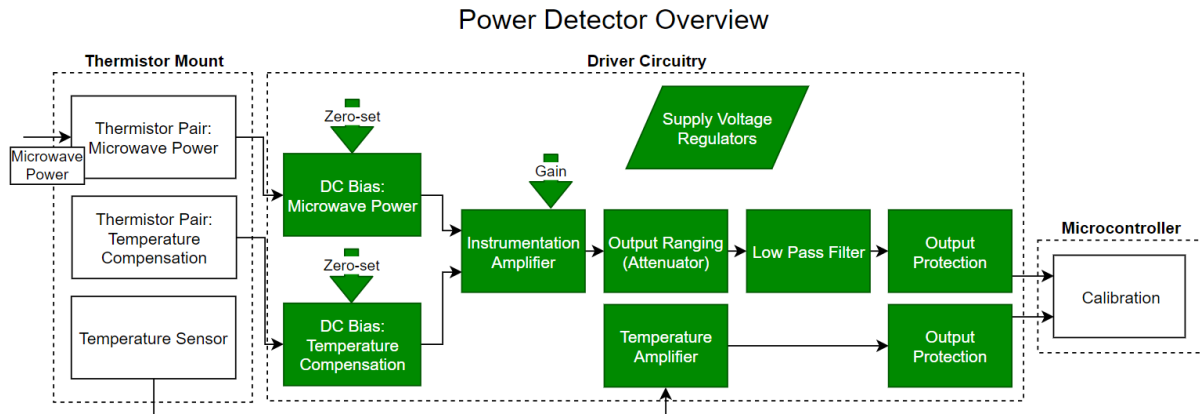
Figure 4.25: Overview of the driver circuitry section.

This section discusses the circuitry that biased the thermistors and it discusses the analog signal processing circuits, as shown in Figure 4.25. This includes the DC bias circuit, the instrumentation amplifier, the attenuator, the low pass filter and the output protection. The amplifier for the LM35 temperature sensor, the power supply and the PCB layout is also discussed.

4.7.2 DC biasing circuit

4.7.2.1 Fundamental concept

A thermistor exhibits a non-linear voltage vs current curve. This non-linearity is exploited in order to bias the thermistor to a certain temperature.
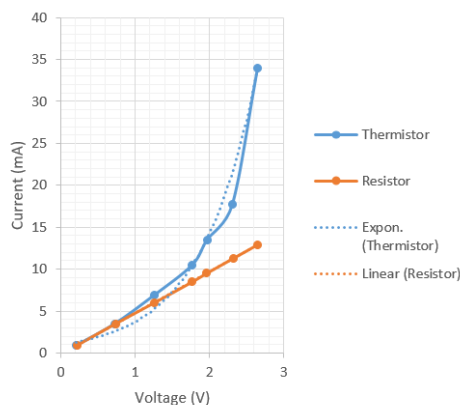
Figure 4.26: Typical resistance curves of a thermistor compared to a resistor.

A quick measurement of a series connection of two muRata thermistors ($100 \, \Omega \, @ \, 25 \, °C$) compared to a $200 \, \Omega$ resistor is shown in Figure 4.26. The non-linearity of the thermistor due to self-heating could clearly be seen.

Consider the circuit given in Figure 4.27. Two voltage dividers were supplied by a voltage source, V_o. The voltage divider on the left (V_s) had two equal resistances, whereas the divider on the right (V_t) had resistance values that differ from each other and from the other divider.
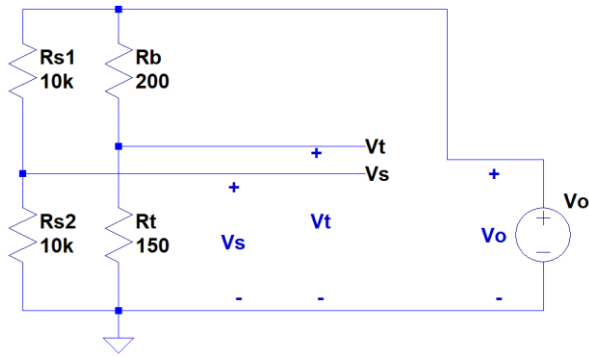
Figure 4.27: Two voltage dividers supplied by a single voltage source.
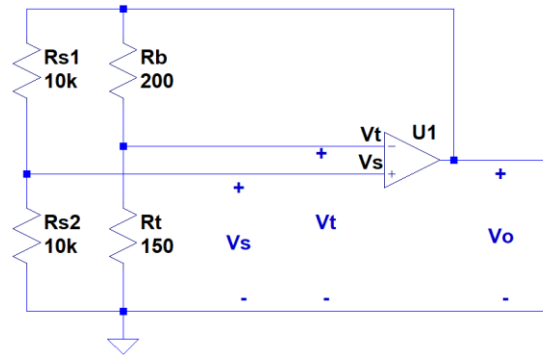
Figure 4.28: Two voltage dividers supplied by an op amp.

A DC sweep of the voltage source, from $0 \leq V_o \leq 10\,V$, showed the voltage transfer function of each divider, plotted in Figure 4.29. Both transfer functions were linear and only crossed each other at $0\,V$.
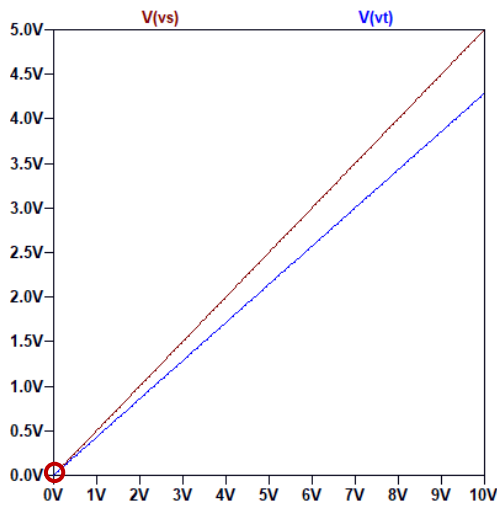
Figure 4.29: A DC sweep of V_o (x-axis), showing the output voltage of the voltage dividers in Figure 4.27. The red circle indicates where $V_s = V_t$.
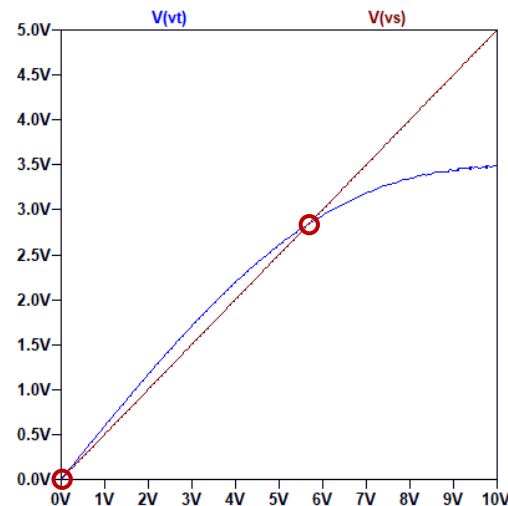
Figure 4.30: A DC sweep of V_o (x-axis), showing the output voltage of the voltage dividers in Figure 4.27, with R_t replaced with a thermistor. The red circles indicates where $V_s = V_t$.

If an ideal op amp was placed between V_t, V_s and V_o, as shown in Figure 4.28, the op amp adjusted V_o such that its input terminals equal one another i.e. $V_t = V_s$. The only valid solution was for $V_o = 0\,V$, indicated by the red circle on Figure 4.29.

If, however, the resistor R_t was replaced with a thermistor ($200\,\Omega$ @ $25\,°C$), the transfer function of V_t was no longer linear, as shown in Figure 4.30. There were now two points of intersection between the transfer functions of V_t and V_s. This meant that for the circuit with the op amp (Figure 4.28), there would have been two possible operating points for the circuit. The non-zero solution would have biased the thermistor to the same resistance as R_b.

There were actually three points of intersection between V_t and V_s (if a thermistor was used). If the DC sweep of V_o from Figure 4.27 was extended to between $-10 \leq V_o \leq 10\,V$, another intersection point became visible. The intersection points are marked by red circles in Figure 4.31. The circuit had to be designed to operate only at the positive non-zero operating point.

69
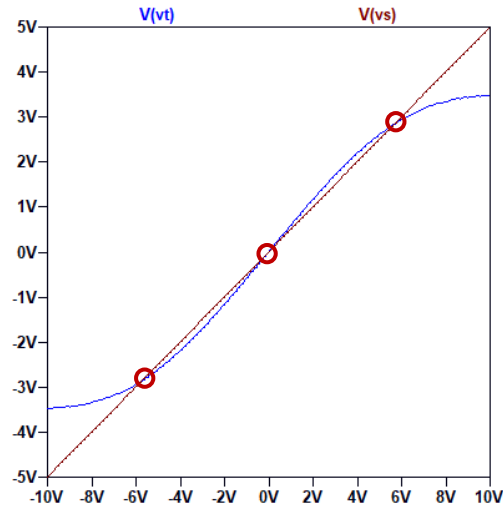
Figure 4.31: A wider DC sweep of V_o (x-axis), showing the output voltage of the voltage dividers in Figure 4.27, with R_t replaced with a thermistor. The red circles indicates where $V_s = V_t$.

In summary, a thermistor is a non-linear device. It could be used in conjunction with an op amp, with a resistive divider feedback loop, to bias the thermistor to a desired resistance and, therefore, a desired temperature. The fundamental circuit is shown in Figure 4.28, where R_t is a thermistor. This circuit is known as a self-balancing bridge [65].

Now, if microwave power was also supplied to the thermistor (without changing the DC voltage across it), the temperature of the thermistor would have risen beyond the desired temperature. However, the op amp's feedback loop compensated for this rise in temperature by decreasing the output voltage V_o, thereby supplying less power to the thermistor. The feedback loop, therefore, ensured that the thermistor remained at the desired temperature. The change in the output voltage, V_o, to compensate for the supply of microwave power was linearly related to the amount of microwave power supplied to the thermistor.

4.7.2.2   Design
As explained in Sec. 4.6, two thermistors were used for R_t. They were connected in series for the DC biasing circuit.

In order to choose an op amp and supply voltages, the rated maximum power dissipation of the thermistor had to be taken into account. The muRata thermistors were limited to $100\ mW$ (see Sec. 4.6.2). Assuming that the thermistor was biased at its operating resistance of $100\ \Omega$, the maximum output voltage of the op amp was calculated as follows:

$$P = \frac{V^2}{R} \tag{28}$$

$$V_{thermistor\_MAX} = \sqrt{P_{max} \cdot R} = \sqrt{0.1 \cdot 100} = 3.16\ V \tag{29}$$

The maximum current was then calculated as follows:

$$I = \frac{V}{R} \tag{30}$$

$$I_{thermistor\_MAX} = \frac{V_{thermistor\_MAX}}{R} = \frac{3.16}{100} = 31.6\ mA \tag{31}$$

Therefore, the maximum permissible voltage across a single thermistor was $3.16\ V$ and $31.6\ mA$ when the thermistor was at operating temperature.

70

Since the pair of thermistors appeared in series to the DC biasing circuit, the maximum voltage over the thermistors were

$$V_{t\_MAX} = 2 \times V_{thermistor\_MAX} = 6.32 \, V. \tag{32}$$

And since $V_t = V_s = \frac{1}{2}V_o$, the maximum output voltage was

$$V_{o\_MAX} = 2 \times V_{t\_MAX} = 12.64 \, V. \tag{33}$$

In order to be able to utilise the full range of the thermistor, the op amp needed to be able to supply V_{o_MAX}. However, since it was not good practice to operate components close to their maximum ratings, a design value of 80 % of V_{o_MAX} was deemed sufficient. Therefore, $V_{o\_MAX\_design} = 10.11 \, V$ was chosen. The design value for the current was $I_{o\_MAX\_design} = 0.8 \times 31.6 = 25.28 \, mA$, assuming that the current draw from the R_s voltage divider was negligible.

Table 4.4 shows a comparison of some of the important op amp parameters for three op amps that were considered. The required properties were also displayed.

Device	Requirement	Texas Instruments TL082 [66]	Texas Instruments TLC2272 [67]	Texas Instruments TLV4112 [68]
Output voltage swing (V)	$0 \, to + 10.11 \, V$	$\pm 12 \, V$ ($\pm 15 \, V \, supply$)	$+4.25 \, V \, at$ $I_O = -1 \, mA$ $-3.5 \, V \, at$ $I_O = 5 \, mA$ ($\pm 5 \, V \, supply$)	$+4.7 \, V \, at$ $I_O = -10 \, mA$ $0.03 \, V \, at$ $I_O = 10 \, mA$ ($+5 \, V \, supply$)
Maximum supply voltage	$> 10.11 \, V$	$\pm 18 \, V$	$\pm 8 \, V$	$0 \, to + 7 \, V$
Output current limit (mA)	$25.28 \, mA$	$17 \, mA$ ($T = 25 \, °C,$ $V_o = 10 \, V$)	$3 \, mA$ ($T = 25 \, °C,$ $V_o = 4 \, V$)	$300 \, mA$ ($T = 25 \, °C,$ $V_o = 4.6 \, V$)
Equivalent Input Noise Voltage ($nV/\sqrt{Hz}$)	Low at near-DC frequencies	$30 \, nV/\sqrt{Hz}$ ($f = 10 \, Hz$)	$50 \, nV/\sqrt{Hz}$ ($f = 10 \, Hz$)	$140 \, nV/\sqrt{Hz}$ ($f = 10 \, Hz$)
Input offset voltage (V at $25 \, °C$)	Small	$15 \, mV \, (max)$	$2.5 \, mV \, (max)$	$3.5 \, mV \, (max)$
Cost factor	Minimal	$R \, 33.54*$	$R \, 38.28*$	$R \, 45.21**$
*Price taken from [69] in Oct 2019. **Price obtained from [70] in Oct 2019.				

Table 4.4: A comparison of important parameters of possible op amps for use in the DC bias circuit. These were compared to the desired op amp properties.

The TL082 was a general purpose op amp that could output a wide voltage range. The TLC2272 was a rail-to-rail op amp. The TLV4112 op amp could supply plenty of current. All of these op amp packages contained 2 op amps (note the 2 suffix in the model numbers). Therefore a single package could be used for both the microwave and ambient thermistor circuits.

The TL082 was the only op amp that could output an adequate voltage output swing. It could not, however, supply sufficient current, which is where the TLV4112 really shined. The TL082 had the lowest equivalent input noise voltage, which was advantageous. It did, however, have a much larger

71

input offset voltage compared to the others, which would affect the exact temperature that the thermistor would have been biased at. This would have slightly affected S_{11} since a perfect $50\,\Omega$ match would not be achieved. The TL082 was the cheapest option available.

The TL082 was primarily chosen for its wide voltage output swing and the low current limit was compensated using a transistor (see below).

A $\pm 12\,V$ supply powered the op amp. As shown in Table 4.4, a *minimum* output voltage swing of $\pm 12\,V$ could have been obtained with a $\pm 15\,V$ supply. The *typical* output voltage swing was $\pm 13.5\,V$ with the same supply [66]. Therefore, an output voltage swing of between $\pm |V_{cc} - 1.5V|$ and $\pm |V_{cc} - 3V|$ was expected. Therefore, with a $\pm 12\,V$ supply, an output voltage swing of between $\pm 10.5\,V$ and $\pm 9\,V$ was expected.

This output voltage swing limited the maximum voltage across the thermistors such that it was always below its maximum power rating. The maximum expected output voltage was 83 % of the maximum permissible voltage across the thermistor, which was 3 % higher than the design value of 80 %. Even if the op amp should have been a rail-to-rail op amp, with a $\pm 12\,V$ output swing, the thermistor would still have been operated below its maximum power rating ($V_{o\_MAX} = 12.64\,V$).

At an output voltage of $V_o = 10\,V$, the TL082 could not supply $17\,mA$, which was less than the required $25\,mA$ to bias the thermistor. In addition, powering the op amp with a dual power supply meant that the DC bias circuit may have operated at any of the three possible operating points (see Figure 4.31).

A dual purpose solution was to use a transistor at the output of the op amp. A 2N2219A NPN transistor was placed within the feedback loop in order to supply sufficient current to the thermistors and to force the circuit to only operate at the positive operating point (Figure 4.32).
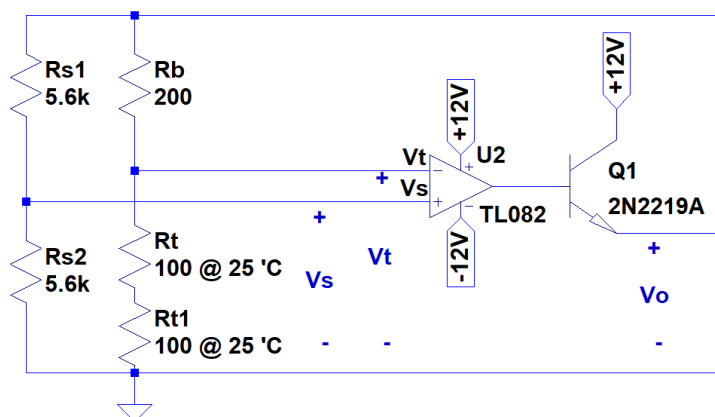
Figure 4.32: Circuit diagram for the DC biasing circuit used to bias the thermistors of the microwave power thermistor

The transistor could supply up to $800\,mA$ of current, which was more than plenty [71].

Since it was an NPN transistor it could only amplify positive voltages and therefore a negative operating point was not possible.

$5.6\,k\Omega$ resistors were used for the R_s resistors. These were sufficiently large in order for the divider to draw negligible current. The resistors had a tolerance of 2 %. Furthermore, several of these 2 % resistors were measured and resistors were chosen that had a value of $R_{s1} = R_{s2} = 5.56\,k\Omega$.

For the DC bias circuit that powered the temperature compensation thermistor pair, R_{s2} was replaced with two potentiometers (pot): a $10\,k\Omega$ pot in series with a $100\,\Omega$ pot. It was very probable that the output from the microwave power DC bias circuit and the temperature compensation DC bias circuit would not be equal. This was due to the tolerances of the thermistors and the differing layouts for the thermistors which affected the dissipation constants of each set of thermistors. In order to correct for

this, the potentiometers were tuned until a particular known difference was reached between the outputs (see Sec. 4.9.3).

4.7.3 Instrumentation amplifier

The purpose of the instrumentation amplifier was to subtract the output of the temperature compensation DC bias circuit from the output of the microwave power DC bias circuit. In this way the ambient temperature changes were removed from the desired signal. It also meant that the output of the detector started from $0\,V$ (i.e. $0\,V$ output equated to $0\,mW$ microwave input power). The instrumentation amplifier also had adjustable gain, which was used to set the output range of the power detector.

With no microwave power applied and at a constant ambient temperature, both DC bias circuits would have provided an output equal to one another (this was fine-tuned using the potentiometers in the compensation circuit). The difference of their outputs was then zero. If a microwave signal was applied to the microwave power thermistor pair, the difference between the outputs was directly proportional to the amount of microwave power that was applied.
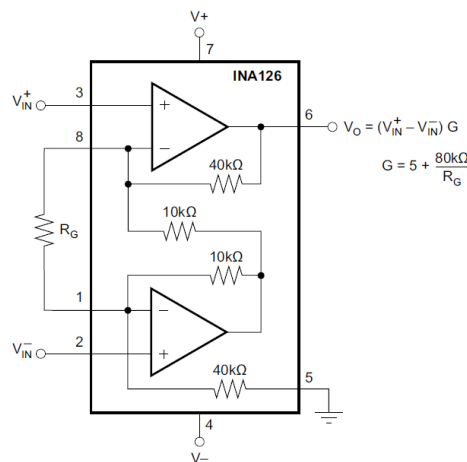
Figure 4.33: Simplified circuit schematic of the INA126 instrumentation amplifier [72].

The Texas Instruments INA126 Instrumentation amplifier was used. It is a general purpose instrumentation amplifier that has a wide operating voltage range, which was important for compatibility with the $\pm 12\,V$ power supply. Some of the INA126's important parameters are shown in Table 4.5.

Device	Requirement	Texas Instruments INA126 [72]
Output voltage swing (V)	$0\ to +10\ V$	$+V_o = V_{cc} - 0.9$ $-V_o = -V_{cc} + 0.95$ (minimum)
Maximum supply voltage	$\pm 12\ V$	$\pm 18\ V$
Gain	Adjustable, wide range	$G = 5\ to\ 10000\ \dfrac{V}{V}$ Set using an external resistor
Equivalent Input Noise Voltage ($nV/\sqrt{Hz}$)	Low at near-DC frequencies	$45\ nV/\sqrt{Hz}$ $(f = 10\ Hz)$
Input offset voltage (V at $25\ °C$)	Small	$0.25\ mV\ (max)$
Cost factor	Minimal	R 61.39 [73]

Table 4.5: Comparison of some properties of the INA126 instrumentation amplifier to the required properties.

The gain of the instrumentation amplifier was controlled by an external resistor. The gain equation was as follows:

$$G = 5 + \frac{80\ k\Omega}{R_G} \tag{34}$$

where R_G refers to the external resistor. A $100\ k\Omega$ potentiometer was used to make the gain settable.

4.7.4 Output ranging (attenuator)

The output from the instrumentation amplifier could range from $-11.05 \leq V_{o\_INA} \leq 0\ V$. This, however, was not compatible with $5V$ signal levels that most microcontrollers require.

An inverting amplifier with a gain smaller than 1 was used to bring the signal level down. The op amp acted as a buffer between the low pass filter at the output and the resistive voltage divider that this circuit employs, safeguarding the filter from being affected by the divider. An op amp was used in the following configuration [74, p. 627]:
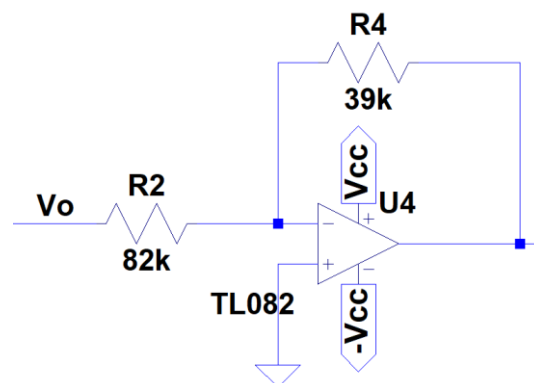
Figure 4.34: The circuit schematic shows the inverting amplifier used to bring the output signal down to $5V$ levels [74, p. 627].

The gain was calculated as follows:

74

$$G = -\frac{R4}{R2} = -\frac{39\ k\Omega}{82\ k\Omega} = -0.476 \tag{35}$$

Therefore, the maximum output signal was

$$V_{inverting} = V_{o\_INA\_MAX} \times G = -11.05 \times -0.476 = 5.23\ V \tag{36}$$

An Arduino Leonardo, with an Atmel Atmega 32u4 microprocessor, was used in this research project. $5.23\ V$ was an acceptable input voltage level at the analog input pins of the microprocessor [49]. In addition, the circuitry described in Sec. 4.7.6 offered additional protection to the microprocessor.

The positive maximum signal was not considered since the instrumentation amplifier was configured such that the output was always $V_{o\_INA} \leq 0\ V$.

4.7.5   Low pass filter

A principal advantage of using thermistors as the sensing element was that the circuit was able to produce a linear output. This meant that, in order to measure the average power of a non-sinusoidal signal, the output could simply be filtered with a low pass filter. A first order RC filter was used.

As shown in the chapter introduction (4.2), the output from a microwave system is pulsed at a frequency of $50\ Hz$. Therefore, in order to remove any $50\ Hz$ components at the output, the filter was designed to have at least $-40\ dB$ attenuation at this frequency.

Using physical component values of $R_f = 10\ k\Omega$ and $C_f = 47\ \mu F$, the following cut-off frequency was determined:

$$f_c = \frac{1}{2\pi R_f C_f} = 0.34\ Hz \tag{37}$$

The filter simulation is shown in Sec. 4.8.4, which verifies an attenuation of less than $-40\ dB$ at $50\ Hz$.

Although this leads to a slow time constant of $\tau = 2.94$ seconds, the system was intended to measure continuous wave signals that varied slowly over time. Alternatively, a next iteration of the design could use a higher order filter that would have a faster time constant.

After the entire power detector was constructed, the filter was measured while the circuit was functioning. The output of the power detector was measured before and after the low pass filter. The signal generator was set up to simulate the power from the magnetron by sending a microwave signal at $50\ Hz$ pulses. The output before and after the filter is shown in Figure 4.35 and Figure 4.36. Note that the mean value, displayed in the top right corner, remains the same.
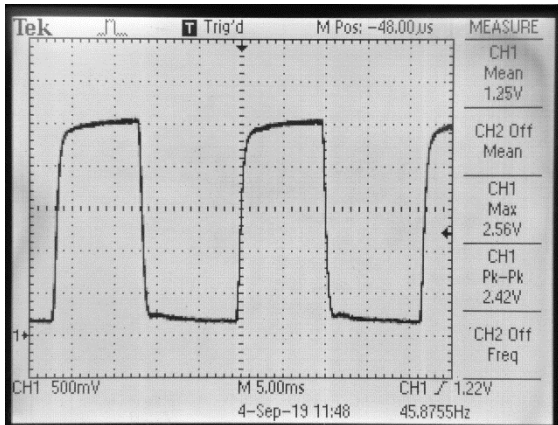
Figure 4.35: Power detector output before the low pass filter.
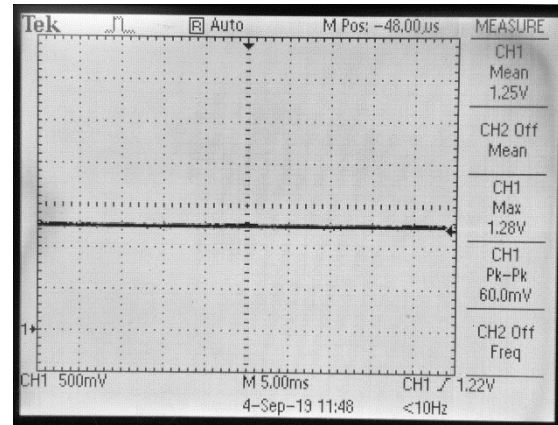
Figure 4.36: Power detector output after the low pass filter.

4.7.6 Output protection

In order to be doubly sure that the microcontroller was protected, two measures were taken to ensure that the microcontroller input voltage limits were not exceeded, as shown in Figure 4.37.
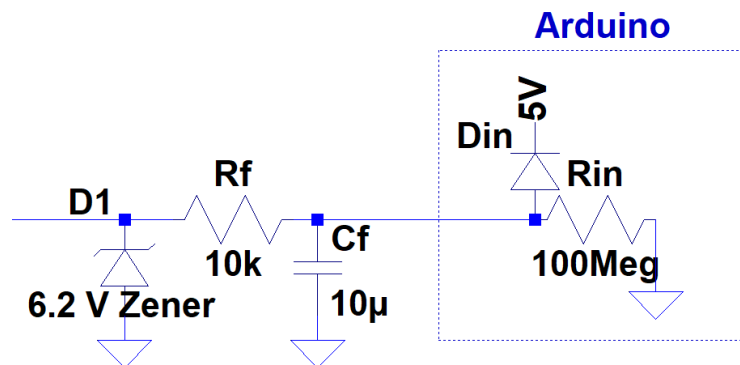
Figure 4.37: Circuit schematic shows measures that were taken to protect the microcontroller input pins.

A $6.2\ V$ Zener diode was placed in parallel with the output from the attenuator. This guaranteed that the output was always between $0 \leq V_o \leq 6.2\ V$. The diode would have provided a short circuit should the voltage have been negative, and it would have limited the voltage to $6.2\ V$ should the voltage have been higher than this.

Zener diodes did not have an ideal on/off switching characteristic. Instead, the diode started to conduct slightly before its specified voltage, causing a voltage drop at the output [75]. Zener diodes with ratings of $5.1, 5.3, 5.6$ and $6.2\ V$ were tested. With all three of the lower voltage Zener diodes, this early conduction effect impacted the output voltage. The $6.2\ V$ diode had a negligible effect on the output voltage.

The other protection method was the resistor that formed part of the RC low pass filter. A high series resistance was used which limited the current flow. The Atmega 32u4 analog input pins contain a protection diode to limit the voltage into the pin. These diodes, however, cannot handle high currents. Therefore, should the diodes have been conducting, the resistor would have limited the current [49].

The internal protection diodes start conducting at about $5.5\ V$ [49]. The maximum current flow would then be

$$I_{MAX} = \frac{V_{MAX}}{R_{limit}} = \frac{5.5}{10\ k\Omega} = 0.55\ mA. \tag{38}$$

The Atmega 32u4 datasheet did not specify a current limit. $I_{MAX} = 0.55\ mA$ was deemed sufficiently small to prevent damage to the microprocessor. At voltages above $6.2\ V$, the Zener diode would have conducted and prevented a further increase in current through the resistor.

At voltages below V_{MAX}, the input impedance of the Atmega 32u4 pin was $R_{in} = 100\ M\Omega$ [76, p. 391]. This meant that there would have been a negligible current draw from the Atmega 32u4 and therefore a negligible voltage drop over the resistor.

4.7.7   Temperature sensor amplifier

An amplifier was used to amplify the signal from the LM35 temperature sensor (described in Sec. 4.6.6).

As shown in Figure 4.23, the output from the LM35 was as follows:

$$V_{temp} = 0.01 \times T\ (V), \tag{39}$$

where T is the temperature in $°C$.

The smallest voltage that the Atmega 32u4 could read with the 10-bit ADC (analog to digital converter) was

$$V_\Delta = \frac{5\ V}{2^{10}} = 4.88\ mV \tag{40}$$

Therefore, the temperature reading was only readable up to half a degree.

To increase the resolution of the temperature reading, a non-inverting amplifier was used, as shown in Figure 4.38 [74, p. 638].
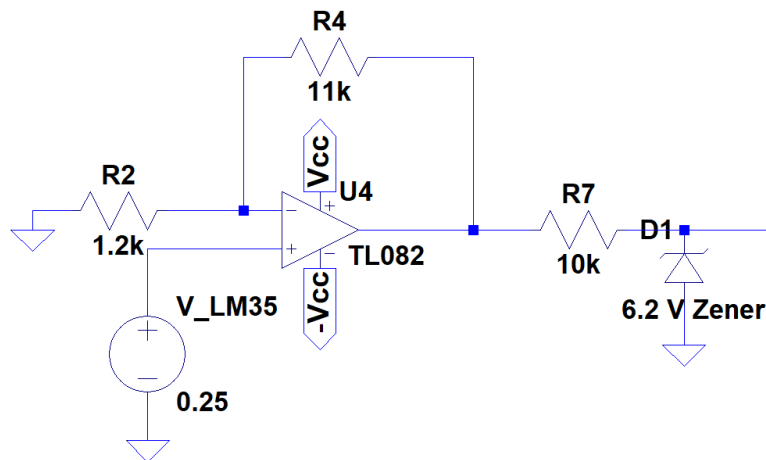
Figure 4.38: Circuit schematic of the amplifier used to amplify the LM35 output [74, p. 638]. *Output protection circuit can be seen at the output.*

The gain was chosen as $G = 10$. Using practical resistor values, the gain was calculated as follows:

$$G = 1 + \frac{R4}{R2} = 1 + \frac{11\ k\Omega}{1.2\ k\Omega} = 10.17 \tag{41}$$

Therefore, the signal from the LM35 was approximately ten times larger. A temperature difference of up to $T_\Delta = 0.05\ °C$ could be read by the microcontroller. The maximum temperature that could now be measured was $T_{MAX} = 50\ °C$, which was well beyond the maximum operating temperature of the thermistors of $25\ °C$.

Similar output protection circuitry was added, as described in Sec. 4.7.6.

4.7.8 Power supply

The driver circuitry had its own $\pm 12\,V$ voltage regulators. Since the circuit was used for sensitive measurements, it was vital that the supply voltages did not fluctuate. Voltage regulators ensured that the same voltages were always applied to the components.
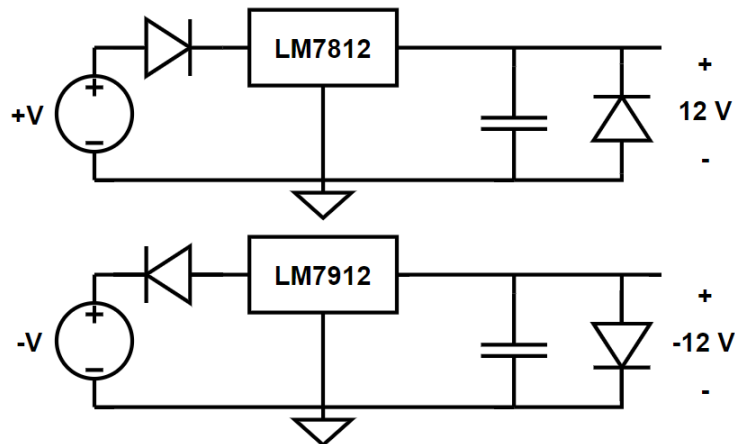
Figure 4.39: Circuit schematic for the voltage regulators.

An LM7812 and LM7912 voltage regulators were configured as shown in Figure 4.39. Diodes were placed in series with the input in order to protect the circuit should the polarity of the external supply voltages have been reversed. A shunt diode on the output side protected the circuitry should an inverse polarity voltage have been applied to the output side. Several decoupling capacitors were added along the output lines to filter any noise on the power supply lines. Only an equivalent capacitor is shown on each supply line in Figure 4.39.

4.7.9 PCB layout

The PCB layout was done using Autodesk EAGLE. Single-sided etching was done for the sake of rapid prototyping. The final PCB layout is shown in Figure 4.40 and the physical, populated PCB is shown in Figure 4.41.

Special attention was given to the ground plane. Thin sections of ground plane could have acted as resistors and caused a voltage drop between sections of the ground plane. Therefore, a ground plane that only had wide sections was designed.

In addition, decoupling capacitors were placed along the power supply line, as close as possible to the component's supply pins. This filtered noise from the power supply and noise induced onto the supply lines. This was good design practise and may have prevented the op amp circuits from oscillating.
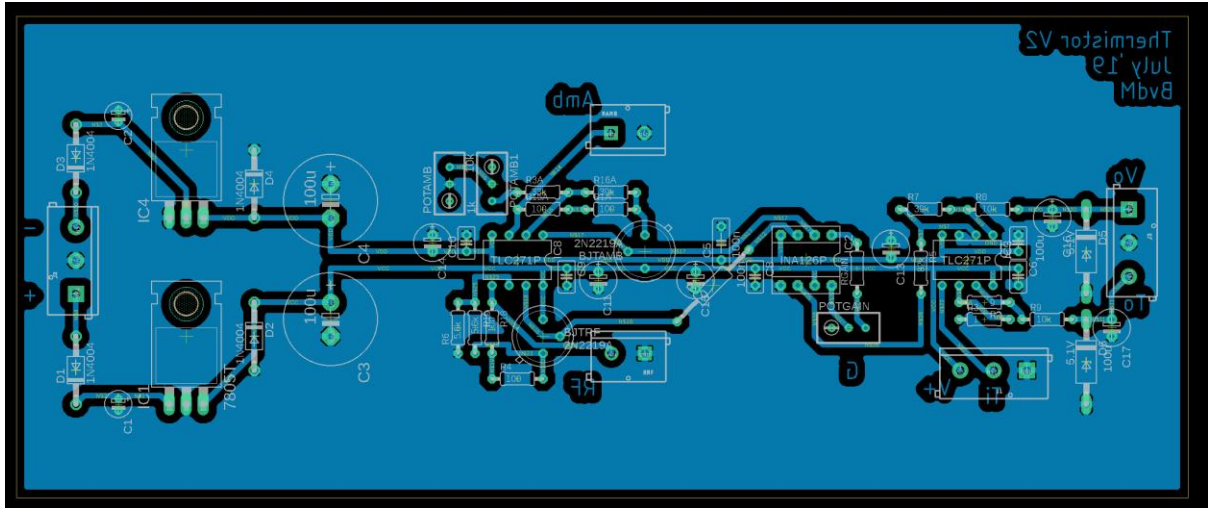
Figure 4.40: Printed circuit board layout for the power detector driving circuit.
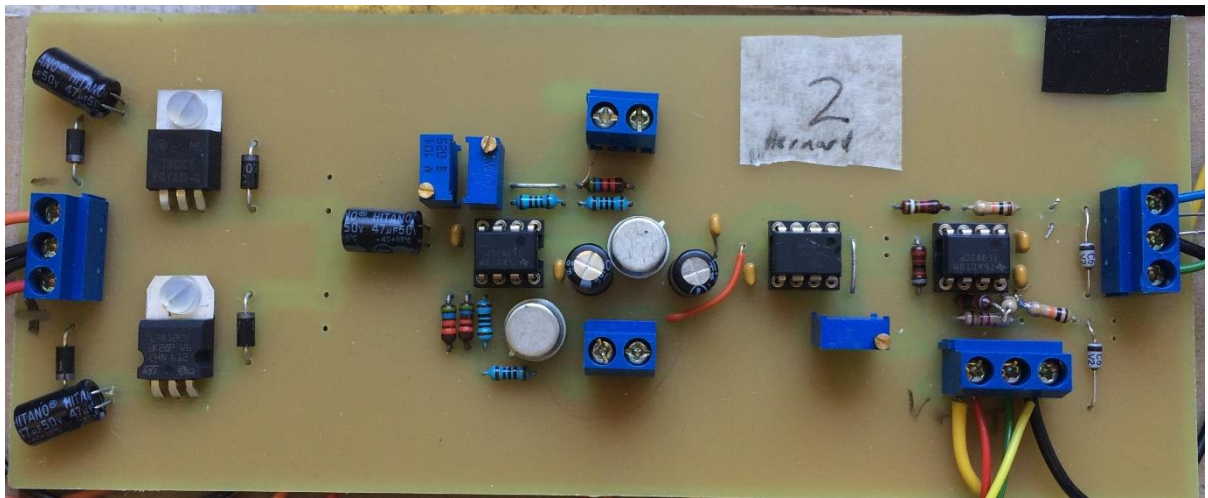
Figure 4.41: Printed circuit board for the power detector driving circuit.

79

4.8 Simulation

4.8.1 Overview
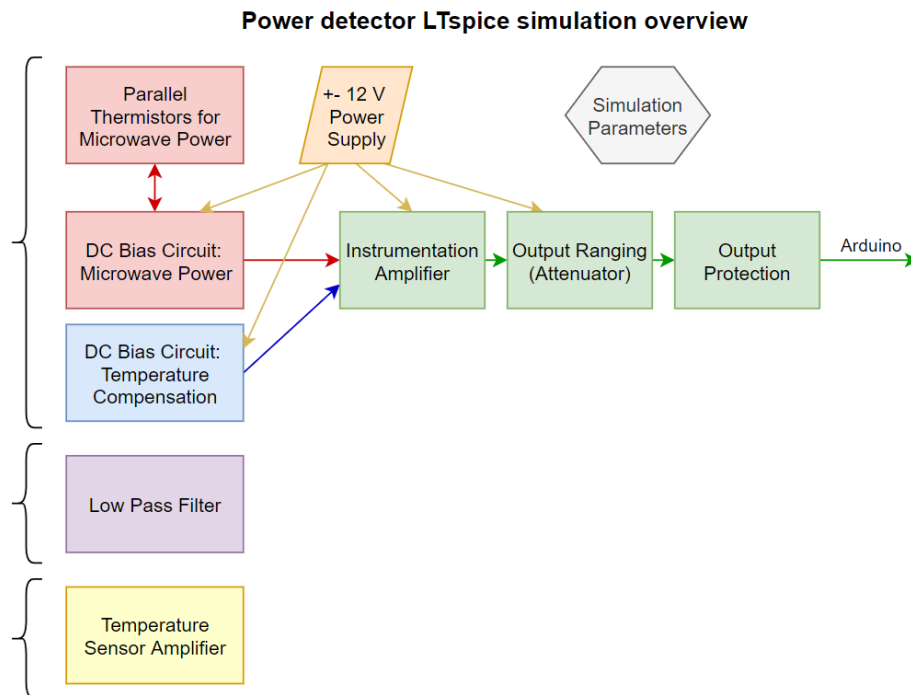
Figure 4.42: Power detector LTspice simulation overview. Curly braces indicate separate simulations.

The DC equivalent circuit of the power detector was simulated using LTspice XVII. Figure 4.42 shows a block diagram overview of how the simulations were put together. The simulation was useful in obtaining ball park figures for outputs (since the dissipation constant was approximate), to test circuit configurations and to help with component choices such as resistor values. Several parameters were modifiable: ambient temperature, individual thermistor parameters (like B and δ), microwave input power and individual component values.

Note that any references in the simulation screenshots that refer to "RF" should technically say "microwave" according to the definition given in Sec. 2.2.1.

For the sake of clarity, all the simulations were drawn in one sketch, shown in Figure 4.43.
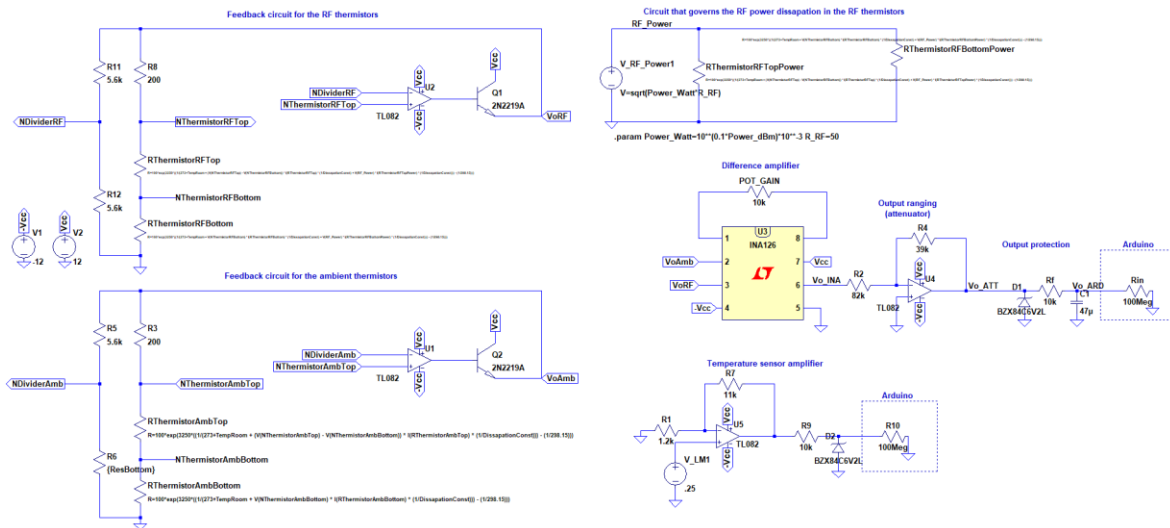
Figure 4.43: Circuit diagram for all the LTspice simulations.

4.8.2 DC biasing circuits

Figure 4.44 shows the simulation circuit of the DC biasing circuit, which is a redrawn version of Figure 4.32.
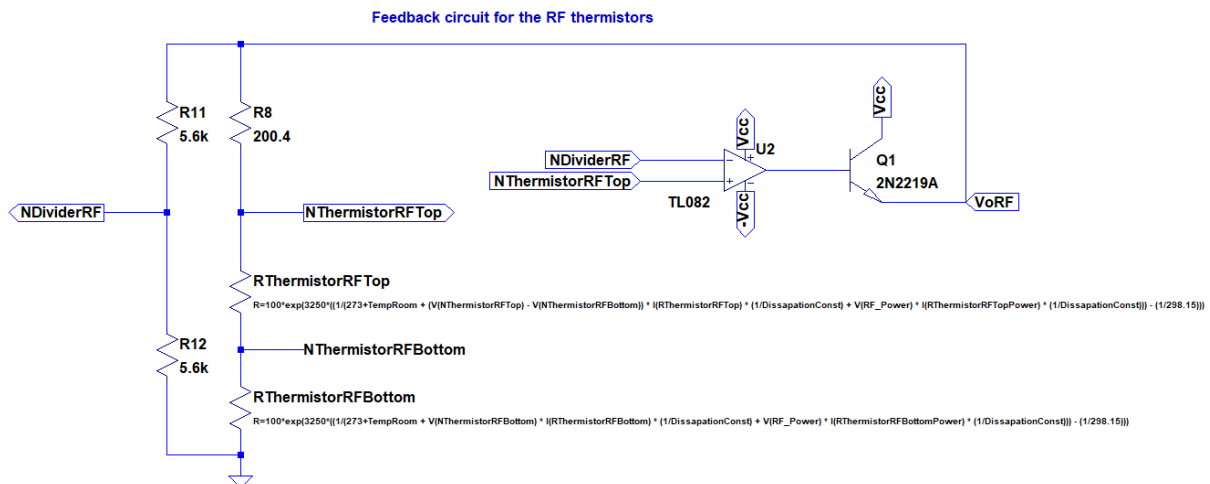
Figure 4.44: Circuit diagram for the LTspice subcircuit used to simulate the DC biasing circuit that biased the thermistors of the microwave power thermistor pair.

Since a thermistor is not a standard LTspice component, a custom component had to be configured. The thermistors were simulated by using a resistor, but with an equation governing its resistance. Eq. 23 was used to define the resistance, repeated here:

$$R = R_0 \exp\left(B \left(\frac{1}{T} - \frac{1}{T_0} \right) \right). \tag{23}$$

R_0 and B was taken from the muRata datasheet in [58] and $T_0 = 298.15\ °C$. T was calculated by adding the ambient temperature to the temperature change caused by the power flowing through the thermistor. The latter was determined using eq. 20:

$$P_{bias} = \delta \times T_\Delta \tag{20}$$

Manipulating this equation lead to

$$T_\Delta = \frac{P_{bias}}{\delta}, \tag{42}$$

81

where

$$P_{bias} = V_{thermistor} \times I_{thermistor} \tag{43}$$

In order to simulate the effect of microwave power into the microwave power thermistor pair, an additional subcircuit was set up. This circuit had a parallel configuration of the same thermistors from the microwave power thermistor pair. A power value could be specified in units of dBm. A DC voltage source supplied the equivalent microwave power to the thermistors. Figure 4.45 shows this subcircuit.

Circuit that governs the RF power dissapation in the RF thermistors

RF_Power

R=100*exp(3250*((1/(273+TempRoom + V(NThermistorRFBottom) * I(RThermistorRFBottom) * (1/DissapationConst) + V(RF_Power) * I(RThermistorRFBottomPower) * (1/DissapationConst))) - (1/298.15)))

RThermistorRFBottomPower

V_RF_Power1

RThermistorRFTopPower

R=100*exp(3250*((1/(273+TempRoom + (V(NThermistorRFTop) - V(NThermistorRFBottom)) * I(RThermistorRFTop) * (1/DissapationConst) + V(RF_Power) * I(RThermistorRFTopPower) * (1/DissapationConst))) - (1/298.15)))

V=sqrt(Power_Watt*R_RF)

.param Power_Watt=10**(0.1*Power_dBm)*10**-3 R_RF=50

Figure 4.45: Circuit diagram for the LTspice subcircuit used to simulate the effect of microwave power on the thermistors.

The power dissipated in the thermistors from the subcircuit was added to the equations used to govern the thermistors.

Note that the full equations to govern the thermistors was included in both the power dissipation subcircuit and in the DC biasing circuit. This made the thermistors exact duplicates, which was necessary since the resistance value affected the power flow through the thermistors. It did, however, increase the simulation complexity since four, instead of two, equations needed to be solved.

For the temperature compensation thermistor pair, the same circuit shown in Figure 4.44 was used to bias the compensation thermistors, except that the addition of microwave power was excluded in the thermistor equations.

Using zero-tolerance components and assuming a dissipation constant of $3\ mW/°C$, an ambient temperature of $22.3\ °C$ and a microwave input power of $6\ dBm$, output voltages of $VoRF = 3.20\ V$ and $VoAmb = 3.65\ V$ were obtained.

4.8.3 Instrumentation amplifier and output circuitry

The simulation model for the difference amplifier, output ranging and output protection is shown in Figure 4.46. The outputs from the DC bias circuits were taken as inputs at pins 2 and 3 of the INA126 – VoAmb and VoRF, respectively. The gain could be adjusted by changing the value of POT_GAIN. The input impedance of the Atmega 32u4 pin was modelled by a $100\ M\Omega$ resistor.

82
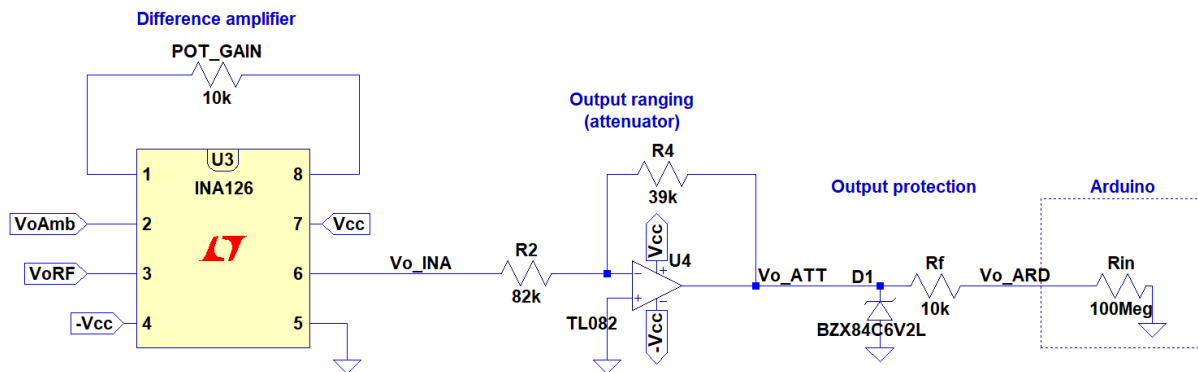
Figure 4.46: Circuit diagram for the LTspice subcircuit used to simulate the difference amplifier, output ranging and output protection.

Running the simulation with the same simulation parameters as specified at the end of the previous section, output voltages of $V_{o\_INA} = -5.82\,V$ and $V_{o\_ATT} = 2.77\,V$, with a difference of $280\,\mu V$ between V_{o_ATT} and V_{o_ARD}, were obtained.

In addition, a sweep of power values were simulated to replicate something similar to the results from Sec. 4.9.4. The input power was swept from -10 to $10\,dBm$. Using the same simulation conditions as before, but with POT_GAIN removed, the following data was obtained (Figure 4.47):
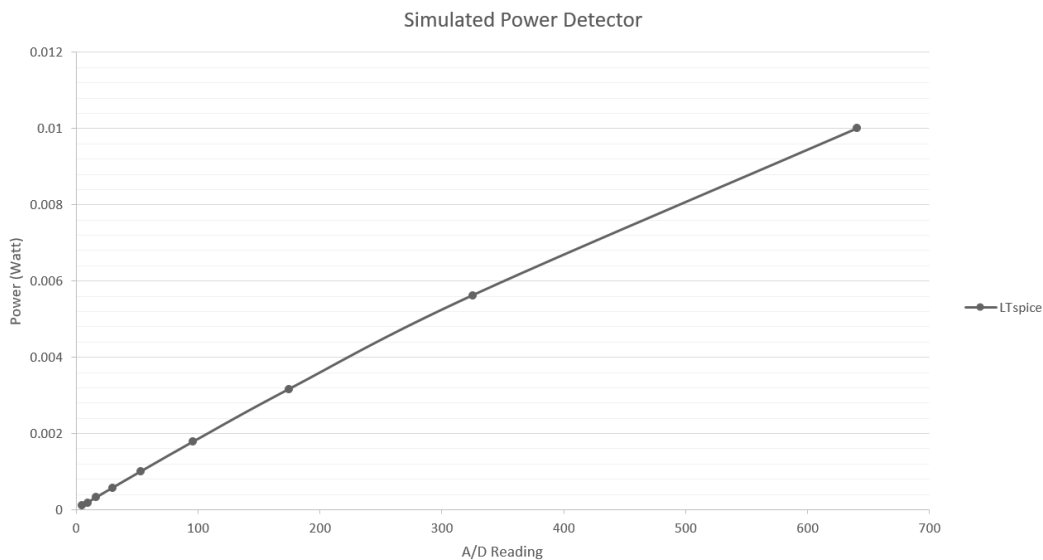
Figure 4.47: LTspice output of the simulated power detector. A sweep of the microwave power was done from -10 to $10\,dBm$.

The data from the simulation matched the results from the calibration qualitatively, but not quantitatively. A fully-fledged attempt was not made to match the simulation to the calibrated data.

4.8.4 Low pass filter

The low pass filter was simulated separately since the main simulation was not designed to take a variable signal as an input. The LTspice circuit is shown in Figure 4.48.
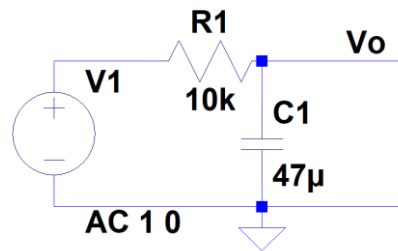
Figure 4.48: Circuit diagram for the LTspice circuit used to simulate the low pass filter.

An AC sweep was done from 0.1 to $200 \, Hz$. The cut-off frequency (or $-3 \, dB$ point) was at $0.343 \, Hz$, which was very close to the design value of $0.34 \, Hz$ that was calculated in Sec. 4.7.5. There was an attenuation of $-43.4 \, dB$ at $50 \, Hz$. The result from the AC sweep is displayed in Figure 4.49.
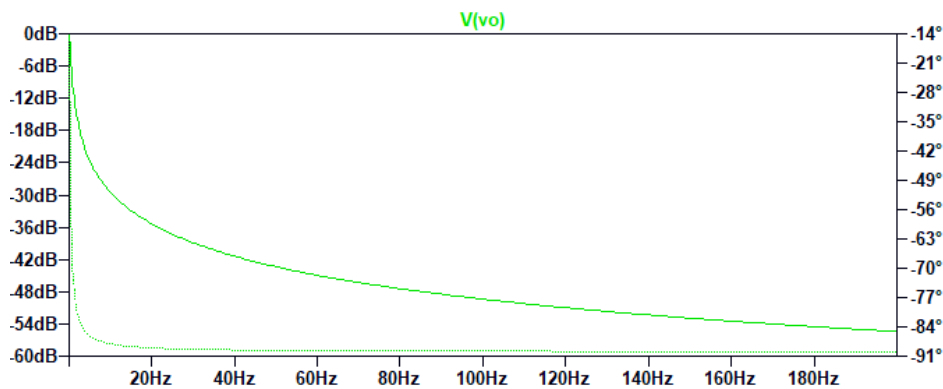
Figure 4.49: Result of the AC sweep of the low pass filter.

4.8.5 Temperature sensor amplifier

The amplifier for the LM35 temperature sensor was simulated to verify the design. The LTspice simulation circuit is shown in Figure 4.50. With a $0.25 \, mV$ input, which corresponds to a temperature of $25 \, °C$, an output of $2.54 \, V$ was obtained. This was an error of $1.6 \, \%$ caused by the gain being slightly more than 10.

The output protection circuitry was included in the simulation, but had a negligible effect on the output voltage.
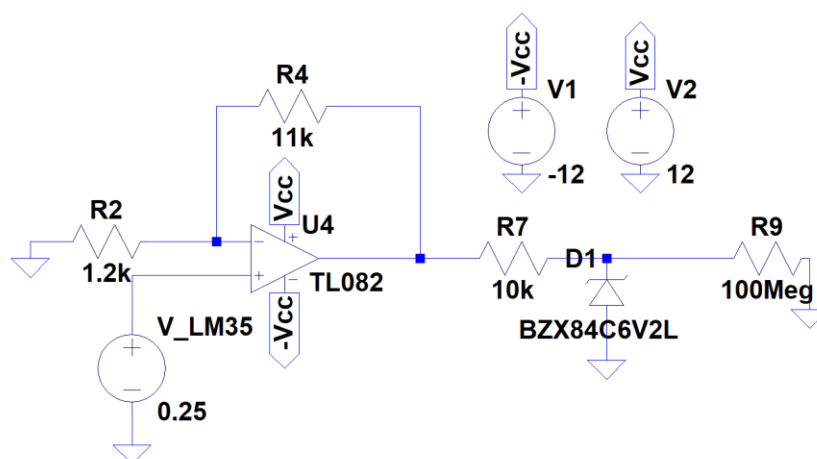
Figure 4.50: Circuit diagram for the LTspice subcircuit used to simulate the temperature sensor amplifier.

4.9 Calibration

4.9.1 Introduction

Power Detector Overview
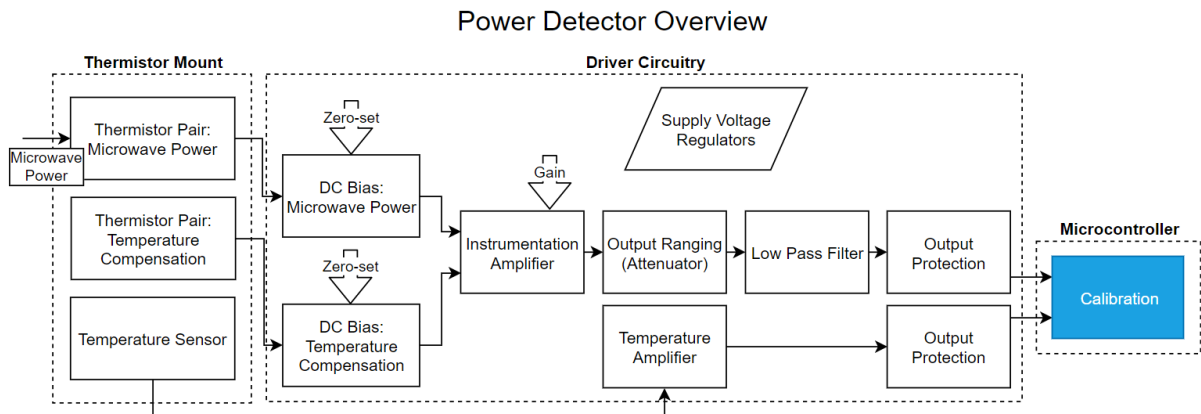
Figure 4.51: Block diagram of where the calibration fits in.

The power detector had to be calibrated to a known standard. Thus the output voltage was calibrated to a known power value. Since the power detector was dependant on the ambient temperature, the ambient temperature was also taken into account.
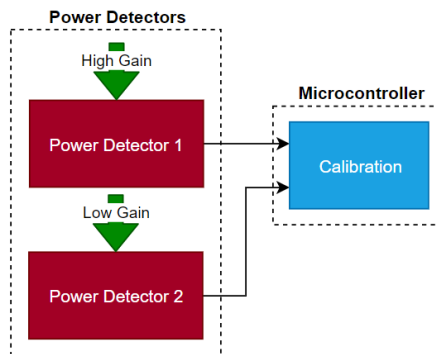
Figure 4.52: Block diagram of the two power detectors.

Two power detectors were built so that both forward and reverse power could be measured in a microwave system.

For the power detectors to achieve similar output voltage levels to one another, power detector 1 required a high gain at the instrumentation amplifier and power detector 2 required a low gain. This meant that effect of ambient temperature fluctuations in the sensor were much more pronounced in power detector 2 and that zero-setting was often required. The difference in gain levels was due to the differing input reflection coefficients of the detectors (see the end of Sec. 4.6.2). In other words, power detector 2 absorbed more of the incoming power, therefore it was more sensitive to input power. Power detector 1 had to compensate for this by having a high gain at the instrumentation amplifier.

In this section, the term 'power detector' refers to the thermistor power detector developed in this research project and the term 'power sensor' refers to the Agilent E4412A CW Power Sensor. The term 'power meter' refers to the Agilent E4417A Power Meter which functions as an interface to the power sensor.

85

4.9.2 Equipment

4.9.2.1 Signal Generator

Figure 4.53: Rohde & Schwarz SMIQ 04B signal generator.

An input signal was generated using a Rohde & Schwarz SMIQ 04B signal generator, as shown in Figure 4.53. It could operate over a frequency range of $300\ kHz$ to $4.4\ GHz$. It could deliver up to $10\ dBm$ of power. It did, however, have an over-range function that could deliver up to $16\ dBm$, but with unknown accuracy [77]. It could not provide an output up to $18.45\ dBm$. The remaining power levels were extrapolated using mathematical functions.

4.9.2.2 Reference

Figure 4.54: Agilent E4417A Power Meter.   *Figure 4.55: Agilent E4412A CW Power Sensor with adapter to SMA.*

The output from the signal generator was measured using an Agilent E4417A Power Meter with an Agilent E4412A CW Power Sensor (CW donates continuous wave), shown in Figure 4.54 and Figure 4.55.

The E4417A Power Meter had a built-in $50\ MHz$ reference that was used to calibrate the power sensor with. The power meter functioned as an interface to the power sensor.

The E4412A CW Power Sensor was a diode based sensor that could measure a frequency range of $10\ MHz$ to $18\ GHz$. It could measure CW signals from -70 to $+20\ dBm$.

86

4.9.3   Method

The equipment was placed in an air conditioned room. This was so that the ambient temperature could be adjusted. The following procedure was followed to perform the calibration, with reference to Figure 4.56:

1. With the power detectors, signal generator and power meter turned on, set the temperature of the air conditioner.
2. Wait for approximately an hour so that the room can reach the set temperature and so that the equipment can reach stable operating temperatures.
3. Calibrate and zero the power sensor by connecting the power sensor to the power meter's reference connector and using the Cal/Zero functionality. Verify that the frequency is set to 2.45 GHz.
4. Connect the power meter to the end of the cable that will be used to interface with the power detectors. Connect the other end to the signal generator.
5. Sweep the signal generator from -10 to 16 dBm at 2.45 GHz. The sweep function of the signal generator may be utilised. Record the measurement.
6. Disconnect the power meter from the end of the cable.
7. Measure each power detector:
   - 7.1. Connect the cable to the power meter.
   - 7.2. Adjust the zero-set potentiometers on the driver circuitry until an ADC value of '1' is consistently read by the Arduino.
   - 7.3. Sweep the signal generator from -10 to 16 dBm at 2.45 GHz. Record the output values as well as the temperature.
8. Repeat step 7 for the other power detector.
9. Repeat steps 1 to 8 with a new air conditioner temperature.
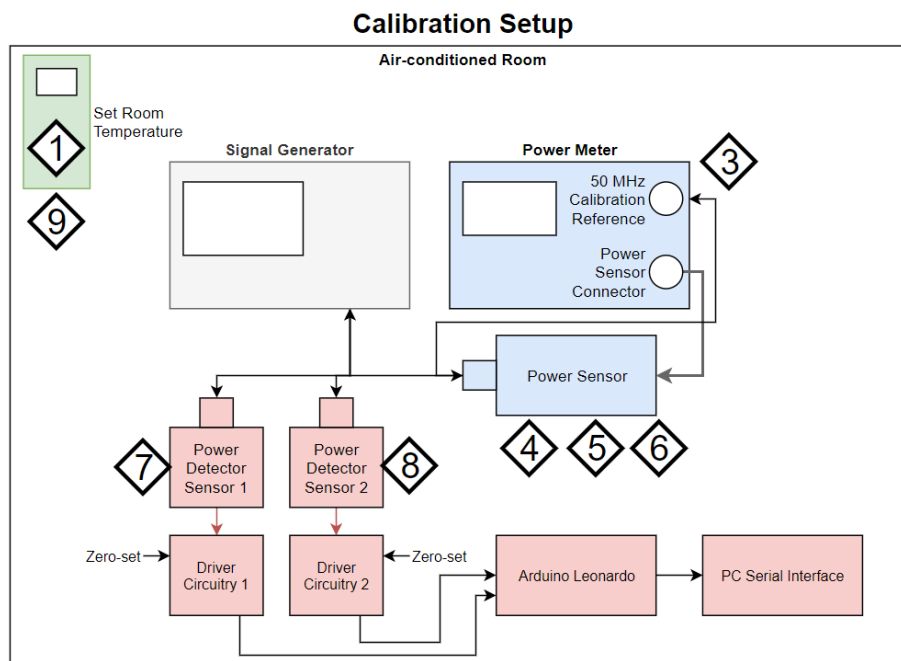
Figure 4.56: Calibration setup. Triangle markers indicate the main equipment used for each step.

87

4.9.4   Results

The data from the calibration showed a linear relationship between the output voltage and the input power (when expressed as $Watts$). Figure 4.57 shows the calibration data from both sensors, where the linear relationship can clearly be seen.
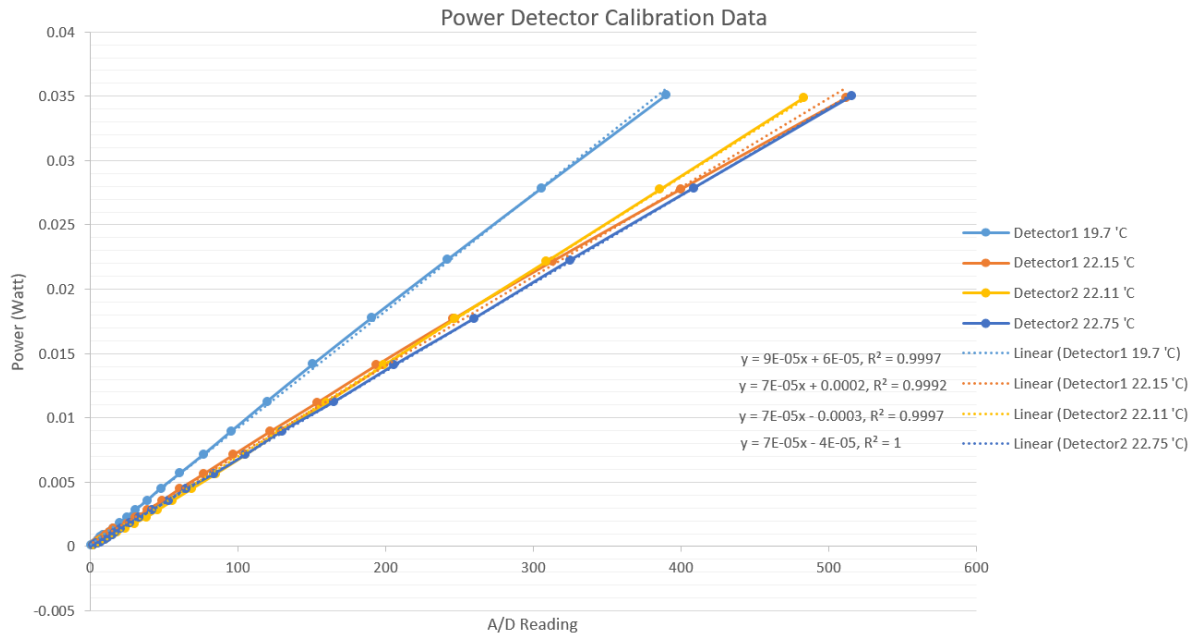
Figure 4.57: Data from the calibration. The input power (Watt) are plotted against the ADC readings. Fitted trend lines, with their equations, are also shown.

The data was very close to a perfect linear relationship. This was indicated by the coefficients of determination, R^2, being very close to 1, where 1 indicates a perfect relationship, shown near the bottom right of Figure 4.57. The data between the two detectors also correlated very well, confirming that the power detectors functioned as designed and that the design could be replicated.

Both data lines for power detector 1 had a slight downward curve. This was due the effect of small changes in the ambient temperature that had a more pronounced effect on power detector 1 due to the high gain required at the instrumentation amplifier.

In order to use the calibration data, a mathematic function was found that could relate any ADC reading and temperature to a power value. Symbolically:

$$P = f(x, t), \tag{44}$$

where x donates the ADC value and t the temperature.

The mathematical function was important so that the power could be calculated at any temperature and so that the data could be extrapolated in order to measure the full power detector range of 0 to $+18.45\ dBm$. A function, and its coefficients, was iteratively determined. The following function offered a good fit:

$$P = a \times t^{-2} \times x, \tag{45}$$

where a denotes a coefficient that was determined iteratively. Slightly different values for a were found for each power detector: $a_1 = 0.0346$ and $a_2 = 0.0353$, for power detector 1 and power detector 2, respectively. Eq. 45 was plotted alongside the data recorded during the calibration, shown in Figure 4.58 and Figure 4.59.
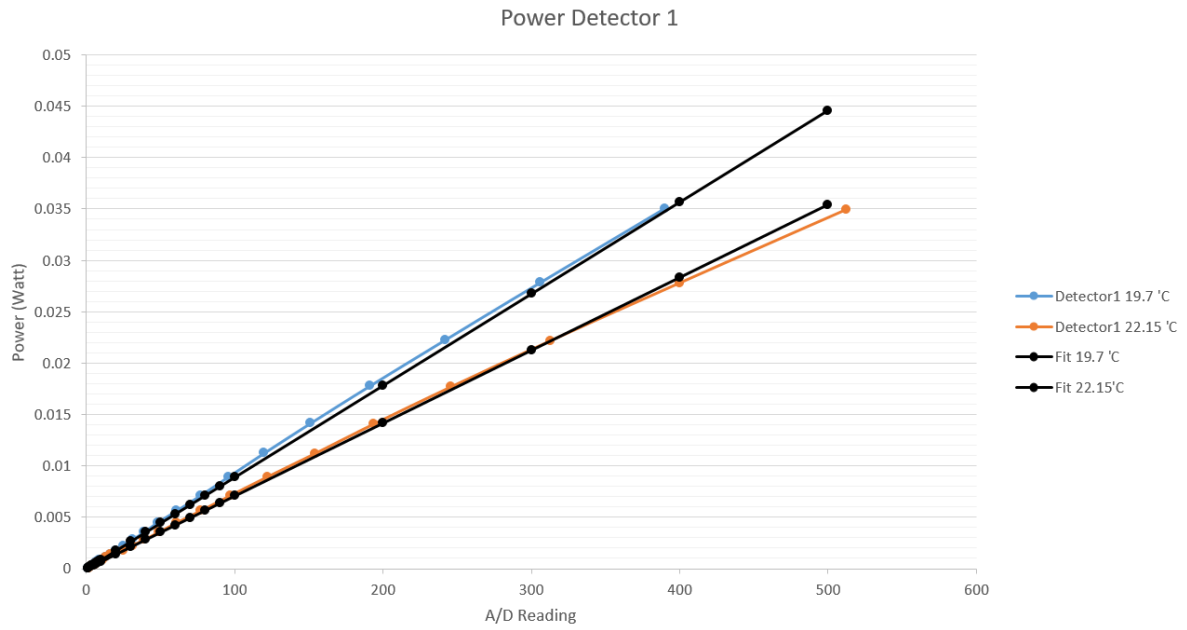
Figure 4.58: A plot of the data from the calibration for power detector 1 and the linear function (black) that fit the data best.

Figure 4.59: A plot of the data from the calibration for power detector 2 and the linear function (black) that fit the data best.

The temperature at which the power detectors could still measure up to $18.45\ dBm$ was calculated. Manipulating eq. 45 to have t as the subject yielded

$$t_{MAX} = \sqrt{\frac{a \times x_{MAX}}{P_{MAX}}} \tag{46}$$

where $x_{MAX} = 1023$ and $P_{MAX} = 70\ mW$.

For power detector 1, with $a_1 = 0.0346$, the maximum operating temperature was $t_{MAX\_1} = 22.49\,°C$. Power detector 2, with $a_2 = 0.0353$, had a maximum operating temperature of $t_{MAX\_2} = 22.71\,°C$. Above these temperatures the input power would heat-up the thermistors to temperatures beyond $25\,°C$, which means that the DC compensation circuit would no longer add any power to thermistors. Thus the readings at high input powers would be incorrect.

Therefore, the power detectors should not be operated at temperatures above these maximum temperatures for them to be able to measure the full power range of up to $18.45\,dBm$. Alternatively, the power detectors can be re-calibrated at higher ambient temperatures.

4.9.5   Calibration conclusion

The calibration confirmed the linearity of the power detector. The calibration also allowed a mathematical function to be found that described the measured data. This was very useful in order to implement the calibration as a single line of code in the microcontroller (as opposed to using a data table that would have consumed a lot of memory).

The calibration did not cover the full power range. Using a high-power amplifier was experimented with, but the output of the amplifier was very sensitive to fluctuations in temperature, including self-heating of the amplifier at differing power outputs. The output was therefore not consistent enough to be used as an accurate reference.

The mathematical functions was used to extend the calibration data to cover the entire measurement range.

4.10 Chapter conclusion

An operational prototype of a thermistor-based power detector was developed that was able to measure the power of a microwave signal at $2.45\,GHz$. It could measure from $0\,dBm$. It was calibrated up to $15.4\,dBm$, and, with mathematical functions, the calibration data was extrapolated to $18.45\,dBm$. It did not, however, have a good input impedance at $2.45\,GHz$, which meant that the prototype was not yet ready to be used in $50\,\Omega$ systems.

The prototype was useful in investigating the fundamental concepts related to a thermistor power detector and for developing a well-functioning driving circuit. The entire circuit worked, which proved that this design was ready to be refined further.

The output of the power detector was linear. This allowed a low pass filter to be used at the output and thereby the average power in a microwave system can be determined.

The circuit's output was dependant on the ambient temperature. This was compensated for with a temperature compensation thermistor pair and by using temperature sensors to calibrate out further ambient temperature fluctuations.

The design was simple, using commonly available circuit components. An enclosure for the thermistor sensors needed to be constructed, but the design for this was also simple.

The system was affordable. The most expensive components were the three op amps and an instrumentation amplifier.

4.11 Chapter recommendations

The next step in the development of the power detector was to redesign the thermistor mount with thermistors that function well at high frequencies. Smaller thermistors should be tested – 0402 thermistors may be small enough. Alternatively, a matching circuit can be investigated.

Although the power detector compensated for changes in the ambient temperature, a better way of removing the dependence on ambient temperature would be to place the thermistor mount in a

temperature controlled enclosure. Then the thermistors would always be at a set temperature and ambient temperature fluctuations would not have an impact on it.

The LTspice simulation can still fine-tuned to match the data from the calibration. The impact of component tolerances and of noise can still be integrated.

5 Microwave applicators

5.1 Chapter summary

This chapter discusses the two applicators that were used to preform pasteurisation tests on Rooibos tea leaves. The magnetron feed circuit is first discussed, since it is used for both applicators. Then the travelling wave applicator and the air-cooling applicator are discussed, after which the conclusions and recommendations are given.

5.2 Chapter introduction
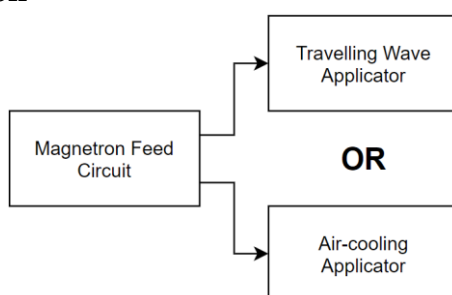
Figure 5.1: Microwave applicators chapter overview.

One of the goals of this research project was to determine whether microwave radiation could be used to pasteurise Rooibos tea leaves. Two cases had to be tested: whether pasteurisation of Rooibos tea leaves was possible using microwave radiation and whether the microwave specific effect was able to pasteurise tea leaves at ambient temperatures.

To prove that microwave radiation was able to pasteurise Rooibos tea leaves, the travelling wave applicator was developed. It heated samples evenly which thereby removed the problem of hotspots that occur in conventional microwave ovens. The waveguide structure that was used ensured that the electric field was uniform across the sample, and therefore the sample was heated evenly. The sample's temperature was measured with an infrared thermometer so that this temperature could be controlled.

In order to test whether a significant microwave specific effect was able to pasteurise Rooibos tea leaves at ambient temperatures, the air-cooling applicator was developed. A beaker with tea leaves was placed within a multi-mode cavity. Room-temperature air was blown onto the tea leaves which created a vortex, both cooling and mixing the tea simultaneously. A mode stirrer was also placed inside the cavity to ensure an even distribution of microwave power.

The directional coupler and power detectors that were developed in Ch. 3 and Ch. 4 was unfortunately not used in either of these systems. Although the power detector prototype was functional, it could not yet be relied upon for accurate measurements due to the bad input match to the thermistors. The travelling wave applicator was developed to rely on sample temperature, rather than absorbed power, to control the system and the air-cooling applicator used an open loop control system.

5.3 Magnetron feed circuit
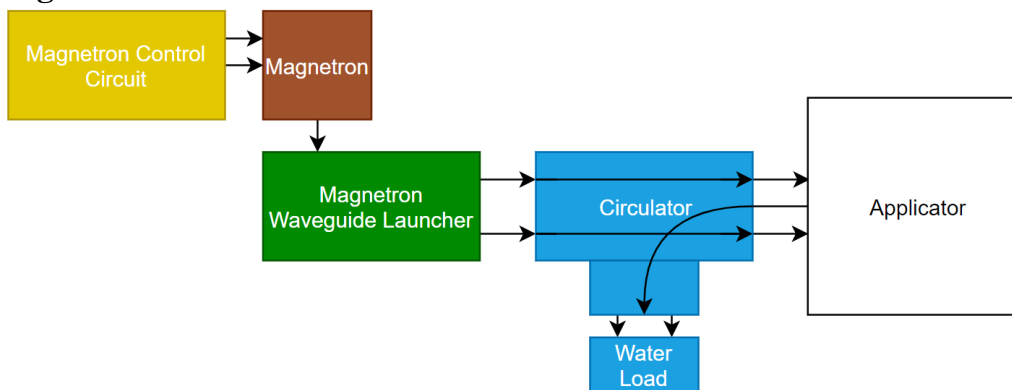
Figure 5.2: Block diagram of the applicator feed circuit.

Both applicators used the same configuration to feed microwave radiation to the applicator, as shown in the block diagram in Figure 5.2. The physical supply circuit is shown in Figure 5.3. This subsection discusses the waveguide components; chapter 6 discusses control of the magnetron and temperature control.

The magnetron was connected to a magnetron waveguide launcher. The magnetron waveguide launcher had a hole through which the magnetron antenna was inserted. The hole was about $\lambda_g/8$ from the back of the guide, as with the waveguide to coaxial transition from Sec. 3.4.2. It also had mounting holes to which the magnetron and a cooling fan for the magnetron was attached.

A circulator was connected to the magnetron waveguide launcher (see the end of Sec. 2.2.3). The circulator had a water load attached to its perpendicular port, which therefore directed any reflected power coming from the applicator into the water load. This not only protected the magnetron from overheating, but also from having its output frequency and power influenced by the load in the applicator.
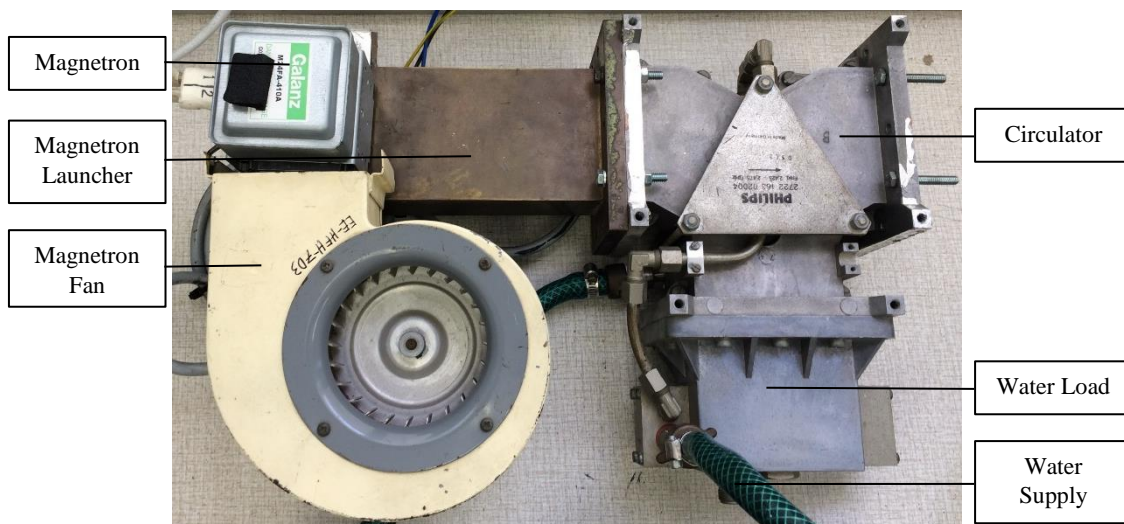
Figure 5.3: Photo of the magnetron feed circuit.

5.4 Travelling wave applicator

5.4.1 Introduction
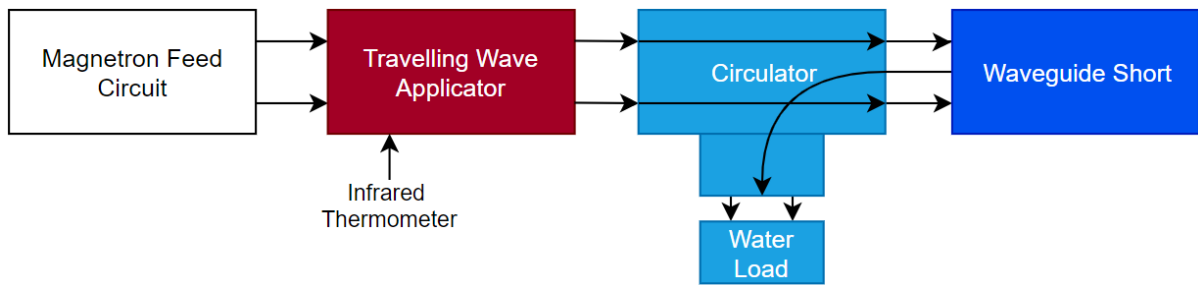
Figure 5.4: Block diagram of how the travelling wave applicator was configured.

The travelling wave applicator consisted of a WR340 waveguide with an observation hole in the side wall and a hole in the broad wall. It was connected to another circulator, as shown in Figure 5.4. The second circulator ensured that no power was reflected back to the applicator, which prevented a standing wave from forming. The setup is shown in Figure 5.5 and the applicator itself is shown in Figure 5.6.
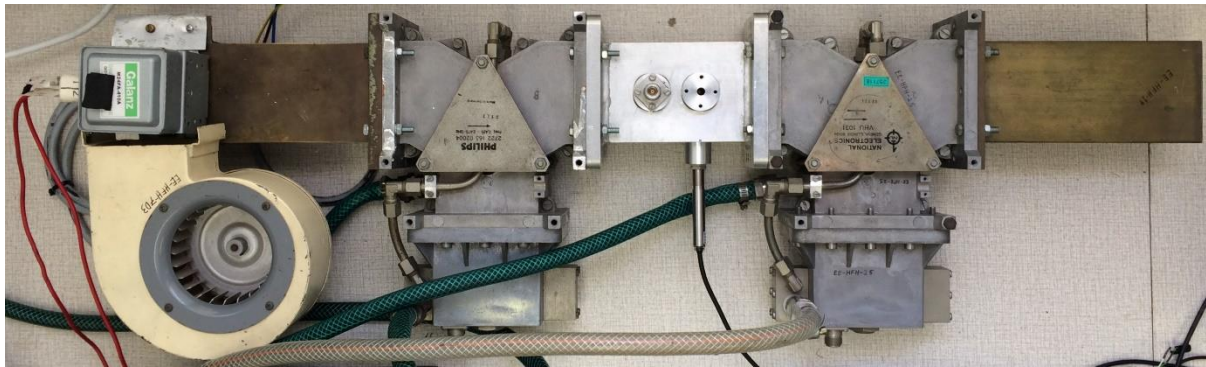
Figure 5.5: Physical layout of how the travelling wave applicator was configured.
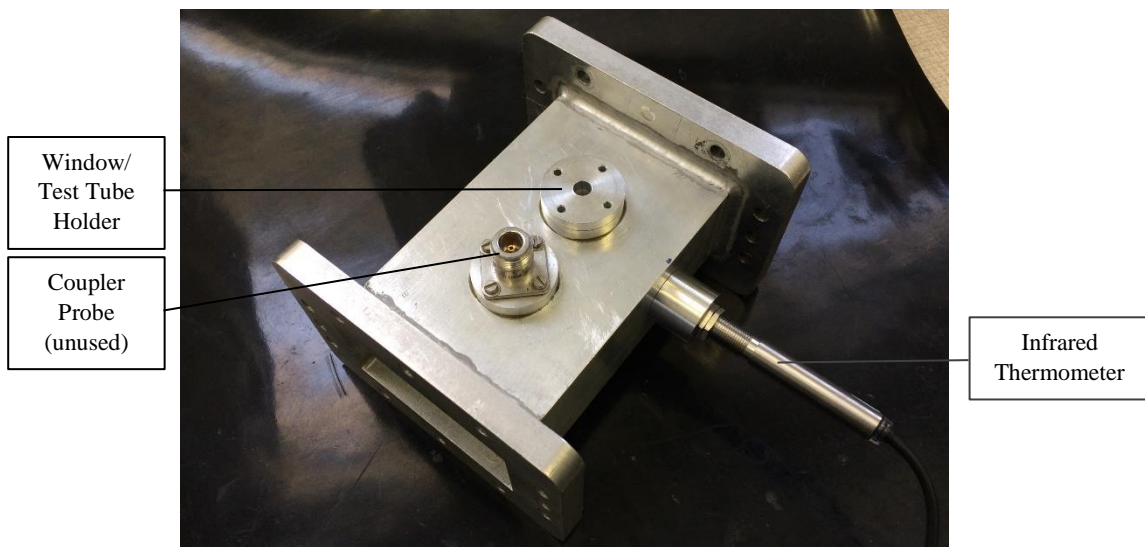
Figure 5.6: The travelling wave applicator.

5.4.2 Sample placement

The hole in the broad wall was previously used to insert a test tube into the applicator. In this research project, however, microcentrifuge tubes were used, which did not fit through the hole. This was because the sample would become contaminated by any particles that remained in the part of the test tube that

94

was not irradiated. The hole was, therefore, only used as a window to ensure that the sample was placed in the correct position. The sample had to be lined up with the infrared thermometer.

A $2\ m\ell$ microcentrifuge tube containing a Rooibos tea leaf sample was placed upright in the centre of the waveguide, as shown in Figure 5.7. It was held in place by a polystyrene holder (which was essentially invisible to the microwave radiation since it had a loss factor around $\epsilon'' = 7.42 \times 10^{-15}$ (at $10\ GHz$) [7, p. 719]). The sample was inserted by disconnecting the travelling wave applicator from the circulator.

Figure 5.7: A microcentrifuge tube containing Rooibos tea leaves was placed inside the travelling wave applicator and kept in place with a polystyrene holder. The observation hole for the infrared thermometer can be seen on the right of the sample.

The travelling wave applicator was tested to see whether it heats a sample evenly. A sample of Rooibos tea leaves were placed in a test tube and heated up using microwave radiation. Since a test tube was used for this experiment, the sample could be removed immediately after processing. Using a visual infrared thermometer (Fluke VT02), the sample was photographed directly after being irradiated. Figure 5.8 shows the thermal image.

Figure 5.8: Infrared photo of a Rooibos tea leaf sample immediately after being irradiated.

The sample was heated evenly. The top and the bottom of the sample was slightly colder – this was most likely due to a larger surface area at these points so more heat would had been lost at these points.

5.4.3   Infrared thermometer

An infrared thermometer was used to measure the temperature of the sample (Optris CS LT). Infrared sensing is a non-contact technology; therefore it did not affect the electric field pattern at all. It was mounted in an aluminium tube that looked into the side wall of the applicator.

The radius of the tube was sufficiently small and the thermometer was placed sufficiently far away from the cavity of the waveguide so that microwave radiation was minimal at the head of the sensor, protecting the sensor from possible damage or measurement errors.

S	6,5	11,6	16,6	21,7	26,7	35	43,3	51,6	59,9 (mm)
D	0	100	200	300	400	500	600	700	800 (mm)
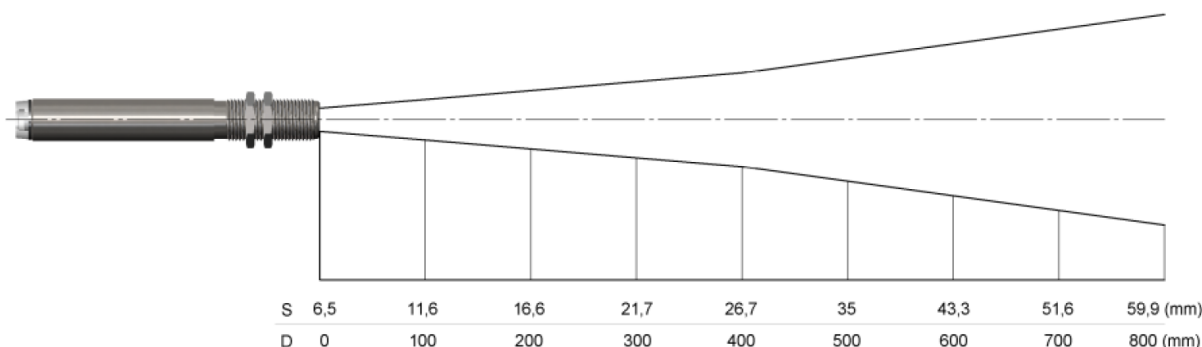
Figure 5.9: Optical chart for the Optris CS LT [78]. S, the top numbers, indicated the radius of the sensing spot. D, the bottom numbers, indicate the distance from the head of the sensor.

An infrared thermometer measures a spot some distance away from the head of the sensor. Figure 5.9 shows how the radius of this spot increases with distance [78].

An infrared thermometer measures thermal radiation. This is radiation that every object radiates, and of which the intensity varies depending on the temperature of the object. The intensity of the radiation is also dependant on the properties of each object [78].

The emissivity (ε) of an object is a measure of how well an object radiates infrared energy. It is a measure between 1 and 0, where 1 represents an ideal radiation source. The emissivity depends on various factors, such as the reflectiveness of the surface, the geometry of the surface and the thickness of the material [78].

Figure 5.10: A photo taken looking into the observation hole of the infrared thermometer.

In the case of the travelling wave applicator, the measured spot of the thermometer included the walls of the aluminium tube, the other side wall of the waveguide and the sample, as shown in Figure 5.10. The emissivity of aluminium is known to be very low ($\varepsilon_{Al} = 0,02 - 0,1$) [78], therefore it radiated very little infrared energy. The emissivity of the plastic microcentrifuge tube containing tea was much higher, probably around $\varepsilon_{sample} = 0.95$ [78]. Therefore the infrared radiation from the aluminium components had a negligible effect on the temperature readings. This assumption was verified by measuring a heated test tube sample with both the infrared thermometer and a thermocouple at the same time.

5.4.4   Conclusion

The travelling wave applicator supported a travelling wave at microwave frequencies. It irradiated a Rooibos tea leaf sample contained within a microcentrifuge tube. An infrared thermometer was able to monitor the temperature of the sample. The sample was heated evenly inside the travelling wave applicator.

5.5 Air-cooling applicator

5.5.1 Introduction
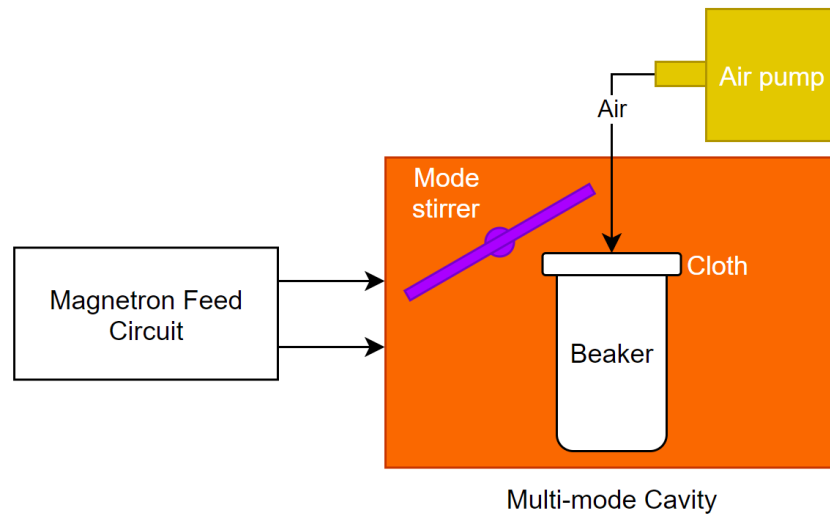
Figure 5.11: Block diagram of the air-cooling applicator.

The air-cooling applicator made use of a multi-mode cavity with a mode stirrer. The mode stirrer ensured that the microwave power was distributed evenly. An air pump pumped air into a beaker containing Rooibos tea leaves. The beaker was closed off with cloth, which allowed air to pass through, but not tea leaves. The incoming air caused a vortex, which meant that all the tea leaves were swirling around in the beaker. The leaves were therefore both stirred and cooled by having air blown on it. A block diagram of the setup is shown in Figure 5.11.

5.5.2 Mode stirrer

A mode stirrer was used to ensure an even distribution of microwave power over a period of time. The mode stirrer consisted of aluminium tape stuck to a Teflon rod, as shown in Figure 5.12. Teflon has a very low loss factor ($\epsilon'' = 0.0003$ [12, p. 30]) so it was essentially invisible to the microwave radiation. The rod extended to the outside of the cavity where it was connected to a slow turning DC motor (about 5 revolutions per minute).

Figure 5.12: The mode stirrer inside the cavity.

It is known that small neon bulbs light up when exposed to microwave radiation [79]. Using an array of neon bulbs, a one dimensional field pattern was observed inside the multi-mode cavity. Such an array confirmed that the mode stirrer was working effectively.

An array of neon bulbs was constructed using a flat piece of polystyrene which was approximately the size of the base of the beaker. Figure 5.13 shows a sequence of photos of the neon bulbs being illuminated by microwave radiation while the mode stirrer was turning.
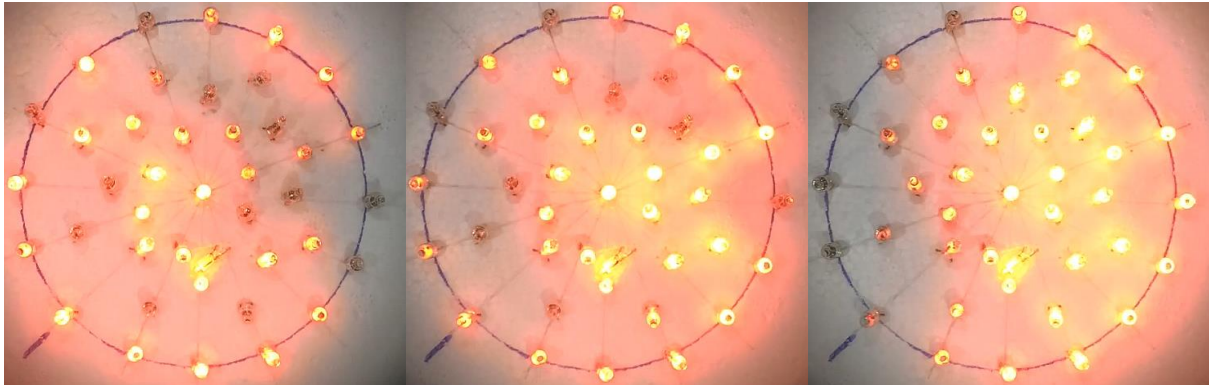
Figure 5.13: An array of neon bulbs was used to observe the electric field pattern inside the multi-mode cavity.

In order to observe the neon bulbs, a $5\ mm$ hole was drilled through the top of the cavity. A camera (Apple iPhone 5s) was used to film the neon bulbs. A simple CST simulation showed that the hole acted as a microwave choke, attenuating the power from the inside of the cavity by at least $-40\ dB$, considering the worst case scenario of an empty cavity. The model is shown in Figure 5.14. Since low power was used to conduct the neon bulb tests ($P_{MW} \leq 300\ W$), the camera was exposed to a maximum of $30\ mW$ of power over the entire hole. This was deemed sufficiently small.
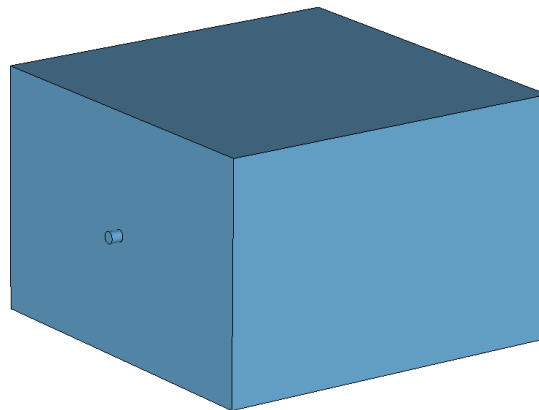
Figure 5.14: CST simulation model of a multi-mode cavity with a small hole through the cavity.

5.5.3   Mixing and cooling

The air-cooling setup can be seen in Figure 5.15. An air bed inflator pumped cool ambient air into the beaker through a silicone pipe. A piece of cloth allowed air to escape, but kept the tea leaves inside the beaker. Figure 5.16 shows snapshots of how the tea moved around inside the beaker.
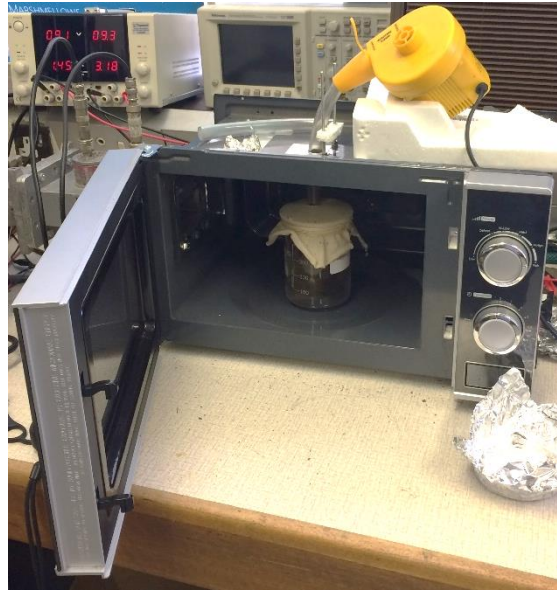
Figure 5.15: The air-cooling setup.
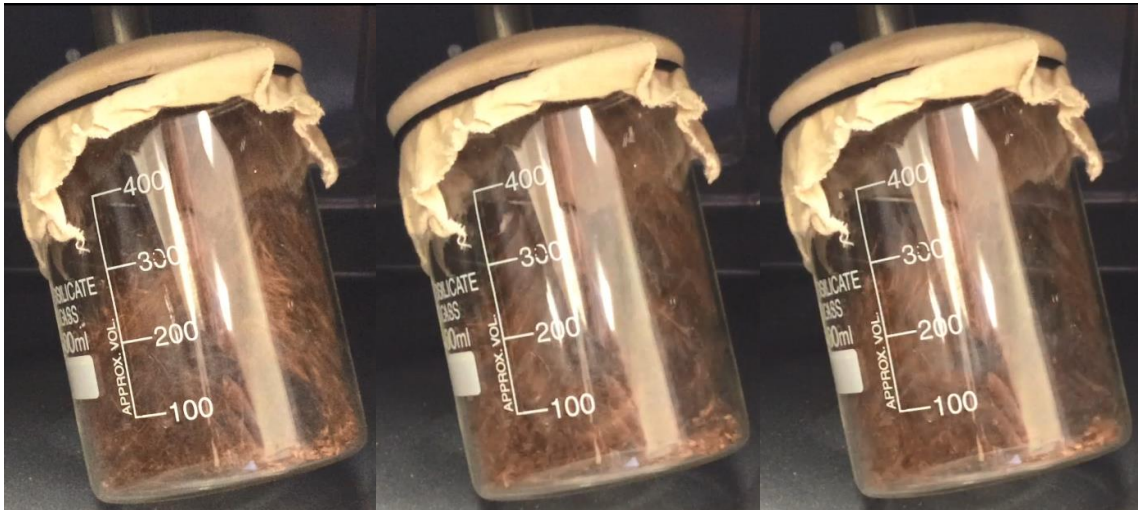
Figure 5.16: The Rooibos tea leaves were swirling rapidly inside the beaker.

5.5.4   Conclusion

The air-cooling applicator effectively cooled and mixed the tea leaves inside the beaker. The mode stirrer was effective at evenly distributing the microwave radiation inside the multi-mode cavity.

5.6   Chapter conclusion

Both applicators worked well. The travelling wave applicator evenly heated a sample of Rooibos tea leaves. The applicator was able to make a contactless temperature measurement of the sample while it was being irradiated. This meant that the temperature of the sample could be controlled using a control system.

The air-cooling applicator effectively cooled and mixed the Rooibos tea leaves while it was being irradiated. A mode stirrer inside the multi-mode cavity ensured that there was an even distribution of microwave radiation inside the cavity.

These applicators allowed effective testing to be made on Rooibos tea leaves to determine whether microwave radiation was an effective was of pasteurising it. The actual tests are discussed in chapter 7: Microwave pasteurisation.

5.7 Chapter recommendations

Although the travelling wave applicator worked well, it could only process a very small sample at a time ($2\ m\ell$). Using a conveyor belt inside the waveguide, a continuous system can be developed so that larger amounts of tea leaves can be processed at a time.

The air-cooling applicator could be redesigned to be a continuous flow system. However, since cooling down the tea was not a successful method of pasteurising the Rooibos tea leaves, further development of this system may not yield any useful results (see Sec. 7.5).

6 Microwave control system

6.1 Chapter summary and introduction

In order to power the magnetron, several standard circuit components were used, as discussed in Sec. 2.2.4. However, a variable power output was required so that a control system was able to heat a sample to a set temperature. As discussed in Sec. 2.2.5.4, control of the magnetron by means of a TRIAC was implemented. The first section of the chapter gives an overview of the system and then discusses each section of the system in further detail.

In addition, this chapter discusses the development of a proportional controller to control the temperature of a sample in the travelling wave applicator.

Finally, the algorithm that controlled the TRIAC is discussed. The algorithm used a timer function with interrupts to accurately time the pulses that controlled the TRIAC.

6.2 System overview

6.2.1 Introduction
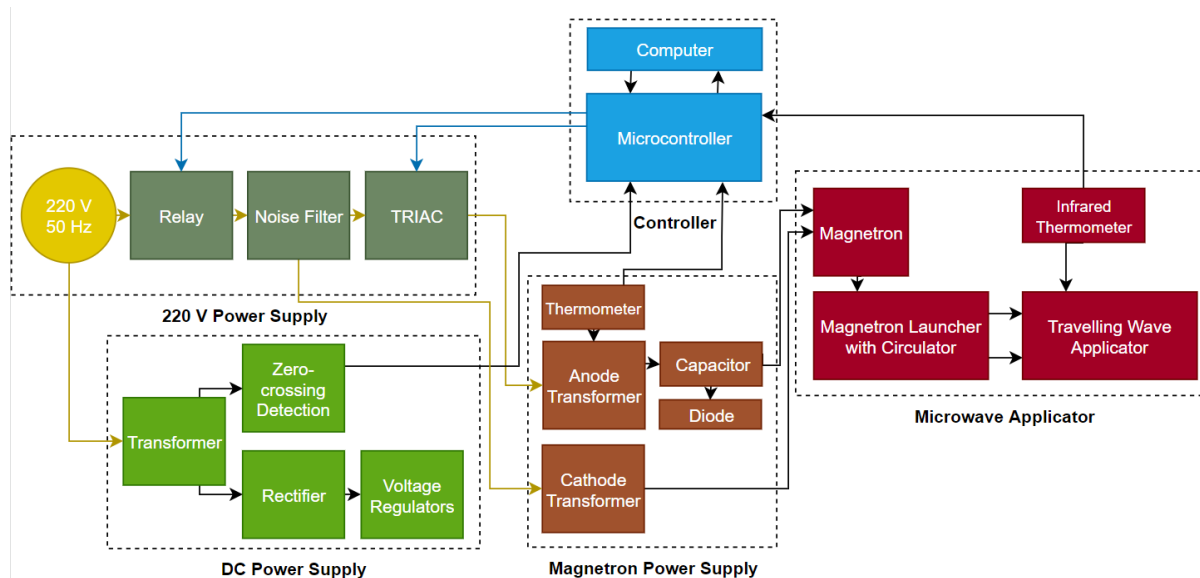
Figure 6.1: Block diagram of the microwave system.

A block diagram overview of the circuit that was used to power the magnetron feed circuit is shown in Figure 2.6. An overview of the system will now be discussed.

The **220 V power supply** supplied mains power to the magnetron power supply and to the DC power supply. The **DC power supply** rectified the mains power to provide DC power to any instruments requiring DC power. It also included a zero-crossing detection circuit. This was necessary in order to synchronise the TRIAC output with the incoming 50 Hz power.

The **magnetron power supply** fed power to the magnetron. The output power of the magnetron was controlled by the TRIAC which supplied power to the anode transformer. This caused the anode transformer to heat up significantly and thus a thermometer was used to monitor the temperature of the transformer. The value of the capacitor determined the maximum possible output power of the magnetron.

The **microwave applicator** is discussed in chapter 5: Microwave applicators. Depicted here is the travelling wave applicator since the air-cooled applicator did not require closed-loop control. The temperature from the infrared thermometer was read by the microcontroller, which was part of the **controller**. By adjusting the phase angle of the TRIAC, the microcontroller used a proportional

controller to adjust the temperature of a sample inside the applicator. The controller is discussed in Sec. 6.3.

6.2.2 220 V Power supply
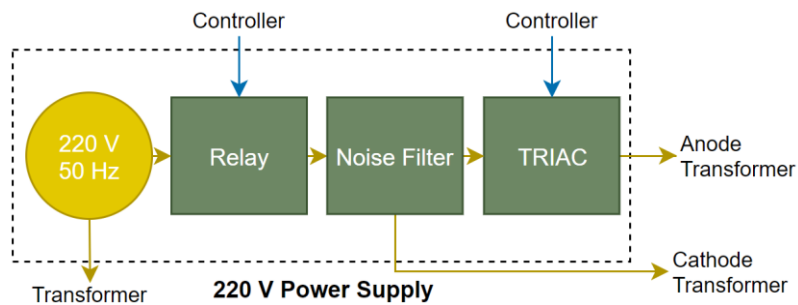
Figure 6.2: Schematic of the 220 V power supply.

The main function of the 220 V power supply was to power and control the magnetron power supply, which powered and controlled the magnetron. The schematic is repeated in Figure 6.2 and the 220 V power supply is shown in Figure 6.3.
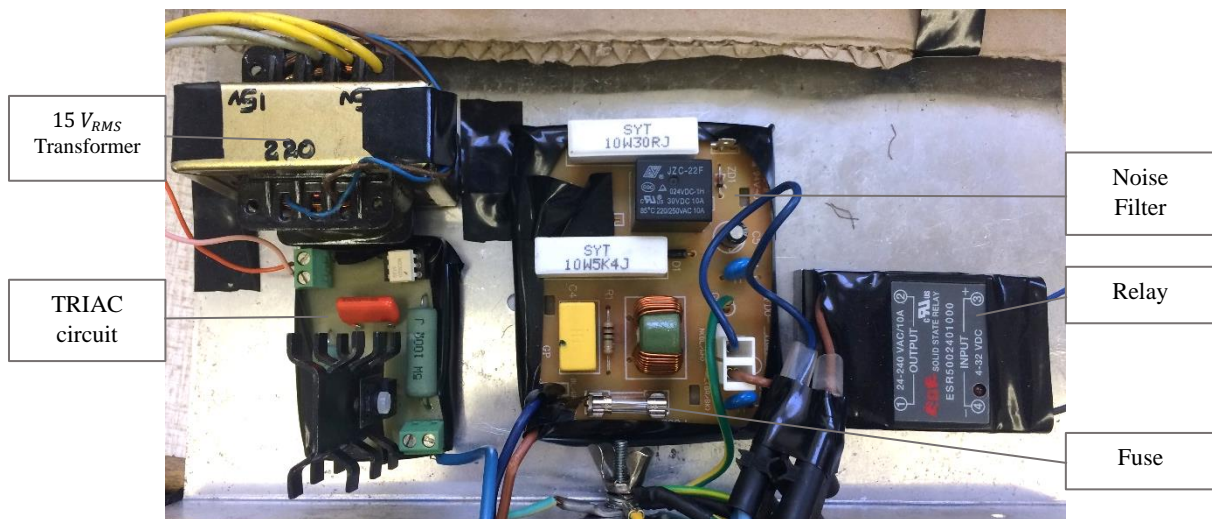
Figure 6.3: Components that made up the 220V power supply. The transformer shown was used in the DC power supply.

The power to the entire system was fed through an emergency stop push button (not shown). This was primarily for the safety of the user, but also to protect the system should anything have gone wrong.

A relay (EGE Solid State Relay) was toggled by the microcontroller to turn the magnetron supply circuitry on.

A noise filter, taken directly from a Defy DMO368 microwave oven, was used to supress any harmonics that the system may have added back onto the mains supply. It contained a fuse which protected the magnetron power supply.

In order to finely control the output power of the magnetron, a TRIAC circuit was used to limit the anode current that was supplied to the magnetron. The theoretical concept is explained in Sec. 2.2.5.4.

A Nexperia BT139X-800 TRIAC was used to switch the power to the anode transformer of the magnetron power supply. The circuit diagram for the circuit that controlled the TRIAC is shown in Figure 6.4.

An RC snubber circuit was used to prevent the TRIAC from switching spontaneously and to protect the TRIAC from high discharge voltages (since the transformer resembled an inductive load) [80]. The

snubber circuit consisted of a series connection of a $2.2\ k\Omega$ resistor and a $100\ nF$ capacitor, placed in parallel with the main terminals of the TRIAC.

The TRIAC was controlled with the microcontroller through a MOC3020 optically isolated TRIAC driver [2]. The TRIAC driver protected the microcontroller from the high voltages and currents that the TRIAC was switching. R_I_Limit limited the current through the TRIAC driver's LED. R_V_Limit lowered the voltage seen at the gate of the TRIAC ($V_{G\ MAX} = 5\ V$ [81]).
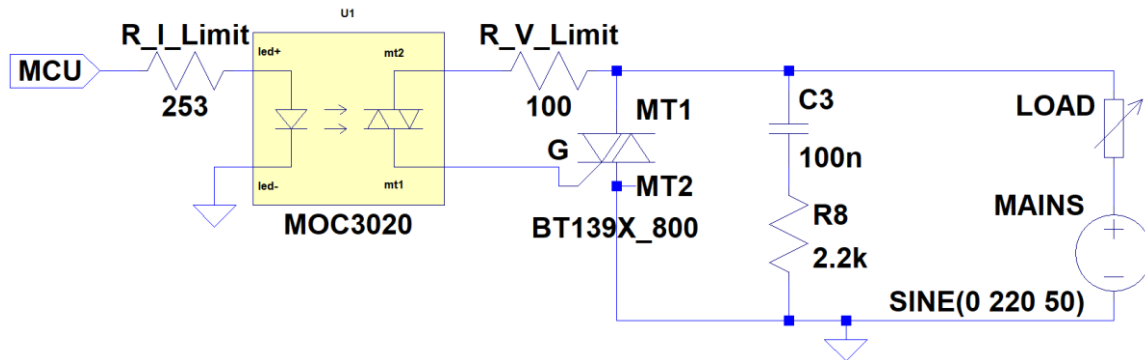
Figure 6.4: The TRIAC circuit with the TRIAC driver and the snubber.

6.2.3 Magnetron power supply
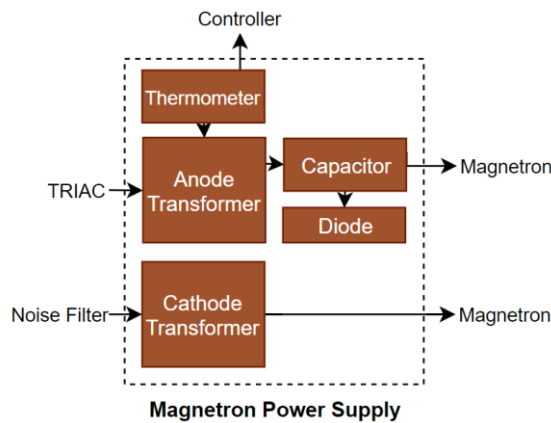
Figure 6.5: Schematic of the magnetron power supply.

The magnetron power supply received power from the 220 V power supply and powered the magnetron. The schematic is repeated in Figure 6.5 and the magnetron power supply is pictured in Figure 6.6. The magnetron power supply was constructed and previously used by van der Merwe [2].
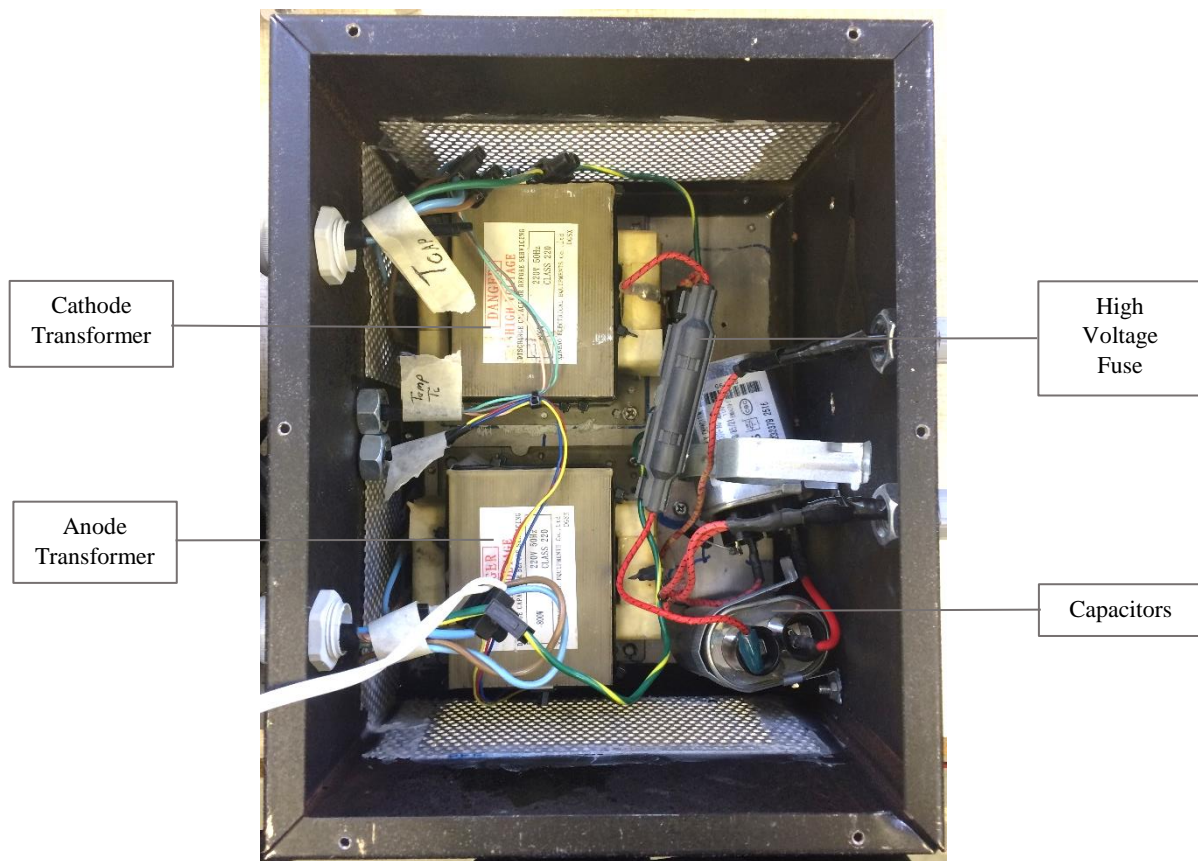
Figure 6.6: The magnetron power supply.

The entire magnetron power supply was contained in a metal box. This protected the user from the high voltages used to power the magnetron. The box also helped to channel air in order to cool down the transformers (the lid of the box contained a fan).

Different transformers were used to power the anode and the cathode of the magnetron. Since the cathode required time to heat up, the cathode may not have been able to heat up sufficiently if the transformer was switched on for only a short period using the TRIAC. Thus the cathode used its own transformer so that it was always heated up and ready to give off electrons as soon as a voltage was applied over the anode of the magnetron.

As described in 2.2.5.3, saturable reactor control was implemented here. The maximum output power of the magnetron was altered by changing the value of the capacitor. In practice, another capacitor (or more) was placed in series with the standard capacitor to decrease the equivalent capacitance, which decreased the maximum output power of the magnetron. A high voltage fuse was placed in series with the capacitors to protect the high voltage circuit.

Since the signal to the anode was switched by the TRIAC, it was no longer a perfect sinusoid. This meant that various harmonics were present. These harmonics caused the anode transformer to heat up faster than with a conventional microwave oven. As such, a thermometer (LM35) was attached to the side of the transformer. The microcontroller measured the temperature of the transformer and turned off the relay should the transformer temperature have exceeded $55\ °C$.

6.2.4 DC power supply
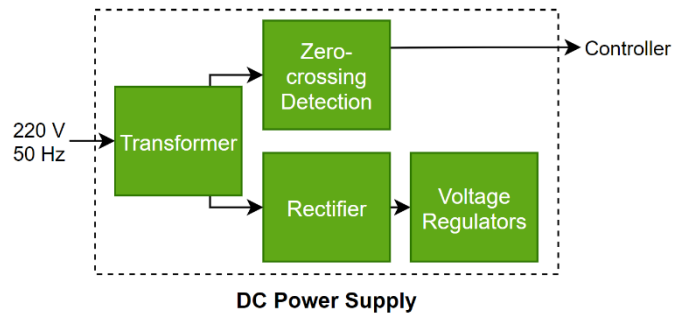
DC Power Supply

Figure 6.7: Schematic of the DC power supply.

As shown in Figure 6.7, the DC power supply consisted of a centre tapped transformer, DC rectification and regulation, and a zero-crossing circuit. Figure 6.8 and Figure 6.9 show the DC power supply. The transformer is pictured in Figure 6.3.
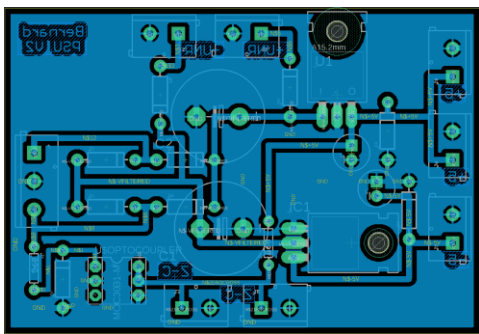
Figure 6.8: Eagle PCB layout for the DC power supply.
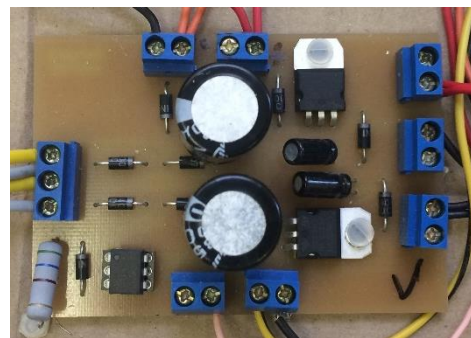
Figure 6.9: The DC power supply. Transformer not

6.2.4.1 Power supply

The DC power supply made use of a centre tapped transformer ($15\ V_{RMS}$) and two full wave rectifiers to provide a positive and negative DC supply. The output of the rectifiers were filtered by $1500\ \mu F$ capacitors. The positive and negative DC voltages were regulated using an LM7805 regulator and an LM7905 regulator to give outputs of $+5\ V$ and $-5\ V$ respectively. However, access to the unregulated power rails were implemented so that this power supply could power circuits that implemented their own voltage regulators.

6.2.4.2 Zero-crossing detector

The zero-crossing detector detected when the $50\ Hz$ power from the mains supply changed polarity. When the $50\ Hz$ supply was positive, a digital LOW ($0.7\ V$) signal was read by the microcontroller, and when it was negative, a HIGH ($5\ V$) was read.

A MOC8050 optoisolator (optical isolator) was used. Using an optoisolator protected the microcontroller from the relatively high voltages supplied by the transformer. The schematic for the zero-crossing detector can be seen in Figure 6.10.
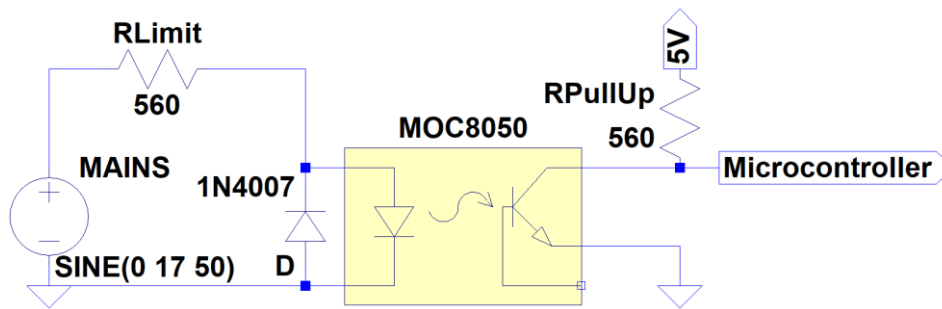
Figure 6.10: The zero-crossing detector circuit.

When enough current flowed through the optoisolator's LED, it caused the transistor to conduct. Therefore, when the $50\,Hz$ signal from the mains supply was positive, the LED conducted and caused the voltage at the output to be pulled down to $V_{ce} = 0.7\,V$. The maximum current that the LED could dissipate was $60\,mA$ [82]. Therefore the $RLimit = 560\,\Omega$ resistor was used to limit the current. $RPullUp = 560\,\Omega$ caused a voltage drop over itself so that the voltage at the microcontroller was equal to $V_{ce} = 0.7\,V$.

When the $50\,Hz$ signal was negative, the 1N4007 diode started to conduct. This prevented a high reverse voltage over the LED ($V_{R\,MAX} = 3\,V$ [82]). Therefore, the transistor did not conduct and thus the microcontroller read an output of $5\,V$.

The turn-on timing of the optoisolator was measured with an oscilloscope. This was important since the microcontroller had to compensate for any errors in the timing. The measurement is shown in Figure 6.11.
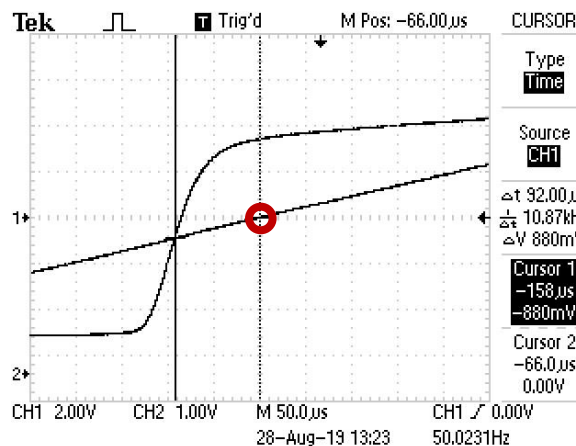
Figure 6.11: Turn-on timing of the zero-crossing circuit compared to the actual zero-crossing of the $50\,Hz$ signal. The zero-crossing point of the $50\,Hz$ signal is marked by a red circle.

When the $50\,Hz$ signal went from negative to positive, the zero-crossing circuit was turned on about $90\,\mu s$ too early.

6.2.5 Controller

An Arduino Leonardo was chosen as the microcontroller for this research project, as shown in Figure 6.12. It is described in more detail in Sec. 6.4.2. It was an affordable microprocessor that was easy to prototype with by using the Arduino software package.

The computer was used to send instructions to the Arduino, such as to turn the relay on, set the power level on the magnetron, to enable the control system and so forth. The Arduino sent back measured data and current settings.
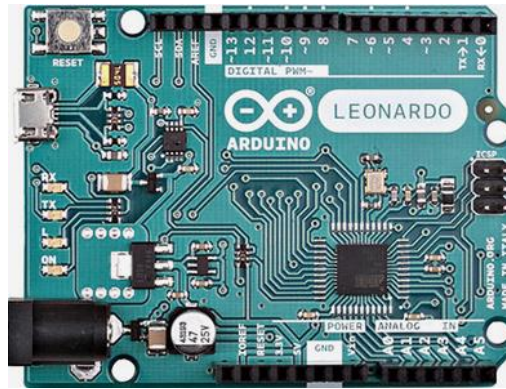
Figure 6.12: The Arduino Leonardo microcontroller [91].

6.2.6 Conclusion

Three different types of power supplies were used to operate the magnetron: the 220 V power supply, the magnetron power supply and the DC power supply with its zero-crossing detector. Together with a controller, the system was able to heat and control the temperature of a sample in the travelling applicator.

6.3 Temperature control

6.3.1 Introduction

This section discusses the control system that was implemented. It controlled the temperature of a sample of Rooibos tea leaves inside the travelling wave applicator. A proportional controller was used.

6.3.2 Transfer function
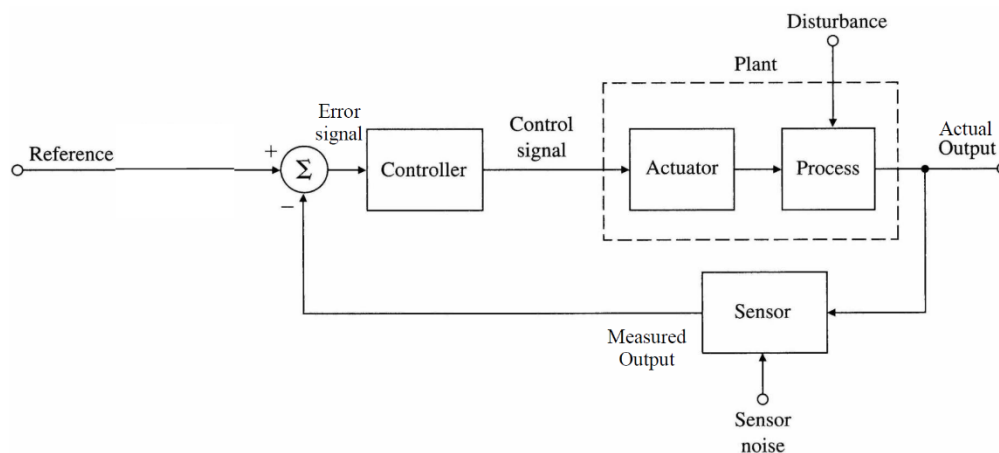
Figure 6.13: Block diagram of a control system [83, p. 25].

Figure 6.13 shows a block diagram of a basic control system. In the case of this research project, the controller was the Arduino Leonardo. The actuator was the TRIAC and the process was the magnetron radiating microwave power. The sensor was the infrared thermometer that measured the temperature of the Rooibos tea leaf sample.
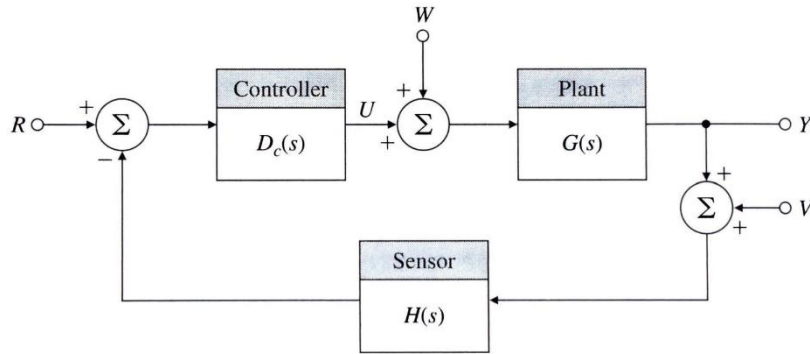
Figure 6.14: Block diagram of a basic control system, represented by Laplace functions [83, p. 256].

The block diagram in Figure 6.13 can also be represented by Laplace functions [83, p. 114]. This is shown in Figure 6.14. Using this diagram, and assuming $H(s) = 1$ and $V = W = 0$, the following transfer function can be derived [83, p. 255]:

$$\frac{Y(s)}{R(s)} = \frac{D_c(s)G(s)}{1 + D_c(s)G(s)} \tag{47}$$

Since a proportional controller was used in this design, the controller was simply

$$D_c(s) = K_p. \tag{48}$$

Therefore, the transfer function of the system was

$$\frac{Y(s)}{R(s)} = \frac{K_p G(s)}{1 + K_p G(s)} \tag{49}$$

6.3.3 System identification

In order to characterise the plant, the step response was measured (the red line in Figure 6.16).

The system followed an S-curve that was approximated by the following transfer function [83, p. 227]:

$$\frac{Y(s)}{U(s)} = \frac{Ae^{-st_d}}{\tau s + 1} \tag{50}$$

Figure 6.15 shows how the variables were determined. A was the maximum value of the step response, τ was the time constant and t_d was the time delay, or lag, of the system.
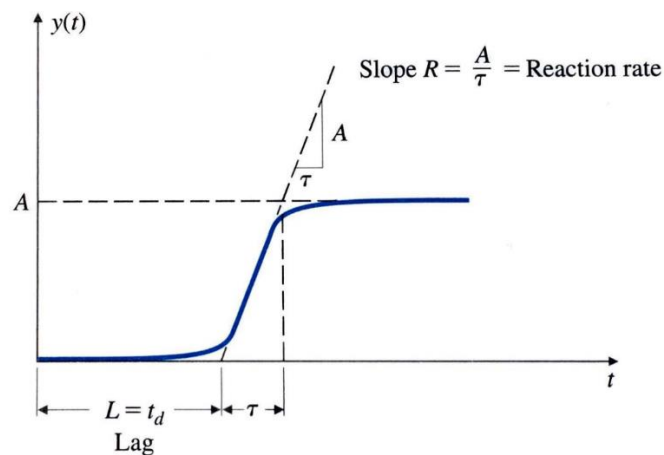
Figure 6.15: S-curve approximation for the step response [83, p. 227].

The infrared thermometer had a fast response time since it was contactless. It was also sampled very quickly – samples were taken every $10\ ms$. In addition, due to the nature of microwave heating, the

sample heated up almost immediately as soon as microwave power was applied. Due to all these factors, the time delay was considered as $t_d \approx 0$.

Thus the approximation of the step response became

$$\frac{Y(s)}{U(s)} = \frac{A}{\tau s + 1} \qquad (51)$$

The values for A and τ were determined using the concepts from Figure 6.15 and were then fine-tuned to match the approximated step response to the actual step response. Values of $A = 133$ and $\tau = 83.5$ were used. The approximated step response is shown in blue in Figure 6.16.
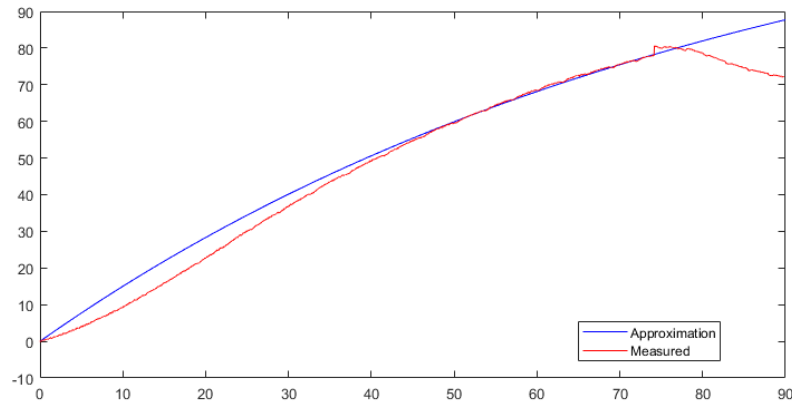
Figure 6.16: The measured and the approximated step response.

The approximation deviated at lower temperatures. This was not very important since all the temperature controlled tests required high temperatures.

6.3.4   Root locus design

At this point, MATLAB's root locus design tool was used to determine an appropriate gain. Due to the simplicity of the approximated step response, a very simple root locus was obtained with a single pole at the origin (Figure 6.17). The gain was chosen as $K_p = 100$. The step response is shown in Figure 6.18.
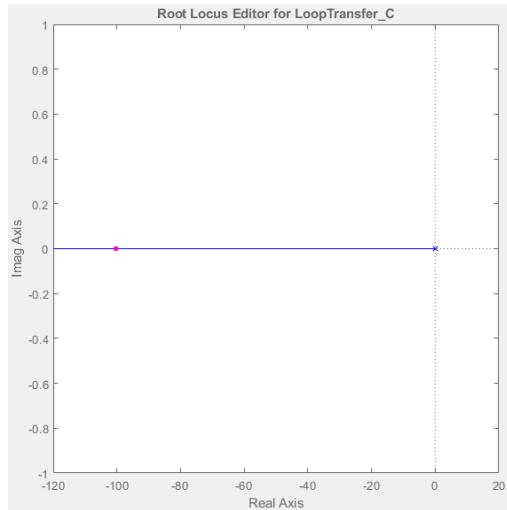
Figure 6.17: Root locus of the system.
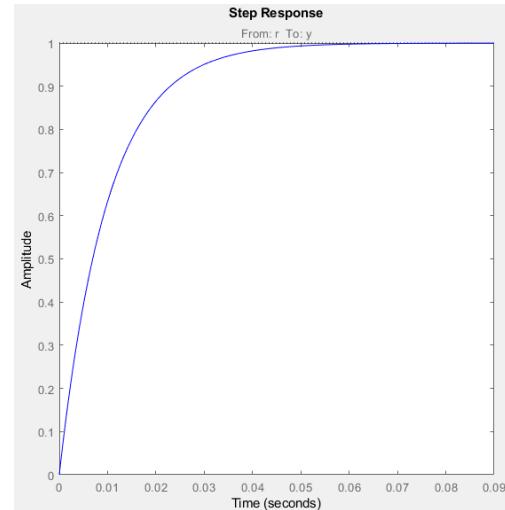
Figure 6.18: The simulated step response for the control system with a gain of $K_p = 100$.

6.3.5 Implementation

The control system was implemented using the microcontroller. The control system performed well at high temperatures. There was, however, an observed steady-state error of about $e_{ss} = 0.6\,°C$. The desired temperature was adjusted slightly to compensate for the steady-state error.

6.3.6 Conclusion

A proportional control system was implemented to control the temperature of a Rooibos tea leaf sample inside the travelling wave applicator. The control system was simple to design and worked well. It did, however, have a small steady state error. This was compensated for by manually adjusting the target temperature.

6.4 Microcontroller software

6.4.1 Introduction

In order to control the output power of the magnetron, a TRIAC was used to control the phase angle at which the supply voltage to the anode transformer was turned on. A microcontroller controlled when the TRIAC was to switch on. The switching of the TRIAC had to be synchronised with the incoming $50\,Hz$ supply. The algorithm used to control the phase angle of the TRIAC is discussed in this subsection.

The algorithm allowed the microcontroller the still perform other functions such as sampling the infrared thermometer, controlling the relay, receiving instructions from the computer and sending data to the computer.

6.4.2 Microcontroller functionality

The Arduino Leonardo that was used in this research project made use of an Atmel Atmega 32u4 processor. The processor ran at $16\,MHz$. The processor had two 16-bit timers, designated as Timer1 and Timer3 [76]. Timer3 was used to implement the timing of the TRIAC in order to avoid potential conflicts with libraries that may use Timer1.

Timer3 had three Output Compare Registers (OCR): OCRA, OCRB and OCRC. When the timer reached the value assigned to any of these registers, the OCR's associated interrupt was fired. For example, if Timer3 was equal to OCRA, then interrupt A would run.

The interrupts were useful for precise timing. It also allowed the microcontroller to perform other functions (such as sampling the temperature) while still controlling the timing of the TRIAC.

110

6.4.3 Algorithm for TRIAC control

Timer3 was set to increment at every 256 counts of the 16 MHz clock, which meant that each count on Timer3 was 16 μs long. Therefore, it took 625 counts of Timer3 for 10 ms to pass, which was the period of half a cycle of the 50 Hz signal.

The power value was given as percentage and was scaled to the 625 counts per half cycle.

The OCR registers were used as follows, with reference to Figure 6.19 (which is plotted for 50 % power):
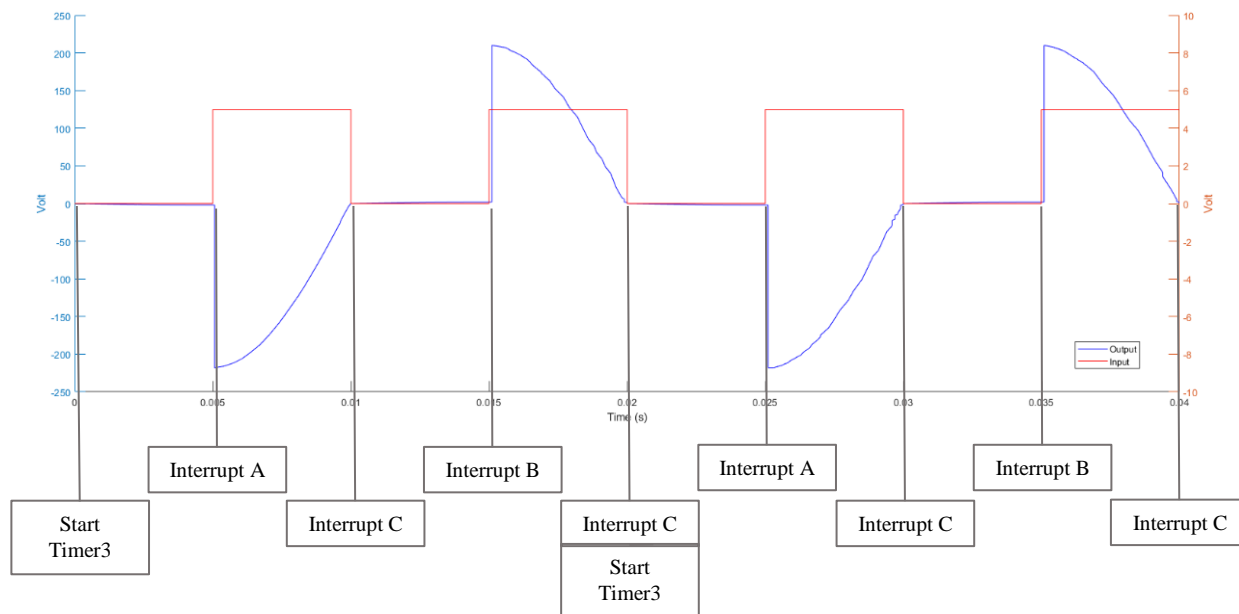
Figure 6.19: Timing diagram for the interrupts that controlled the TRIAC.

OCRA was set to the amount of time that needed to pass before the TRIAC was to turn on. In this case $OCRA = \frac{625}{2} = 312$. OCRB was set to the sum of one half cycle plus the time that needed to pass before the TRIAC was to turn on. In this case, $OCRB = 625 + \frac{625}{2} = 937$.

Timer3 was started when the microcontroller read a rising edge from the zero-crossing circuit. Once Timer3 reached the value for OCRA, interrupt A set the output HIGH and set OCRC to the value of OCRA plus the length of the pulse. Therefore, $OCRC = 625$. Interrupt C set the output LOW. Interrupt B set the output HIGH and set OCRC to the end of the second half cycle ($OCRC = 1250$). At OCRC, interrupt C set the output LOW again. At this point a rising edge was detected from the zero-crossing circuit and the cycle restarted.

The values for each OCR was fine-tuned to compensate for the timing error introduced by the zero-crossing circuit (see Figure 6.11).

6.4.4 Conclusion

The algorithm developed for the microcontroller effectively controlled the TRIAC. It synced the microcontroller with the 50 Hz input signal and was able to control the phase angle of the TRIAC. The algorithm also allowed the microcontroller to perform other functions such as reading the infrared thermometer and interfacing with the computer.

6.5 Chapter conclusion

This chapter discussed the system that was used to power and control the magnetron. The system used a proportional controller to control the temperature of a Rooibos tea leaf sample in the travelling wave applicator. The microcontroller used timers with interrupts to control the TRIAC.

The system worked well and was able to control the output power of the magnetron in order to heat a sample to a required temperature, and to maintain that temperature for a set period of time.

7 Microwave pasteurisation

7.1 Chapter summary

This chapter investigated whether microwave radiation was a viable alternative to steam pasteurisation of Rooibos tea leaves.

After introducing the chapter, the basic methodology for the tests is explained. Thereafter, each of the five tests are described.

Tests were conducted by inoculating rooibos tea leaves with two bacterial species, namely *Lactococcus lactis* (Tests 2 and 3) and *Escherichia coli* (Tests 1 and 4). Test 1 samples were treated in a conventional microwave oven. In test 2, samples were cooled down while being irradiated. Test 3 samples were processed in a travelling wave applicator at low and at high temperatures. In test 4 samples were processed at high temperatures with the travelling wave applicator. Test 5 was conducted on unsterilised Rooibos tea leaves in the travelling wave applicator at a high temperature.

The chapter then concludes and gives some recommendations.

7.2 Chapter introduction

Using microwave radiation to pasteurise Rooibos tea leaves possibly posed a major advantage over using steam: improved taste and quality of the final product. Unlike steam, using microwave radiation did not add moisture to the product. There was also a possibility that microwave radiation could pasteurise the product at a low temperature due to microwave specific effects.

Initial tests determined whether microwave radiation was able to eliminate bacteria in dry media. The low moisture content of dry media, such as Rooibos tea leaves, were of concern since microwave radiation is more effective at heating products with a high moisture content.

The next stage was to conduct tests at a low temperature in order to determine whether the microwave specific effects were significant. If they were, it would have meant that pasteurisation could have been performed at a lower temperature than what was used with steam.

The last stage was to conduct tests at high temperatures so that some sense of comparison could be draw with steam pasteurisation. Gram-positive and Gram-negative bacteria were tested. These tests established whether microwave radiation may be a suitable way of pasteurising Rooibos tea leaves.

7.3 Basic methodology

The tests all used a similar method of preparing, processing and doing post-processing on the samples in order to determine bacterial viability. The preparation and post-processing of the samples was done Dr ADP van Staden at the Department of Microbiology at Stellenbosch University.

With reference to Figure 7.1, the following steps were typically taken (although the order was sometimes altered and additional steps were taken):

1) Cells were grown the appropriate growth media supplemented with antibiotics*. Cells were allowed to grow at optimal temperature overnight. The overnight culture was centrifuged at $8\,000\ rpm$ for $10\ min$ and the cell pellet was suspended in 10% (wt/vol) skim milk solution.

2) The culture was combined with sterilised Rooibos tea leaves.

3) The mixture of leaves and culture was freeze dried. The samples were then placed in a suitable container for processing.

4) The samples were processed by microwave radiation or a water bath.

5) The processed samples were suspended in sterile saline (0.75 % NaCl) and serially diluted. The solution series was used to plate onto agar.

6) The plates were incubated at $37\ °C$ until the colonies were countable.

7) Colonies were counted and the amount of $CFU/m\ell$ or CFU/g was determined.

* Luria Bertani broth, supplemented with $50\ \mu g/m\ell$ kanamycin, was used for *E. coli* and M17, with $7.5\ \mu g/m\ell$ chloramphenicol, was used for *L. lactis*.
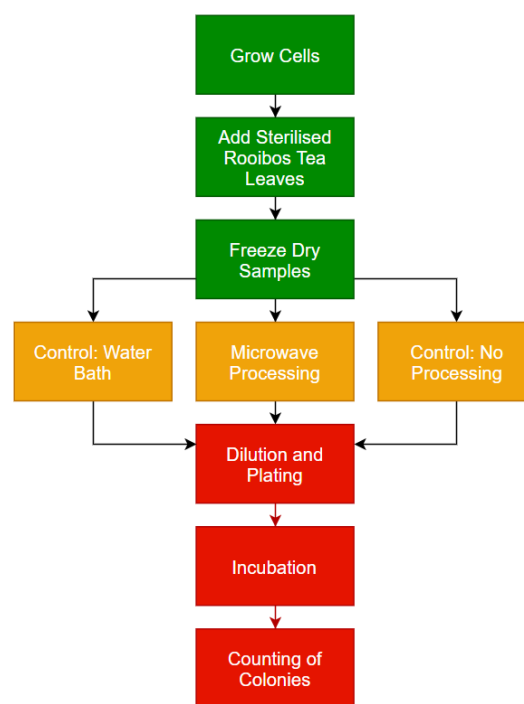
Figure 7.1: Block diagram of the typical steps taken in each test.

Figure 7.2: A mixture of Rooibos tea leaves and bacterial culture that was placed in a $2\ m\ell$ microcentrifuge tube for processing in the travelling wave applicator.
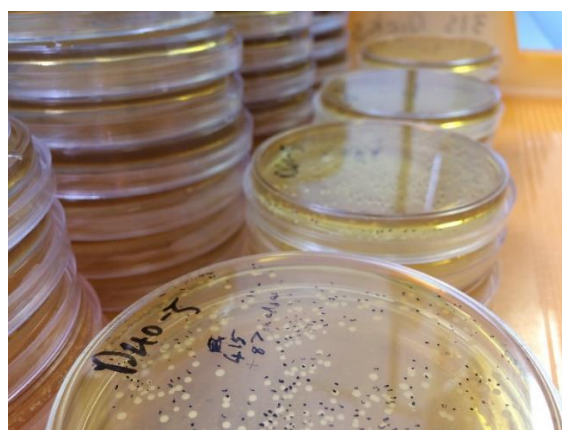
Figure 7.3: Post-incubation agar plates that have been counted.

114

7.4 Test 1: E.coli in a conventional microwave oven

7.4.1 Objectives

The first test that was conducted determined whether pasteurisation of dry media was possible by using microwave radiation. It also tested the heat distribution of a sample in a petri dish to determine whether it was a suitable applicator.

7.4.2 Hardware and bacterial setup

A probiotic strain of *E. coli* was suspended in a freeze dried sugar solution. The freeze dried sugar solution was placed into a petri dish and spread out.

The processing was done by irradiating samples for various time periods using a $700\,W$ conventional microwave oven (Defy DMO 368). The samples were placed in the centre of the turntable. The approximate temperature of the samples were taken after processing using a thermal camera (Fluke VT02).

7.4.3 Results

The results of the test are shown in Table 7.1 and Figure 7.4.

Test #	Weight of Sample (mg)	Method	Processing Time (m:ss)	Peak Temperature Observed ($°C$)	Colonies Count ($CFU/m\ell$)
1	200	Control	−	18.6	3.55×10^7
2	140	Microwave Oven	$0:15$	42.7	1.83×10^7
3	200	Microwave Oven	$0:30$	61.0^*	2.00×10^7
4	210	Microwave Oven	$0:45$	130.2^{**}	6.00×10^5
* Traces of caramelisation were present					
**Sample caramelised and then burnt due to thermal runaway					

Table 7.1: Results of test 1.
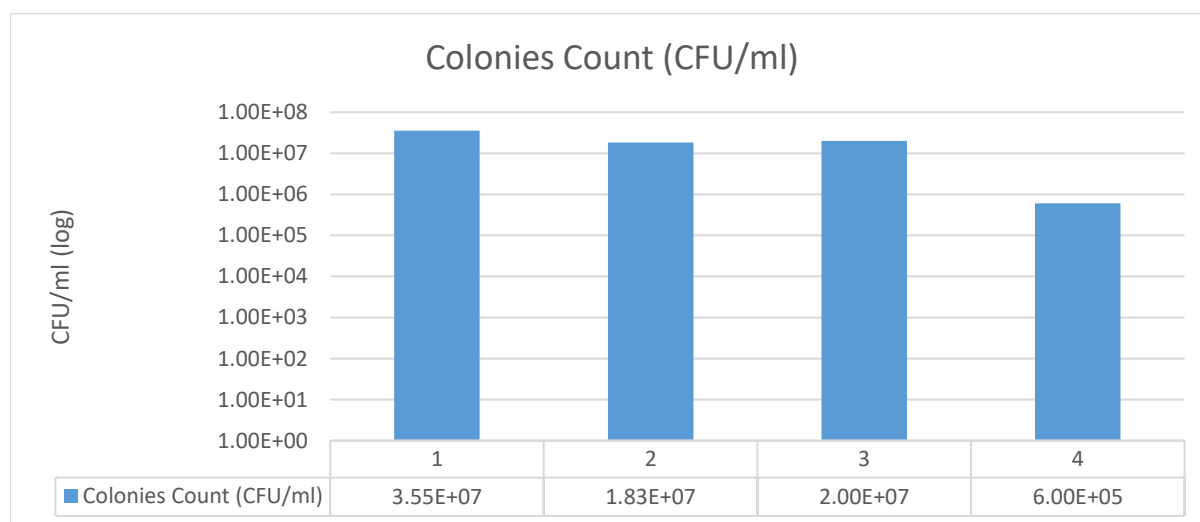
Figure 7.4: Results of test 1 shown in a bar graph.

Hotspots were observed using the thermal camera, as seen in Figure 7.5. This meant that the media did not heat up evenly. The high temperatures of thermal runaway can be seen in Figure 7.6.
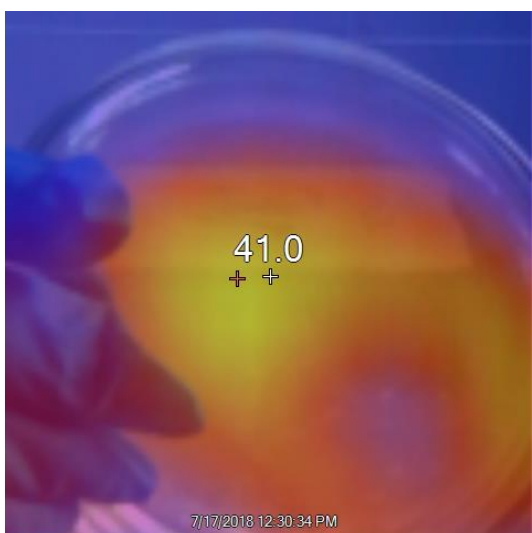
Figure 7.5: Hotspots were observed in the processed samples.
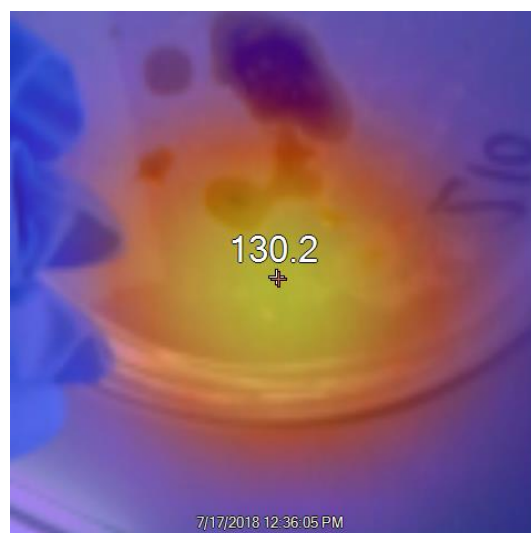
Figure 7.6: The dry media reached very high temperatures once caramelisation and thermal runaway occurred.

7.4.4 Conclusions

Test 1 was partially successful in proving that microwave radiation was able to reduce the amount of bacteria in dry media. However, using a sugar solution did not provide consistent results since thermal runaway effects were observed. Hotspots also occurred within the samples in the petri dishes.

7.4.5 Recommendations

A better applicator was required – and therefore the air-cooling applicator and the travelling wave applicator was developed (Ch. 5Microwave applicators). Further tests also used Rooibos tea leaves, in combination with freeze dried milk powder solutions, as the media.

7.5 Test 2: Air-cooled Rooibos with *L. lactis*

7.5.1 Objectives

This test determined whether microwave specific effects were sufficient to pasteurise Rooibos tea leaves at ambient temperatures.

7.5.2 Hardware and bacterial setup

Tests were done using a strain of *L. lactis* with an antibiotic marker (chloramphenicol). The antibiotic marker was present to eliminate other bacteria should accidental contamination have taken place. Bacteria were suspended in a milk powder solution ($10\% \; wt/vol$) and freeze dried. The freeze dried solution was mixed into samples of sterilised Rooibos tea.

The processing was done using the air-cooling applicator (Ch. 5.5). The applicator blew ambient air onto the sample while it was being irradiated. The air both cooled and mixed the sample. A mode stirrer was present inside the multi-mode cavity.

7.5.3 Results

A pilot test was done to investigate the capability of the system to reduce the amount of bacteria in rooibos tea. A sample with a volume of $5 \; m\ell$ was irradiated at full power ($700 \; W$) for $30 \; min$. A thermal image of the beaker after processing is shown in Figure 7.8. The leaves did not heat up significantly.

The control sample was also placed inside the applicator with air blown on it, but with the magnetron switched off. The results are indicated in the Table 7.2 and are plotted in Figure 7.7.

Test #	Power Level (W)	Processing Time (min)	Colonies Count ($CFU/m\ell$)
1	0 ($Control$)	30	5.5×10^6
2	700	30	1.2×10^7

Table 7.2: Results of test 2.
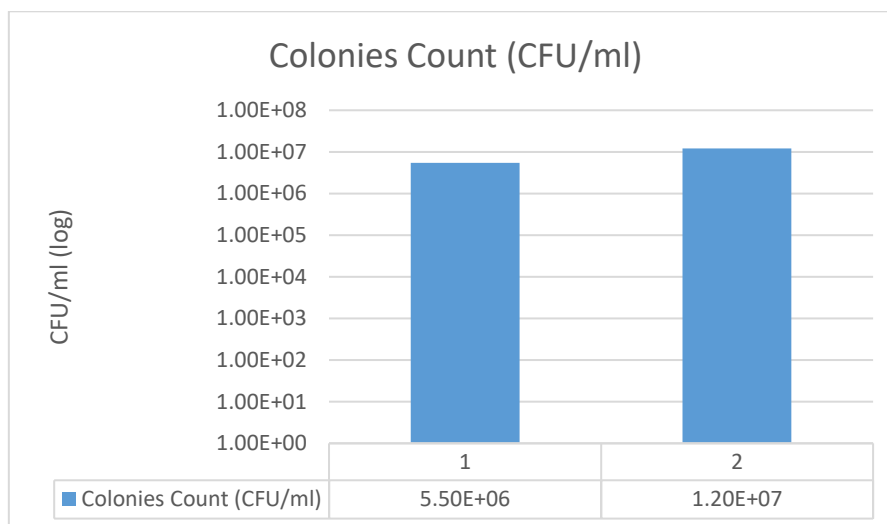
Figure 7.7: Results of test 2 shown in a bar graph.
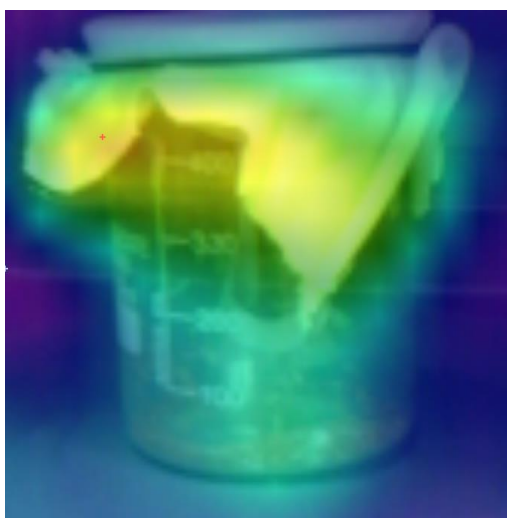
Figure 7.8: The thermal image of the beaker (taken after processing) shows that the part of the cloth that did not receive airflow heated up, but that everything else was cool.

7.5.4   Conclusions

More bacteria was present on the processed sample compared to the control sample. This may have been because the heat from the microwave radiation and the cooling effect of the air together raised the sample's temperature slightly so as to encourage bacterial growth.

Based on these observations it was hypothesized that pasteurisation using microwave radiation was based on a thermal effect and that microwave specific effects did not seem to damage bacteria at ambient temperatures.

7.5.5 Recommendations

The air-cooled applicator suggested that higher temperatures were required to pasteurise Rooibos tea leaves. Therefore the travelling wave applicator was used for the remainder of the tests so that the temperature of the samples could be monitored and controlled.

7.6 Test 3: Rooibos with *L. lactis* in the travelling wave applicator

7.6.1 Objectives

This test determined the effectiveness of pasteurising Rooibos tea leaves that were inoculated with Gram-positive *L. lactis* using the travelling wave applicator. A low temperature test was conducted to determine if a microwave specific effect had any impact on bacteria at a non-lethal temperature. A high temperature test was done to determine the killing efficiency of microwave radiation on Gram-positive bacteria.

7.6.2 Hardware and bacterial setup

As with the previous test, a strain of *L. lactis*, with an antibiotic marker, was used. As before, the bacteria were suspended in a freeze dried milk powder solution. The freeze dried solution was mixed into a samples of sterilised Rooibos tea.

The samples were transferred into $2\ m\ell$ microcentrifuge tubes and processed using the travelling wave applicator (Ch. 5.4). The travelling wave applicator heated the sample evenly. It made use of a control system to heat samples to a desired temperature for a desired length of time. The microwave control system was set up to be able to output a maximum of $400\ W$ of microwave power (see 6.2.3: Magnetron power supply).

7.6.3 Results

The low temperature samples were held at $37\ °C$, which is a non-lethal temperature for *L. lactis* [84]. Therefore no reduction in viable cells were expected. However, a small reduction was observed with the irradiated sample, and a small increase was observed with the water bath sample.

The high temperature tests produced a two- and four-fold reduction in $CFU/m\ell$ ($70\ °C$ and $100\ °C$, respectively). Even though the $100\ °C$ test was shorter, it had a greater reduction of bacteria than the $70\ °C$ test.

The test parameters and results are shown in Table 7.3 and the results are plotted in Figure 7.9.

Test #	Method	Target Temperature (°C)	Starting Temperature (°C)	Heat-up time (m:ss)	Time at Target (m:ss)	Colonies Count ($CFU/m\ell$)
1	Control	*Room*	23.0	−	−	1.8×10^6
2	Microwave	37	23.0	$0:57$	$10:01$	1.3×10^6
3	Water Bath	37	*Room*	$0:00$	$10:00$	2.2×10^6
4	Microwave	70	22.7	$1:37$	$10:00$	3.8×10^4
5	Microwave	100	23.0	$3:44$	$5:00$	4.4×10^2

Table 7.3: Results of test 3.
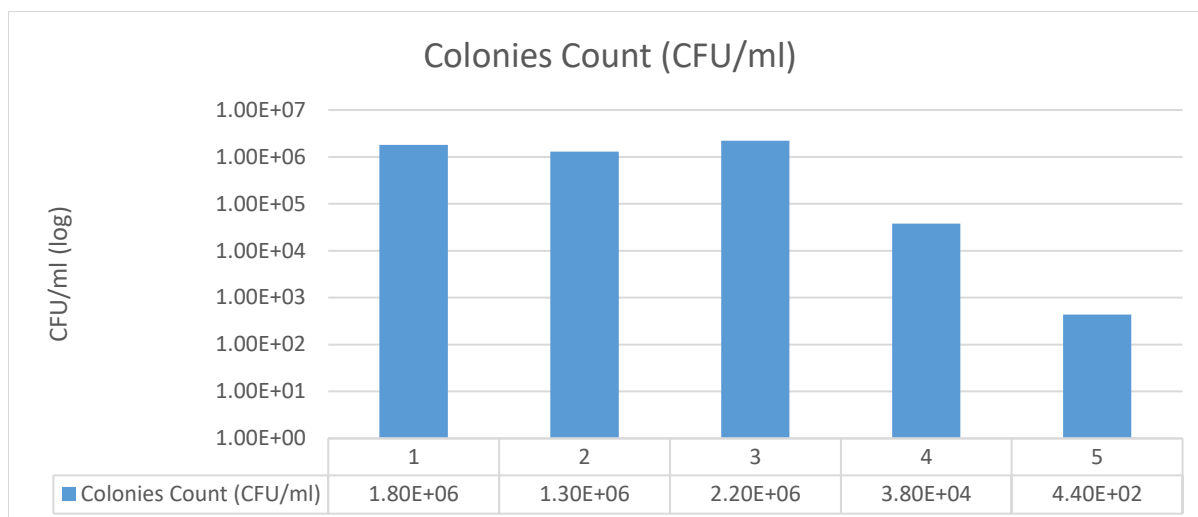
Figure 7.9: Results of test 3 shown in a bar graph.

7.6.4   Conclusions

The low temperature test indicated a small decrease in bacteria in comparison to the water bath and the control samples. However, the reduction was not significant. It may have been that a microwave specific effect caused the slight reduction. However, the effect was far too small to be considered a viable method to pasteurise Rooibos tea leaves with.

The high temperature tests indicated that a significant reduction of bacteria was obtained. This indicated great potential to use microwave radiation as an alternative pasteurisation method.

7.6.5   Recommendations

At this point, two tests had been conducted at low temperatures to establish that a microwave specific effect was unable pasteurise Rooibos tea leaves. Therefore, no further low temperature tests were conducted.

The high temperature tests showed great potential; however, *L. lactis* is not considered a source of contamination on Rooibos tea leaves. Two pathogens of concern that are found on Rooibos tea are *E. coli* and Salmonella. Both of these are Gram-negative and should be easier to eliminate than the Gram-positive *L. lactis*. A Gram-negative bacterium therefore needed to be tested.

7.7   Test 4: Rooibos with *E. coli* in the travelling wave applicator

7.7.1   Objective

This test determined the effectiveness of pasteurising Rooibos tea leaves that were inoculated with Gram-negative *E. coli*. *Escherichia coli* is a contaminant that is commonly found Rooibos tea. The test conditions were set up so that the processing was comparable to the steam processing that was used in industry ($\approx 90\,°C$ for $2{:}30\,min$) [85]. Samples were also weighed so that the amount of colonies could be compared to the microbiological safety standards for Rooibos tea in South Africa, which requires units of CFU/g. Since the results of this test were compared to the microbiological safety standards, the test was carried out in triplicate.

7.7.2   Hardware and bacterial setup

In this test, *E. coli* bacteria was used. It was suspended in a milk powder solution. After being suspended, it was mixed with sterile Rooibos tea leaves. The mixture was then freeze dried. Initial tests showed that there was too little moisture left in the leaves for it to heat up to the desired temperature in the microwave system. As such, sterile (autoclaved and not freeze dried) tea was added to the mixture in a 1:1 ratio. Samples were also weighed so that the results could be converted to CFU/g. These tests were carried out in triplicate.

Once again, $2\ m\ell$ microcentrifuge tubes were used and the samples were processed in the travelling wave applicator. Since the samples still had a lower moisture content compared to test 3, the maximum power of the microwave system was set to $700\ W$. Similar heat up times were thus achieved, despite lower moisture levels.

7.7.3 Results

To emulate the conditions of steam processing, a water bath sample was kept at $90\ °C$ for $2{:}30\ min$. The same time and temperature conditions were used with microwave test (#2). A $10{:}00\ min$ test was also conducted, should the $2{:}30\ min$ test have not eliminated all the bacteria.

The water bath test showed a two-fold reduction. Both microwave tests had no observable growth. The test parameters and results are shown in Table 7.4 and the results are plotted in Figure 7.10.

Test #	Method	Target Temperature ($°C$)	Starting Temperature ($°C$)	Average heat-up time (m:ss)	Time at Target (m:ss)	Colonies Count Mean ($CFU/m\ell$)	Colonies Count Mean (CFU/g)
1	Control	Room	−	−	−	1.6×10^4	6.4×10^4
2	Water Bath	90	Room	$0{:}00$	$2{:}30$	$< 3.0 \times 10^1$	$< 1.13 \times 10^2$
3	Microwave	90	26.2	$3{:}36$	$2{:}30$	0	0
4	Microwave	90	25.4	$2{:}54$	$10{:}00$	0	0

Table 7.4: Results of test 4.
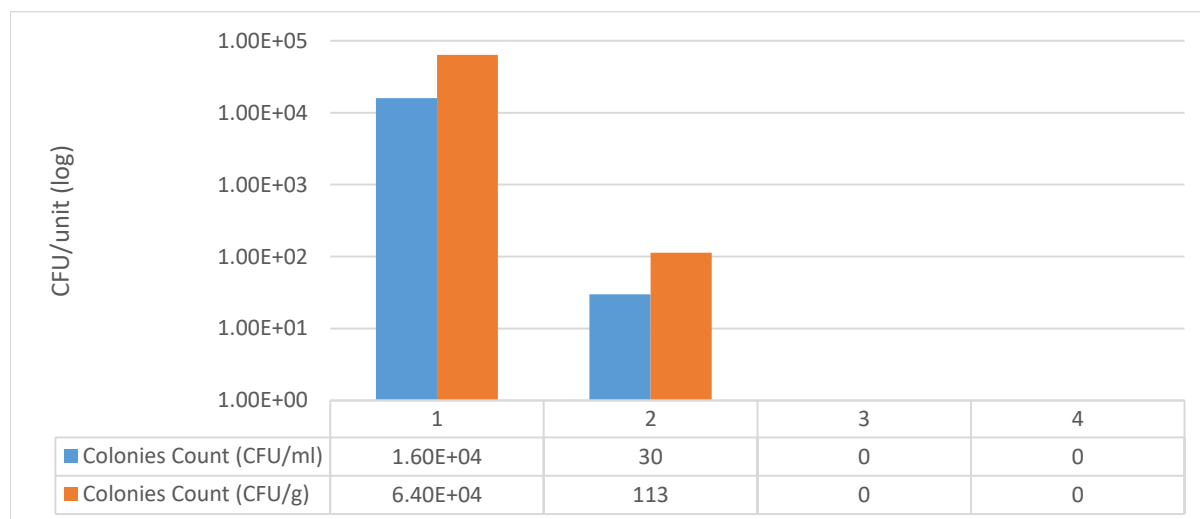
Figure 7.10: Results of test 4 shown in a bar graph.

7.7.4 Conclusions

Heating the samples to $90\ °C$ using microwave radiation was very effective – there was no observable *E. coli* growth at all. Using the water bath produced similar results, although not all of the cells were eliminated ($>$ 99.8 % reduction).

This test established that microwave radiation was a viable alternative to using steam to eliminate *E. coli* from Rooibos tea leaves. The results conformed to the microbiological safety standards for Rooibos tea in South Africa, where a maximum of $2.0 \times 10^1\ CFU/g$ of *E. coli* is permitted [85].

7.7.5 Recommendations

This test successfully showed that microwave radiation can be used as an alternative to steam, using similar processing times, to eliminate *E. coli*. However, there are many other types of bacteria that occur naturally on Rooibos tea leaves. Irradiating unsterilised Rooibos tea leaves needed to be tested.

7.8 Test 5: Unsterilised Rooibos in the travelling wave applicator

7.8.1 Objective and description

This test was to establish, qualitatively, how well microwave radiation pasteurises unsterilised (fermented but untreated) Rooibos tea leaves.

7.8.2 Hardware and bacterial setup

In this test, unsterilised Rooibos tea leaves were placed in a $2\,m\ell$ microcentrifuge tube and was processed in the travelling wave applicator. After processing, a sterile saline solution was added to the leaves. This was used to plate onto a Luria Bertani agar plate (i.e. it was not diluted further).

Similarly, sterile saline solution was also added to an unprocessed sample of Rooibos tea leaves and was plated onto an agar plate. The Rooibos tea leaves were taken directly from a Rooibos tea farm.

The plates were incubated at $37\,°C$ for several hours until sufficient growths were observable.

7.8.3 Results

The test parameters are shown in Table 7.5:

Test #	Method	Target Temperature ($°C$)	Starting Temperature ($°C$)	Heat-up time (m:ss)	Time at Target (m:ss)
1	Raw Control	*Room*	−	−	−
2	Raw Microwave	90	26.9	$2:50$	$10:00$

Table 7.5: Test parameters for test 5.

The growth on the agar plates are shown in Figure 7.11.

Figure 7.11: Post-incubation agar plates. The processed sample is shown on the left and the unprocessed sample is on the right.

7.8.4 Conclusions

Although there was a noteworthy decrease in growths with the sample that was irradiated, there were still growths present, even after being held at $90\,°C$ for 10 minutes. The type of bacteria was not identifiable from this test. It may, or may not, have been pathogenic.

7.8.5 Recommendations

Additional tests are required to identify which bacteria survived and how much bacteria survived the microwave treatment. A comparison with steam-treated Rooibos tea leaves may also be insightful.

7.9 Chapter conclusion

Test #	Bacteria	Applicator	Summarised result
1	*Escherichia coli*	Petri dish	Promising
2	*Lactococcus lactis*	Air-cooling applicator	Completely ineffective
3	*Lactococcus lactis*	Travelling wave applicator	Somewhat effective
4	*Escherichia coli*	Travelling wave applicator	Completely effective
5	*Lactococcus lactis*	Travelling wave applicator	Somewhat effective

Table 7.6: Simplified summary of tests.

This chapter showed that microwave radiation may be a viable way of pasteurising Rooibos tea leaves. A simplified summary of the tests is shown in Figure 7.6. The advantage of microwave pasteurisation is that no moisture is added to the product. Therefore a higher quality product is obtained.

Tests in this chapter showed that using microwave radiation at low temperatures was not a viable option. The microwave specific effect, if present, was not pronounced enough to significantly reduce the amount of bacteria.

High temperature tests on Gram-positive bacteria (*L. lactis*) showed up to a four-fold reduction in bacteria.

High temperature tests on Gram-negative bacteria (*E. coli*, which is commonly found on Rooibos tea leaves) totally eliminated the bacteria. This test was conducted using similar time and temperature conditions as with steam pasteurisation. The samples conformed to the microbiological standards enforced in South Africa.

7.10 Chapter recommendations

Further testing is recommended on unsterilised Rooibos tea. This would confirm whether microwave radiation is an appropriate way of pasteurising Rooibos tea leaves.

If these tests are successful, a better applicator will be required to scale up the system. An applicator that can process larger batches or that can do a continuous flow of tea leaves will be required.

8 Conclusion

8.1 Summary

This chapter reflects on the objectives stated in Ch. 1. It discusses how each of the objectives were achieved.

8.2 Objective 1: Microwave pasteurisation hardware

In fulfilment of objective 1, this research project developed a system that was able to investigate the use of microwave radiation to pasteurise Rooibos tea leaves.

The output power of the magnetron was controlled with two methods: TRIAC control and saturable reactor control. TRIAC control was a dynamic control method that changed the phase angle of the voltage that supplied power to the magnetron transformer. This controlled the anode current, which controlled the output power of the magnetron. Saturable reactor control was a static control method in which the maximum power was set by changing the value of the high voltage capacitor.

An applicator was developed that cooled the Rooibos tea leaves with ambient air while the tea was being irradiated (the air-cooling applicator). Air was blown onto a Rooibos tea leaf sample which both cooled and mixed the sample. A mode stirrer was developed and installed into the multi-mode cavity that was used in order to create an even distribution of microwave power.

A second applicator was developed that used a travelling wave inside a waveguide to heat up a sample of Rooibos tea leaves. The electric field pattern was well defined inside the waveguide and therefore the sample was placed such that it heated evenly. An infrared thermometer was used to record the temperature of the sample. The temperature readings were used to develop a control system that was able to heat samples to a desired temperature.

8.3 Objective 2: Pasteurisation using microwave radiation

It was tested whether microwave radiation was a viable method of pasteurising Rooibos tea leaves. Sterile Rooibos tea leaves were inoculated with bacteria and were processed in the travelling wave applicator. Gram-positive bacteria (*L. lactis*) were reduced four-fold, but not eliminated, when it was irradiated for 5 minutes at a temperature of $100\,°C$. All Gram-negative bacteria (*E. coli*), however, were eliminated after being irradiated for 2.5 minutes at $90\,°C$. This was the same time and temperature profile that industrial steam processing uses and therefore made the results directly comparable. These tests showed that microwave radiation may be a better way of pasteurising Rooibos tea leaves when compared to steam pasteurisation.

It was also tested whether there was a significant microwave specific effect present that was able to pasteurise Rooibos tea leaves at ambient temperatures. Sterile Rooibos tea leaves were inoculated with *L. lactis* and were tested at low temperatures in both the air-cooling applicator and the travelling wave applicator. The tests in the air-cooling applicator indicated an increase in bacteria. The tests in the travelling wave applicator showed a slight decrease in bacteria, but the decrease was not a noteworthy amount. It was concluded that the microwave specific effect was insignificant at low temperatures and was not able to pasteurise Rooibos tea leaves.

8.4 Objective 3: Electro Heating Group hardware

Hardware was developed that may assist the future development of microwave systems in the Electro Heating Group. An innovative waveguide directional coupler was developed. It operated over the microwave oven frequencies of $2.4 - 2.5\,GHz$, where it had a directivity greater than $20\,dB$ and a constant coupling of $35\,dB$. A prototype for a thermistor-based microwave power detector was also developed. It produced an output that was linearly proportional to the input power.

The project achieved its stated aims. It showed that microwave pasteurisation of Rooibos tea leaves may be viable and the associated hardware was successfully developed.

9 Recommendations

This chapter discusses some recommendations for the different sections of this project. It follows the same order of the objectives discussed in Ch. 8.

9.1 Objective 1: Microwave pasteurisation hardware

The TRIAC control used to control the output power of the magnetron worked well. However, the anode transformer heated up significantly. A different transformer can be investigated that can handle the high currents and harmonics better.

The travelling wave applicator was a good applicator for lab tests. However, it could only process very small batches at a time and was not suitable for a commercial application. A new travelling wave applicator can be developed that uses a conveyor belt to function as a continuous processing plant.

9.2 Objective 2: Pasteurisation using microwave radiation

The tests on Rooibos tea leaves revealed that microwave radiation may be a viable alternative pasteurisation method. The tests were done with Rooibos tea leaves that were sterilised and then inoculated with bacteria. The next stage of tests should test the pasteurisation of unsterilised Rooibos tea leaves. These tests should also be compared with a sample that was pasteurised with steam at a commercial processing plant.

9.3 Objective 3: Electro Heating Group hardware

The directional coupler worked well over the required frequency range. It can be made more robust and compact by removing the SMA connectors between the waveguide with pins and the branch-line hybrid. The frequency range may be improved by using wider pins and by using a multi-section branch-line hybrid. The branch-line hybrid can be redesigned using stripline so that it would be less susceptible to interference.

The prototype power detector proved that the design works. The next step in the development is to use thermistors that function well at high frequencies. The thermistor mount should also be redeveloped into a temperature-controlled enclosure. This would remove the impact of ambient temperature fluctuations.

Appendix A   Calculations

A.1   Double voltage seen across quadrupled resistor

The double voltage mentioned in Ch. 4.6.1 is explained as follows. Consider a resistor with a resistance of R, compared to a resistance of value $4R$, as shown in Figure A.1.
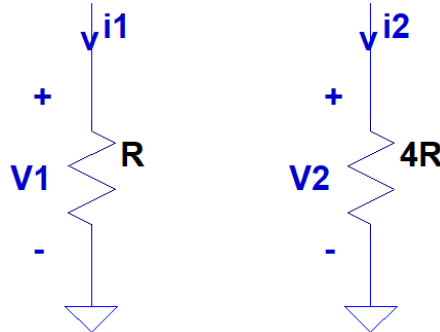
Figure A.1: Circuit schematic for two resistors that receive the same amount of power.

The power dissipated in a resistor is described by $= \frac{V^2}{R}$. Now, if the same amount of power was dissipated into each thermistor, we have

$$P = \frac{V_1^2}{R} \ and \ P = \frac{V_2^2}{4R} \tag{52}$$

Equating these two equations and deriving:

$$\frac{V_1^2}{R} = \frac{V_2^2}{4R} \tag{53}$$

$$V_2 = 2V_1 \tag{54}$$

Therefore double the voltage was required to bias the series thermistors compared to a single thermistor.

In addition, half the amount of current was required. This is evident when it was considered that the equation for power could also be written as $P = VI$. If, for the same amount of power, double the voltage was required, then half the amount of current was required.

Appendix B Transitions

B.1 Introduction

Figure B.1: Microstrip bend and coaxial to microstrip transitions are discussed in this subsection.

This subsection discusses several transitions that were particularly relevant to the branch-line hybrid. Figure B.1 shows how App. B fits in with the Ch. 3.
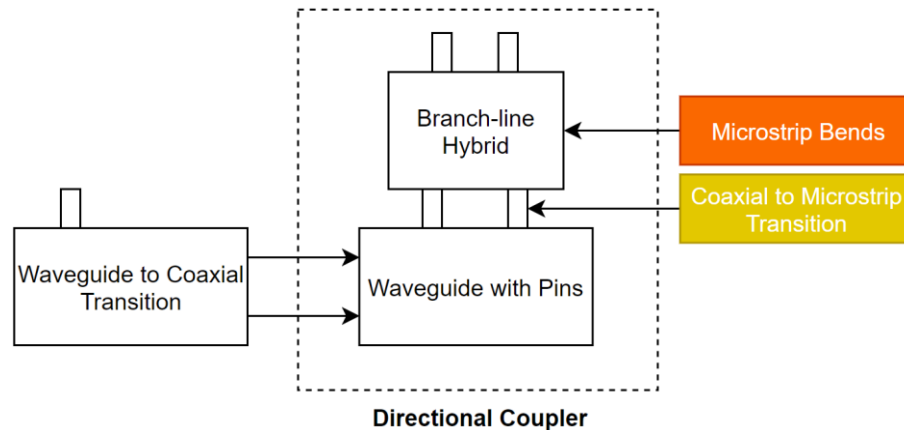
B.2 Microstrip Bends

Since the input ports of the branch line hybrid had to fit the exact dimensions of the waveguide with pins, the distance between the input ports into the branch line hybrid had to be widened. To shift the input ports, the input lines required some bends in their lines. Microstrip bends can introduce various errors and mismatches since the sharp corners can introduce a parasitic reactance [7, p. 209].

Several common microstrip bends were simulated in CST. The models are shown in Figure B.2. Results are shown in Table B.1, Figure B.3 and Figure B.4.
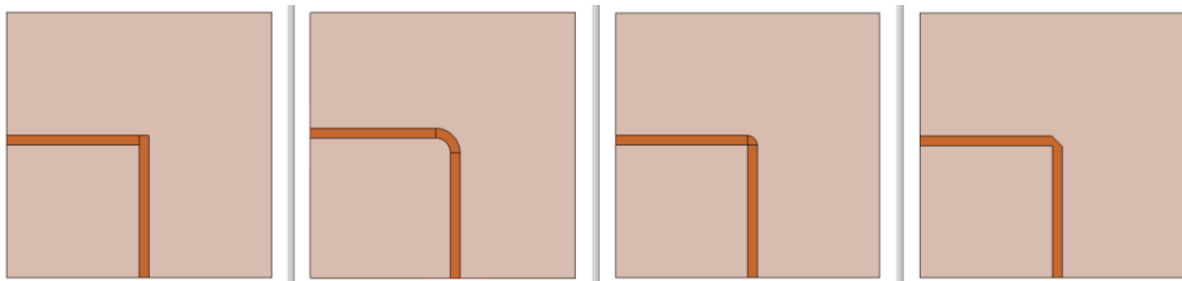
Figure B.2: Different microstrip bends that were simulated. From left to right: 1) Square 2) Curve 3) Rounded 4) Mitred.

Frequency	Square	Curve	Rounded	Mitred
2.45 GHz	$-18.01\ dB$	$-24.08\ dB$	$-20.36\ dB$	$-29.18\ dB$

Table B.1: Magnitude of S11 for different microstrip bends.
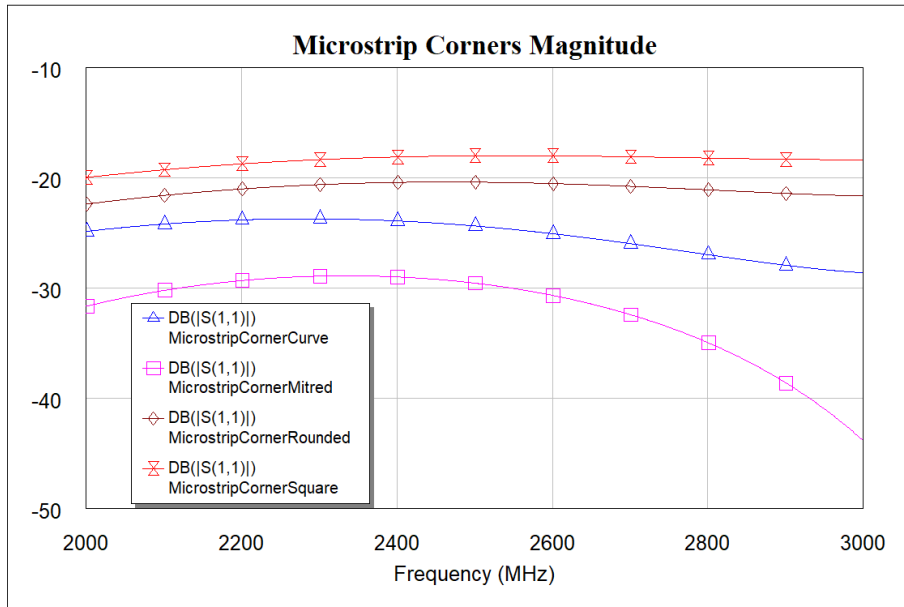
Figure B.3: Magnitude of S_{11} for different microstrip bends.
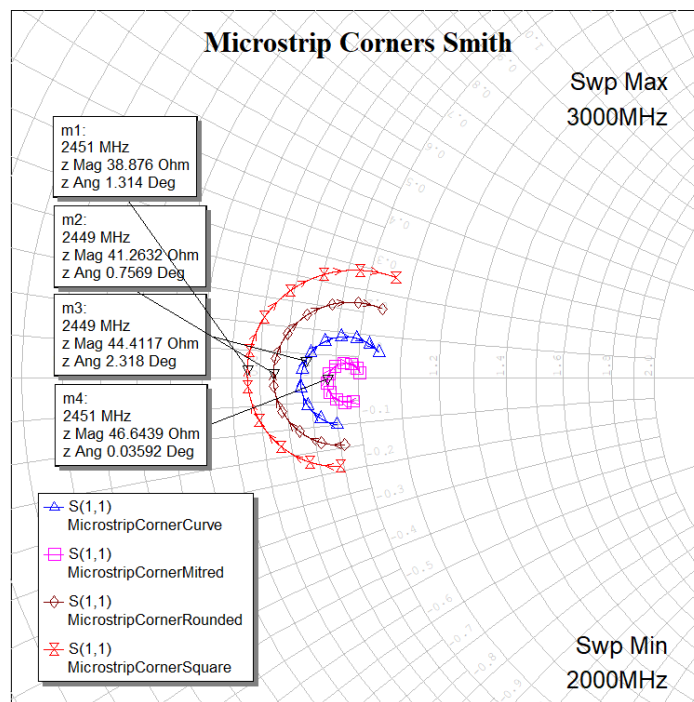
Figure B.4: A Smith chart plot of S_{11} of different microstrip bends.

The mitred bend was clearly the best bend with an improvement of $11.17\ dB$ over the worst bend, the square bend. As such, the branch-line hybrid was constructed using mitred bends.

B.3   Coaxial to Microstrip Transition

The directional coupler was designed using modular pieces. In order to measure each piece separately, a standard coaxial interface was used. The SubMiniature version A (SMA) standard interface was chosen because of its availability and its small form factor.

For accurate measurements, the reflection coefficient (S_{11}) of the transitions had to be minimal ($< -20\ dB$).

Two ways of interfacing between an SMA line and a microstrip line are discussed: a bottom-feed transition and an edge-connected transition.

B.4 Bottom-Feed Coaxial (SMA) to Microstrip Transition

The most practical way of connecting the branch-line hybrid to the waveguide with pins was by using a bottom-feed coaxial to microstrip transition. In order for a good impedance match to be achieved, the insertion point had to be carefully selected. This insertion point was determined using parameter sweeps in a full 3D simulation in CST. The simulation model is presented in Figure B.5.
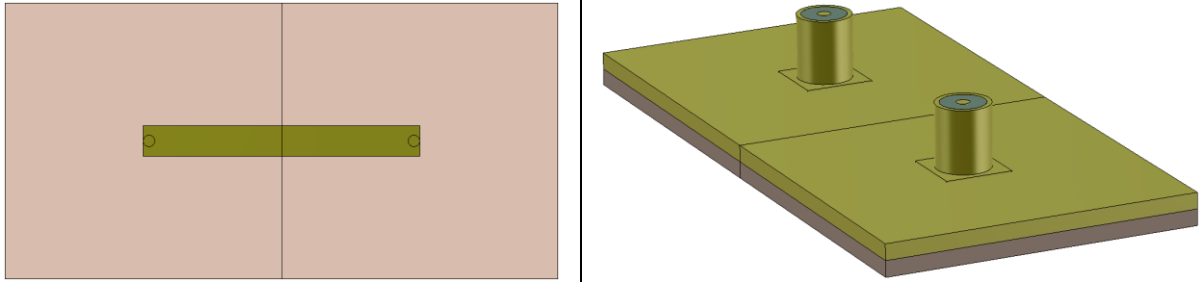
Figure B.5: Top view and bottom-side perspective view of the CST model of the bottom-feed coaxial to microstrip transitions.

The model was built and then measured up using a VNA (N5242A PNA-X Microwave Network Analyzer). Figure B.6 shows the physical build. 3D simulation versus measured results can be seen in Figure B.7.
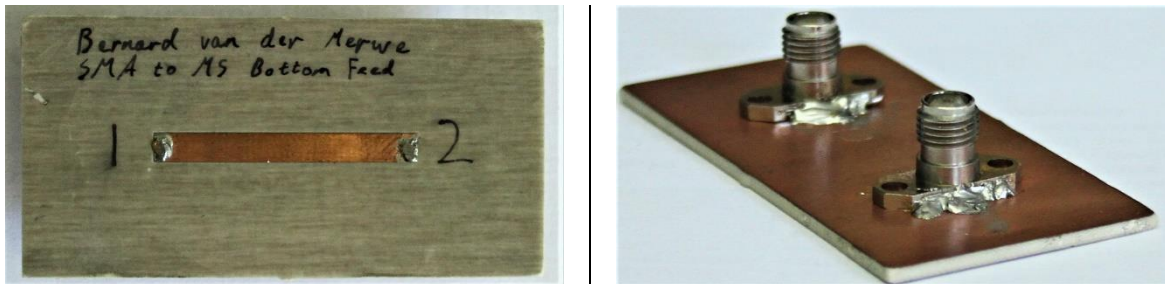
Figure B.6: Top view and bottom-side perspective view of the constructed bottom-feed coaxial to microstrip transitions.
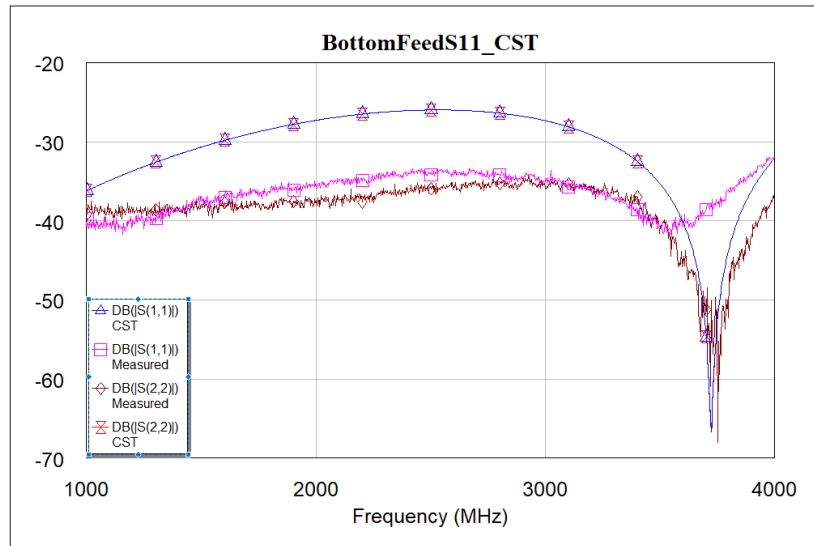
Figure B.7: Comparison of S_{11} and S_{22} between the 3D simulation and the measured data for a bottom-feed SMA to microstrip transition.

The input reflection coefficients, S_{11} and S_{22}, were meant to be equal, since this was a passive device. However, the difference in the measured S_{11} and S_{22} was due to the microstrip bending from the mechanical stress of the measuring cables. Nonetheless, the results were pleasing. Between 2 and 3 GHz an improvement of more than 10 dB was seen over the simulation.

In order to determine the S-parameters of a single coaxial to microstrip transition, the measured results had to be de-embedded. Using AWR, an equivalent circuit model of the two transitions, with a length of microstrip between them, was set up [86]. See Figure B.9. The reference planes were defined as shown in Figure B.8 [7, p. 193]. The two transitions were assumed to be identical.
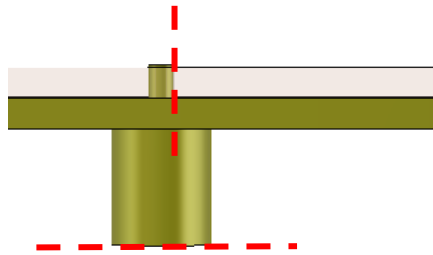
Figure B.8: Reference planes used in de-embedding the bottom-feed SMA to microstrip transition.

130
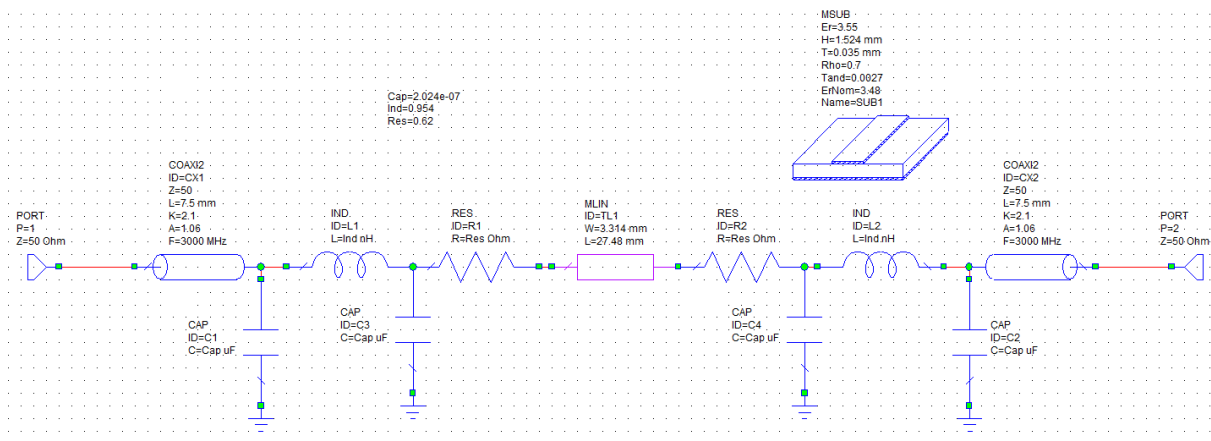
Figure B.9: AWR schematic showing the equivalent circuit models for the bottom-feed SMA to microstrip transitions, with a section of microstrip line in between.

The values of the circuit components were fine tuned to match the measured results. The circuit model of only one connector was extracted and its S-parameters was determined.

Figure B.10 and Figure B.11 shows a comparison of S-parameters between the measured results, the model that matches the simulation and the extraction of a single transition.
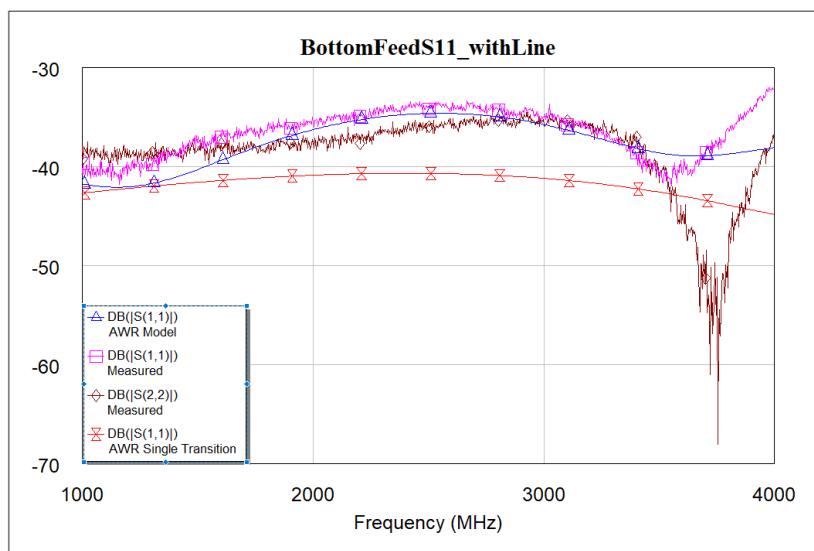
Figure B.10: Comparison of S_{11} between measured results, the AWR model that matches the simulation and the extraction of a single transition for a bottom-feed SMA to microstrip transition.

131
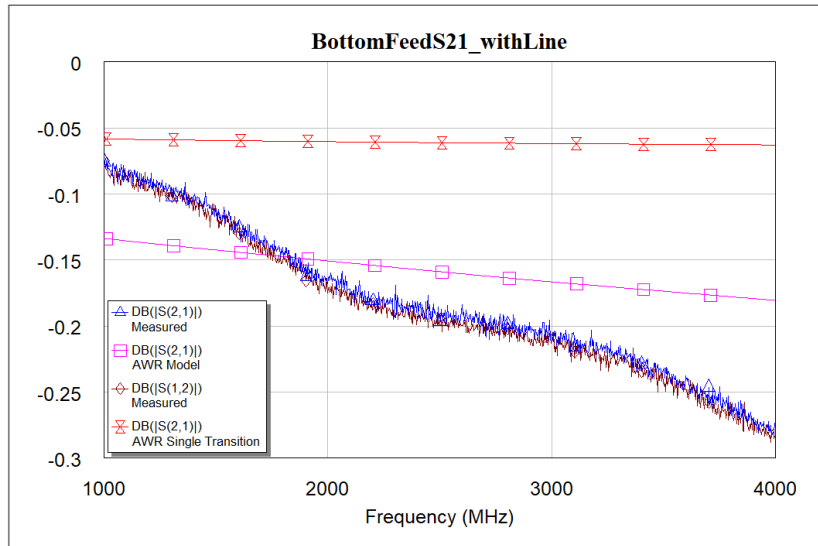
Figure B.11: Comparison of S_{21} between measured results, the AWR model that matches the simulation and the extraction of a single transition for a bottom-feed SMA to microstrip transition.

The extracted parameters showed an S_{11} of smaller than $-40\ dBm$ between 1 and $4\ GHz$. This was a very good transition and confirmed that the insertion point was well selected.

B.5 Edge-Connected Coaxial to Microstrip Transition

The microstrip line was wide relative to the size of the connector centre pin. This caused capacitive effects to appear from the legs of the connector to the microstrip line (Figure B.12). Capacitive effects were also observed between the base plate of the connector and the microstrip line (Figure B.13). There was also a discontinuity where the coaxial line met the microstrip line. To reduce these capacitive effects and to smoothen the discontinuity, removing the 'legs' of the connector and tapering the end of the microstrip line were investigated.
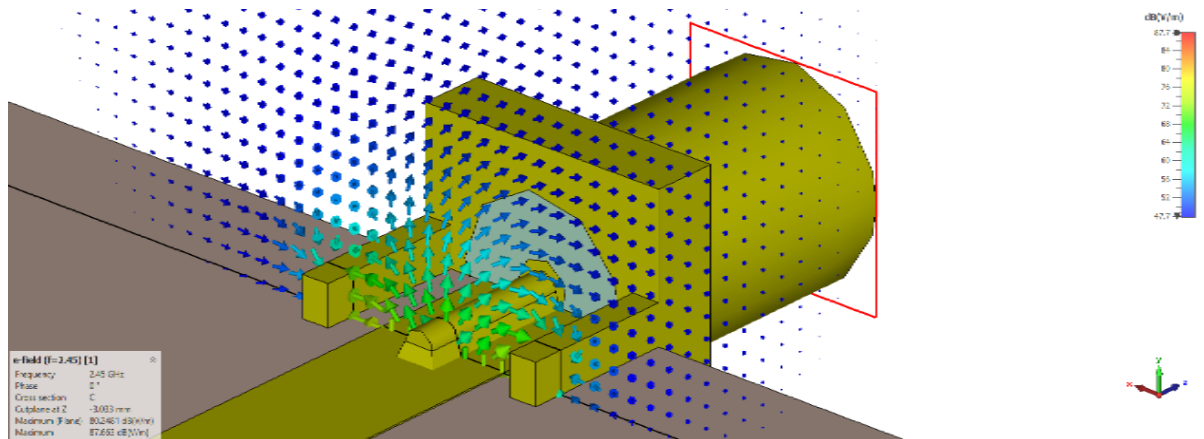
Figure B.12: The cross section of the E-field shows the capacitive effects between the microstrip line and the SMA connector's legs.
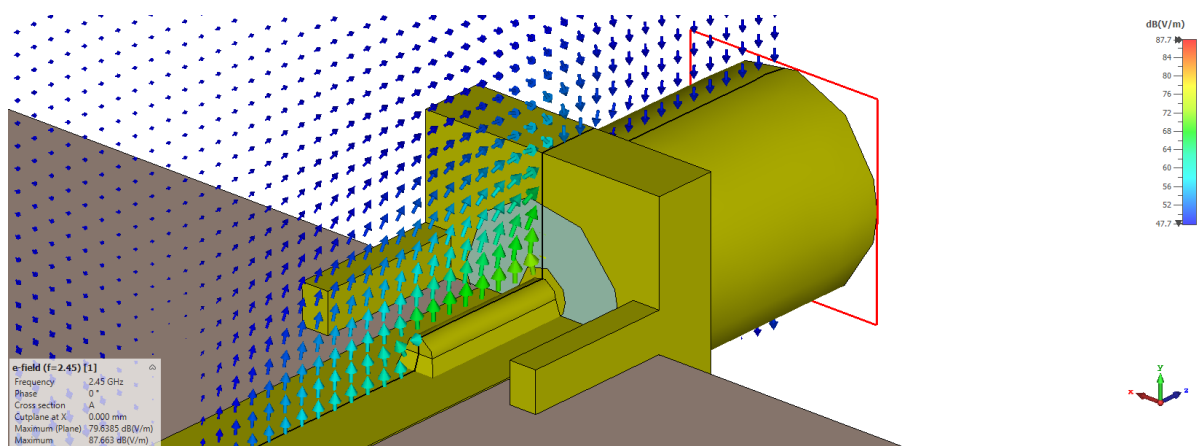
Figure B.13: The cross section of the E-field shows the capacitive effects between the microstrip line and the SMA connector's base plate.

The tests were done by simulating the transition in CST. The model is shown in Figure B.14. Rogers 4003C substrate, with a thickness of $1.52\ mm$, was used, and a perfect electrical conductor was assumed for all metallic parts. The dielectric was made of Teflon. The optimal dimensions of the tapers were determined through simulation runs and are shown in Figure B.15 and Figure B.16. The final results are shown in Table B.2 and Figure B.17.
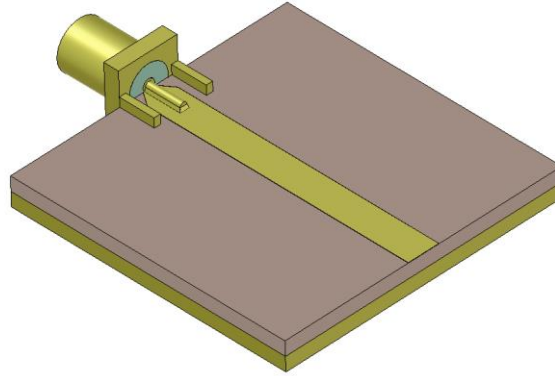
Figure B.14: Simulation model of the SMA to microstrip transition (shown here with connector legs intact and a taper at the end of the microstrip line).
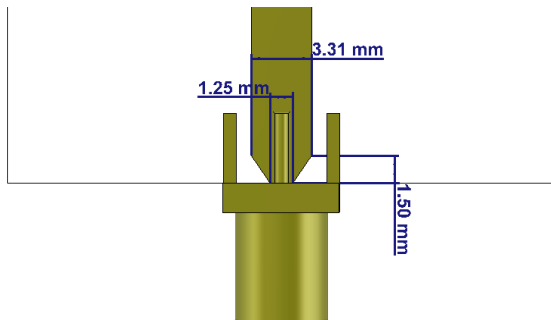
Figure B.15: Optimal taper dimensions for a SMA to microstrip line where the connector has legs on the top side of the board.
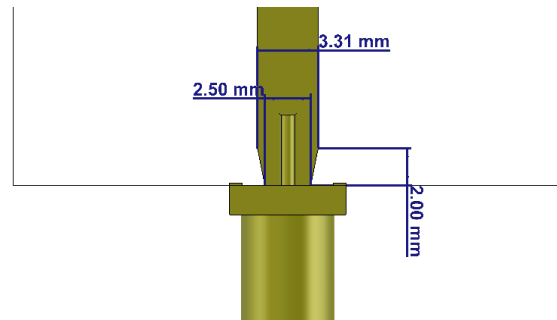
Figure B.16: Optimal taper dimensions for a SMA to microstrip line where the connector does not have legs on the top side of the board.

#	Connector with:	$|S_{11}|$ at $2\ GHz\ (dB)$	$|S_{11}|$ at $2.45\ GHz\ (dB)$	$|S_{11}|$ at $3\ GHz\ (dB)$
1	Legs, No Taper	-27.63	-26.52	-25.74
2	Legs, Optimal Taper	-32.43	-34.46	-35.33
3	No Legs, No Taper	-31.74	-32.29	-33.48
4	No Legs, Optimal Taper	-34.72	-37.89	-35.98

Table B.2: Comparison between different configurations of an SMA to microstrip transition.

For the simplest case, where the legs of the connector were present and with no taper, an S_{11} of $-26.52\ dB$ was found (at $2.45\ GHz$). This was smaller than $-20\ dB$, which was sufficient. However, a better match could still have been obtained.

With the second case, with the legs present and an optimised taper added to the end of the microstrip line, an S_{11} of $-34.46\ dB$ was found ($2.45\ GHz$). This was significantly better – an improvement of $7.94\ dB$ over the simplest case.

The third case had no taper and the legs of the connector were removed. An S_{11} of $-32.29\ dB$ was determined at $2.45\ GHz$. This is still a lot better than the case with legs and no taper (difference of $5.77\ dB$). So a better transition could have been made with little additional effort simply by not having the legs of the connector on the top of the board.

The fourth and final case had no connector legs and it had an optimised taper. An S_{11} of $-37.89\ dB$ was determined at $2.45\ GHz$. This was the best result. It had an improvement of $11.37\ dB$ over the first case (with legs and no taper).
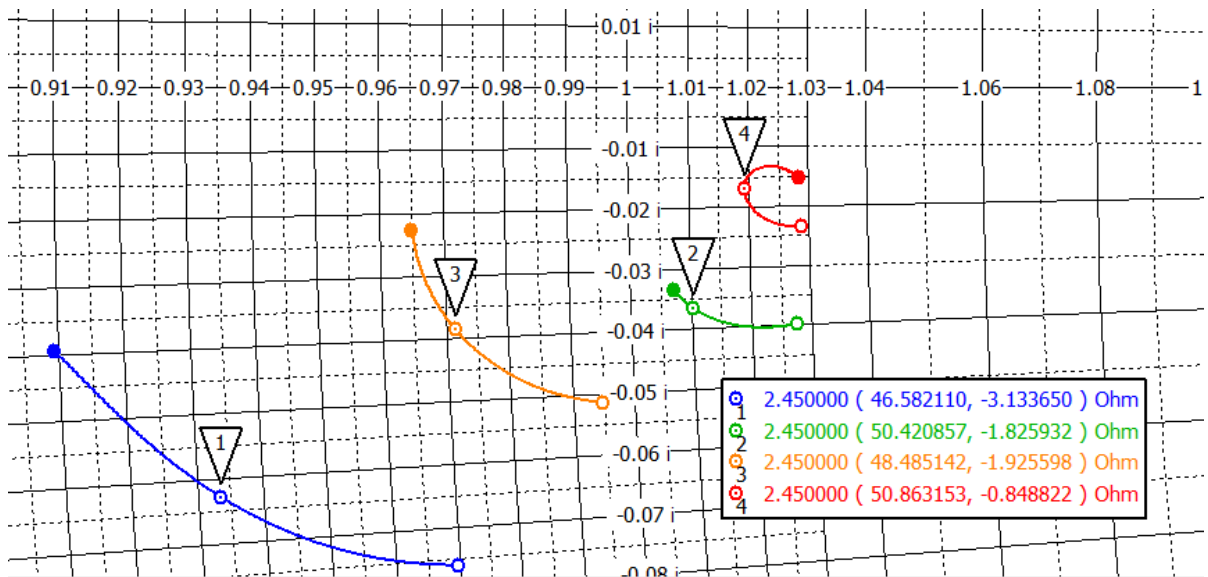
Figure B.17: S_{11} of the four different types of SMA to microstrip transitions plotted on a Smith chart from 2 to 3 GHz.

The S_{11} parameter of the transition was always capacitive, as expected (in the bottom half of the Smith chart, see Figure B.17). This was because there were capacitive effects between the base plate of the connector and the microstrip, and between the legs of the connector and the microstrip.

Similar to the bottom-feed transition, an edge connected to edge connected transition setup was also simulated and constructed for the sake of de-embedding, shown in Figure B.18 and Figure B.19.
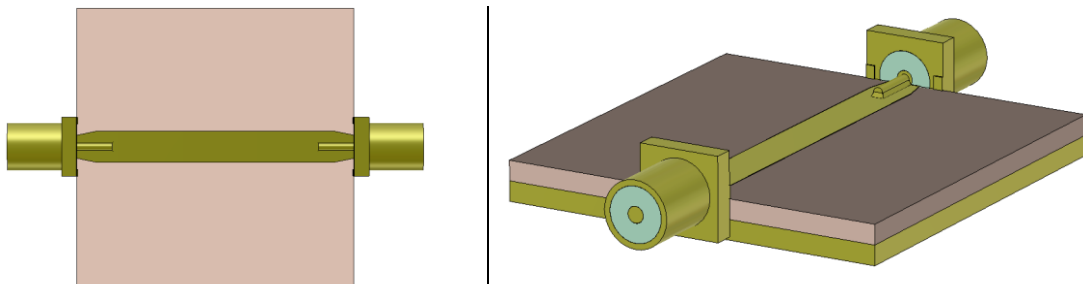
Figure B.18: Top view and perspective view of the CST model of the edge connected coaxial to microstrip transitions.
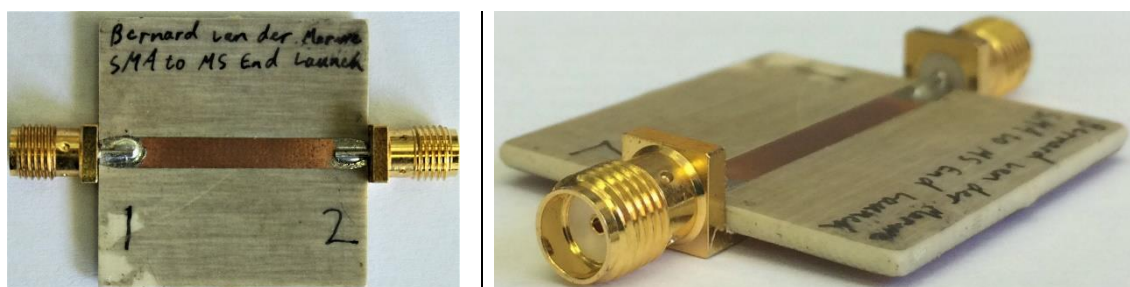
Figure B.19: Top view and perspective view of the constructed edge connected coaxial to microstrip transitions.

Figure B.20 shows a comparison between the CST simulation and the measured data.

135
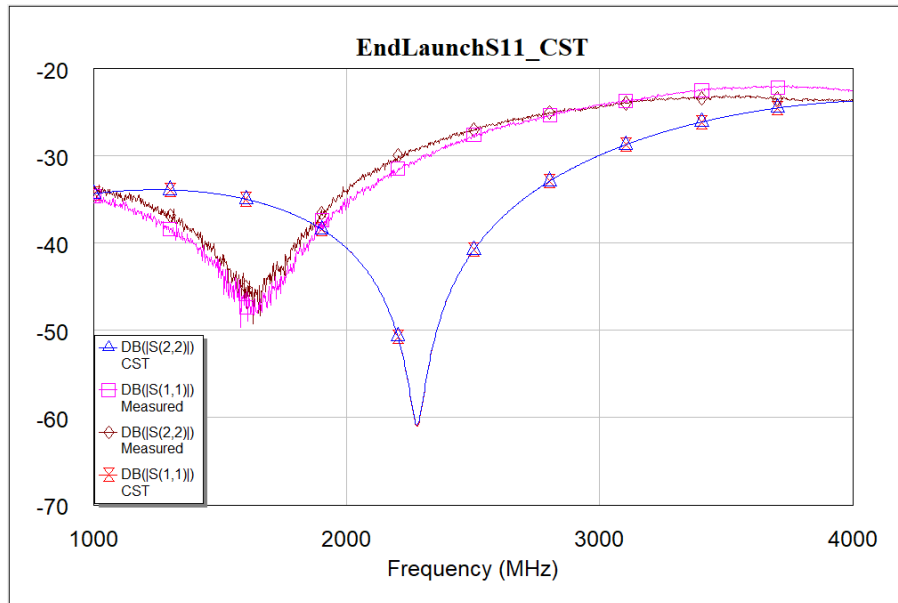
Figure B.20: Comparison of S11 between the 3D simulation and the measured data for an edge connected SMA to microstrip transition.

The lowest point in the graph had shifted down in frequency compared to the CST simulation. There was not a clear reason for this. It may have been due to slight variations in the dimensions of the physical connectors compared to the simulation model. It may have been due to a construction defect such as a cold joint or the connectors being slightly misaligned.

In order to determine the S-parameters for a single transition, the same method was followed as for the bottom-feed transition. The same model, as shown in Figure B.9, was re-tuned to match the edge connected transition. The reference planes were defined as shown in Figure B.21.
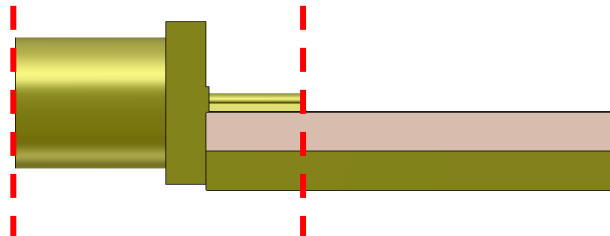
Figure B.21: Reference planes used in de-embedding the edge connected SMA to microstrip transition.

Figure B.22 and Figure B.23 shows a comparison of S-parameters between the measured results, the model that matches the simulation and the extraction of a single transition.
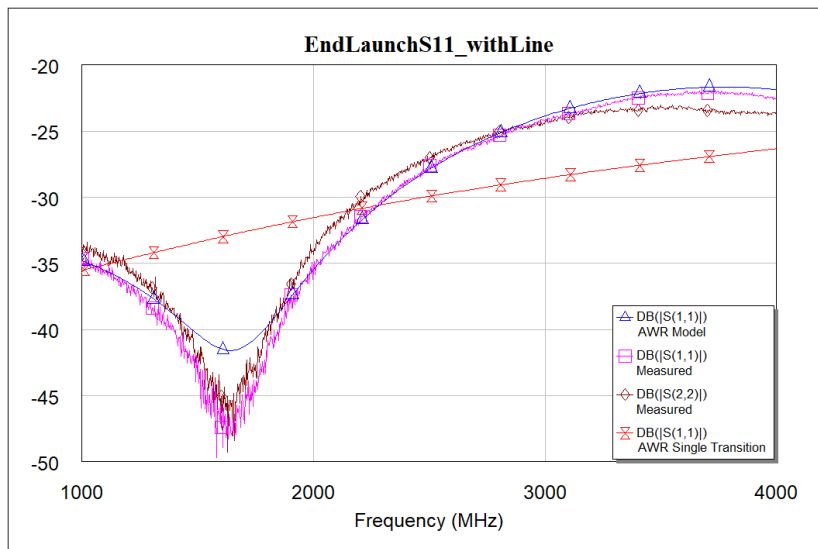
Figure B.22: Comparison of S_{11} between measured results, the AWR model that matches the simulation and the extraction of a single transition for an edge connected SMA to microstrip transition.
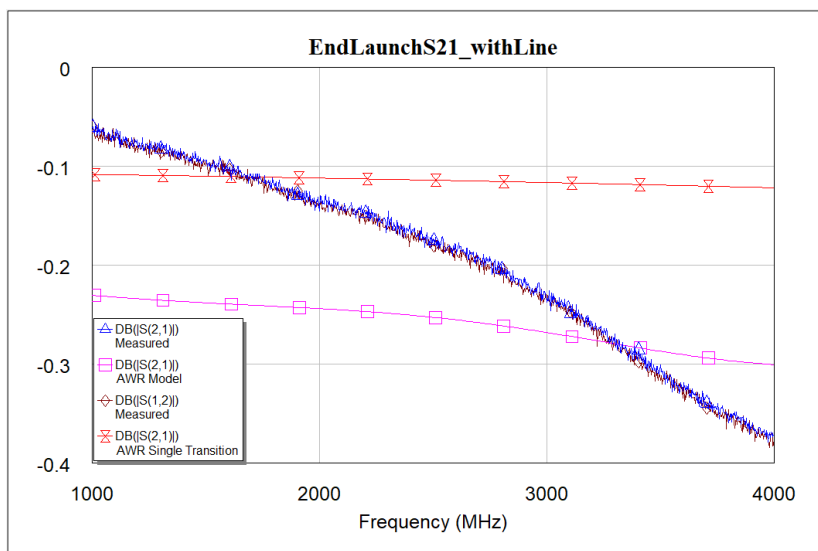
Figure B.23: Comparison of S_{21} between measured results, the AWR model that matches the simulation and the extraction of a single transition for an edge connected SMA to microstrip transition.

An S_{11} of less than $-28\ dB$ was seen between 2 and $3\ GHz$ for the single transition. This was still a good transition, but not as good as the bottom feed transition (which was smaller than $-40\ dB$ over a wider range). The edge connected transition could, however, still be fine-tuned to have its minimum point at $2.5\ GHz$.

137

Bibliography

[1]   A. E. Oberholzer, "Development of a continuous flow sterilisation system using microwaves," 2017.

[2]   J. P. Van der Merwe, "Magnetron output power controller used in the application of rooibos tea sterilisation," 2019.

[3]   M. C. Herbst, "Fact Sheet on Rooibos Tea."

[4]   "ROOIBOS INDUSTRY FACT SHEET 2018."

[5]   P. Gouws, T. Hartel, and R. van Wyk, "The influence of processing on the microbial risk associated with Rooibos (Aspalathus linearis) tea," *J. Sci. Food Agric.*, vol. 94, no. 15, pp. 3069–3078, 2014.

[6]   S. Kumar and S. Shukla, *Concepts and applications of microwave engineering*. PHI Learning, 2014.

[7]   D. Pozar, *Microwave Engineering Fourth Edition*. 2005.

[8]   Litton Industries 1965, "Litton - For Heat, Tune to 915 or 2450 Megacycles." [Online]. Available: http://www.smecc.org/litton_-_for_heat,_tune_to_915_or_2450_megacycles.htm. [Accessed: 30-Sep-2019].

[9]   "Radiation - definition of radiation by The Free Dictionary." [Online]. Available: https://www.thefreedictionary.com/radiation. [Accessed: 30-Sep-2019].

[10]   Biology Dictionary, "Polar Molecule - Definition and Examples | Biology Dictionary." [Online]. Available: https://biologydictionary.net/polar-molecule/. [Accessed: 03-Oct-2019].

[11]   "polarization," *American Heritage® Dictionary of the English Language, Fifth Edition*, 2011. [Online]. Available: https://www.thefreedictionary.com/polarization. [Accessed: 03-Oct-2019].

[12]   A. C. Metaxas and R. J. (Roger J. . Meredith, *Industrial microwave heating*. P. Peregrinus on behalf of the Institution of Electrical Engineers, 1983.

[13]   R. Chen and N. Marathe, "Dielectric Polarization - Engineering LibreTexts," 2019. [Online]. Available: https://eng.libretexts.org/Bookshelves/Materials_Science/Supplemental_Modules_(Materials_Science)/Optical_Properties/Dielectric_Polarization. [Accessed: 03-Oct-2019].

[14]   M. J. Kamaruddin, M. S. B. M. Yusof, N. Ngadi, Z. Y. Zakaria, A. Arsad, and K. Kidam, "Dielectric Properties for Extraction of Orthosiphon Stamineus (Java Tea) Leaves," *Chem. Eng. Trans.*, vol. 56, pp. 1771–1776, Mar. 2017.

[15]   L. W. Turner, *Electronics engineer's reference book*. Newnes-Butterworths, 1976.

[16]   C. Wolff, "Radar Basics - Magnetron." [Online]. Available: http://www.radartutorial.eu/08.transmitters/Magnetron.en.html. [Accessed: 07-Oct-2019].

[17]   K. Nuanyai, N. Puangngernmak, and S. Chalermwisutkul, "A Novel Low Cost Magnetron Power Control for Microwave Heating Applications."

[18]   A. C. Metaxas, *Foundations of electroheat : a unified approach*. Wiley, 1996.

[19]   D. Haguenauer, "Microwave oven power granularity." [Online]. Available: http://www.kurokatta.org/grumble/2018/08/microwave-oven-power. [Accessed: 15-Oct-2019].

[20]   J. P. Van Der Merwe and J. B. De Swardt, "Power control of a domestic microwave oven," *2017 IEEE AFRICON Sci. Technol. Innov. Africa, AFRICON 2017*, pp. 574–578, 2017.

[21]   "Triac Tutorial and Triac Switching Circuits." [Online]. Available: https://www.electronics-tutorials.ws/power/triac.html. [Accessed: 21-Oct-2019].

[22]   A. Shazman, S. Mizrahi, U. Cogan, and E. Shimoni, "Examining for possible non-thermal effects during heating in a microwave oven," *Food Chem.*, vol. 103, no. 2, pp. 444–453, 2007.

[23]   Y. Shamis, R. Croft, A. Taube, R. J. Crawford, and E. P. Ivanova, "Review of the specific effects of microwave radiation on bacterial cells," *Applied Microbiology and Biotechnology*, vol. 96, no. 2. pp. 319–325, Oct-2012.

[24]   F. Celandroni *et al.*, "Effect of microwave radiation on Bacillus subtilis spores," *J. Appl. Microbiol.*, vol. 97, no. 6, pp. 1220–1227, 2004.

[25]   "Bacterial Endospores | Department of Microbiology." [Online]. Available: https://micro.cornell.edu/research/epulopiscium/bacterial-endospores/. [Accessed: 06-Nov-2019].

[26]   G. Sumnu and S. Sahin, "Recent Developments in Microwave Heating-16," in *Emerging Technologies for Food Processing*, 2005, pp. 419–444.

[27]   D. M. Bozhilova, "Difference Between Sterilization and Pasteurization | Difference Between," 2019. [Online]. Available: http://www.differencebetween.net/science/difference-between-sterilization-and-pasteurization/. [Accessed: 21-Nov-2019].

[28]   "Denature | Definition of Denature by Merriam-Webster." [Online]. Available: https://www.merriam-webster.com/dictionary/denature. [Accessed: 07-Nov-2019].

[29]   S. R. S. Dev, S. L. Birla, G. S. V. Raghavan, and J. Subbiah, "Microbial Decontamination of Food by Microwave (MW) and Radio Frequency (RF)," in *Microbial Decontamination in the Food Industry - Novel Methods and Applications*, Elsevier, 2012.

[30]   "Gram-negative Bacteria | NIH: National Institute of Allergy and Infectious Diseases." [Online]. Available: https://www.niaid.nih.gov/research/gram-negative-bacteria. [Accessed: 07-Nov-2019].

[31]   "Heat: Sanitation and Sterilization | Viticulture and Enology." [Online]. Available: https://wineserver.ucdavis.edu/industry-info/enology/methods-and-techniques/winery-lab-techniques/heat-sanitation-and-sterilization. [Accessed: 07-Nov-2019].

[32]   "E. coli - Symptoms and causes - Mayo Clinic." [Online]. Available: https://www.mayoclinic.org/diseases-conditions/e-coli/symptoms-causes/syc-20372058. [Accessed: 07-Nov-2019].

[33]   "Featured Microbe: Lactococcus lactis." [Online]. Available: http://textbookofbacteriology.net/featured_microbe.html. [Accessed: 07-Nov-2019].

[34]   "Viability | Definition of Viability at Dictionary.com." [Online]. Available: https://www.dictionary.com/browse/viability. [Accessed: 07-Nov-2019].

[35]   "Types of Agar Plates." [Online]. Available: https://sciencing.com/types-agar-plates-8131230.html. [Accessed: 07-Nov-2019].

[36]   "What Is a CFU in Microbiology?" [Online]. Available: https://sciencing.com/cfu-microbiology-15601.html. [Accessed: 07-Nov-2019].

[37]   D. D. Muir, "The stability and shelf life of milk and milk products," *Food Beverage Stab. Shelf Life*, pp. 755–778, Jan. 2011.

[38]   S. B. Cohn and R. Levy, "History of Microwave Passive Components with Particular Attention to Directional Couplers," *IEEE Trans. Microw. Theory Tech.*, vol. 32, no. 9, pp. 1046–1054, Sep. 1984.

[39] Y. Blanchard, G. Galati, and P. van Genderen, "The Cavity Magnetron: Not Just a British Invention [Historical Corner]," *IEEE Antennas Propag. Mag.*, vol. 55, no. 5, pp. 244–254, Oct. 2013.

[40] "Microwaves101 Coupler Fundamentals." [Online]. Available: https://www.microwaves101.com/encyclopedias/coupler-fundamentals. [Accessed: 15-Jun-2018].

[41] Robert E. Collin, *Foundations for Microwave Engineering, 2nd Edition*. 2000.

[42] T. N. Anderson, "Directional Coupler Design Nomograms," *Microw. J.*, vol. 2, pp. 34–38, 1959.

[43] P. P. Lombardini, R. F. Schwartz, and P. J. Kelly, "Criteria for the Design of Loop-Type Directional Couplers for the L Band," in *IRE Transactions on Microwave Theory and Techniques*, 1956, pp. 234–239.

[44] S. Kumar, C. Tannous, and T. Danshin, "A Multisection Broadband Impedance Transforming Branch-Line Hybrid," *IEEE Trans. Microw. Theory Tech.*, vol. 43, no. 11, pp. 2517–2523, 1995.

[45] "WR-340 Waveguides." [Online]. Available: https://www.pasternack.com/wr-340-waveguides-category.aspx. [Accessed: 01-Nov-2019].

[46] "Waveguide Sizes | Dimensions & Cutoff Frequency - everything RF." [Online]. Available: https://www.everythingrf.com/tech-resources/waveguides-sizes. [Accessed: 01-Nov-2019].

[47] C. A. Balanis, *Advanced engineering electromagnetics*. Wiley, 1989.

[48] "Antenna-Theory.com - Fractional Bandwidth." [Online]. Available: http://www.antenna-theory.com/definitions/fractionalBW.php. [Accessed: 30-Aug-2019].

[49] "10 Ways to Destroy an Arduino — Rugged Circuits." [Online]. Available: https://www.rugged-circuits.com/10-ways-to-destroy-an-arduino. [Accessed: 28-Oct-2019].

[50] B. Schweber, "Solving the RF Power-Detection Challenge | DigiKey," 2016. [Online]. Available: https://www.digikey.com/en/articles/techzone/2016/apr/solving-the-rf-power-detection-challenge. [Accessed: 07-Oct-2019].

[51] Keysight Technologies, "Fundamentals of RF and Microwave Power Measurements (Part 2) (AN 1449-2)."

[52] "THERMISTOR BASICS – Wavelength Electronics." [Online]. Available: https://www.teamwavelength.com/thermistor-basics/. [Accessed: 08-Oct-2019].

[53] Panasonic, "Multilayer NTC Thermistors."

[54] A. Mehmood and D. J. Fang, "RF and microwave power detection with Schottky diodes," Munich, 2018.

[55] MACOM Technology Solutions, "MA4E2054 Series."

[56] Minicircuits, "Power Detector ZX47-40+," Brooklyn, 2015.

[57] Keysight Technologies, "Keysight 8478B Thermistor Mount," Penang, 2018.

[58] "NCP18XF101J03RB | Murata NCP18XF101J03RB Thermistor 0603 100Ω, 1.6 x 0.8 x 0.8mm | RS Components." [Online]. Available: https://za.rs-online.com/web/p/thermistor-ics/0110453/. [Accessed: 10-Oct-2019].

[59] "MA4E20541-1141T M/A-Com Technology Solutions | Discrete Semiconductor Products | DigiKey." [Online]. Available: https://www.digikey.co.za/product-detail/en/m-a-com-technology-solutions/MA4E20541-1141T/1465-1219-1-ND/4429916?_ga=2.47400163.596735909.1570470088-1015595530.1532090103. [Accessed:

10-Oct-2019].

[60] "Mini-Circuits ZX47-40-S+." [Online]. Available: https://www.minicircuits.com/WebStore/dashboard.html?model=ZX47-40-S%2B. [Accessed: 10-Oct-2019].

[61] Unknown Author, "Microwaves101 | Quarter-wave Tricks." [Online]. Available: https://www.microwaves101.com/encyclopedias/quarter-wave-tricks#biastee. [Accessed: 16-Oct-2019].

[62] "Negative Temperature Coefficient Chip Thermistors Datasheet," Manchester.

[63] R. K. Hoffmann and H. H. Howe, *Handbook of Microwave Integrated Circuits*. Norwood: Artech House, 1987.

[64] Texas Instruments Incorporated, "LM35 Precision Centigrade Temperature Sensors Datasheet," Dallas, 2019.

[65] A. Fong *et al.*, "Measurements and Analysis," in *Reference Data for Engineers*, Elsevier, 2002, pp. 12-1-12–39.

[66] Texas Instruments, "TL08xx JFET-Input Operational Amplifiers," 2015.

[67] Texas Instruments, "TLC227x, TLC227xA: Advanced LinCMOS Rail-to-Rail Operational Amplifiers," 2016.

[68] Texas Instruments, "TLV4110, TLV4111, TLV4112, TLV4113 FAMILY OF HIGH OUTPUT DRIVE OPERATIONAL AMPLIFIERS WITH SHUTDOWN," 2006.

[69] "Op Amps | RS Components." [Online]. Available: https://za.rs-online.com/web/c/semiconductors/amplifiers-comparators/op-amps/?searchTerm=tlc2272&redirect-relevancy-data=636F3D3126696E3D4931384E53656172636847656E65726963266C753D656E266D6D3D6D61746368616C6C7061727469616C26706D3D5E5B5C707B4C7D5C707B4E647D2D2C2F255C2E5D2B2426706F3D31333326736E3D592673723D2673743D4B4559574F52445F53494E474C455F414C5048415F4E554D455249432673633D592677633D4E4F4E452675737373743D746C6332323732267374613D746C633232373226&r=f&searchHistory=%7B%22enabled%22:true%7D. [Accessed: 23-Oct-2019].

[70] "TLV4110IP Texas Instruments | Integrated Circuits (ICs) | DigiKey." [Online]. Available: https://www.digikey.co.za/products/en/integrated-circuits-ics/linear-amplifiers-instrumentation-op-amps-buffer-amps/687?k=tlv4110&k=&pkeyword=tlv4110&sv=0&pv69=411897&sf=0&quantity=&ColumnSort=0&page=1&pageSize=25. [Accessed: 23-Oct-2019].

[71] Philips Semiconductor, "Philips 2N2219; 2N2219A NPN switching transistors," 1997.

[72] Texas Instruments, "INA126, INA2126 Datasheet," 2015.

[73] "INA126P Texas Instruments | Integrated Circuits (ICs) | DigiKey." [Online]. Available: https://www.digikey.co.za/product-detail/en/texas-instruments/INA126P/INA126P-ND/254672. [Accessed: 27-Oct-2019].

[74] D. A. Neamen, *Microelectronics : circuit analysis and design*. McGraw-Hill, 2010.

[75] "Zener Diode | Definition | Working Principle | Characteristics | Applications | Electrical Academia." [Online]. Available: http://electricalacademia.com/electronics/zener-diode-definition-working-principle-characteristics-applications/. [Accessed: 31-Oct-2019].

[76] Atmel Corporation, "Atmel ATmega16U4/ATmega32U4 Datasheet," 2015.

[77]   "ROHDE & SCHWARZ SMIQ04B Datasheet."

[78]   Optris GmbH, "Optris CS LT User Manual."

[79]   "Neon Bulb Array Technical Data Sheet." [Online]. Available: https://www.emsdiasum.com/microscopy/technical/datasheet/97036.aspx. [Accessed: 18-Nov-2019].

[80]   "AN437 Application note RC snubber circuit design for TRIACs," 2007.

[81]   "NXP Semiconductors BT139X-600F."

[82]   Motorola, "Motorola Optoelectronics Device Data 6-Pin DIP Optoisolators Darlington Output (No Base Connection)."

[83]   G. F. Franklin, J. D. Powell, and A. Emami-Naeini, *Feedback control of dynamic systems*, 7th ed. Pearson Education Limited, 2015.

[84]   W. S. Kim, J. Ren, and N. W. Dunn, "Differentiation of *Lactococcus lactis* subspecies *lactis* and subspecies *cremoris* strains by their adaptive response to stresses," *FEMS Microbiol. Lett.*, vol. 171, no. 1, pp. 57–65, Feb. 1999.

[85]   P. Gouws, T. Hartel, and R. van Wyk, "The influence of processing on the microbial risk associated with Rooibos (*Aspalathus linearis*) tea," *J. Sci. Food Agric.*, vol. 94, no. 15, pp. 3069–3078, Dec. 2014.

[86]   "De-Embedding and Embedding S-Parameter Networks Using a Vector Network Analyzer."

[87]   "LG 2M213 SERIES Datasheet."

[88]   Defy, "Circuit Schematic Diagram for Defy DMO368." .

[89]   "Bulk Loose Teas – Khoisan Gourmet." [Online]. Available: http://www.khoisantea.com/bulk-loose-rooibos-greenrooibos-teas/#iLightbox[158fef2b93d8bdf28a0]/0. [Accessed: 07-Nov-2019].

[90]   "1-1478967-0 | TE Connectivity Straight 50Ω Panel Mount SMA Connector, Solder Termination Coaxial | RS Components." [Online]. Available: https://za.rs-online.com/web/p/sma-connectors/4683233/. [Accessed: 06-Nov-2019].

[91]   "Arduino - ArduinoBoardLeonardo." [Online]. Available: https://www.arduino.cc/en/Main/Arduino_BoardLeonardo. [Accessed: 20-Nov-2019].